Theoretical Astroparticle Physics

Contents

1. Topics

- Electron-positron plasma
  - Relaxation timescales in the pair plasma
  - Degenerate electron-positron plasma
  - Hydrodynamic phase of GRBs
  - Thermal spreading of the fireshell
- Neutrinos in cosmology
  - Massive neutrino and structure formation
  - Cellular structure of the Universe
  - Lepton asymmetry of the Universe
- Dark Matter in the Universe
  - Dark Matter candidates
  - Indirect Detection of Dark Matter
  - Estimation of cosmological paremeters

2. Participants

2.1. ICRANet participants

- Carlo Luciano Bianco
- Massimiliano Lattanzi
- Remo Ruffini
- Gregory Vereshchagin
- She-Sheng Xue

2.2. Past collaborators

- Marco Valerio Arbolino (DUNE s.r.l., Italy)
- Andrea Bianconi (INFN Pavia, Italy)
- Neta A. Bahcall (Princeton University, USA)
- Daniella Calzetti (University of Massachusets, USA)
- Jaan Einasto (Tartu Observatory, Estonia)
- Roberto Fabbri (University of Firenze, Italy)
- Long-Long Feng (University of Science and Technology of China, China)
- Jiang Gong Gao (Xinjiang Institute of Technology, China)
- Mauro Giavalisco (University of Massachusets, USA)
- Gabriele Ingrosso (INFN, University of Lecce, Italy)
- Yi-peng Jing (Shanghai Astronomical Observatory, China)
- Hyung-Won Lee (Inje University, South Korea)
- Marco Merafina (University of Rome "Sapienza", Italy)
- Houjun Mo (University of Massachusetts, USA)

- Enn Saar (Tartu Observatory, Estonia)
- Jay D. Salmonson (Livermore Lab, USA)
- Luis Alberto Sanchez (National University Medellin, Colombia)
- Costantino Sigismondi (ICRA and University of Rome ”La Sapienza”, Italy)
- Doo Jong Song (Korea Astronomy Observatory, South Korea)
- Luigi Stella (Astronomical Observatory of Rome, Italy)
- William Stoeger (Vatican Observatory, University of Arizona USA)
- Sergio Taraglio (ENEA, Italy)
- Gerda Wiedenmann (MPE Garching, Germany)
- Jim Wilson (Livermore Lab, USA)
- Roustam Zalaletdinov (Tashkent University, Uzbekistan)

2.3. Ongoing collaborations

- Alexey Aksenov (ITEP, Russia)
- Valeri Chechetkin (Keldysh Institute, Russia)
- Urbano França (Instituto de Física Corpuscular, Valencia, Spain)
- Julien Lesgourgues (CERN, Theory Division, Geneva, Switzerland)
- Alessandro Melchiorri (Univ. “Sapienza” di Roma, Italy)
- Lidia Pieri (Institute d’Astrophysique, Paris, France)
- Sergio Pastor (Instituto de Física Corpuscolar, Valencia, Spain)
- Joseph Silk (Oxford University, UK)

2.4. Students

- Gustavo de Barros (IRAP PhD, Brazil)
- Alberto Benedetti (Erasmus Mundus IRAP PhD, Italy)
- Wien Biao Han (IRAP PhD, China)
- Eloisa Menegoni (IRAP PhD, Italy)
- Stefania Pandolfi (IRAP PhD, Italy)
- Ivan Siutsou (IRAP PhD, Belarus)

3. Brief description

Astroparticle physics is a new field of research emerging at the intersection of particle physics, astrophysics and cosmology. Theoretical development in these fields is mainly triggered by the growing amount of experimental data of unprecedented accuracy, coming both from the ground based laboratories and from the dedicated space missions.

3.1. Electron-positron plasma

Electron-positron plasma is of interest in many fields of astrophysics, e.g. in the early universe, gamma-ray bursts, active galactic nuclei, the center of our Galaxy, hypothetical quark stars. It is also relevant for the physics of ultraintense lasers and thermonuclear reactions. We study some properties of dense and hot electron-positron plasmas. In particular, we are interested in the issues of its creation and relaxation, its kinetic properties and hydrodynamic description, baryon loading, transition to transparency and radiation from such plasmas.

Two completely different states exist for electron-positron plasma: optically thin and optically thick. Optically thin pair plasma may exist in active galactic nuclei and in X-ray binaries. The theory of relativistic optically thin nonmagnetic plasma and especially its equilibrium configurations was established in the 80s by Svensson, Lightman, Gould and others. It was shown that relaxation of the plasma to some equilibrium state is determined by a dominant reaction, e.g. Compton scattering or bremsstrahlung.

Developments in the theory of gamma ray bursts from one side, and observational data from the other side, unambiguously point out on existence of optically thick pair dominated non-steady phase in the beginning of formation of GRBs. The spectrum of radiation from optically thick plasma is assumed to be thermal. However, in such a transient phenomena as gamma-ray bursts there could be not enough time for the plasma to relax into complete equilibrium.

3.1.1. Pair plasma relaxation timescales

In previous works (Aksenov et al. (2007), Aksenov et al. (2009b)) relaxation timescales were computed explicitly only in few cases. Systematic exploration of the space of parameters is performed in a separate publication by

Aksenov et al. (2010), see Appendix A. These parameters are: total energy density ρ and the baryonic loading parameter $B = \rho_b/\rho_{e,\gamma}$, the ratio between the energy densities of baryons and of electron-positron pairs and photons. We focused on the time scales of electromagnetic interactions only.

Thermalization timescales are computed for a wide range of values of both the total energy density (10^{23}erg/cm$^3 \leq \rho \leq 10^{33}$erg/cm^3) and of the baryonic loading parameter ($10^{-3} \leq B \leq 10^3$). This also allows to study such interesting limiting cases as the almost purely electron-positron plasma or electron-proton plasma as well as intermediate cases.

Both dependencies (thermalization time scales of electron-positron-photon component and final thermalization time scale of pair plasma with baryonic loading) cannot be fitted by simple power laws, though decrease monotonically with increasing total energy density, see Figs. A.1,A.2. Thermalization time scales are not monotonic functions of the baryonic loading parameter.

The relaxation to thermal equilibrium always occurs on a time scale less than 10^{-9} sec. It is interesting that the electron-positron-photon component and/or proton component can thermalize earlier than the time at which complete thermal equilibrium is reached. The relevant time scales are given and compared with the order-of-magnitude estimates.

These results appear to be important both for laboratory experiments aimed at generating optically thick pair plasmas as well as for astrophysical models in which electron-positron pair plasmas play a relevant role.

3.1.2. Degenerate electron-positron plasma

The kinetic code, which is used to compute the evolution of nonequilibrium distribution functions of electrons, positrons, photons and protons towards thermal equilibrium, is designed in such a way that particles are considered nondegenerate. The assumption of nondegeneracy simplifies the computation, but more importantly, it substantially reduces the computational time. When temperatures increase the degeneracy of electron-positron-photon component increases as well.

It is the aim of the work described in Appendix B to explore the sensitivity of the timescales of thermalization when degeneracy of pairs and photons is allowed. The code has been modified in order to take into account Pauli blocking and Bose enhancment factors in binary reactions involving leptons. These modifications allow to compute evolution of pair plasma with baryonic loading towards kinetic equilibrium, taking into account degeneracy of the pair plasma. It is shown, that the timescales indeed increase due to degeneracy, especially for temperatures above 0.5 MeV.

3.1.3. Hydrodynamic phase of GRBs

Having established the thermalization timescales of electron-positron plasma with baryonic loading we turn to hydrodynamic evolution of this plasma on much longer timescales. Given that the optical depth of the pair plasma in GRB sources is huge, of the order of 10^{15}, the dynamical equations are the total energy-momentum conservation as well as the continuity equation for baryonic component.

The fireshell model, unlike the fireball model, properly takes into account nonequilibrium processes in the pair plasma by the rate equation of electron-positron component. However, it only operates with volume-averaged macroscopic quantities such as average number densities, average energy densities, average bulk Lorentz factors etc.

We developed an Eulerian relativistic code, which solves hydrodynamic equations in spherically symmetric case (de Barros et al. (2009)), see Appendix C. We were mainly interested in the issue how different initial spatial distribution for energy and mass densities influence the early evolution of the pair plasma with baryonic loading. We found that deviations from a simple "frozen radial profile" advocated by Piran et al. (1993), see also Piran (1999) in spatial distributions of energy and matter densities are possible. In fact when the expansion occurs not in vacuum but in a cold medium, two shocks are formed, one propagating into the external medium and another occuring in the expanding shell. It is surprizing that the reverse shock does not propagate into the expanding shell during its acceleration. Such complex structures in the energy and matter spatial distributions of the expanding plasma, if survived when transparency is reached, will be reflected in the light curves of P-GRBs. This gives a fascinating possibility to probe the structure of energy and matter distributions withing the sources of GRBs where the energy is released.

3.1.4. Thermal spreading of the fireshell

Within the fireshell model, based on the hydrodynamic approach, the duration of the P-GRB is determined by the initial size of electron-positron plasma and is expected to be $\Delta t \simeq R_0/c \simeq 10^{-2}$ sec. In Appendix D we present the results of evaluation of the thermal spreading of the fireshell due to nonzero velocity dispersion. This spreading is a kinetic effect and is not accounted for in hydrodynamic approximation. The possibility of such spreading for GRBs is discussed first in Mészáros et al. (1993). However, the authors of Mészáros et al. (1993) overestimate the spreading since they consider it independent on the temperature, while the latter changes during expansion of the fireshell.

Our results suggest that the value of thermal spreading is actually significant and may reach $\Delta R \simeq 8R_0$. Thus the P-GRB is expected to last about 8 times longer, than the estimates based on the initial size of the fireshell give.

3.2. Neutrinos in cosmology

Many observational facts make it clear that luminous matter alone cannot account for the whole matter content of the Universe. Among them there is the cosmic background radiation anisotropy spectrum, that is well fitted by a cosmological model in which just a small fraction of the total density is supported by baryons.

In particular, the best fit to the observed spectrum is given by a flat ΛCDM model, namely a model in which the main contribution to the energy density of the Universe comes from vacuum energy and cold dark matter. This result is confirmed by other observational data, like the power spectrum of large scale structures.

Another strong evidence for the presence of dark matter is given by the rotation curves of galaxies. In fact, if we assume a spherical or ellipsoidal mass distribution inside the galaxy, the orbital velocity at a radius r is given by Newton's equation of motion. The peculiar velocity of stars beyond the visible edge of the galaxy should then decrease as $1/r$. What is instead observed is that the velocity stays nearly constant with r. This requires a halo of invisible, dark, matter to be present outside the edge. Galactic size should then be extended beyond the visible edge. From observations is follows that the halo radius is at least 10 times larger than the radius of visible part of the galaxy. Then it follows that a halo is at least 10 times more massive than all stars in a galaxy.

Neutrinos were considered as the best candidate for dark matter about twenty years ago. Indeed, it was shown that if these particles have a small mass $m_\nu \sim 30\,\mathrm{eV}$, they provide a large energy density contribution up to critical density. Tremaine and Gunn (1979) have claimed, however, that massive neutrinos cannot be considered as dark matter. Their paper was very influential and turned most of cosmologists away from neutrinos as cosmologically important particles.

Tremaine and Gunn paper was based on estimation of lower and upper bounds for neutrino mass; when contradiction with these bounds was found, the conclusion was made that neutrinos cannot supply dark matter. The upper bound was given by cosmological considerations, but compared with the energy density of clustered matter. It is possible, however, that a fraction of neutrinos lays outside galaxies.

Moreover, their lower bound was found on the basis of considerations of galactic halos and derived on the ground of the classical Maxwell-Boltzmann statistics. Gao and Ruffini (1980) established a lower limit on the neutrino mass by the assumption that galactic halos are composed by degenerate neutrinos. Subsequent development of their approach Arbolino and Ruffini (1988) has shown that contradiction with two limits can be avoided.

At the same time, in 1977 the paper by Lee and Weinberg (1977) appeared, in which authors turned their attention to massive neutrinos with $m_\nu >> 2\,\mathrm{GeV}$. Such particles could also provide a large contribution into the energy density of the Universe, in spite of much smaller value of number density.

Recent experimental results from laboratory (see Dolgov (2002) for a review) rule out massive neutrinos with $m_\nu > 2\,\mathrm{GeV}$. However, the paper by Lee and Weinberg was among the first where very massive particles were considered as candidates for dark matter. This can be considered as the first of cold dark matter models.

Today the interest toward neutrinos as a candidate for dark matter came down, since from one side, the laboratory limit on its mass do not allow for significant contribution to the density of the Universe, and from other side, conventional neutrino dominated models have problems with formation of structure on small scales. However, in these scenarios the role of the chemical potential of neutrinos was overlooked, while it could help solving both problems.

3.2.1. Massive neutrino and structure formation

Lattanzi et al. (2003) have studied the possible role of massive neutrinos in the large scale structure formation. Although now it is clear, that massive light neutrinos cannot be the dominant part of the dark matter, their influence on the large scale structure formation should not be underestimated. In particular, large lepton asymmetry, still allowed by observations, can affect cosmological constraints on neutrino mass.

3.2.2. Cellular structure of the Universe

One of the interesting possibilities, from a conceptual point of view, is the change from the description of the physical properties by a continuous function, to a new picture by introducing a self-similar fractal structure. This approach has been relevant, since the concept of homogeneity and isotropy formerly apply to any geometrical point in space and leads to the concept of a Universe observer-homogeneous (Ruffini (1989)). Calzetti et al. (1987), Giavalisco (1992), Calzetti et al. (1988) have defined the correlation length of a fractal

$$r_0 = \left(1 - \frac{\gamma}{3}\right)^{1/\gamma} R_S, \tag{3.2.1}$$

where R_S is the sample size, $\gamma = 3 - D$, and D is the Hausdorff dimension of the fractal. Most challenging was the merging of the concepts of fractal, Jeans mass of dark matter and the cellular structure in the Universe, advanced by Ruffini et al. (1988). The cellular structure emerging from this study is repre-

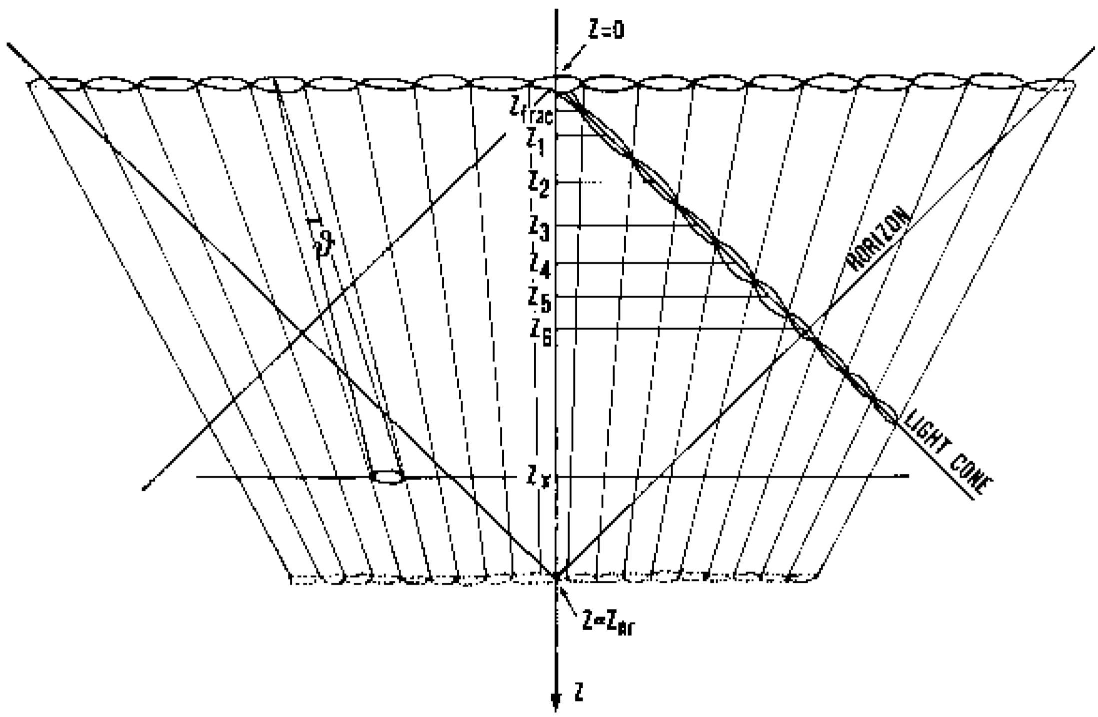

Figure 3.1.: Cellular structure of the Universe.

sented in Figure 3.1. There the upper cutoff in the fractal structure $R_{\mathrm{cutoff}} \approx$ 100 Mpc, was associated to the Jeans mass of the "ino" $M_{\mathrm{cell}} = \left(\frac{m_{pl}}{m_{ino}}\right)^2 m_{pl}$.

3.2.3. Lepton asymmetry of the Universe

Lattanzi et al. (2005), Lattanzi et al. (2006) studied how the cosmological constraints on neutrino mass are affected by the presence of a lepton asymmetry. The main conclusion is that while constraints on neutrino mass do not change by the inclusion into the cosmological model the dimensional chemical potential of neutrino, as an additional parameter, the value of lepton asymmetry allowed by the present cosmological data is surprisingly large, being

$$L = \sum_{\nu} \frac{n_\nu - n_{\bar{\nu}}}{n_\gamma} \lesssim 0.9, \qquad (3.2.2)$$

Therefore, large lepton asymmetry is not ruled out by the current cosmological data. Details see in Appendix C.

3.3. Dark Matter in the Universe

The existence in the Universe of an exotic, non-luminous matter component, the so-called *dark matter* (DM), is supported, at least indirectly, by a large number of astrophysical and cosmological observations at different scales. The most convincing and direct evidence for the existence of DM on galactic scales comes from observations of the rotation curves of galaxies, that do not have the shape that would be expected just in the presence of the luminous matter visible in the galaxy (see e.g. Begeman et al., 1991). A similar discrepancy between the total mass, as estimated through dynamical means, and the visible mass exists at the scale of galaxy clusters; in fact, the mass-to-light ratio of galaxy clusters, as inferred from measurements of the velocity dispersion of galaxies, exceeds the value in the solar neighborhood by two orders of magnitude (see e.g. Bahcall and Fan, 1998). Finally, according to the standard cosmological model, motivated by measurements of temperature anisotropies in the Cosmic Microwave Background (CMB) (Spergel et al., 2003, 2007; Komatsu et al., 2009; Dunkley et al., 2009; Larson et al., 2010), the large scale distribution of galaxies (Cole et al., 2005; Tegmark et al., 2006b), and by evidence of the accelerated expansion of the Universe from supernova observations (Astier et al., 2006; Wood-Vasey et al., 2007), the Universe is spatially flat and roughly 27% of its matter-energy content is made by non-relativistic matter (the remaining 73% being given by an even more mysterious component with negative pressure, dubbed dark energy). However these observations also indicate that only 4% is baryonic in nature, implying that the remaining 23% consists of a non-baryonic component, i.e., the DM. The fact that the evidences for this "missing mass" come from observations at very different scales (ranging from the galactic scale $\sim$ 10kpc, up to the cosmological scales, $\sim 10^3$ Mpc) makes quite difficult to find alternative explanations for these anomalies, although some (mainly modifications of Einstein's theory of gravity) are being considered by the scientific community.

Despite this compelling evidence for the existence of DM, its precise nature is still a topic of debate. Even if there is no DM candidate in the framework of the standard model of particle physics, there is definitely no shortage of well-motivated candidates, since many particle physics theories predict the existence of plausible DM candidates beyond the standard model. The most intensely studied DM candidate is definitely the neutralino, a weakly-interacting massive particle (WIMP) motivated by supersymmetric extensions of the Standard Model of particle physics. In many of these extensions the neutralino is the lightest supersymmetric particle (LSP). In theories where the LSP is stable, for example theories where R-Parity is a conserved quantum number (Weinberg, 1982), the neutralino is thus a highly-motivated DM candidate. Furthermore, an attractive feature of neutralinos is that a large region of the relevant supersymmetric parameter space can be investigated using CERN's Large Hadron Collider (LHC)[1]. A WIMP DM candidate also appears in the framework of theories of extra-dimensions, like Kaluza-Klein (KK) theories, and is usually represented by the first KK excitation of the standard-model B boson. For a review on supersymmetric and KK dark matter, see Bertone et al. (2005). Other than WIMPs, there are many other candidates, like for example the sterile neutrino (Dodelson and Widrow, 1994) and the axion (Weinberg, 1978; Wilczek, 1978). The axion is an exampe of a pseudo Nambu-Goldstone boson, associated to the spontaneous breaking of an (approximate) global symmetry, namely the Pecce-Quinn $U(1)$ symmetry necessary to solve the strong CP problem. The axion can also be incorporated in the framework of theories of supergravity (Gates et al., 2009) and of gravity with torsion (Mercuri, 2009; Lattanzi and Mercuri, 2010). Another example of a DM candidate of this kind is the Majoron (Akhmedov et al., 1992; Berezinsky and Valle, 1993; Lattanzi and Valle, 2007; Bazzocchi et al., 2008; Lattanzi, 2010), namely the pseudo Nambu-Goldstone boson associated to the spontaneous breaking of lepton number, and possibly related to the mechanism of neutrino mass generation.

However, all the evidences about the existence of DM are based on its gravitational influence. There is hope that in the next decade or so the dark matter particle will be detected either directly (by producing it in accelerators, or revealing it in specifically-designed detection experiments) or indirectly (through the observation of its decay/annihilation products in an astrophysical or cosmological setting), thus shedding light on its nature.

The research line on DM can be divided in two sub-lines. The first one, more oriented towards model building, deals with the study of specific DM candidates, motivated by high-energy physics models, and with the constraints that cosmological observations put on their properties. The second line, more phenomenological, deals with the prospects for indirect dark matter detection, either through the observations of its decay/annihilation products (electrons and positrons, photons, neutrinos) or through its heating and ionization effects on the intergalactic medium.

3.3.1. Dark Matter Candidates

The research on this topic has focused on two particular candidates: the Majoron and the Barbero-Immirzi (BI) axion. For details see Appendix E.

The Majoron. While solar and atmospheric neutrino experiments (Fukuda et al., 1998; Ahmad et al., 2002; Eguchi et al., 2003) are confirmed by recent data from reactors (Abe et al., 2008) and accelerators indicating unambiguously that neutrinos oscillate and have mass (Maltoni et al., 2004), current limits on

[1] www.cern.ch/LHC

the absolute neutrino mass scale,

$$m_\nu \lesssim 1 \text{ eV} \tag{3.3.1}$$

that follow from beta (Drexlin, 2005) and double beta decay studies (Avignone et al., 2008), together with cosmological observations of the cosmic microwave background (CMB) (Komatsu et al., 2009; Dunkley et al., 2009) and large scale structure (Lesgourgues and Pastor, 2006) preclude neutrinos from playing a *direct* role as dark matter, at least in the framework of the standard cosmological model.

However, the *mechanism* of neutrino mass generation may provide the clue to the origin and nature of DM. If neutrino masses arise from the spontaneous violation of ungauged lepton number there must exist a pseudoscalar gauge singlet Nambu-Goldstone boson, the *Majoron* (Chikashige et al., 1981; Schechter and Valle, 1982). This may pick up a mass from non-perturbative gravitational effects that explicitly break global symmetries (Coleman, 1988; Giddings and Strominger, 1988; Akhmedov et al., 1993). Despite the fact that the majorons produced at the corresponding spontaneous L–violation phase will decay, mainly to neutrinos, they could still provide a sizeable fraction of the DM in the Universe since its couplings are rather tiny (Akhmedov et al., 1992; Berezinsky and Valle, 1993) and thus its lifetime can be very long, of the order of the age of the Universe. In Lattanzi and Valle (2007) and Lattanzi (2010), the constraints on the Majoron mass and lifetime have been reassessed in light of the more recent cosmological data. This has also allowed to put constraints on the Majoron-neutrino coupling in the framework of a definite see-saw model.

In general the Majoron has also a sub-dominant decay to two photons leading to a mono-energetic emission line which can be used as a test of the Majoron scenario. Bazzocchi et al. (2008) have compared the expected photon emission rates with observations in order to obtain model-independent restrictions on the relevant parameters, especially on the effective Majoron-photon coupling.

The BI axion. One of the most successful attempts to construct a non-perturbative quantum theory of gravity is Loop Quantum Gravity (Ashtekar and Lewandowski, 2004). Its classical starting point is the Ashtekar-Barbero canonical formulation of General Relativity (GR) (Ashtekar, 1987, 1986; Barbero G., 1995a,b), which, classically, corresponds to a modification of the Hilbert-Palatini (HP) action as demonstrated by Holst. This modification consists in adding to the usual HP action a new term which vanishes on (half-)shell

$$S[e,\omega] = S_{HP}[e,\omega] + S_{Hol}[e,\omega] = -\frac{1}{16\pi G}\int e_a \wedge e_b \wedge (\star R^{ab} + \beta R^{ab}) \tag{3.3.2}$$

where β is a constant known as Barbero-Immirzi (BI) parameter (Immirzi, 1997a,b). The parameter β is not fixed by the theory and its origin is still debated. The quantum theory is, basically, the result of the Dirac quantization procedure applied to the constraints of classical GR in the Ashtekar-Barbero formulation.

Recently, Mercuri (2009) gave a general argument to provide the motivation to consider the BI parameter as a field. Furthermore, by identifying the BI field with the QCD axion, the strong *CP* problem can be solved through the Peccei–Quinn mechanism. A specific energy scale for the Peccei–Quinn symmetry breaking is naturally predicted by this model. Lattanzi and Mercuri (2010) have shown that this provides a complete dynamical setting to evaluate the contribution of such an axion to the DM of the Universe. Furthermore, a tight upper bound on the tensor-to-scalar ratio production of primordial gravitational waves can be fixed, representing a strong experimental test for this model.

3.3.2. Indirect Detection of Dark Matter

The motivation for studying dark matter annihilation signatures (see e.g. Bertone et al. (2005)) has received considerable recent attention following reports of a 100 GeV excess in the PAMELA data on the ratio of the fluxes of cosmic ray positrons to electrons Adriani et al. (2009). In the absence of any compelling astrophysical explanation, the signature is reminiscent of the original prediction of a unique dark matter annihilation signal Silk and Srednicki (1984), although there are several problems that demand attention before any definitive statements can be made. By far the most serious of these is the required annihilation boost factor. The remaining difficulties with a dark matter interpretation, including most notably the gamma ray signals from the Galactic Centre and the inferred leptonic branching ratio, are plausibly circumvented or at least alleviated. Recent data from the ATIC balloon experiment provides evidence for a cut-off in the positron flux near 500 GeV that supports a KK-like candidate for the annihilating particle Chang et al. (2008) or a neutralino with incorporation of suitable radiative corrections (Bergstrom et al., 2008).

In a pioneering paper, it was noted (Profumo, 2005) that the annihilation signal can be boosted by a combination of coannihilations and Sommerfeld corrrection. We remark first that the inclusion of coannihilations to boost the annihilation cross-section modifies the relic density, and opens the 1-10 TeV neutralino mass window to the observed (WMAP5-normalised) dark matter density. As found by Lavalle et al. (2008), the outstanding problem now becomes that of normalisation. A boost factor of around 100 is required to explain the HEAT data in the context of a 100 GeV neutralino. The flux is suppressed by between one and two powers of neutralino mass, and the problem becomes far more severe with the 1-10 TeV neutralino required by the PAMELA/ATIC data (Cirelli et al., 2009b), a boost of 10^4 or more being required. These latter authors included a Sommerfeld correction appropriate to our $\beta \equiv v/c = 0.001$ dark halo and incorporated channel-dependent boost factors to fit the data, but the required boosts still fell short of plausible values by at least an order of magnitude.

Recently Lattanzi and Silk (2009) proposed a solution to the boost problem via Sommerfeld correction in the presence of a model of substructure that incorporates a plausible phase space structure for CDM, also reassessing the difficulty with the leptonic branching ratio and showing that it is not insurmountable for SUSY candidates. They also evaluated the possibility of independent confirmation via photon channels.

Then, Pieri et al. (2009b) studied the expected γ-ray flux from two local dwarf galaxies for which Cherenkov Telescope measurements are available, namely Draco and Sagittarius, incorporating the Sommerfeld enhancement of the annihilation cross-section. They used recent stellar kinematical measurements to model the dark matter halos of the dwarfs, and the results of numerical simulations to model the presence of an associated population of subhalos. They compared their predictions with the observations of Draco and Sagittarius performed by MAGIC and HESS, respectively, and derived exclusion limits on the effective annihilation cross-section. They also studied the sensitivities of Fermi and of the future Cherenkov Telescope Array to cross-section enhancements. It is found that the boost factor due to the Sommerfeld enhancement is already constrained by the MAGIC and HESS data, with enhancements greater than $\sim 10^4$ being excluded.

Another way to (indirectly) observe DM annihilations is to look for the heating and ionization effects associated to the DM annihilation products. In fact, some of the annihilation products (especially photons and electron-positron pairs) can interact with the particles in the intergalactic medium (IGM) and in this way alter the heating and ionization history of the IGM. This leads to some observable consequences: for example, it changes the optical depth to the last scattering surface, a quantity that can be measured through the observations of the CMB anisotropy spectrum (Chen and Kamionkowski, 2004; Padmanabhan and Finkbeiner, 2005). Another possible observational target is the 21 cm cosmic radiation, that is a powerful tracer of the abundance and temperature of neutral hydrogen in the Universe (Barkana and Loeb, 2007; Madau et al., 1997). Recently, Cumberbatch et al. (2010) studied the 21 cm signature of different DM candidates, fully considering the enhancements to the annihilation rate from DM halos and substructures within them, and assessed the necessary level of sensitivity that experiments measuring the global 21 cm signal should reach in order to detect the signatures of DM annihilations, at least in the most optimistic scenarios. Details of the approaches described are covered by Appendix F.

3.4. Estimation of cosmological parameters

Precision measurement of the cosmological observables have led to believe that we leave in a flat Friedmann Universe, seeded by nearly scale-invariant adiabatic primordial fluctuations Komatsu et al. (2009). The majority ($\sim 70\%$) of the energy density of the Universe is in the form of a fluid with a cosmological constant-like equation of state ($w \sim -1$), dubbed dark energy, that is responsible for the observed acceleration of the Universe Frieman et al. (2008). This so-called "concordance model" is adequately described by just six parameters, namely the baryon density, the cold dark matter density, the Hubble constant, the reionization optical depth, the amplitude and the spectral index of the primordial spectrum of density fluctuations. These parameters are measured to a very high precision Komatsu et al. (2009).

However, even if the concordance model gives a very satisfactory fit of all available data, it is worth to consider extended models and to constraint their parameters. In some cases these extended models simply arise when considering properties that, to a first approximation, can be neglected when interpreting cosmological data. This is the case for parameters like the neutrino mass and the curvature of the Universe. Both are very small and can be put to zero as a first approximation; however, allowing them to vary allows to put useful constraints on their value. For recent constraints on the neutrino mass from cosmology, see e.g. Melchiorri et al. (2010); Archidiacono et al. (2010). Another example is given by the reionization history: in the concordance model, this is assumed to happen istantaneously. A more realistic description is definetely in order. These more realistic, and more general, reionization scenarios can be constrained by the observations. It is also important to check how considering more general models impacts the determination of the concordance parameters (Pandolfi et al., 2010b,c). Models with a non-standard spectrum of primordial perturbations have been considered by Pandolfi et al. (2010a), also in relation to previous claims that in this class of models the CMB observations can be fitted with $\Omega_\Lambda = 0$. Models with a dynamical dark energy have been considered by Serra et al. (2009).

A second kind of extended models are those that, in a very general sense, arise from some new physics. This is the case of models in which the fundamental constants are allowed to vary with time (Menegoni et al., 2009; Martins et al., 2010; Menegoni et al., 2010; Menegoni, 2010) (for details see Appendix G).

4. Publications

4.1. Publications before 2005

1. R. Ruffini, D. J. Song, and L. Stella, "On the statistical distribution of massive fermions and bosons in a Friedmann universe" Astronomy and Astrophysics, Vol. 125, (1983) pp. 265-270.

   The distribution function of massive Fermi and Bose particles in an expanding universe is considered as well as some associated thermodynamic quantities, pressure and energy density. These considerations are then applied to cosmological neutrinos. A new limit is derived for the degeneracy of a cosmological gas of massive neutrinos.

2. R. Ruffini and D. J. Song, "On the Jeans mass of weakly interacting neutral massive leptons", in Gamow cosmology, eds. F. Melchiorri and R. Ruffini, (1986) pp. 370–385.

   The cosmological limits on the abundances and masses of weakly interacting neutral particles are strongly affected by the nonzero chemical potentials of these leptons. For heavy leptons ($m_x >$ GeV), the value of the chemical potential must be much smaller than unity in order not to give very high values of the cosmological density parameter and the mass of heavy leptons, or they will be unstable. The Jeans' mass of weakly interacting neutral particles could give the scale of cosmological structure and the masses of astrophysical objects. For a mass of the order 10 eV, the Jeans' mass could give the scenario of galaxy formation, the supercluster forming first and then the smaller scales, such as clusters and galaxies, could form inside the large supercluster.

3. D. Calzetti, M. Giavalisco, R. Ruffini, J. Einasto, and E. Saar, "The correlation function of galaxies in the direction of the Coma cluster", Astrophysics and Space Science, Vol. 137 (1987) pp. 101-106.

   Data obtained by Einasto et al. (1986) on the amplitude of the correlation function of galaxies in the direction of the Coma cluster are compared with theoretical predictions of a model derived for a self-similar observer-homogeneous structure. The observational samples can be approximated by cones of angular width alpha of about 77 deg. Eliminating sources of large observational error, and by making a specified correction, the observational data are found to agree very well with the theoretical predictions of Calzetti et al. (1987).

4. R. Ruffini, D. J. Song, and S. Taraglio, “The ’ino’ mass and the cellular large-scale structure of the universe”, Astronomy and Astrophysics, Vol. 190, (1988) pp. 1-9.

   Within the theoretical framework of a Gamow cosmology with massive ”inos”, the authors show how the observed correlation functions between galaxies and between clusters of galaxies naturally lead to a ”cellular” structure for the Universe. From the size of the ”elementary cells” they derive constraints on the value of the masses and chemical potentials of the cosmological ”inos”. They outline a procedure to estimate the ”effective” average mass density of the Universe. They also predict the angular size of the inhomogeneities to be expected in the cosmological black body radiation as remnants of this cellular structure. A possible relationship between the model and a fractal structure is indicated.

5. D. Calzetti, M. Giavalisco, and R. Ruffini, “The normalization of the correlation functions for extragalactic structures”, Astronomy and Astrophysics, Vol. 198 (1988), pp. 1-15.

   It is shown that the spatial two-point correlation functions for galaxies, clusters and superclusters depend explicitly on the spatial volume of the statistical sample considered. Rules for the normalization of the correlation functions are given and the traditional classification of galaxies into field galaxies, clusters and superclusters is replaced by the introduction of a single fractal structure, with a lower cut-off at galactic scales. The roles played by random and stochastic fractal components in the galaxy distribution are discussed in detail.

6. M. V. Arbolino and R. Ruffini, “The ratio between the mass of the halo and visible matter in spiral galaxies and limits on the neutrino mass”, Astronomy and Astrophysics, Vol. 192, (1988) pp. 107-116.

   Observed rotation curves for galaxies with values of the visible mass ranging over three orders of magnitude together with considerations involving equilibrium configurations of massive neutrinos, impose constraints on the ratio between the masses of visible and dark halo comporents in spiral galaxies. Upper and lower limits are derived for the mass of the particles making up the dark matter.

7. A. Bianconi, H. W. Lee, and R. Ruffini, “Limits from cosmological nucleosynthesis on the leptonic numbers of the universe”, Astronomy and Astrophysics, Vol. 241 (1991) pp. 343-357.

   Constraints on chemical potentials and masses of ’inos’ are calculated using cosmological standard nucleosynthesis processes. It is shown that the electron neutrino chemical potential (ENCP) should not be greater than a value of the order of 1, and that the possible effective chemical potential of the other neutrino species should be about 10 times the ENCP in order not to conflict with observational data. The allowed region (consistent with the He-4 abundance observations) is insensitive to the baryon to proton ratio η, while those imposed by other light elements strongly depend on η.

8. R. Ruffini, J. D. Salmonson, J. R. Wilson, and S.-S. Xue, "On the pair electromagnetic pulse of a black hole with electromagnetic structure", Astronomy and Astrophysics, Vol. 350 (1999) pp. 334-343.

   We study the relativistically expanding electron-positron pair plasma formed by the process of vacuum polarization around an electromagnetic black hole (EMBH). Such processes can occur for EMBH's with mass all the way up to $6 \cdot 10^5 M_\odot$. Beginning with a idealized model of a Reissner-Nordstrom EMBH with charge to mass ratio $\xi = 0.1$, numerical hydrodynamic calculations are made to model the expansion of the pair-electromagnetic pulse (PEM pulse) to the point that the system is transparent to photons. Three idealized special relativistic models have been compared and contrasted with the results of the numerically integrated general relativistic hydrodynamic equations. One of the three models has been validated: a PEM pulse of constant thickness in the laboratory frame is shown to be in excellent agreement with results of the general relativistic hydrodynamic code. It is remarkable that this precise model, starting from the fundamental parameters of the EMBH, leads uniquely to the explicit evaluation of the parameters of the PEM pulse, including the energy spectrum and the astrophysically unprecedented large Lorentz factors (up to $6 \cdot 10^3$ for a $10^3\ M_\odot$ EMBH). The observed photon energy at the peak of the photon spectrum at the moment of photon decoupling is shown to range from 0.1 MeV to 4 MeV as a function of the EMBH mass. Correspondingly the total energy in photons is in the range of 10^{52} to 10^{54} ergs, consistent with observed gamma-ray bursts. In these computations we neglect the presence of baryonic matter which will be the subject of forthcoming publications.

9. R. Ruffini, J. D. Salmonson, J. R. Wilson, and S.-S. Xue, "On the pair-electromagnetic pulse from an electromagnetic black hole surrounded by a baryonic remnant", Astronomy and Astrophysics, Vol. 359 (2000) pp. 855-864.

   The interaction of an expanding Pair-Electromagnetic pulse (PEM pulse) with a shell of baryonic matter surrounding a Black Hole with electromagnetic structure (EMBH) is analyzed for selected values of the baryonic mass at selected distances well outside the dyadosphere of an EMBH. The dyadosphere, the region in which a super critical field exists for the creation of e^+e^- pairs, is here considered in the special case of a Reissner-Nordstrom geometry. The interaction of the PEM pulse with the baryonic matter is described using a simplified model of a slab of constant thickness in the laboratory frame (constant-thickness approximation) as well as performing the integration of the general relativistic hydrodynamical equations. Te validation of the constant-thickness approximation, already presented in a previous paper Ruffini et al. (1999) for a

PEM pulse in vacuum, is here generalized to the presence of baryonic matter. It is found that for a baryonic shell of mass-energy less than 1% of the total energy of the dyadosphere, the constant-thickness approximation is in excellent agreement with full general relativistic computations. The approximation breaks down for larger values of the baryonic shell mass, however such cases are of less interest for observed Gamma Ray Bursts (GRBs). On the basis of numerical computations of the slab model for PEM pulses, we describe (i) the properties of relativistic evolution of a PEM pulse colliding with a baryonic shell; (ii) the details of the expected emission energy and observed temperature of the associated GRBs for a given value of the EMBH mass; $10^3 M_\odot$, and for baryonic mass-energies in the range 10^{-8} to 10^{-2} the total energy of the dyadosphere.

10. M. Lattanzi, R. Ruffini, and G. Vereshchagin, "On the possible role of massive neutrinos in cosmological structure formation", in Cosmology and Gravitation, eds. M. Novello and S. E. Perez Bergliaffa, Vol. 668 of AIP Conference Series, (2003) pp. 263–287.

    In addition to the problem of galaxy formation, one of the greatest open questions of cosmology is represented by the existence of an asymmetry between matter and antimatter in the baryonic component of the Universe. We believe that a net lepton number for the three neutrino species can be used to understand this asymmetry. This also implies an asymmetry in the matter-antimatter component of the leptons. The existence of a nonnull lepton number for the neutrinos can easily explain a cosmological abundance of neutrinos consistent with the one needed to explain both the rotation curves of galaxies and the flatness of the Universe. Some propedeutic results are presented in order to attack this problem.

4.2. Publications (2005 – 2009)

1. A.G. Aksenov, R. Ruffini and G.V. Vereshchagin, "Thermalization of the mildly relativistic plasma", Physical Review D, Vol. 79 (2009) 043008.

    In the recent Letter Aksenov et al. (2007) we considered the approach of nonequilibrium pair plasma towards thermal equilibrium state adopting a kinetic treatment and solving numerically the relativistic Boltzmann equations. It was shown that plasma in the energy range 0.1-10 MeV first reaches kinetic equilibrium, on a timescale $t_{\mathrm{k}} \lesssim 10^{-14}$ sec, with detailed balance between binary interactions such as Compton, Bhabha and Møller scattering, and pair production and annihilation. Later the electron-positron-photon plasma approaches thermal equilibrium on a timescale $t_{\mathrm{th}} \lesssim 10^{-12}$ sec, with detailed balance for all direct and inverse reactions. In the present paper we systematically present details of the computational scheme used in Aksenov et al. (2007), as well as generalize our treatment, considering proton loading of the pair plasma. When proton loading is large, protons thermalize first by proton-proton scattering, and then with the electron-positron-photon plasma by proton-electron scattering. In the opposite case of small proton loading proton-electron scattering dominates over proton-proton one. Thus in all cases the plasma, even with proton admixture, reaches thermal equilibrium configuration on a timescale $t_{\rm th} \lesssim 10^{-11}$ sec. We show that it is crucial to account for not only binary but also triple direct and inverse interactions between electrons, positrons, photons and protons. Several explicit examples are given and the corresponding timescales for reaching kinetic and thermal equilibria are determined.

2. A. G. Aksenov, R. Ruffini, and G. V. Vereshchagin, "Thermalization of pair plasma with proton loading" in the Proceedings of "PROBING STELLAR POPULATIONS OUT TO THE DISTANT UNIVERSE" meeting, AIP Conference Proceedings 1111 (2009) 344-350.

   We study kinetic evolution of nonequilibrium optically thick electron-positron plasma towards thermal equilibrium solving numerically relativistic Boltzmann equations with energy per particle ranging from 0.1 to 10 MeV. We generalize our results presented in Aksenov et al. (2007), considering proton loading of the pair plasma. Proton loading introduces new characteristic timescales essentially due to proton-proton and proton-electron Coulomb collisions. Taking into account not only binary but also triple direct and inverse interactions between electrons, positrons, photons and protons we show that thermal equilibrium is reached on a timescale $t_{\rm th} \simeq 10^{-11}$ sec.

3. M. Lattanzi, J. Silk "Can the WIMP annihilation boost factor be boosted by the Sommerfeld enhancement? ", in Phys. Rev. D79, 083523 (2009).

   We demonstrate that the Sommerfeld correction to cold dark matter (CDM) annihilations can be appreciable if even a small component of the dark matter is extremely cold. Subhalo substructure provides such a possibility given that the smallest clumps are relatively cold and contain even colder substructure due to incomplete phase space mixing. Leptonic channels can be enhanced for plausible models and the solar neighbourhood boost required to account for PAMELA/ATIC data is plausibly obtained, especially in the case of a few TeV mass neutralino for which the Sommerfeld-corrected boost is found to be $\sim 10^4 - 10^5$. Saturation of the Sommerfeld effect is shown to occur below $\beta \sim 10^{-4}$, thereby making this result largely independent on the presence of substructures below $\sim 10^5 M_\odot$. We find that the associated diffuse gamma ray signal from annihilations would exceed EGRET constraints unless the channels annihilating to heavy quarks or to gauge bosons are suppressed. The lepton channel gamma rays are potentially detectable by the FERMI satellite, not from the inner galaxy where substructures are tidally disrupted, but rather as a quasi-isotropic background from the outer halo, unless the outer substructures are much less concentrated than the inner substructures and/or the CDM density profile out to the virial radius steepens significantly.

4. L. Pieri, M. Lattanzi, J. Silk "Constraining the Sommerfeld enhancement with Cherenkov telescope observations of dwarf galaxies", in Mon. Not. Roy. Astron. Soc., 399, 2033 (2009).

   The presence of dark matter in the halo of our galaxy could be revealed through indirect detection of its annihilation products. Dark matter annihilation is one possible interpretation of the recently measured excesses in positron and electron fluxes, provided that boost factors of the order of 10^3 or more are taken into account. Such boost factors are actually achievable through the velocity-dependent Sommerfeld enhancement of the annihilation cross-section. Here we study the expected γ-ray flux from two local dwarf galaxies for which Cherenkov Telescope measurements are available, namely Draco and Sagittarius. We use recent stellar kinematical measurements to model the dark matter halos of the dwarfs, and the results of numerical simulations to model the presence of an associated population of subhalos. We incorporate the Sommerfeld enhancement of the annihilation cross-section. We compare our predictions with the observations of Draco and Sagittarius performed by MAGIC and HESS, respectively, and derive exclusion limits on the effective annihilation cross-section. We also study the sensitivities of Fermi and of the future Cherenkov Telescope Array to cross-section enhancements. We find that the boost factor due to the Sommerfeld enhancement is already constrained by the MAGIC and HESS data, with enhancements greater than $\sim 10^4$ being excluded.

5. M. Lattanzi, "Mass Varying Neutrinos: A model-independent approach", in Nucl. Phys. Proc. Suppl. 188, 40, (2009).

   In Mass Varying Neutrinos (MaVaNs) models, the neutrinos are coupled with the quintessence field supposed to be responsible for the acceleration of the Universe. Here we propose a new parameterization for the neutrino mass variation that is independent on the details of the scalar field potential and still captures the essential of most MaVaNs models. We also find an upper limit on the mass variation in the case of decreasing mass models, independent of the particular parameterization.

6. U. Franca, M. Lattanzi, J. Lesgourgues, S. Pastor "Model independent constraints on mass-varying neutrino scenarios", in Phys. Rev. D80, 083506 (2009).

   Models of dark energy in which neutrinos interact with the scalar field supposed to be responsible for the acceleration of the universe usually imply a variation of the neutrino masses on cosmological time scales. In this work we propose a parameterization for the neutrino mass variation that captures the essentials of those scenarios and allows to constrain them in a model independent way, that is, without resorting to any particular scalar field model. Using WMAP 5yr data combined with the matter power spectrum of SDSS and

2dFGRS, the limit on the present value of the neutrino mass is $m_0 \equiv m_\nu(z = 0) < 0.43$ (0.28) eV at 95% C.L. for the case in which the neutrino mass was lighter (heavier) in the past, a result competitive with the ones imposed for standard (*i.e.*, constant mass) neutrinos. Moreover, for the ratio of the mass variation of the neutrino mass Δm_ν over the current mass m_0 we found that $\log[|\Delta m_\nu|/m_0] < -1.3$ (-2.7) at 95% C.L. for $\Delta m_\nu < 0$ $(\Delta m_\nu > 0)$, totally consistent with no mass variation.

7. A.G. Aksenov, R. Ruffini and G.V. Vereshchagin, "Thermalization of nonequilibrium electron-positron-photon plasmas", Physical Review Letters, Vol. 99 (2007) No 12, 125003.

   Starting from a nonequilibrium configuration we analyze the role of the direct and the inverse binary and triple interactions in reaching thermal equilibrium in a homogeneous isotropic pair plasma. We focus on energies in the range $0.1 - 10$ MeV. We numerically integrate the relativistic Boltzmann equation with the exact QED collisional integrals taking into account all binary and triple interactions. We show that first, when a detailed balance is reached for all binary interactions on a time scale $t_k < 10^{-14}$ sec, photons and electron-positron pairs establish kinetic equilibrium. Subsequently, when triple interactions satisfy the detailed balance on a time scale $t_{eq} < 10^{-12}$ sec, the plasma reaches thermal equilibrium. It is shown that neglecting the inverse triple interactions prevents reaching thermal equilibrium. Our results obtained in the theoretical physics domain also find application in astrophysics and cosmology.

8. C.L. Bianco, R. Ruffini, G.V. Vereshchagin and S.-S. Xue, "Equations of Motion and Initial and Boundary Conditions for Gamma-ray Burst", Journal of the Korean Physical Society, Vol. 49 (2006) No. 2, pp. 722-731.

   We compare and contrast the different approaches to the optically thick adiabatic phase of GRB all the way to the transparency. Special attention is given to the role of the rate equation to be self consistently solved with the relativistic hydrodynamic equations. The works of Shemi and Piran (1990), Piran, Shemi and Narayan (1993), Meszaros, Laguna and Rees (1993) and Ruffini, Salmonson, Wilson and Xue (1999,2000) are compared and contrasted. The role of the baryonic loading in these three treatments is pointed out. Constraints on initial conditions for the fireball produced by electro-magnetic black hole are obtained.

9. P. Singh, K. Vandersloot and G.V. Vereshchagin, "Nonsingular bouncing universes in loop quantum cosmology", Physical Review D, Vol. 74 (2006) 043510.

   Nonperturbative quantum geometric effects in loop quantum cosmology (LQC) predict a ρ^2 modification to the Friedmann equation at high energies. The quadratic term is negative definite and can lead to generic bounces when the matter energy density becomes equal to a critical value of the order of the Planck density. The nonsingular bounce is achieved for arbitrary matter without violation of positive energy conditions. By performing a qualitative analysis we explore the nature of the bounce for inflationary and cyclic model potentials. For the former we show that inflationary trajectories are attractors of the dynamics after the bounce implying that inflation can be harmoniously embedded in LQC. For the latter difficulties associated with singularities in cyclic models can be overcome. We show that nonsingular cyclic models can be constructed with a small variation in the original cyclic model potential by making it slightly positive in the regime where scalar field is negative.

10. M. Lattanzi, R. Ruffini and G.V. Vereshchagin, "Joint constraints on the lepton asymmetry of the Universe and neutrino mass from the Wilkinson Microwave Anisotropy Probe", Physical Review D, Vol. 72 (2005) 063003.

    We use the Wilkinson Microwave Anisotropy Probe (WMAP) data on the spectrum of cosmic microwave background anisotropies to put constraints on the present amount of lepton asymmetry L, parametrized by the dimensionless chemical potential (also called degeneracy parameter) xi and on the effective number of relativistic particle species. We assume a flat cosmological model with three thermally distributed neutrino species having all the same mass and chemical potential, plus an additional amount of effectively massless exotic particle species. The extra energy density associated to these species is parametrized through an effective number of additional species $\Delta N_{others}{}^{eff}$. We find that $0 < |\xi| < 1.1$ and correspondingly $0 < |L| < 0.9$ at 2σ, so that WMAP data alone cannot firmly rule out scenarios with a large lepton number; moreover, a small preference for this kind of scenarios is actually found. We also discuss the effect of the asymmetry on the estimation of other parameters and, in particular, of the neutrino mass. In the case of perfect lepton symmetry, we obtain the standard results. When the amount of asymmetry is left free, we find at 2sigma. Finally we study how the determination of $|L|$ is affected by the assumptions on ΔN^{eff}_{others}. We find that lower values of the extra energy density allow for larger values of the lepton asymmetry, effectively ruling out, at 2sigma level, lepton symmetric models with $\Delta N^{eff}_{others} \simeq 0$.

11. G.V. Vereshchagin, "Gauge Theories of Gravity with the Scalar Field in Cosmology", in "Frontiers in Field Theory", edited by O. Kovras, Nova Science Publishers, New York, (2005), pp. 213-255 (ISBN: 1-59454-127-2).

    Brief introduction into gauge theories of gravity is presented. The most general gravitational lagrangian including quadratic on curvature, torsion and nonmetricity invariants for metric-affine gravity is given. Cosmological implica-

tions of gauge gravity are considered. The problem of cosmological singularity is discussed within the framework of general relativity as well as gauge theories of gravity. We consider the role of scalar field in connection to this problem. Initial conditions for nonsingular homogeneous isotropic Universe filled by single scalar field are discussed within the framework of gauge theories of gravity. Homogeneous isotropic cosmological models including ultrarelativistic matter and scalar field with gravitational coupling are investigated. We consider different symmetry states of effective potential of the scalar field, in particular restored symmetry at high temperatures and broken symmetry. Obtained bouncing solutions can be divided in two groups, namely nonsingular inflationary and
oscillating solutions. It is shown that inflationary solutions exist for quite general initial conditions like in the case of general relativity. However, the phase space of the dynamical system, corresponding to the cosmological equations is bounded. Violation of the uniqueness of solutions on the boundaries of the phase space takes place. As a result, it is impossible to define either the past or the future for a given solution. However, definitely there are singular solutions and therefore the problem of cosmological singularity cannot be solved in models with the scalar field within gauge theories of gravity.

12. R. Ruffini, M. G. Bernardini, C. L. Bianco, L. Caito, P. Chardonnet, M. G. Dainotti, F. Fraschetti, R. Guida, M. Rotondo, G. Vereshchagin, L. Vitagliano, S.-S. Xue,
"The Blackholic energy and the canonical Gamma-Ray Burst" in Cosmology and Gravitation: XIIth Brazilian School of Cosmology and Gravitation, edited by M. Novello and S.E. Perez Bergliaffa, AIP Conference Proceedings, Vol. 910, Melville, New York, 2007, pp. 55-217.

    Gamma-Ray Bursts (GRBs) represent very likely "the" most extensive computational, theoretical and observational effort ever carried out successfully in physics and astrophysics. The extensive campaign of observation from space based X-ray and γ-ray observatory, such as the Vela, CGRO, BeppoSAX, HETE-II, INTEGRAL, Swift, R-XTE, Chandra, XMM satellites, have been matched by complementary observations in the radio wavelength (e.g. by the VLA) and in the optical band (e.g. by VLT, Keck, ROSAT). The net result is unprecedented accuracy in the received data allowing the determination of the energetics, the time variability and the spectral properties of these GRB sources. The very fortunate situation occurs that these data can be confronted with a mature theoretical development. Theoretical interpretation of the above data allows progress in three different frontiers of knowledge: a) the ultrarelativistic regimes of a macroscopic source moving at Lorentz gamma factors up to ~ 400; b) the occurrence of vacuum polarization process verifying some of the yet untested regimes of ultrarelativistic quantum field theories; and c) the first evidence for extracting, during the process of gravitational collapse leading to the formation of a black hole, amounts of energies up to 10^{55} ergs of blackholic energy — a new form of energy in physics and astrophysics. We outline how this progress leads to the confirmation of three interpretation paradigms for GRBs proposed in July 2001. Thanks mainly to the observations by Swift and the optical observations by VLT, the outcome of this analysis points to the existence of a "canonical" GRB, originating from a variety of different initial astrophysical scenarios. The communality of these GRBs appears to be that they all are emitted in the process of formation of a black hole with a negligible value of its angular momentum. The following sequence of events appears to be canonical: the vacuum polarization process in the dyadosphere with the creation of the optically thick self accelerating electron-positron plasma; the engulfment of baryonic mass during the plasma expansion; adiabatic expansion of the optically thick "fireshell" of electron-positron-baryon plasma up to the transparency; the interaction of the accelerated baryonic matter with the interstellar medium (ISM). This leads to the canonical GRB composed of a proper GRB (P-GRB), emitted at the moment of transparency, followed by an extended afterglow. The sole parameters in this scenario are the total energy of the dyadosphere E_{dya}, the fireshell baryon loading M_B defined by the dimensionless parameter $B = M_B c^2 / E_{dya}$, and the ISM filamentary distribution around the source. In the limit $B \longrightarrow 0$ the total energy is radiated in the P-GRB with a vanishing contribution in the afterglow. In this limit, the canonical GRBs explain as well the short GRBs. In these lecture notes we systematically outline the main results of our model comparing and contrasting them with the ones in the current literature. In both cases, we have limited ourselves to review already published results in refereed publications. We emphasize as well the role of GRBs in testing yet unexplored grounds in the foundations of general relativity and relativistic field theories.

13. M. Lattanzi, R. Ruffini and G.V. Vereshchagin, "Do WMAP data constraint the lepton asymmetry of the Universe to be zero?" in Albert Einstein Century International Conference, edited by J.-M. Alimi, and A. Füzfa, AIP Conference Proceedings, Vol. 861, Melville, New York, 2006, pp.912-919.

    It is shown that extended flat ΛCDM models with massive neutrinos, a sizeable lepton asymmetry and an additional contribution to the radiation content of the Universe, are not excluded by the Wilkinson Microwave Anisotropy Probe (WMAP) first year data. We assume a flat cosmological model with three thermally distributed neutrino species having all the same mass and chemical potential, plus an additional amount of effectively massless exotic particle species X. After maximizing over seven other cosmological parameters, we derive from WMAP first year data the following constraints for the lepton asymmetry L of the Universe (95% CL): $0 < |L| < 0.9$, so that WMAP data alone cannot firmly rule out scenarios with a large lepton number; moreover, a small preference for this kind of scenarios is actually found. We also find for the neutrino mass $m_\nu < 1.2 eV$ and for the effective number of relativistic particle species $-0.45 < \Delta N^{eff} < 2.10$, both at 95% CL. The limit on ΔN^{eff} is more restrictive man others found in the literature, but we argue that this is due to our choice of priors.

14. R. Ruffini, C.L. Bianco, G.V. Vereshchagin, S.-S. Xue "Baryonic loading and e^+e^- rate equation in GRB sources" to appear in the proceedings of "Relativistic Astrophysics and Cosmology - Einstein's Legacy" Meeting, November 7-11, 2005, Munich, Germany.

    The expansion of the electron-positron plasma in the GRB phenomenon is compared and contrasted in the treatments of Meszaros, Laguna and Rees, of Shemi, Piran and Narayan, and of Ruffini et al. The role of the correct numerical integration of the hydrodynamical equations, as well as of the rate equation for the electron-positron plasma loaded with a baryonic mass, are outlined and confronted for crucial differences.

15. G.V. Vereshchagin, M. Lattanzi, H.W. Lee, R. Ruffini, "Cosmological massive neutrinos with nonzero chemical potential: I. Perturbations in cosmological models with neutrino in ideal fluid approximation", in proceedings of the Xth Marcel Grossmann Meeting on Recent Developments in Theoretical and Experimental General Relativity, World Scientific: Singapore, 2005, vol. 2, pp. 1246-1248.

    Recent constraints on neutrino mass and chemical potential are discussed with application to large scale structure formation. Power spectra in cosmological model with hot and cold dark matter, baryons and cosmological term are calculated in newtonian approximation using linear perturbation theory. All components are considered to be ideal fluids. Dissipative processes are taken into account by initial spectrum of perturbations so the problem is reduced to a simple system of equations. Our results are in good agreement with those obtained before using more complicated treatments.

16. M. Lattanzi, H.W. Lee, R. Ruffini, G.V. Vereshchagin, "Cosmological massive neutrinos with nonzero chemical potential: II. Effect on the estimation of cosmological parameters", in proceedings of the Xth Marcel Grossmann Meeting on Recent Developments in Theoretical and Experimental General Relativity, World Scientific: Singapore, 2005, vol. 2, pp. 1255-1257.

    The recent analysis of the cosmic microwave background data carried out by the WMAP team seems to show that the sum of the neutrino mass is ¡ 0.7 eV. However, this result is not model-independent, depending on precise assumptions on the cosmological model. We study how this result is modified when the assumption of perfect lepton symmetry is dropped out.

17. R. Ruffini, M. Lattanzi and G. Vereshchagin, "On the possible role of massive neutrinos in cosmological structure formation" in Cosmology

and Gravitation: Xth Brazilian School of Cosmology and Gravitation, edited by M. Novello and S.E. Perez Bergliaffa, AIP Conference Proceedings, Vol. 668, Melville, New York, 2003, pp.263-287.

In addition to the problem of galaxy formation, one of the greatest open questions of cosmology is represented by the existence of an asymmetry between matter and antimatter in the baryonic component of the Universe. We believe that a net lepton number for the three neutrino species can be used to understand this asymmetry. This also implies an asymmetry in the matter-antimatter component of the leptons. The existence of a nonnull lepton number for the neutrinos can easily explain a cosmological abundance of neutrinos consistent with the one needed to explain both the rotation curves of galaxies and the flatness of the Universe. Some propedeutic results are presented in order to attack this problem.

18. A.G. Aksenov, C.L. Bianco, R. Ruffini and G.V. Vereshchagin, "GRBs and the thermalization process of electron-positron plasmas" in the Proceedings of the "Gamma Ray Bursts 2007" meeting, AIP Conf.Proc. 1000 (2008) 309-312.

    We discuss temporal evolution of the pair plasma, created in Gamma-Ray Bursts sources. A particular attention is paid to the relaxation of plasma into thermal equilibrium. We also discuss the connection between the dynamics of expansion and spatial geometry of plasma. The role of the baryonic loading parameter is emphasized.

19. A. G. Aksenov, R. Ruffini, and G. V. Vereshchagin, "Thermalization of Electron-Positron-Photon Plasmas with an Application to GRB" in RELATIVISTIC ASTROPHYSICS: 4th Italian-Sino Workshop, AIP Conference Proceedings, Vol. 966, Melville, New York, 2008, pp. 191-196.

    The pair plasma with photon energies in the range $0.1 - 10$MeV is believed to play crucial role in cosmic Gamma-Ray Bursts. Starting from a nonequilibrium configuration we analyze the role of the direct and the inverse binary and triple interactions in reaching thermal equilibrium in a homogeneous isotropic pair plasma.We numerically integrate the relativistic Boltzmann equation with the exact QED collisional integrals taking into account all binary and triple interactions. We show that first, when a detailed balance is reached for all binary interactions on a time scale $t_k = 10^{-14}$sec , photons and electronpositron pairs establish kinetic equilibrium. Subsequently, when triple interactions satisfy the detailed balance on a time scale $t_{eq} = 10^{-12}$sec , the plasma reaches thermal equilibrium. It is shown that neglecting the inverse triple interactions prevents reaching thermal equilibrium. Our results obtained in the theoretical physics domain also find application in astrophysics and cosmology.

20. R. Ruffini, and G. V. Vereshchagin, S.-S. Xue, "Vacuum Polarization and Electron-Positron Plasma Oscillations" in RELATIVISTIC ASTRO-

PHYSICS: 4th Italian-Sino Workshop, AIP Conference Proceedings, Vol. 966, Melville, New York, 2008, pp. 207-212.

We study plasma oscillations of electrons-positron pairs created by the vacuum polarization in an uniform electric field. Our treatment, encompassing the case of $E > E_c$, shows also in the case $E < E_c$the existence of a maximum Lorentz factor acquired by electrons and positrons and allows determination of the a maximal length of oscillation. We quantitatively estimate how plasma oscillations reduce the rate of pair creation and increase the time scale of the pair production.

4.3. Publications (2010)

1. A.G. Aksenov, R. Ruffini and G.V. Vereshchagin, "Pair plasma relaxation time scales", Physical Review E, Vol. 81 (2010) 046401.

   By numerically solving the relativistic Boltzmann equations, we compute the time scale for relaxation to thermal equilibrium for an optically thick electron-positron plasma with baryon loading. We focus on the time scales of electromagnetic interactions. The collisional integrals are obtained directly from the corresponding QED matrix elements. Thermalization time scales are computed for a wide range of values of both the total energy density (over 10 orders of magnitude) and of the baryonic loading parameter (over 6 orders of magnitude). This also allows us to study such interesting limiting cases as the almost purely electron-positron plasma or electron-proton plasma as well as intermediate cases. These results appear to be important both for laboratory experiments aimed at generating optically thick pair plasmas as well as for astrophysical models in which electron-positron pair plasmas play a relevant role.

2. R. Ruffini, G.V. Vereshchagin and S.-S. Xue, "Electron-positron pairs in physics and astrophysics: from heavy nuclei to black holes" Physics Reports, Vol. 487 (2010) No 1-4, pp. 1-140.

   From the interaction of physics and astrophysics we are witnessing in these years a splendid synthesis of theoretical, experimental and observational results originating from three fundametal physical processes. They were originally proposed by Dirac, by Breit and Wheeler and by Sauter, Heisenberg, Euler and Schwinger. For almost seventy years they have all three been followed by a continued effort of experimental verification on Earth-based experiments. The Dirac process, $e^+e^- \rightarrow 2\gamma$, has been by far the most successful. It has obtained extremely accurate experimental verification and has led as well to an enormous number of new physics in possibly one of the most fruitful experimental avenue by introduction of storage rings in Frascati and followed by the largest accelerators worldwide: DESY, SLAC etc. The Breit-Wheeler process,

$2\gamma \to e^+e^-$, although conceptually simple, being the inverse process of the Dirac one, has been by far one of the most difficult to be verified experimentally. Only recently, through the technology based on free electron X-ray laser and its numerous applications in Earth-based experiments, some first indications of its possible verification have been reached. The vacuum polarization process in strong electromagnetic field, pioneered by Sauter, Heisenberg, Euler and Schwinger, introduced the concept of critical electric field $E_c = m_e^2c^3/e\hbar$. It has been searched without success for more than forty years by heavy-ion collisions in many of the leading particle accelerators worldwide. The novel situation today is that these same processes can be studied on a much more grandiose scale during the gravitational collapse leading to the formation of a black hole being observed in Gamma Ray Bursts (GRBs). This report is dedicated to the scientific race in act. The theoretical and experimental work developed in Earth-based laboratories is confronted with the theoretical interpretation of space-based observations of phenomena originating on cosmological scales. What has become clear in the last ten years is that all the three above mentioned processes, duly extended in the general relativistic framework, are necessary for the understanding of the physics of the gravitational collapse to a black hole. Vice versa, the natural arena where these processes can be observed in mutual interaction and on an unprecedented scale, is indeed the realm of relativistic astrophysics. We systematically analyze the conceptual developments which have followed the basic work of Dirac and Breit-Wheeler. We also recall how the seminal work of Born and Infeld inspired the work by Sauter, Heisenberg and Euler on effective Lagrangian leading to the estimate of the rate for the process of electron-positron production in a constant electric field. In addition of reviewing the intuitive semi-classical treatment of quantum mechanical tunneling for describing the process of electron-positron production, we recall the calculations in *Quantum Electro-Dynamics* of the Schwinger rate and effective Lagrangian for constant electromagnetic fields. We also review the electron-positron production in both time-alternating electromagnetic fields, studied by Brezin, Itzykson, Popov, Nikishov and Narozhny, and the corresponding processes relevant for pair production at the focus of coherent laser beams as well as electron beam-laser collision. We finally report some current developments based on the general JWKB approach which allows to compute the Schwinger rate in spatially varying and time varying electromagnetic fields. We also recall the pioneering work of Landau and Lifshitz, and Racah on the collision of charged particles as well as experimental success of AdA and ADONE in the production of electron-positron pairs. We then turn to the possible experimental verification of these phenomena. We review: A) the experimental verification of the $e^+e^- \to 2\gamma$ process studied by Dirac. We also briefly recall the very successful experiments of e^+e^- annihilation to hadronic channels, in addition to the Dirac electromagnetic channel; B) ongoing Earth based experiments to detect electron-positron production in strong fields by focusing coherent laser beams and by electron beam-laser collisions; and C) the multiyear attempts to detect electron-positron production in Coulomb fields for a large atomic number $Z > 137$ in heavy ion collisions. These attempts follow the classical theoretical work of Popov and Zeldovich, and Greiner and their schools. We then turn to astrophysics. We first review the basic work on the energetics and electrodynamical properties of an electromagnetic black hole and the application of the Schwinger formula around Kerr-Newman black holes as pioneered by Damour and Ruffini. We only focus on black hole masses larger than the critical mass of neutron stars, for convenience assumed to coincide with the Rhoades and Ruffini upper limit of $3.2 M_{\odot}$. In this case the electron Compton wavelength is much smaller than the spacetime curvature and all previous results invariantly expressed can be applied following well established rules of the equivalence principle. We derive the corresponding rate of electron-positron pair production and the introduction of the concept of Dyadosphere. We review recent progress in describing the evolution of optically thick electron-positron plasma in presence of supercritical electric field, which is relevant both in astrophysics as well as ongoing laser beam experiments. In particular we review recent progress based on the Vlasov-Boltzmann-Maxwell equations to study the feedback of the created electron-positron pairs on the original constant electric field. We evidence the existence of plasma oscillations and its interaction with photons leading to energy and number equipartition of photons, electrons and positrons. We finally review the recent progress obtained by using the Boltzmann equations to study the evolution of an electron-positron-photon plasma towards thermal equilibrium and determination of its characteristic timescales. The crucial difference introduced by the correct evaluation of the role of two and three body collisions, direct and inverse, is especially evidenced. We then present some general conclusions. The results reviewed in this report are going to be submitted to decisive tests in the forthcoming years both in physics and astrophysics. To mention only a few of the fundamental steps in testing in physics we recall the starting of experimental facilities at the National Ignition Facility at the Lawrence Livermore National Laboratory as well as corresponding French Laser the Mega Joule project. In astrophysics these results will be tested in galactic and extragalactic black holes observed in binary X-ray sources, active galactic nuclei, microquasars and in the process of gravitational collapse to a neutron star and also of two neutron stars to a black hole giving origin to GRBs. The astrophysical description of the stellar precursors and the initial physical conditions leading to a gravitational collapse process will be the subject of a forthcoming report. As of today no theoretical description has yet been found to explain either the emission of the remnant for supernova or the formation of a charged black hole for GRBs. Important current progress toward the understanding of such phenomena as well as of the electrodynamical structure of neutron stars, the supernova explosion and the theories of GRBs will be discussed in the above mentioned forthcoming report. What is important to recall at this stage is only that both the supernovae and GRBs processes are among the most energetic and transient phenomena ever observed in the Universe: a supernova can reach energy of ~10^{54} ergs on a time scale of a few months and GRBs can have emission of up to ~10^{54} ergs in a time scale as short as of a few seconds. The central role of neutron stars in the description of supernovae, as well as of black holes and the electron-positron plasma, in the description of GRBs, pioneered by one of us (RR) in 1975, are widely recognized. Only the theoretical basis to address these topics are discussed in the present report.

3. A. G. Aksenov, R. Ruffini, and G. V. Vereshchagin, "Kinetics of the Mildly Relativistic Plasma and GRBs" in the Proceedings of "The Sun, the stars, the Universe and General Relativity" meeting in honor of 95th Anniversary of Ya. B. Zeldovich in Minsk, AIP Conference Proceedings 1205 (2010) 11-16.

   We consider optically thick photon-pair-proton plasma in the framework of Boltzmann equations. For the sake of simplicity we consider the uniform and isotropic plasma. It has been shown that arbitrary initial distribution functions evolve to the thermal equilibrium state through so called kinetic equilibrium state with common temperature of all particles and nonzero chemical potentials. For the plasma temperature $0.1 - 10$ MeV relevant for GRB (Gamma-Ray Burst) sources we evaluate the thermalization time scale as function of total energy density and baryonic loading parameter.

4. D. Cumberbatch, M. Lattanzi, J. Silk, "Signatures of clumpy dark matter in the global 21 cm background signal ", in Phys. Rev. D82, 103508 (2010).

   We examine the extent to which the self-annihilation of supersymmetric neutralino dark matter, as well as light dark matter, influences the rate of heating, ionisation and Lyman-α pumping of interstellar hydrogen and helium and the extent to which this is manifested in the 21 cm global background signal. We fully consider the enhancements to the annihilation rate from DM halos and substructures within them. We find that the influence of such structures can result in significant changes in the differential brightness temperature, δT_b. The changes at redsfhits $z < 25$ are likely to be undetectable due to the presence of the astrophysical signal; however, in the most favourable cases, deviations in δT_b, relative to its value in the absence of self-annihilating DM, of up to $\simeq 20$ mK at $z = 30$ can occur. Thus we conclude that, in order to exclude these models, experiments measuring the global 21 cm signal, such as EDGES and CORE, will need to reduce the systematics at 50 MHz to below 20 mK.

5. M. Lattanzi, S. Mercuri, "A solution of the strong CP problem via the Peccei-Quinn mechanism through the Nieh-Yan modified gravity and cosmological implications" in Phys. Rev. D81, 125015 (2010). By identifying the recently introduced Barbero–Immirzi field with the QCD axion, the strong *CP* problem can be solved through the Peccei–Quinn mechanism. A

specific energy scale for the Peccei–Quinn symmetry breaking is naturally predicted by this model. This provides a complete dynamical setting to evaluate the contribution of such an axion to the cold dark matter content of the Universe. Furthermore, a tight upper bound on the tensor-to-scalar ratio production of primordial gravitational waves can be fixed, representing a strong experimental test for this model.

6. S. Pandolfi, E. Giusarma, M. Lattanzi, A. Melchiorri, "Inflation with primordial broken power law spectrum as an alternative to the concordance cosmological model" in Phys. Rev. D81, 103007 (2010).

   We consider cosmological models with a non scale-invariant spectrum of primordial perturbations and assess whether they represent a viable alternative to the concordance ΛCDM model. We find that in the framework of a model selection analysis, the WMAP and 2dF data do not provide any conclusive evidence in favour of one or the other kind of model. However, when a marginalization over the entire space of nuisance parameters is performed, models with a modified primordial spectrum and $\Omega_\Lambda = 0$ are strongly disfavoured.

7. M. Lattanzi, "The majoron: a new dark matter candidate "in J. Kor. Phys. Soc 56, 1677 (2010).

   We review our recent proposal of the majoron as a suitable dark matter candidate. The majoron is the Goldstone boson associated to the spontaneous breaking of ungauged lepton number, one of the mechanisms proposed to give rise to neutrino masses. The majoron can acquire a mass through quantum gravity effects, and can possibly account for the observed dark matter component of the Universe. The majoron dark matter scenario is consistent with the current observations of the cosmic microwave background anisotropy provided that its lifetime $\tau \gtrsim 250$ Gyr. In the case of thermal production, the majoron should lie in the range 0.13 keV $< m_J <$ 0.17 keV, although these limits are modified in the non-thermal case. Applying this results to a given seesaw model for the generation of neutrino masses, it is found that the energy scale for the lepton number breaking phase transition is constrained to be $E_L \gtrsim 10^6$ GeV. We thus find that the majoron decaying dark matter (DDM) scenario fits nicely in models where neutrino masses arise *a la seesaw*, and may lead to other possible cosmological implications.

8. M. Archidiacono, A. Cooray, A. Melchiorri, S. Pandolfi, "CMB neutrino mass bounds and reionization", Phys. Rev. D 82, 087302 (2010).

   Abstract: Current cosmic microwave background (CMB) bounds on the sum of the neutrino masses assume a sudden reionization scenario described by a single parameter that determines the onset of reionization. We investigate the bounds on the neutrino mass in a more general reionization scenario based on a principal component approach. We found the constraint on the sum of the neutrino masses from CMB data can be relaxed by a $\sim$ 40% in a generalized reionization scenario. Moreover, the amplitude of the r.m.s. mass fluctuations $\sigma_8$is also considerably lower providing a better consistency with a low amplitude of the Sunyaev-Zel'dovich signal.

9. S. Pandolfi, A.Cooray, E.Giusarma, E.W.Kolb, A.Melchiorri, O.Mena and P.Serra, "Harrison-Zel'dovich primordial spectrum is consistent with observations", Phys. Rev. D 81, 123509 (2010).

   Abstract: Inflation predicts primordial scalar perturbations with a nearly scale-invariant spectrum and a spectral index approximately unity (the Harrison–Zel'dovich (HZ) spectrum). The first important step for inflationary cosmology is to check the consistency of the HZ primordial spectrum with current observations. Recent analyses have claimed that a HZ primordial spectrum is excluded at more than 99% c.l.. Here we show that the HZ spectrum is only marginally disfavored if one considers a more general reionization scenario. Data from the Planck mission will settle the issue.

10. P. Serra, A. Cooray, D. E. Holz, A. Melchiorri, S. Pandolfi, and D. Sarkar, "No evidence for dark energy dynamics from a global analysis of cosmological data", Phys. Rev. D 80, 121302 (2009).

    Abstract: We use a variant of principal component analysis to investigate the possible temporal evolution of the dark energy equation of state, w(z). We constrain w(z) in multiple redshift bins, utilizing the most recent data from Type Ia supernovae, the cosmic microwave background, baryon acoustic oscillations, the integrated Sachs-Wolfe effect, galaxy clustering, and weak lensing data. Unlike other recent analyses, we find no significant evidence for evolving dark energy; the data remains completely consistent with a cosmological constant. We also study the extent to which the time-evolution of the equation of state would be constrained by a combination of current- and future-generation surveys, such as Planck and the Joint Dark Energy Mission.

11. E. Menegoni, S. Pandolfi, S. Galli, M. Lattanzi, A. Melchiorri "Constraints on the dark energy equation of state in presence of a varying fine structure constant" in Int. J. Mod. Phys D19, 507 (2010).

    We discuss the cosmological constraints on the dark energy equation of state in the pres- ence of primordial variations in the fine structure constant. We find that the constraints from CMB data alone on w and the Hubble constant are much weaker when variations in the fine structure constant are permitted. Vice versa, constraints on the fine struc- ture constant are relaxed by more than 50% when dark energy models different from a cosmological constant are considered.

12. C.J.A.P. Martins, E. Menegoni, S. Galli and A. Melchiorri, "Varying couplings in the early universe: correlated variations of α and G, Physical Review D 82 023532 (2010)

The cosmic microwave background anisotropies provide a unique opportunity to constrain simultaneous variations of the fine-structure constant α and Newton's gravitational constant G. Those correlated variations are possible in a wide class of theoretical models. In this brief paper we show that the current data, assuming that particle masses are constant, give no clear indication for such variations, but already prefer that any relative variations in α should be of the same sign of those of G for variations of 1%. We also show that a cosmic complementarity is present with big bang nucleosynthesis and that a combination of current CMB and big bang nucleosynthesis data strongly constraints simultaneous variations in α and G. We finally discuss the future bounds achievable by the Planck satellite mission.

13. E. Menegoni, "New Constraints on Variations of Fine Structure Constant from Cosmic Microwave Background Anisotropies", GRAVITATIONAL PHYSICS: TESTING GRAVITY FROM SUBMILLIMETER TO COSMIC: Proceedings of the VIII Mexican School on Gravitation and Mathematical Physics. AIP Conference Proceedings, Volume 1256, pp. 288-292 (2010).

    The recent measurements of Cosmic Microwave Background temperature and polarization anisotropy made by the ACBAR, QUAD and BICEP experiments substantially improve the cosmological constraints on possible variations of the fine structure constant in the early universe. In this work I analyze this recent data obtaining the constraint $\alpha/\alpha 0$ = 0.987+/-0.012 at 68% c.l.. The inclusion of the new HST constraints on the Hubble constant further increases the bound to $\alpha/\alpha 0$ = 1.001+/-0.007 at 68% c.l., bringing possible deviations from the current value below the 1% level.

14. A. Melchiorri, F. De Bernardis, E. Menegoni, "Limits on the neutrino mass from cosmology". GRAVITATIONAL PHYSICS: TESTING GRAVITY FROM SUBMILLIMETER TO COSMIC: Proceedings of the VIII Mexican School on Gravitation and Mathematical Physics. AIP Conference Proceedings, Volume 1256, pp. 96-106 (2010).

    We use measurements of luminosity-dependent galaxy bias at several different redshifts, SDSS at z = 0.05, DEEP2 at z = 1 and LBGs at z = 3.8, combined with WMAP five-year cosmic microwave background anisotropy data and SDSS Red Luminous Galaxy survey three-dimensional clustering power spectrum to put constraints on cosmological parameters.

4.4. Invited talks at international conferences

1. "Thermalization of the pair plasma"

    (with A.G. Aksenov and R. Ruffini)

Korean Physical Society 2010 Fall Meeting, Pyeong-chang, Korea, 20-22 October, 2010.

2. "The spatial structure of expanding optically thick relativistic plasma and the onset of GRBs"

   (with A.G. Aksenov, G. de Barros and R. Ruffini)

   GRB 2010 / Dall'eV al TeV tutti i colori dei GRB, Secondo Congresso Italiano sui Gamma-ray Burst, Cefalu' 15-18 Giugno 2010.

3. "From thermalization mechanisms to emission processes in GRBs"

   (G.V. Vereshchagin)

   XII Marcel Grossmann Meeting, Paris, 12-18 July 2009.

4. "Kinetics of the mildly relativistic plasma and GRBs"

   (A.G. Aksenov R. Ruffini, and G.V. Vereshchagin)

   "The Sun, the Stars, the Universe, and General Relativity" - International conference in honor of Ya. B. Zeldovich 95th Anniversary, Minsk, Belarus, April 19-23, 2009.

5. "Pair plasma around compact astrophysical sources: kinetics, electrodynamics and hydrodynamics"

   (G.V. Vereshchagin and R. Ruffini)

   Invited seminar at RMKI, Budapest, February 24, 2009.

6. "Thermalization of the pair plasma with proton loading"

   (G.V. Vereshchagin, R. Ruffini, and A.G. Aksenov)

   Probing Stellar Populations out to the Distant Universe, Cefalu', Italy, September 7-19, 2008.

7. "Thermalization of the pair plasma with proton loading"

   (G.V. Vereshchagin, R. Ruffini, and A.G. Aksenov)

   3rd Stueckelberg Workshop, Pescara, Italy, 8-18 July, 2008.

8. "Thermalization of the pair plasma"

   (G.V. Vereshchagin, R. Ruffini, and A.G. Aksenov)

9. "Non-singular solutions in Loop Quantum Cosmology"

   (G.V. Vereshchagin)

   2nd Stueckelberg Workshop, Pescara, Italy, 3-7 September, 2007.

10. "(From) massive neutrinos and inos and the upper cutoff to the fractal structure of the Universe (to recent progress in theoretical cosmology)"

    (G.V. Vereshchagin, M. Lattanzi and R. Ruffini)

    A Century of Cosmology, San Servolo, Venice, Italy, 27-31 August, 2007.

11. "Pair creation and plasma oscillations"

    (G.V. Vereshchagin, R. Ruffini, and S.-S. Xue)
    4th Italian-Sino Workshop on Relativistic Astrophysics, Pescara, Italy, 20-29 July, 2007.

12. "Thermalization of electron-positron plasma in GRB sources"

    (G.V. Vereshchagin, R. Ruffini, and A.G. Aksenov)
    Xth Italian-Korean Symposium on Relativistic Astrophysics, Pescara, Italy, 25-30 June, 2007.

13. "Kinetics and hydrodynamics of the pair plasma"

    (G.V. Vereshchagin, R. Ruffini, C.L. Bianco, A.G. Aksenov)

14. "Pair creation and plasma oscillations"

    (G.V. Vereshchagin, R. Ruffini and S.-S. Xue)
    Cesare Lattes Meeting on GRBs, Black Holes and Supernovae, Mangaratiba-Portobello, Brazil, 26 February - 3 March 2007.

15. "Cavallo-Rees classification revisited"

    (G.V. Vereshchagin, R.Ruffini and S.-S. Xue)

    On recent developments in theoretical and experimental general relativity, gravitation and relativistic field theories: XIth Marcel Grossmann Meeting, Berlin, Germany, 23-29 July, 2006.

16. "Kinetic and thermal equilibria in the pair plasma"

    (G.V. Vereshchagin)

    The 1st Bego scientific rencontre, Nice, 5-16 February 2006.

17. "From semi-classical LQC to Friedmann Universe"

    (G.V. Vereshchagin)

    Loops '05, Potsdam, Golm, Max-Plank Institut für Gravitationsphysik (Albert-Einstein-Institut), 10-14 October 2005.

18. "Equations of motion, initial and boundary conditions for GRBs"

    (G.V. Vereshchagin, R. Ruffini and S.-S. Xue)

    IXth Italian-Korean Symposium on Relativistic Astrophysics, Seoul, Mt. Kumgang, Korea, 19-24 July 2005.

19. “On the Cavallo-Rees classification and GRBs”

    (G.V. Vereshchagin, R. Ruffini and S.-S. Xue)

    II Italian-Sino Workshop on Relativistic Astrophysics, Pescara, Italy, 10-20 June, 2005.

20. “Primordial gravitional waves as a probe of the cosmic expansion history”

    (M. Lattanzi)

    16th International Symposium on Particles, Strings and Cosmology, Valencia, Spain, 19-23 July 2010.

21. “Detecting Signatures of the Cosmic Thermal History through Pulsar Observations”

    (M. Lattanzi)

    14th Gravitational Waves Data Analysis Workshop, Rome, Italy, 26-29 January 2010.

22. “On the Propagation of Gravitational Waves across the Universe: Interaction with the Neutrino Component”

    (M. Lattanzi)

    2nd Italian-Pakistani Workshop on Relativistic Astrophysics, Pescara, Italy, 8-10 July 2009.

23. “Enhancement of the Darl Matter Annihilation Cross-Section in Cold Substructures”

    (M. Lattanzi)

    12th Marcel Grossmann Meeting on General Relativity, Paris, France, 12-18 July 2009.

24. “On the Propagation of Gravitational Waves across the Universe: Interaction with the Neutrino Component”

    (M. Lattanzi)

    12th Marcel Grossmann Meeting on General Relativity, Paris, France, 12-18 July 2009.

25. “Constraining Dark Matter Models Through 21cm Observations”

    (M. Lattanzi)

    2nd Universenet School and Meeting, Oxford, UK, 22-26 September 2008.

26. "Constraints on Mass-Varying Neutrino Scenarios"

    (M. Lattanzi)

    Neutrino Oscillation Workshop 2008, Otranto (Lecce), Italy, 6-13 September 2008.

27. "Constraining Dark Matter Models Through 21cm Observations"

    (M. Lattanzi)

    3rd Stueckelberg Workshop on Quantum Field Theories, Pescara, Italy, 8-18 July 2008.

28. "Cosmological Constraints on Neutrino Physics"

    (M. Lattanzi)

    Theta13 Half Day Meeting, Oxford, UK, 24 September 2007.

29. "Decaying warm dark matter, neutrino masses and the cosmic microwave background"

    (M. Lattanzi)

    2nd Meeting of the "Red Nacional Tem‡tica de Astroparticulas" (RENATA), Valencia, Spain, 17-19 September 2007.

30. "Decaying majoron dark matter and neutrino masses"

    (M. Lattanzi)

    Workshop "The Path to Neutrino Mass", Aarhus, Denmark, 3-6 September 2007.

31. "Decaying majoron dark matter and neutrino masses"

    (M. Lattanzi)

    4rd Italian-Sino Workshop on Relativistic Astrophysics, Pescara, Italy, 20-30 July 2007.

32. "Decaying majoron dark matter and neutrino masses"

    (M. Lattanzi)

    10th Italian-Korean Symposium on Relativistic Astrophysics, Pescara, Italy, 25-30 June 2007.

33. "Constraints on the neutrino asymmetry of the Universe from cosmological data"

    (M. Lattanzi)

    11th Marcel Grossmann Meeting, Berlin, Germany, 23-29 July 2006.

34. "Effect of cosmological neutrinos on the propagation of primordial gravitational waves"

    (M. Lattanzi)

    11th Marcel Grossmann Meeting, Berlin, Germany, 23-29 July 2006.

35. "Does WMAP data constrain the lepton asymmetry of the Universe to be zero?"

    (M. Lattanzi)

    "Albert Einstein Century" International Conference, Paris, France, 18-22 July 2005.

36. "On the interaction bewteen relic neutrinos and primordial gravitational waves"

    (M. Lattanzi)

    II Sino-Italian Workshop on Cosmology and Relativistic Astrophysics, Pescara, Italy, 10-20 June 2005.

37. Impact of general reionization scenarios on inflation

    (S. Pandolfi)

    Horiba International Conference, COSMO/CosPa 2010, 30th September 2010, at The University of Tokyo, Tokyo, Japan.

38. Impact of general reionization scenarios on inflation

    (S. Pandolfi)

    Cosmolo Meeting, 8th September 2010, at IFIC, Instituto de Fisica Corpuscular, Valencia, Spain.

39. Inflation in general reionization scenarios

    (S. Pandolfi)

    Summer School in Cosmology, 19-31 July 2010, at ICTP–the Abdus Salam International Centre for Theoretical Physics, Trieste, Italy.

40. Harrison Zel'dovich spectrum is consistent with observation

    (S. Pandolfi)

    2nd Galileo-XuGuangqi meeting, 12-17 July 2010, Giardini Botanici Hanbury, Ventimiglia, Italy

41. Inflation in a general reionization scenario

    (S. Pandolfi)

    Xth School of Cosmology, 5-10 July 2010 at IESC, Cargese, Corse, France

42. Harrison-Zel'dovich primordial spectrum is consistent with observations

    (S. Pandolfi)

    10th Great Lakes Cosmology Workshop, 14-16 June 2010, KICP at the University of Chicago (IL), USA.

43. Inflation and Reionization

    (S. Pandolfi)

44. University of Michigan, 23rd June, Ann Arbor (MI), USA

45. Inflation with the CMB

    (S. Pandolfi)

46. Brookhaven National Laboratory, 8th June 2010

47. Inflation in a General Reionization Scenario

    (S. Pandolfi)

48. IberiCos2010 (5th Iberian Cosmology Meeting), Porto, Portugal, 29-31 March 2010

4.5. Posters

1. "Constraints on the cosmological lepton asymmetry"

   (M. Lattanzi)

   XIXmes Rencontres de Blois: "Matter and Energy in the Universe: from nucleosynthesis to cosmology", Blois, France, 20-25

   May, 2007.

2. "The interaction between relic neutrinos and cosmological gravitational waves: implication for interferometric detectors"

   (M. Lattanzi)

   "Albert Einstein Century" International Conference, Paris, France, 18-22 July 2005.

4.6. Lecture courses

1. "Relativistic kinetic theory and its applications in astrophysics and cosmology"

   (G.V. Vereshchagin)

   Lecture course for International Relativistic Astrophysics PhD, Erasmus Mundus Joint Doctorate Program from the

   European Commission, September 6-24, 2010, University of Nice Sophia Antipilis, Nice, France.

2. "Relativistic kinetic theory and its applications", IRAP Ph.D. lectures

   (G.V. Vereshchagin)

   February 1-19, 2010, Observatoire de la Cote d'Azur, Nice, France.

3. Inflationary Constraints and reionization

   (S. Pandolfi)

   IRAP Ph.D. Lectures in Nice, Observatoire de la Cote d'Azur, 12-16 February 2010

5. APPENDICES

A. Pair plasma relaxation time scales

Current interest in electron-positron plasmas is due to the exciting possibility of generating such plasmas in laboratory facilities already operating or under construction, see e.g., Myatt et al. (2009); Thoma (2009), for a review see Ruffini et al. (2010). Impressive progress made with ultra-intense lasers Chen et al. (2009) has led to the creation of positrons at an unprecedented density of 10^{16} cm^{-3} using ultra-intense short laser pulses, in a region of space with dimensions on the order of the Debye length. However, such densities have not yet reached those necessary for the creation of an optically thick pair plasma Katz (2000); Mustafa and Kämpfer (2009). Particle pairs are created at the focal point of ultra-intense lasers via the Bethe-Heitler conversion of hard x-ray bremsstrahlung photons Myatt et al. (2009) in the collisionless regime Wilks et al. (1992). The approach to an optically thick phase may well be envisaged in the near future.

Electron-positron plasmas are known to be present in compact astrophysical objects, leaving their characteristic imprint in the observed radiation spectra Churazov et al. (2005). Optically thick electron-positron plasmas do indeed play a crucial role in the gamma-ray burst phenomenon Ruffini et al. (2010, 2009).

From the theoretical point of view electron-positron pair plasmas are interesting because of the mass symmetry between the plasma components. This symmetry results in the absence of both acoustic modes and Faraday rotation; waves and instabilities in such plasmas differ significantly from asymmetric electron-ion plasmas, see e.g. Zank and Greaves (1995). Besides, theoretical progress in understanding quark-gluon plasma in the high-temperature limit is linked to understanding QED plasma since the results in these two cases differ only by trivial factors containing the QCD degrees of freedom (color and flavor) Thoma (2009).

Most theoretical considerations so far have assumed that an electron-positron plasma is formed either in thermal equilibrium (common temperature, zero chemical potentials) or in chemical equilibrium (nonzero chemical potentials), see e.g. Thoma (2009) and references therein. However, it is necessary to establish the time scale for actually reaching such a configuration. The only way for particles to thermalize, i.e., reach equilibrium distributions (Bose-Einstein or Fermi-Dirac) is via collisions. Collisions become relevant when the mean free path of the particles becomes smaller than the spatial dimensions of the plasma, and so the optical thickness condition is crucial for thermalization to occur.

Thermalization (chemical equilibration) time scales for optically thick plasmas are estimated in the literature by order of magnitude arguments using essentially just the reaction rates of the dominant particle interaction processes, see e.g. Gould (1981); Stepney (1983). They have been computed using various approximations. In particular, electrons have been considered ultrarelativistic, and Coulomb logarithm has been replaced by a constant. The accurate determination of such time scales as presented here is instead accomplished by solving the relativistic Boltzmann equations including the collisional integrals representing all possible particle interactions. In this case the Boltzmann equations become highly nonlinear coupled partial integro-differential equations which can only be solved numerically.

We developed a relativistic kinetic code treating the plasma as homogeneous and isotropic and have previously determined the thermalization time scales for an electron-positron plasma for selected initial conditions Aksenov et al. (2007). This approach was generalized to include protons in Aksenov et al. (2009b). We focus only on the electromagnetic interactions, which have a time scale of less than 10^{-9} sec for our system, and therefore on the proton and leptonic component of the plasma. The presence of neutrons and their possible equilibrium due to weak interactions will occur only on much longer time scales.

In this paper we report on the systematic results obtained by exploring the large parameter space characterizing pair plasmas with baryonic loading. The two basic parameters are the total energy density ρ and the baryonic loading parameter

$$B \equiv \frac{\rho_b}{\rho_{e,\gamma}} \simeq \frac{n_p m_p c^2}{\rho_{e,\gamma}}, \tag{A.0.1}$$

where ρ_b and $\rho_{e,\gamma}$ are respectively the total energy densities of baryons and electron-positron-photon plasma, n_p and m_p are the proton number density and proton mass, and c is the speed of light. We choose the following range of plasma parameters

$$10^{23} \leq \rho \leq 10^{33} \text{ erg/cm}^3, \tag{A.0.2}$$

$$10^{-3} \leq B \leq 10^3, \tag{A.0.3}$$

allowing us to also treat the limiting cases of almost pure electron-positron plasma with $B \ll 1$, and almost pure electron-ion plasma with $B \simeq m_p/m_e$, respectively. The temperatures in thermal equilibrium corresponding to (A.0.2) are $0.1 \lesssim k_B T \lesssim 10$ MeV.

Given the smallness of the plasma parameter $g = (n_e \lambda_D^3)^{-1} \ll 1$, where λ_D is the Debye length and n_e is the electron number density, it is sufficient to use one-particle distribution functions. In fact, for the pure electron-positron

Binary interactions	Radiative and pair producing variants
Møller and Bhabha $e_1^{\pm}e_2^{\pm} \longrightarrow e_1^{\pm\prime}e_2^{\pm\prime}$ $e^{\pm}e^{\mp} \longrightarrow e^{\pm\prime}e^{\mp\prime}$	Bremsstrahlung $e_1^{\pm}e_2^{\pm} \leftrightarrow e_1^{\pm\prime}e_2^{\pm\prime}\gamma$ $e^{\pm}e^{\mp} \leftrightarrow e^{\pm\prime}e^{\mp\prime}\gamma$
Single Compton $e^{\pm}\gamma \longrightarrow e^{\pm}\gamma'$	Double Compton $e^{\pm}\gamma \leftrightarrow e^{\pm\prime}\gamma'\gamma''$
Pair production and annihilation $\gamma\gamma' \leftrightarrow e^{\pm}e^{\mp}$	Radiative pair production and 3-photon annihilation $\gamma\gamma' \leftrightarrow e^{\pm}e^{\mp}\gamma''$ $e^{\pm}e^{\mp} \leftrightarrow \gamma\gamma'\gamma''$
	$e^{\pm}\gamma \leftrightarrow e^{\pm\prime}e^{\mp}e^{\pm\prime\prime}$

Table A.1.: Microphysical processes in the pair plasma.

Binary interactions (Coulomb scattering)	Radiative and pair producing variants
$p_1p_2 \longrightarrow p_1'p_2'$	$pe^{\pm} \leftrightarrow p'e^{\pm\prime}\gamma$
$pe^{\pm} \longrightarrow p'e^{\pm\prime}$	$p\gamma \leftrightarrow p'e^{\pm}e^{\mp}$

Table A.2.: Microphysical processes in the pair plasma involving protons. For details see also Ruffini et al. (2010).

plasma, the inequality $3 \cdot 10^{-3} \leq g \leq 10^{-2}$ holds in the region of the temperatures of interest. In a homogeneous and isotropic plasma the distribution functions $f(\epsilon, t)$ depend on the energy ϵ of the particle and on the time t. We treat the plasma as nondegenerate, neglecting neutrino channels as well as the creation and annihilation of baryons and the weak interactions (Aksenov et al. (2009b)).

The relativistic Boltzmann equations (Belyaev and Budker (1956); Mihalas and Mihalas (1984)) for photons, electrons, positrons, and protons in our case are

$$\frac{1}{c}\frac{\partial f_i}{\partial t} = \sum_q (\eta_i^q - \chi_i^q f_i), \tag{A.0.4}$$

where the index i denotes the type of particle and η_i^q, χ_i^q are the emission and the absorption coefficients for the production of the ith-particle via the reaction labeled by q. We account for all relevant binary and triple interactions between electrons, positrons, photons, and protons as summarized in Tables A.1 and A.2.

It has been shown (Aksenov et al. (2007)) that independent of the functional form of the initial distribution functions $f_i(\epsilon, 0)$, plasma evolves to a

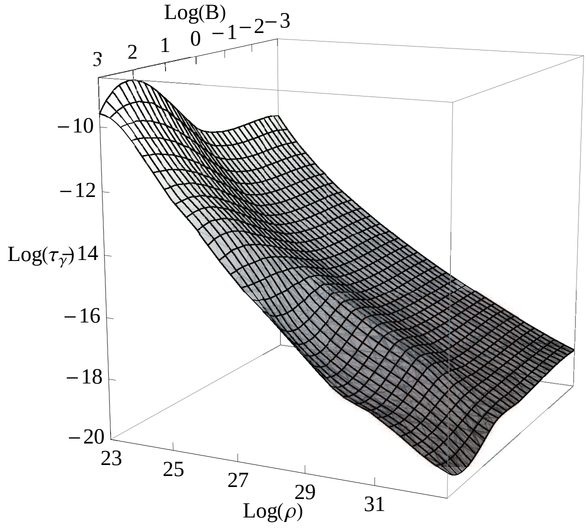

Figure A.1.: The thermalization time scale of the electron-positron-photon component of plasma as a function of the total energy density and the baryonic loading parameter. The energy density is measured in erg/cm^3, time is seconds.

thermal equilibrium state through the kinetic equilibrium, when the distribution functions of all the particles acquire the same form

$$f_i(\varepsilon) = \exp\left(-\frac{\varepsilon - \varphi_i}{\theta_i}\right), \tag{A.0.5}$$

where $\varepsilon_i = \epsilon_i/(m_i c^2)$ is the energy of the particles, $\varphi_i \equiv \mu_i/(m_i c^2)$ and $\theta_i \equiv k_B T_i/(m_i c^2)$ are their chemical potentials and temperatures, and k_B is Boltzmann's constant. The unique signature of kinetic equilibrium is the equal temperatures of all the particles and the nonzero chemical potential of the photons. In fact the same is also true for a pair plasma with proton loading (Aksenov et al. (2009b)). The approach to complete thermal equilibrium is more complicated in this latter case and depends on the baryon loading. For $B \ll \sqrt{m_p/m_e}$, protons are rare and thermalize via proton-electron (positron) elastic scattering, while in the opposite case $B \gg \sqrt{m_p/m_e}$, proton-proton Coulomb scattering dominates over the proton-electron scattering and brings protons into thermal equilibrium first with themselves. Then protons thermalize with the pair plasma through triple interactions, for details see Aksenov et al. (2009b). The two-body time scales involving protons should be compared with the three-body time scales bringing the electron-positron-photon plasma into thermal equilibrium. In fact we found that for $B \ll 1$, the electron-positron-photon plasma reaches thermal equilibrium at a given temperature, while protons reach thermal equilibrium with themselves at a different temperature; only later the plasma evolves to complete thermal equilibrium with

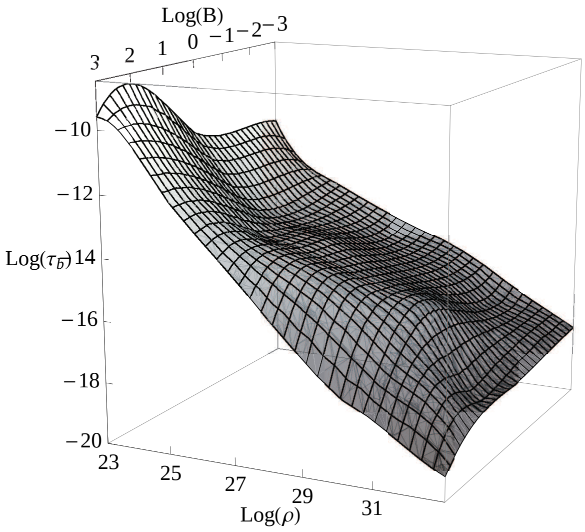

Figure A.2.: The final thermalization time scale of a pair plasma with baryonic loading as a function of the total energy density and the baryonic loading parameter. The energy density is measured in erg/cm^3, time is seconds.

the single temperature on a time scale

$$\tau_{th} \simeq \mathrm{Max}\left[\tau_{3p}, \mathrm{Min}\left(\tau_{ep}, \tau_{pp}\right)\right], \tag{A.0.6}$$

where

$$\tau_{ep} \simeq \frac{m_p c}{\epsilon_e \sigma_{\mathrm{T}} n_e}, \tag{A.0.7}$$

$$\tau_{pp} \simeq \sqrt{\frac{m_p}{m_e}} \left(\sigma_{\mathrm{T}} n_p c\right)^{-1}, \tag{A.0.8}$$

$$\tau_{3p} \simeq \left(\alpha \sigma_{\mathrm{T}} n_e c\right)^{-1} \tag{A.0.9}$$

are the proton-electron (positron) elastic scattering time scale, the proton-proton elastic scattering time scale, and the three-particle interaction time scale respectively, while σ_{T} is the Thomson cross-section and α is the fine structure constant. In (A.0.7)–(A.0.9) the energy dependence of the corresponding time scales is neglected.

The chemical relaxation (thermalization) time scale is usually computed as

$$\tau_i = \lim_{t\to\infty} \left\{ \left[F_i(t) - F_i(\infty)\right] \left(\frac{dF_i}{dt}\right)^{-1} \right\}, \tag{A.0.10}$$

where $F_i = \exp\left(\varphi_i/\theta_i\right)$ is the fugacity of a particle of type i. Instead of F_i we use one of the quantities θ_i, φ_i, n_i, or ρ_i in this computation.

We solved the Boltzmann equations with parameters (ρ, B) in the range

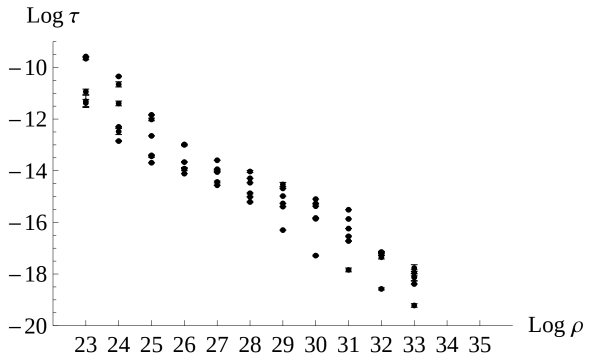

Figure A.3.: The final thermalization time scale of pair plasma with baryonic loading as a function of the total energy density for selected values of the baryonic loading parameter $B = (10^{-3}, 10^{-1.5}, 1, 10, 10^2, 10^3)$. The energy density is measured in erg/cm^3, time is seconds. Error bars correspond to one standard deviation of the time scale (A.0.11) away from the average value τ_{th} over the interval $t_{in} \leq t \leq t_{fin}$.

given by Eqs. (A.0.2) and (A.0.3). In total 78 models were computed, starting from a nonequilibrium configuration until reaching a steady state solution on the computational grid with 20 intervals for the particle energy and 16 intervals for the angles, for details see Aksenov et al. (2009b). For each model we computed the corresponding time scales for all particles of the ith kind. For practical purposes, instead of (A.0.10) we used the following approximation

$$\tau_{th} = \frac{1}{t_{fin} - t_{in}} \int_{t_{in}}^{t_{fin}} \left[\theta(t) - \theta(t_{\max})\right] \left(\frac{d\theta}{dt}\right)^{-1} dt, \tag{A.0.11}$$

with $t_{in} < t_{fin} < t_{\max}$, where $t_{\max}$ is the moment of time where the steady solution is reached and t_{in} and t_{fin} are the boundaries of the time interval over which the averaging is performed, for details see Aksenov et al. (2009a).

The thermalization time scale of the electron-positron-photon component is shown in Fig. A.1 as a function of the total energy density of the plasma and the baryonic loading parameter. The time scales of electrons, positrons and photons coincide. The final thermalization time scale of pair plasma with baryonic loading is shown in Fig. A.2. Its dependence on either variable cannot be fit by a simple power law, although it decreases monotonically with increasing total energy density, while it is not even a monotonic function of the baryonic loading parameter.

In Fig. A.3 the final thermalization time scale is shown for all the models we computed, along with the "error bars" which mark one standard deviation of the time scale (A.0.11) away from the average value τ_{th} in the averaging interval $t_{in} \leq t \leq t_{fin}$. The largest source of error comes from the small values of the time derivative in (A.0.11), although errors are typically below

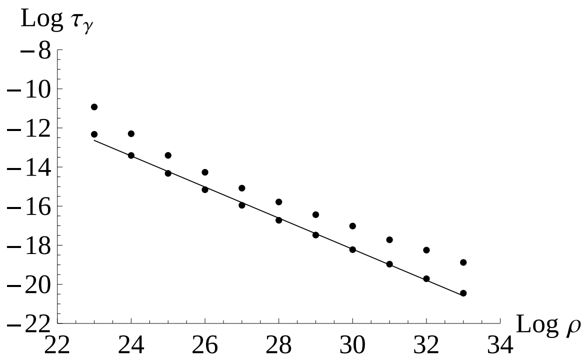

Figure A.4.: The thermalization time scale of the electron-positron-photon component of the plasma as a function of the total energy density (points), compared with the τ_{3p} time scale (joined points) computed using (A.0.9) for $B = 1$. The energy density is measured in erg/cm^3, time is seconds.

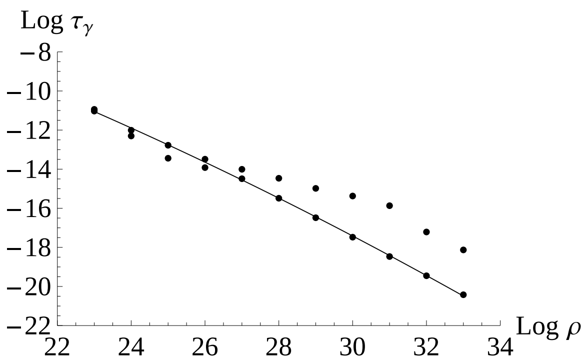

Figure A.5.: The final thermalization time scale of a pair plasma with baryonic loading as a function of the total energy density (points), compared with the τ_{th} time scale (joined points) computed using (A.0.6) for $B = 1$. The energy density is measured in erg/cm^3, time is seconds.

a few percent.

In Fig. A.4 we compare for $B = 1$ the actual value of the thermalization time scale of the electron-positron-photon component with the value estimated from (A.0.9). Both values clearly differ significantly. Actually the systematic underestimation by more than one order of magnitude which occurs for $B \leq 1$ disappears for larger baryonic loading.

In Fig. A.5 we present the computed values of the final thermalization time scale of the pair plasma with baryonic loading together with the value estimated from (A.0.6), again for $B = 1$. Unlike the previous case, the final thermalization time scale is a more complex function of the total energy density. Interestingly, less significant deviations from the value (A.0.6) occur at the extremes of the interval (A.0.3).

In this paper we have computed for the first time the time scale of thermalization for an electron-positron plasma with proton loading over wide ranges of both the total energy density (10 orders of magnitude) and baryonic loading parameter (6 orders of magnitude) allowing the treatment of the limiting cases of almost pure electron-positron plasma, almost pure electron-ion plasma as well as intermediate cases. The final result is presented in Fig. A.1 and A.2. The relaxation to thermal equilibrium for the total energy density (A.0.2) always occurs on a time scale less than 10^{-9} sec. It is interesting that the electron-positron-photon component and/or proton component can thermalize earlier than the time at which complete thermal equilibrium is reached. The relevant time scales are given and compared with the order-of-magnitude estimates. Unlike previous work there are no simplifying assumptions in our method since collisional integrals in the Boltzmann equations are computed directly from the corresponding QED matrix elements, e.g. from the first principles.

These results may be of relevance for the ongoing and future laboratory experiments aimed at creating electron-positron plasmas. Current optical lasers producing pulses during $\sim 10^{-15}$ sec carrying energy $\sim 10^2$ J= 10^9 erg are capable to produce positrons with the number density 10^{16} cm^{-3} (Chen et al. (2009)). There are claims that densities of the order of 10^{22} cm^{-3} are reachable (Shen and Meyer-Ter-Vehn (2002)). These densities today are yet far from 10^{28} cm^{-3} required for the plasma with the size $r_0 \simeq \mu m$ to be optically thick (Katz (2000)). Notice, that the expansion timescale of such plasma will be $r_0/c \sim 10^{-14}$ sec, while the timescale to establish kinetic equilibrium for the number density considered is of the same order of magnitude. These arguments show that theoretical results obtained assuming thermal or kinetic equilibrium, such as in Thoma (2009), cannot be applied to pair plasma, generated by ultraintense lasers.

However, results presented in this paper are important for understanding astrophysical systems observed today in which optically thick electron-positron plasmas are present. As specific example we recall that electron-positron pairs play the crucial rule in the dynamics of GRB sources. Considering typical energies and initial radii for GRB progenitors (Piran (1999))

$$10^{48}\text{erg} < E_0 < 10^{54}\text{erg}, \quad 10^{7}\text{cm} < R_0 < 10^{8}\text{cm}, \tag{A.0.12}$$

we estimate the range for the energy density in GRB sources

$$10^{23}\frac{\text{erg}}{\text{cm}^3} < \rho < 10^{32}\frac{\text{erg}}{\text{cm}^3}, \tag{A.0.13}$$

which coincides with (A.0.2). As for the baryonic loading of GRBs it is typically in the lower range of (A.0.2), namely (Ruffini et al. (2009))

$$10^{-3} < B < 10^{-2}. \tag{A.0.14}$$

Such high energy density leads to large number density of electron-positron pairs in the source of GRB, of the order of

$$10^{30}\ \mathrm{cm}^{-3} < n < 10^{37}\ \mathrm{cm}^{-3}, \tag{A.0.15}$$

making it opaque to photons with huge optical depth of the order of

$$10^{13} < \tau < 10^{18}. \tag{A.0.16}$$

In fact, the radiative pressure of optically thick electron-positron plasma in these systems is responsible for the effect of accelerated expansion (Ruffini et al. (1999, 2000); Bianco et al. (2006); Ruffini et al. (2009)), leading to unprecedented Lorentz factors attained $\Gamma \simeq B^{-1}$, up to 10^3, see e.g. Abdo et al. (2009); Izzo and et al. (In press, 2010). The role of the baryon admixture in electron-positron plasma in GRBs is to transfer internal energy of pairs and photons into kinetic energy of the bulk motion thus giving origin to afterglows of GRBs (Piran (1999); Ruffini et al. (2009)). Notice that in GRBs the timescales of thermalization are much shorter than the dynamical timescales $R_0/c \sim 10^{-3}$ sec, which implies that expanding electron-positron plasma even in the presence of baryons is in thermal equilibrium during the accelerating optically thick phase (Aksenov et al. (2008)).

After completion of this work we learned about the publication of Kuznetsova et al. (2010) where work similar to ours has been performed. Between this paper and our work conceptual differences should be noted which concern the attribution of thermalization to two-body Møller and Bhabha scattering, while we have pointed out explicitly that three-body interactions play an essential role. The thermalization time scales obtained by us have been computed with reference to these three-body interactions.

Acknowledgements. We thank both anonymous referees for their remarks which allowed to improve remarkably the paper.

B. Degenerate plasma relaxation

B.1. Introduction

The description of processes in electron-positron plasma is of great importance for physics and astrophysics (Ruffini et al., 2010). Firstly, the Big Bang theory involves lepton era with abundant presence of electron-positron pairs which at high temperature are in thermal equilibrium (Weinberg, 2008). Secondly, strong electromagnetic fields are generated in laser experiments aiming at production of electron-positron pairs. When this fields approach critical values copious pair production is expected leading to formation of electron-positron plasma (Gerstner, 2010; Chen et al., 2009; Mustafa and Kämpfer, 2009). Such supercritical electromagnetic fields are thought to occur in astrophysical conditions, near compact objects, such as pulsars and black holes (Damour and Ruffini, 1975; Churazov et al., 2005; Mereghetti, 2008), in the center of our Galaxy (Prantzos et al., 2010) and during the gravitational collapse of massive star cores (Bethe, 1990; Janka et al., 2007).

Relaxation of electron-positron plasma to thermal equilibrium has been considered in Aksenov et al. (2007, 2009b). There relativistic Boltzmann equations with exact QED collisional integrals taking into account all relevant two-particle (Compton scattering etc.) and three-particle interactions (relativistic bremsstrahlung etc.) were solved numerically. It was confirmed that a metastable state called "kinetic equilibrium" (Pilla and Shaham, 1997) exists in such plasma, which is characterized by the same temperature of all particles, but nonnull chemical potentials. Such state occurs when the detailed balance of all two-particle reactions is established. It was pointed out in Aksenov et al. (2007, 2009b) that direct and inverse 3p interactions are essential in bringing el-p plasma to thermal equilibrium.

In Aksenov et al. (2010) relaxation timescales for optically thick electron-positron plasma in a wide range of temperatures and proton loadings were computed numerically using the kinetic code developed in Aksenov et al. (2007, 2009b). These timescales were previously estimated in the literature by order of magnitude arguments using the reaction rates of the dominant processes (Gould, 1981; Stepney, 1983). It was shown that these numerically obtained timescales differ from previous estimations by several orders of magnitude.

Notice that temperature range considered in Aksenov et al. (2007, 2009b, 2010)

$$0.1 < \frac{kT}{m_e c^2} < 10 \tag{B.1.1}$$

was selected in order to avoid production of other particles such as neutrino Ruffini et al. (2010). At high temperatures the quantum nature of particle statistics has to be taken into account. The degeneracy parameter

$$D = \frac{1}{n_e \lambda_t h^3} = \frac{(kT)^3}{n_e \hbar^3 c^3} \tag{B.1.2}$$

determines the temperature when such effects become important. Thermal electron-positron plasma becomes degenerate ($D < 1$) at $kT \gtrsim 3 m_e c^2$.

In uniform isotropic pair plasma relativistic Boltzmann equation for distribution function f_i of the particle specie i has the following form:

$$\frac{1}{c}\frac{d}{dt} f_i(\mathbf{p}_i, t) = \sum_q \left(\eta_i^q - \chi_i^q f_i(\mathbf{p}_i, t)\right), \tag{B.1.3}$$

where the sum is taken over all two- and three-particle reactions q, η_i^q and χ_i^q are, respectively, the emission and absorption coefficients.

These coefficients for interaction of two particles having 4-momenta $(\epsilon_k, \mathbf{p}_k)$ and $(\epsilon_l, \mathbf{p}_l)$ before the reaction and $(\epsilon_i, \mathbf{p}_i)$ and $(\epsilon_j, \mathbf{p}_j)$ after it are

$$\eta_i = \int d^3\mathbf{p}_k d^3\mathbf{p}_l d^3\mathbf{p}_j [1 \pm f_i(\mathbf{p}_i, t)][1 \pm f_j(\mathbf{p}_j, t)] W_{\mathbf{p}_k, \mathbf{p}_l; \mathbf{p}_i, \mathbf{p}_j} f_k(\mathbf{p}_k, t) f_l(\mathbf{p}_l, t) \tag{B.1.4}$$

and

$$\chi_i = \int d^3\mathbf{p}_k d^3\mathbf{p}_l d^3\mathbf{p}_j [1 \pm f_k(\mathbf{p}_k, t)][1 \pm f_l(\mathbf{p}_l, t)] W_{\mathbf{p}_i, \mathbf{p}_j; \mathbf{p}_k, \mathbf{p}_l} f_j(\mathbf{p}_j, t), \tag{B.1.5}$$

where $1 \pm f(\mathbf{p}, t)$ are respectively Bose enhancement (+) and Pauli blocking ($-$) factors (Uehling and Uhlenbeck, 1933; Uehling, 1934).

These factors were not included in Aksenov et al. (2007, 2009b, 2010). It was pointed out in Aksenov et al. (2007) that for nondegenerate plasma two-particle interactions are generally $\alpha^{-1} \sim 137$ times faster than three-particles ones. This fact permitted to treat three-particle interactions assuming that kinetic equilibrium is established and maintained by the detailed balance in two-particle interactions. In that case the expressions for three-particle emission and absorption coefficients can be obtained analytically by the averaging with Boltzmann distributions.

For high temperatures Pauli blocking factors are expected to delay relaxation process to kinetic equilibrium. Besides there are no analytic expressions for averaged emission and absorbtion coefficients of three-particle interactions even in kinetic equilibrium due to the presence of Fermi and Bose

Electron-positron interactions	Proton interactions
Coulomb, Møller and Bhabha scattering	
$e_1^{\pm}e_2^{\pm} \longrightarrow e_1^{\pm\prime}e_2^{\pm\prime}$ $e_1^{\pm}e_2^{\mp} \longrightarrow e_1^{\pm\prime}e_2^{\mp\prime}$	$p_1p_2 \longrightarrow p_1'p_2'$ $pe^{\pm} \longrightarrow p'e^{\pm\prime}$
Compton scattering	
$e^{\pm}\gamma \longrightarrow e^{\pm\prime}\gamma'$	
Creation/annihilation	
$e_1^{\pm}e_2^{\mp} \longleftrightarrow \gamma_1\gamma_2$	

Table B.1.: Binary particles interactions in the pair plasma.

integrals. The three-particle interaction rates then have to be numerically integrated. It implies additional integration in phase space and consequent significant increase in computational time. In the present work we are interested in relaxation timescales to kinetic equilibrium taking into account the quantum nature of particle statistics. We include in our scheme all relevant two-particles interactions (Table B.1).

B.2. The computational scheme

The main difficulty arising for quantum statistics treatment is that the rate of particle emission/absorbtion now depends not only on this particle distribution function, but also on the density of second particle resulting from the interaction. We adopt a new approach to solve this issue which we call "reaction-oriented" instead of previous "particle-oriented" one.

Recall that the finite difference conservative scheme used in Aksenov et al. (2007, 2009b, 2010) (see also Aksenov et al. (2004)) instead fo distribution functions operates with spectral energy densities E_i

$$E_i(\epsilon_i) = \frac{4\pi\epsilon_i^3\beta_i f_i}{c^3}, \tag{B.2.1}$$

where $\beta_i = \sqrt{1-(m_ic^2/\epsilon_i)^2}$ (m_i, is the mass of i-th particle specie), in the energy phase space ϵ_i. The number density of particle is given by

$$n_i = \int f_i d\mathbf{p}_i = \int \frac{E_i}{\epsilon_i} d\epsilon_i, \qquad dn_i = f_i d\mathbf{p}_i, \tag{B.2.2}$$

while the corresponding energy density is

$$\rho_i = \int \epsilon_i f_i d\mathbf{p}_i = \int E_i d\epsilon_i.$$

In these variables the Boltzmann equations (B.1.3) read

$$\frac{1}{c}\frac{dE_i}{dt} = \sum_q (\tilde{\eta}_i^q - \chi_i^q E_i), \tag{B.2.3}$$

where $\tilde{\eta}_i^q = (4\pi\epsilon_i^3\beta_i/c^3)\eta_i^q$.

To obtain emission and absorbtion coefficients the computational grids are introduced in phase spaces $\{\epsilon_i, \mu_i, \phi_i\}$, where $\mu_i = \cos\vartheta_i$, ϑ_i and ϕ_i are usual angles in spherical coordinates of particle momentum space $\mathbf{p}_i$. The zone boundaries are $\epsilon_{i,\omega\mp 1/2}$, $\mu_{k\mp 1/2}$, $\phi_{l\mp 1/2}$ for $1 \leq \omega \leq \omega_{\max}$, $1 \leq k \leq k_{\max}$, $1 \leq l \leq l_{\max}$. The length of the i-th interval is $\Delta\epsilon_{i,\omega} \equiv \epsilon_{i,\omega+1/2} - \epsilon_{i,\omega-1/2}$. On the finite grid the functions (B.2.1) become

$$E_a = E_{i,\omega} \equiv \frac{1}{\Delta\epsilon_{i,\omega}}\int_{\Delta\epsilon_{i,\omega}} d\epsilon\, E_i(\epsilon), \tag{B.2.4}$$

where for simplification of formulae we introduce collective indices $a = \{i\omega\}$.

The collisional integrals in (B.2.3) are replaced by the corresponding sums. When particles are treated classically we have for time derivative of each variable the following expression

$$\dot{E}_a = \sum_{b,c} A_{(b,c|a,d)} E_b E_c - \sum_{b,c} B_{(a,b|c,d)} E_a E_b, \tag{B.2.5}$$

where first sum on the right side is for emission in reaction $b + c \to a + d$ and second is for absorbtion in reaction $a + b \to c + d$. There is no third summation (by index d) because of delta-function in the initial integrals originating from the energy conservation. This can be effectively rewritten as just one sum

$$\dot{E}_a = \sum_{b,c} A^a_{b,c} E_b E_c, \tag{B.2.6}$$

$$A^a_{b,c} = A_{(b,c|a,d)} - \delta^c_a \sum_e B_{(a,b|e,d)}, \tag{B.2.7}$$

and this sum can be found by direct computation without any complications.

When the quantum statistics effects are included we have instead

$$\begin{aligned}\dot{E}_a = \sum_{b,c} &(1 \pm E_a/g_a)(1 \pm E_d/g_d) A_{(b,c|a,d)} E_b E_c \\ &- \sum_{b,c} (1 \pm E_d/g_d)(1 \pm E_c/g_c) B_{(a,b|c,d)} E_a E_b,\end{aligned} \tag{B.2.8}$$

which g_a is spectral energy density corresponding to occupation numbers equal to unity. It turns out that while the sums on the right-hand side of

(B.2.8) can be reduced to one sum only, but due to different structure of Bose enhancement and Pauli blocking multipliers the numerical scheme based on the resulting expression will not be optimal.

Instead noticing that the phase space blocking/enhancement coefficient $(1 \pm E_d/g_d)(1 \pm E_e/g_e)$ are the same for all four particles involved in the process $b + c \to d + e$ (a is one of the b, c, d, e), the corresponding parts of collisional integrals arising in the above-mentioned sums can be computed only once instead of four times. As a result it is convenient not to fix a and sum over all possible b, c, as in (B.2.8), which we refer to as "particle-oriented" approach, but instead sum over all possible reactions, which we refer to as "reaction-oriented" approach. It means that at each step of calculations we fix b, c and for all possible reaction results the emission rates of outcomes d and e and the absorbtion rates of incomes b, c are added to array of derivatives $\dot{E}_a$. This approach considerably reduces the computational time and memory consumption.

In our method exact energy and number of particles conservation laws are satisfied, as we adopt interpolation of grid functions E_a inside the energy intervals. The number of energy intervals is 40, while internal grid of angles has 32 points in μ_i and ϕ_i.

B.3. Fitting the results

It is convenient to use the following dimensionless variables for energy distribution function: energy $\varepsilon_i = \epsilon_i/m_e c^2$, temperature $\theta_i = kT_i/m_e c^2$, and another particle-specific dimensionless quantity ν_i connected to chemical potential μ_i

$$\nu_i = \frac{1}{\theta_i}\left(\frac{\mu_i}{m_e c^2} - \frac{m_i}{m_e}\right). \tag{B.3.1}$$

In kinetic equilibrium we have for total energy distribution as function of kinetic energy ε_i

$$\begin{aligned}\frac{d\rho_i^t}{d\epsilon_i} &= \frac{1}{\pi^2 \lambda_c^3} \frac{(\varepsilon_i + m_i/m_e)^2 \sqrt{\varepsilon_i^2 + 2\varepsilon_i m_i/m_e}}{\exp(\varepsilon_i/\theta_i - \nu_i) \pm 1} \\ &= 2.08 \cdot 10^{30} \frac{(\varepsilon_i + m_i/m_e)^2 \sqrt{\varepsilon_i^2 + 2\varepsilon_i m_i/m_e}}{\exp(\varepsilon_i/\theta_i - \nu_i) \pm 1} \ \mathrm{cm}^{-3},\end{aligned} \tag{B.3.2}$$

and kinetic energy distribution function is just

$$\frac{d\rho_i}{d\epsilon_i} = \frac{\varepsilon_i}{\varepsilon_i + m_i/m_e} \frac{d\rho_i^t}{d\epsilon_i}. \tag{B.3.3}$$

The same expressions as (B.3.2), (B.3.3), but without ± 1 in denominator, hold in the case of classical Boltzmann statistics. In the previous works Aksenov et al. (2007, 2009b, 2010) instead of procedure of fitting of real spectra by thermal ones another approach was used. It was based on the one-to-one correspondence of particle density n_i and total energy density ρ_i to temperature θ_i and chemical potential ν_i of Boltzmann distribution. New approach provides accurate estimation of temperature based on the maximum of the energy spectra. Every step we calculate also the quality of fits by the coefficient of determination R^2. The fit is considered meaningful when R^2 exceeds 0.9.

The parameters θ and ν obtained from fits are used to determine relaxation timescales. For that purpose we fit dependencies of θ and ν on time in the chosen intervals by functions

$$f(t) = C_1 + C_2 t + C_3 \exp(-t/C_4), \tag{B.3.4}$$

with constants C_i, $i = 1, 2, 3, 4$, representing respectively the final value, the linear drift, the magnitude of initial deviation from equilibrium and the timescale of relaxation. It is important to account for the linear drift since not all the processes share the same timescale but usually timescales of processes are well separated (by at least an order of magnitude), so that slower processes can be treated as introducing linear perturbations to the spectral parameters. Validity of such an approximation was approved by the fact that in all cases for time intervals inspected $C_2 \Delta t \ll C_1$ (usually $C_2 \Delta t / C_1 \lesssim 10^{-3}$).

B.4. Case A

As the first example we treat the case which is the same as Case III of Aksenov et al. (2009b) with the total energy density $\rho = 4.85 \cdot 10^{26}$ erg/cm^3. The initial ratio between concentrations of electrons and protons is taken to be $\varsigma = n_p/n_- = 10^{-3}$. We set up flat initial spectrum for photons $E_\gamma(\epsilon_i) = \text{const}$, and power law spectra for the pairs $E_\pm(\epsilon_\pm) \propto \left[\epsilon_\pm - mc^2\right]^{-2}$ and protons $E_p(\epsilon_p) \propto \left[\epsilon_p - Mc^2\right]^{-4}$. In the regions where the energy density for fermions was larger than admissible by Pauli principle we take $E = 0.95 E_{max}$. Finally, the ratio of initial and final concentrations of positrons is chosen to be $n_+ = 10^{-1} n_+^{\text{th}}$. Given these initial conditions the baryon loading parameter is $\mathbf{B} = 0.2$. The initial energy spectra are shown in Fig. B.1. The temperature of kinetic equilibrium in this case is $\theta \simeq 2$.

In Fig. B.2 and B.3 we compare the results of evolution for temperatures and chemical potentials in two cases: when blocking/enhancement factors *a*) are taken into account and *b*) are omitted in evolution equations (B.2.8).

The overall qualitative character of evolution is unchanged when we account for phase space blocking/enhancement, however the timescales increase, as it is illustrated in Tab. B.2. The main source of such an increase is

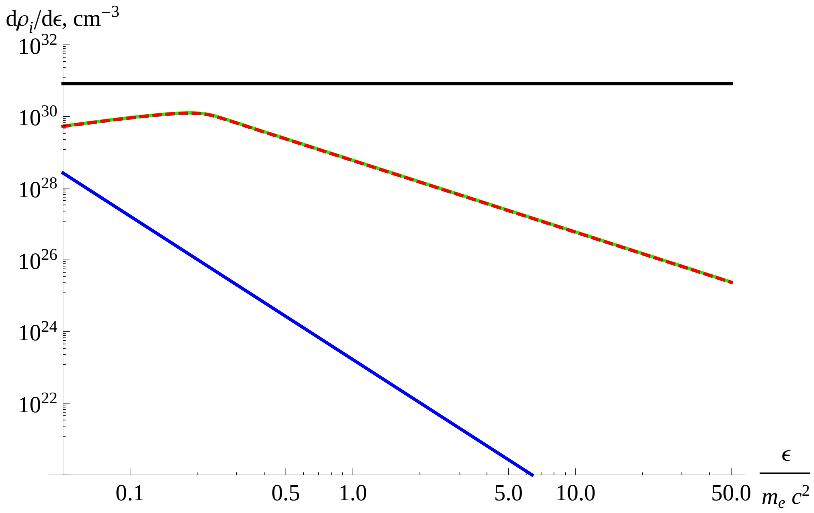

Figure B.1.: Initial kinetic energy spectral densities as functions of particle kinetic energy in the case A. The spectrum of protons is chosen to be steeper than the one of electrons and positrons. Black, green, red, blue curves correspond to spectrum of photons, electrons, positrons (they coincide within the accuracy of the plot) and protons, respectively.

the change of reaction rates in low-energy range, where coherent effects in reactions involving photons are damped by the Pauli blocking of electrons and positrons. As a result establishment of the kinetic equilibrium takes two times longer than in the case of classical statistics ($5.9 \cdot 10^{-17}$ s versus $11.8 \cdot 10^{-17}$ s).

The differences in the final spectra of particles are illustrated in Fig. B.4. The difference between classical and quantum statistics is seen in photon spectrum, which is changed almost by half of order of magnitude in low-energy part, see Fig. B.5.

B.5. Case B

The second example was chosen in such a way that the total energy density $\rho = 2.43 \cdot 10^{25}$ erg/cm^3 was 20 times less than in previous case A. The same spectrum shapes and ratios between energy in components were chosen. The temperature of kinetic equilibrium in this case is $\theta \simeq 1$.

In this case distribution functions in the final state of kinetic equilibrium are very close to Boltzmann ones, see Fig. B.6. Quantum corrections are tiny as it follows from limits of ν values $\nu_{\mathrm{lim}} = -7.7$ (corresponding occupation numbers are lower than $e^{-7.7} = 4.5 \cdot 10^{-4}$). Nevertheless relaxation timescales for classical and quantum statistics differ by $\sim 10\%$, see Tab. B.2.

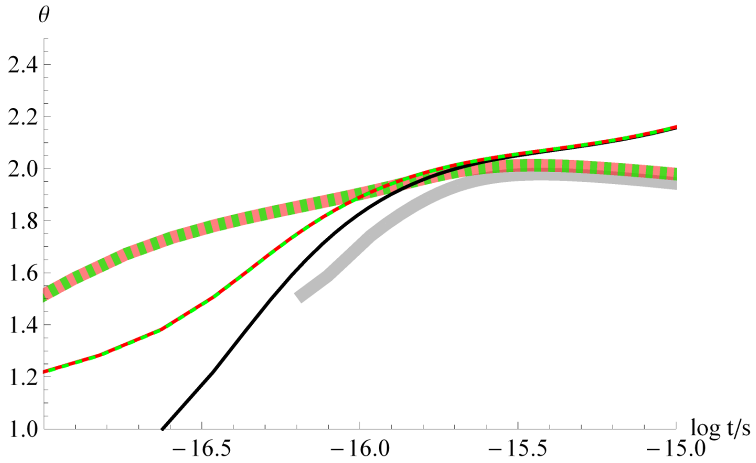

Figure B.2.: Comparison of dimensionless temperature evolution for classical and quantum statistics in the case A. Wide lines represent quantum statistics case while thin ones are for classical Boltzmann statistics. Values for fits with coefficient of determination $R^2 > 0.9$ are shown. Colors are the same as at Fig. B.1.

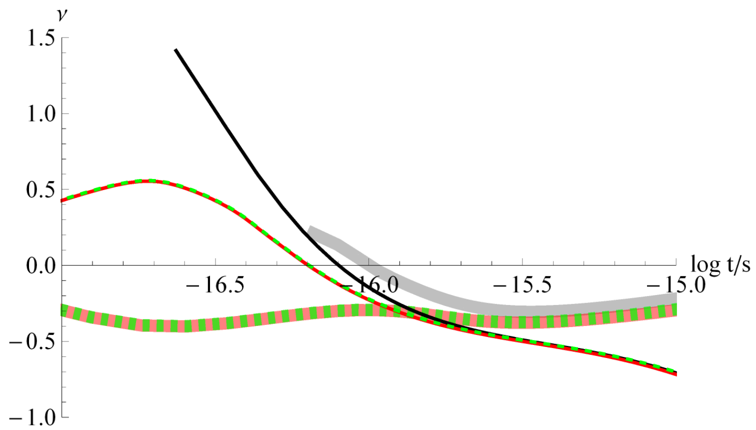

Figure B.3.: Comparison of dimensionless chemical potential evolution for classical and quantum statistics in the case A. Colors are the same as at Fig. B.1, B.2.

Table B.2.: Comparison of relaxation timescales for temperatures and chemical potentials for classical and quantum particles treatment

Particle	θ timescale, s		ν timescale, s	
	Classical	*Quantum*	*Classical*	*Quantum*
Case A, time interval $10^{-16} \div 10^{-15}$ s				
γ	$5.7 \cdot 10^{-17}$	$7.2 \cdot 10^{-17}$	$5.6 \cdot 10^{-17}$	$7.7 \cdot 10^{-17}$
e^-	$5.9 \cdot 10^{-17}$	$9.4 \cdot 10^{-17}$	$5.7 \cdot 10^{-17}$	$11.7 \cdot 10^{-17}$
e^+	$5.9 \cdot 10^{-17}$	$9.4 \cdot 10^{-17}$	$5.7 \cdot 10^{-17}$	$11.8 \cdot 10^{-17}$
Case B, time interval $5 \cdot 10^{-16} \div 1.5 \cdot 10^{-14}$ s				
γ	$5.1 \cdot 10^{-16}$	$5.4 \cdot 10^{-16}$	$5.1 \cdot 10^{-16}$	$5.5 \cdot 10^{-17}$
e^-	$3.4 \cdot 10^{-16}$	$3.8 \cdot 10^{-16}$	$3.2 \cdot 10^{-16}$	$3.6 \cdot 10^{-17}$
e^+	$3.4 \cdot 10^{-16}$	$3.8 \cdot 10^{-16}$	$3.2 \cdot 10^{-16}$	$3.6 \cdot 10^{-17}$
Case C, time interval $5 \cdot 10^{-19} \div 4 \cdot 10^{-18}$ s				
γ	$2.0 \cdot 10^{-19}$	–	$2.0 \cdot 10^{-19}$	–
$e^\pm$	$1.8 \cdot 10^{-19}$	$2.3 \cdot 10^{-19}$	$1.8 \cdot 10^{-19}$	$2.4 \cdot 10^{-19}$
Case C, time interval $3 \cdot 10^{-16} \div 2 \cdot 10^{-15}$ s				
γ	–	$1.9 \cdot 10^{-16}$	–	$2.2 \cdot 10^{-16}$
$e^\pm$	–	$2.2 \cdot 10^{-16}$	–	$2.8 \cdot 10^{-16}$

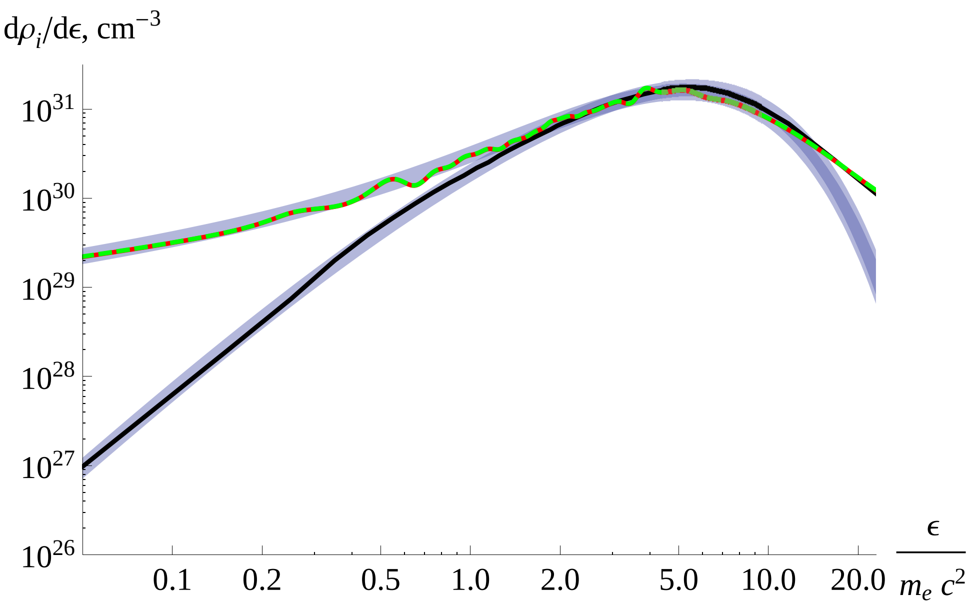

Figure B.4.: Final spectral densities and their thermal fits (blue lines) at time moment 10^{-15} s as functions of particle kinetic energy in the case A. Colors are the same as at Fig. B.1.

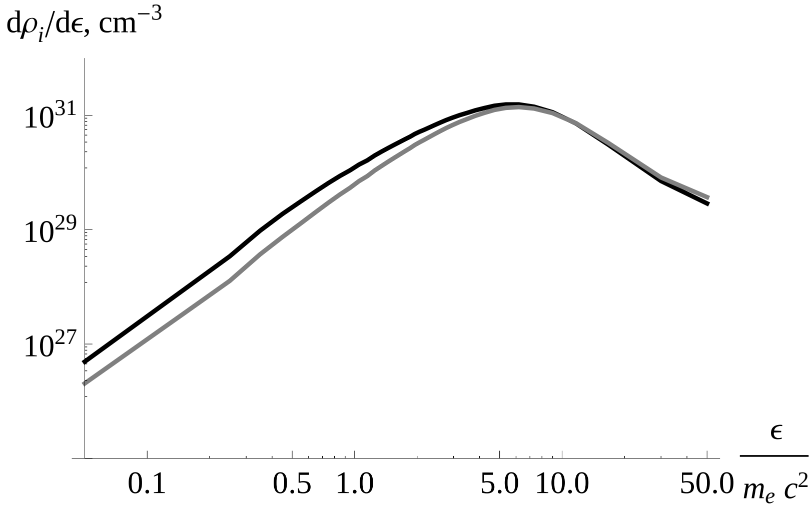

Figure B.5.: Final photon spectral densities at time 10^{-15} s as functions of particle kinetic energy in the case A. Black curve (higher) represents the spectrum for quantum statistics and grey (lower) shows results of classical calculations.

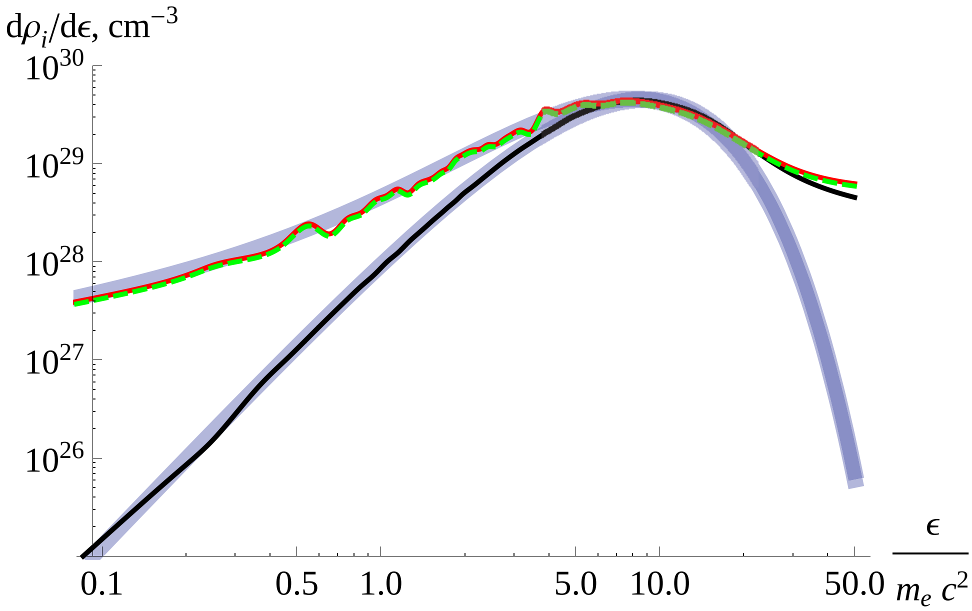

Figure B.6.: Final spectral densities and their thermal fits (in blue) at time $1.5 \cdot 10^{-14}$ s as functions of particle kinetic energy for initial conditions B. Both spectra and fits for quantum and classical particle treatments are coinciding within the accuracy of the plot. Colors are the same as at Fig. B.1.

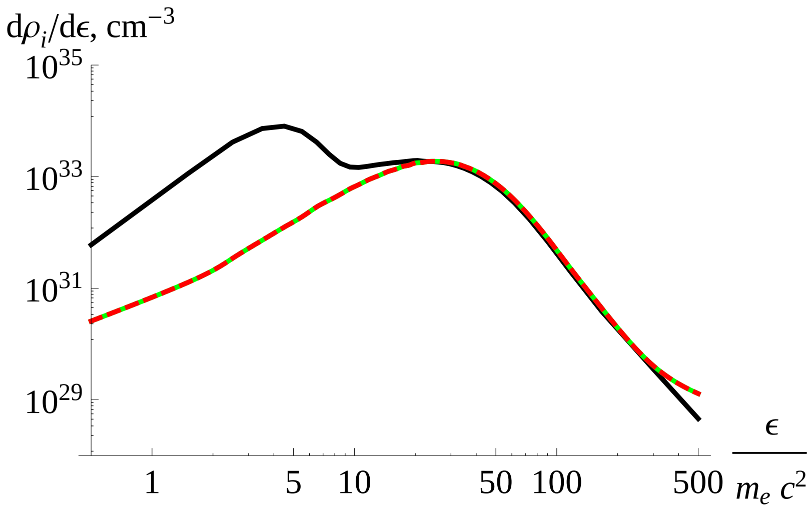

Figure B.7.: Spectral densities at time 10^{-17} s as functions of particle kinetic energy for initial conditions C. A profound excess of photons at low energies is obvious. Colors are the same as at Fig. B.1.

B.6. Case C

As a third case we treat high energy density $\rho = 2.04 \cdot 10^{29}$ erg/cm^3 without protons, which is at the edge of applicability of our method because of neutrino interactions becoming substantial with higher energy densities. The corresponding temperature in kinetic equilibrium is about $\theta = 10$.

Instead of relaxation to kinetic equilibrium at timescale comparable to 10^{-19} s, which was found in the case of Boltzmann statistics in Aksenov et al. (2010), there is a process of relaxation on this timescale, but resulting photon distribution are not really kinetic one (see Fig. B.7). Pair distribution in principle could be described as thermalized and corresponding timescale is shown in Table B.2. Thermalization of photons occurs on much longer timescale of $2 \cdot 10^{-16}$ s, so remnants of photon excess in low-energy part can be seen in distribution function up to $\sim 10^{-15}$ s (Fig. B.8).

B.7. Discussion

The form of kinetic equilibrium distributions is complicated and depends on the relation between parameters m_i/m_e, θ_i and ν_i. For photons generally there are two power-law intervals. For $\varepsilon \ll \theta|\nu|$ we have $\frac{d\rho}{d\epsilon} \propto \varepsilon^3$ due to strong degeneracy. For $\theta|\nu| \ll \varepsilon \ll \theta$ we have $\frac{d\rho}{d\epsilon} \propto \varepsilon^2$, while for higher energy the spectral shape is exponential as in the case of classical Boltzmann distribution.

For electrons and positrons instead with small enough $\varepsilon \ll 1$ the spectrum

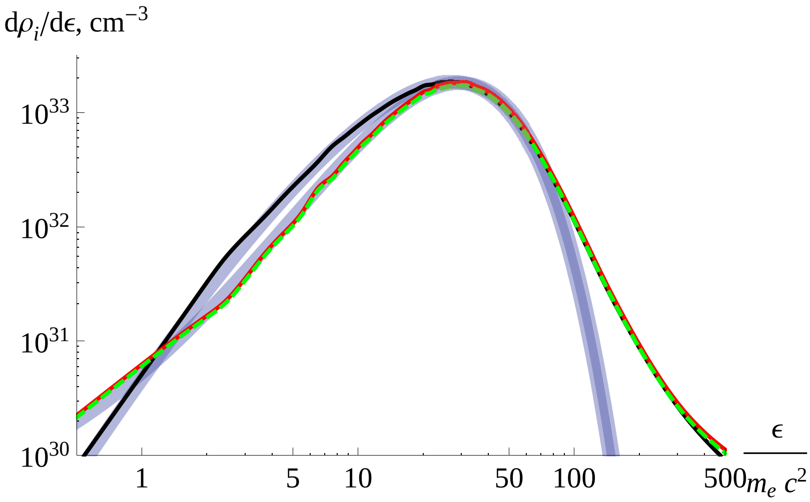

Figure B.8.: Spectral densities and their thermal fits (in blue) at time 10^{-15} s as functions of particle kinetic energy for initial conditions C. Note the tiny difference in fit and distribution function of photons at $\epsilon/m_e c^2 \sim 2$, this is the remnant of initial photon excess at this energy. Colors are the same as at Fig. B.1.

is $\frac{d\rho}{d\epsilon} \propto \varepsilon^{1/2}$, while for intermediate region $1 \ll \varepsilon \ll \theta|\nu|$ the spectrum shape is $\frac{d\rho}{d\epsilon} \propto \varepsilon^3$, and then again exponential dependence.

As the temperature increases, occupation numbers in electron-positron field and photon field increase as well. This leads to the damping of the reaction rates involving not only fermions in the final state, but also for damping of interactions between bosons and fermions which are enhanced by coherent effects of bosons. If the occupation numbers n of given states for fermion and boson are the same then the product of blocking/enhancement multipliers $(1+n)(1-n) = 1-n^2$ for the reaction is still less than 1. As a result when in the system there is no direct interaction between bosons, which is the case of QED, we have only damping in the reaction rates with the increase of temperature.

In the case C the temperature in kinetic equilibrium is $\theta \simeq 10$ and damping of two-particles interactions leads to increase of relaxation timescale by more than three orders of magnitude. This new timescale is even longer than the thermalization timescale in the case of classical statistics. Therefore taking into account quantum nature of particle statistics for temperatures above the electron rest mass energy, where the degeneracy effects become important, there is no clear distinction between two-particle and three-particle interaction timescales. By the same argument as in the previous paragraph we can suppose that the rate of some three-particle reactions will be damped even more than that of two-particle ones. For example, bremsstrahlung rate $e^\pm + e^\pm \longrightarrow e^\pm + e^\pm + \gamma$ will be damped by two Pauli blocking factors and increased by one Bose enhancement factor. For the other three-particle reactions involving two photons in the final state we have overall increase of rates, so the sum of these two effects is uncertain.

Correct estimation of the thermalization timescale for proton component of plasma also demands three-particle interactions to be taken into account. Since the inclusion of three-particle interactions requires substantial revision of the code and will demand much longer computational time in this Letter we concentrated on two-particle interactions only and consequently on the relaxation towards kinetic equilibrium.

B.8. Conclusions

In this Letter we have showed that timescale of establishment of kinetic equilibrium in electron-positron plasma is substantially affected by the effect of phase space blocking/enhancing of two-particles reaction rates as temperature of the plasma is higher than $\theta \simeq 1$. Degeneracy of the main part of electron-positron pairs increases the timescale in spite of reaction rates enhancement by the coherent effects of photons. We show that the processes rates at $\theta = 10$ are damped so strong that timescale of photon relaxation to kinetic equilibrium t_{ph} is more than three orders of magnitude larger than the corresponding timescale of classical thermalization t_{cl}. It is interesting that on the timescale slightly larger than t_{cl} some marginally stable solution occurs, that evolves in time towards thermal equilibrium with timescale t_{ph}.

C. Hydrodynamic phase of GRBs

C.1. Introduction

When the importance of ultrarelativistic expansion with application to GRBs has been realized (the compactness problem) several papers appeared, both numerical (Piran et al. (1993), Mészáros et al. (1993)) and analytical (Shemi and Piran (1990), Bisnovatyi-Kogan and Murzina (1995)) dealing with conversion of internal energy of relativistic plasma into its kinetic energy of expansion. Baryons play crucial role in this scenario since their inertia is used as the storage of the energy which was initially released in the source of GRBs. The results of these investigations showed that initially energy dominated plasma with baryon loading forms a shell which self accelerates until it becomes matter dominated.

The next step has been the proposal of relativistic shocks as the mechanism to convert back (release) the kinetic energy of relativistic baryons into thermal energy of electrons which can be then emitted in the form of GRBs. In this respect two alternative scenarios were considered: external shock (Rees and Meszaros (1992)) and internal shock (Narayan et al. (1992), Rees and Meszaros (1994)) models. In the external shock model the key ingredient is the low density environment which decelerates the expanding shell. In the internal shock model the presence of multiple subshells having different Lorentz factors is postulated, and attributed to the activity of a central engine.

In Ruffini et al. (2000) yet different proposal has been made considering electron-positron plasma formed in the source of GRBs. In this model the baryon matter is located outside the source of e^+e^- pairs, the dyadosphere Preparata et al. (1998), in the form of a thin shell at rest, containing the mass fullfilling the Ruffini-Wilson relation. This constraint on baryonic mass is essential in two aspects:

- even if the interaction with the baryonic shell produce some episodic deceleration of the expanding shell it nevertheless allows that the acceleration continues until reaching ultrarelativistic Lorentz factors;
- the interaction between the two shells does not change the thickness of the expanding shell measured in the laboratory frame (constant thickness approximation holds).

In this chapter we revisit the issue of the hydrodynamic phase in GRB sources, by studying numerically the evolution of an optically thick plasma.

In simulations of this kind in literature, one of the main conclusions derived from the simulations of Piran et al. (1993) is that in the reference frame of the explosion, short after the beginning of the expansion most of the matter and energy becomes concentrated in a narrow shell which propagates at nearly the speed of light with a single peaked "frozen radial profile". This profile can be reproduced in subsequent time moments by the set of scaling laws.

Such a simple profile results in single burst of radiation emitted when the expanding shell becomes transparent for photons (Shemi and Piran (1990); Ruffini et al. (2001)). In the fireshell model the radiation emitted at this moment is called proper gamma ray burst (P-GRB). Recent observations show that the P-GRB may have a more complex light curve, see figure C.1.

In this thesis we propose a mechanism for generation of structured P-GRB light curves. The general idea is to attribute the structure of the light curve of P-GRBs to the structure of the expanding plasma. For this reasons we seek for deviations from the "frozen radial profile". As we will see below the possible presence of an external medium in the acceleration phase of the plasma expansion indeed may be responsible for the generation of this structure.

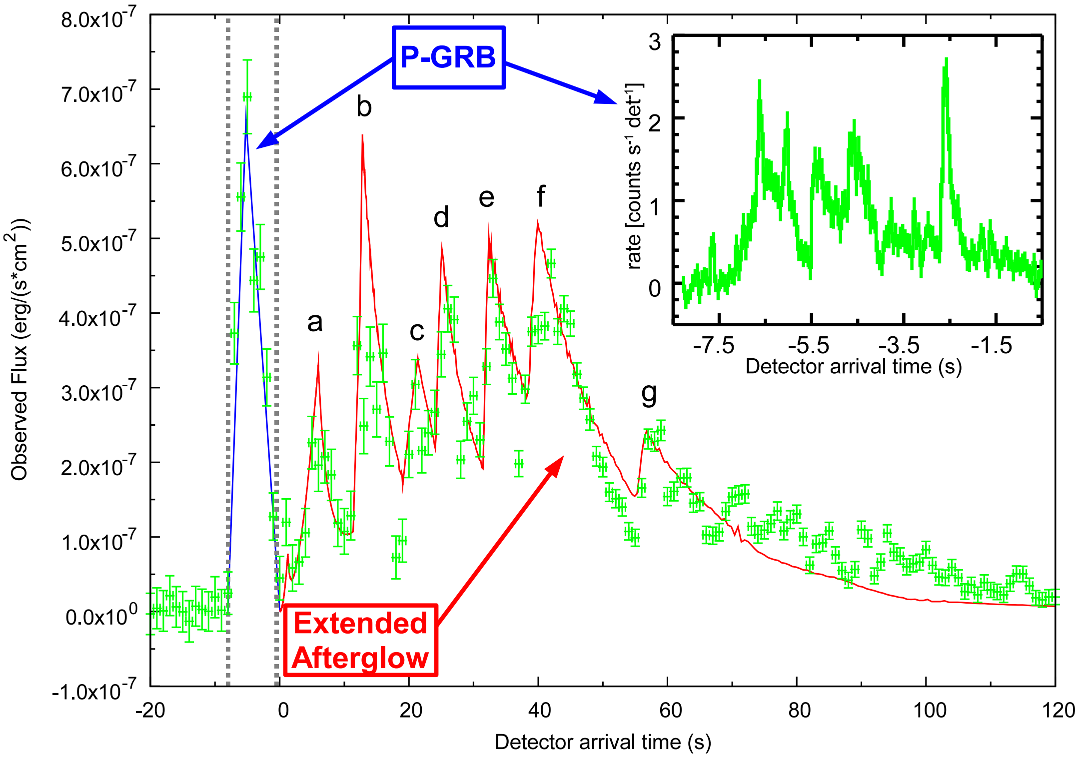

Figure C.1.: The BAT data and the theoretical simulation for the afterglow within the fireshell model for GRB060614. In the corner above and right is shown the structured P-GRB with details. The fireshell model does not predict a structure for the P-GRB, just its energy. One of the basic motivations of this thesis is to propose a mechanism of formation of multiple peaks in P-GRB. Figure reproduced from Caito et al. Caito et al. (2009).

In some recent works results which differs from the "frozen radial profile" were found and discussed as well. In particular, formation of relativistic jets in collapsar models (Aloy et al. (2000)), gaussian jets (Zhang et al. (2004)) and jets due to neutrino-antineutrino annihilation in compact object mergers was studied in Aloy et al. (2005), and Poynting jet models were studied in McKinney (2006) and Barkov and Komissarov (2008). In the fireshell model in line with observations of Swift and Fermi satellites which never observed the expected achromatic breaks in the light curve, we do address the issue of jets in GRBs. In this sense the fireshell model is at variance from the research such as Aloy et al. (2000), Zhang et al. (2004), McKinney (2006), who consider the case of jets and magneto-hydrodynamic structure.

Contrary to the model of collapsar which purports the GRB process to occur inside the star, we focus on process occurring in a vicinity of the forming black hole with baryonic remnants surrounding the black hole. This approach has been verified by the fit of 10 sources, see figure C.2, and Ruffini et al. (2009). The observations by Swift and more recently by Fermi have given a clear confirmation to one of the major prediction of the fireshell model: the existence of the P-GRB, emitted when the electron-positron-baryon plasma reaches transparency. In the case of Swift, following previous pioneering observations of Beppo-SAX in 1997-2005 the P-GRB has been clearly identified as the crucial feature to explain the disguised short GRBs. Two GRBs with this characteristic (Bernardini et al. (2007); Caito et al. (2009)) have been analyzed. The sharp emission has been observed to be of the order of few seconds and in some cases to be highly structured, see figure C.1 and Gehrels et al. (2005). Similarly, in the case of Fermi a set of sources has been found with Lorentz factor larger than 10^3 and again having a very prominent P-GRB with a duration of the order of few seconds followed by ultra-high energy emission in the GeV region. It is worth noting that within the fireshell model the emission of the P-GRB is assumed to be thermal, see Ruffini et al. (2009), and it is crucial therefore to study the corresponding light curve based on the radial structure of the expanding plasma.

With the assumption of spherical symmetry we focus on the issue how different possible initial spatial distributions of matter and energy may influence subsequent evolution of the plasma. We solve the same equations as in Piran et al. (1993) and Ruffini et al. (1999) focusing on various different initial profiles. In addition to considering expansion of γ, e^+, e^-, b in vacuum, we also study the case with expansion into an extended uniform distribution of baryons still satisfying the Ruffini-Wilson condition.

C.2. Physical evolution

We study the evolution of a thermal plasma in the hydrodynamic approximation, considering the relativistic energy-momentum tensor.

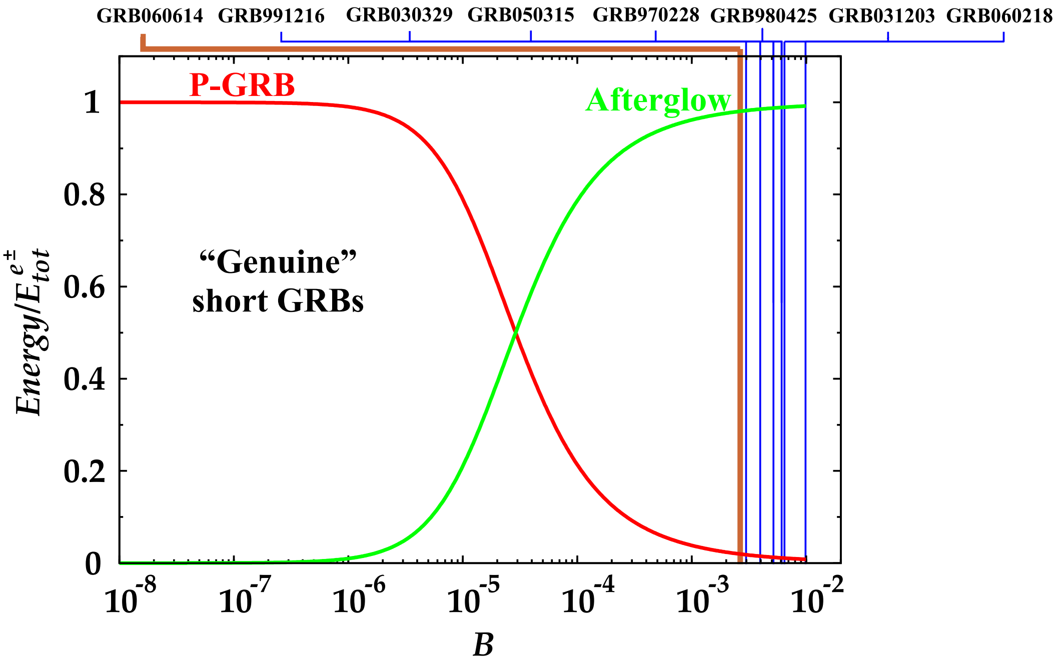

Figure C.2.: The energies emitted in the P-GRB (red line) and in the extended afterglow (green line), in units of the total energy of the plasma, are plotted as functions of the B parameter. When $B \lesssim 10^{-5}$, the P-GRB becomes predominant over the extended afterglow, giving rise to a "genuine" short GRB. In the figure are also marked in blue the values of the B parameters corresponding to some GRBs analyzed in the framework of fireshell model, see Ruffini et al. (2007). All belonging to the class of long GRBs, together with the GRB060614 one (thick brown line). Figure reproduced from Caito et al. Caito et al. (2009)

Assuming that particles are: non relativistic baryons, and ultrarelativistic photons, electrons and positrons, the fluid variables will be [1]:

$$\begin{aligned} \epsilon_r &= \epsilon_- + \epsilon_+ + \epsilon_\gamma, \\ \rho_r &= \rho_\gamma + \rho_+ + \rho_-, \\ p_r &= p_\gamma + p_- + p_+, \end{aligned}$$

where the subscript "r" denotes relativistic component, "-" denotes electrons, "+" denotes positrons and "γ" denotes photons. We also have

$$\begin{aligned} \rho_{nr} &= \rho_b, \\ p_{nr} &= p_b \simeq 0, \end{aligned}$$

where the subscript "nr" denotes non relativistic component and "b" denotes baryons. The hydrodynamics velocity of both components is the same since

[1] In this Appendix the speed of light will be $c = 1$

they are coupled by collisions, so we have:

$$\epsilon = \epsilon_{nr} + \epsilon_r \simeq \epsilon_r, \tag{C.2.1}$$
$$\rho = \rho_{nr} + \rho_r \simeq \rho_b, \tag{C.2.2}$$
$$p = p_r + p_{nr} \simeq (\rho_r \epsilon_r)/3. \tag{C.2.3}$$

It is useful to introduce new variables following Bowers and Wilson (1991):

$$D = \rho\Gamma \qquad \text{mass density in the laboratory frame,} \tag{C.2.4}$$
$$E = \epsilon D \qquad \text{energy density in the laboratory frame,} \tag{C.2.5}$$
$$S = (D + E + \Gamma p)U \qquad \text{radial momentum.} \tag{C.2.6}$$

In spherically symmetric case we get from the energy-momentum and number of particles conservation equations:

$$\frac{\partial D}{\partial t} = -\frac{\partial(r^2 D v)}{r^2 \partial r}, \tag{C.2.7}$$
$$\frac{\partial E}{\partial t} = -\frac{\partial(r^2 E v)}{r^2 \partial r} - p\frac{\partial(r^2 U)}{r^2 \partial r} - p\frac{\partial \Gamma}{\partial t}, \tag{C.2.8}$$
$$\frac{\partial S}{\partial t} = -\frac{\partial(r^2 S v)}{r^2 \partial r} - \frac{\partial p}{\partial r}, \tag{C.2.9}$$

where U, v and Γ are related as follows:

$$\Gamma = \sqrt{1 + U^2} \qquad v = U/\Gamma. \tag{C.2.10}$$

Equations (C.2.7)-(C.2.9) form a coupled system of partial differential equations, and its solutions cannot be found without further approximations. We implemented a numerical code to solve this system of equations, following Bowers and Wilson (1991) and Wilson and Mathews (2003).

C.3. Numerical approach

Finite-difference methods can be applied to solve partial differential equations (C.2.7)-(C.2.9). One approach to the solution of resulting system of coupled nonlinear algebraic equations involves matrix inversion which turns out to be particularly time consuming for our purposes. Instead we follow another simpler approach called operator splitting. We implement the second order method described in Bowers and Wilson (1991) and Wilson and Mathews (2003) successfully applied to relativistic hydrodynamic problems (see e.g.

Ruffini et al. (1999), Ruffini et al. (2000)). For further developments and implementations of this technique see Anninos et al. (2005).

Below we briefly illustrate the main steps applied for our case.

The main idea of the operator splitting method is to compute separately the contributions to the left hand side of equations (C.2.7)-(C.2.9) from different terms on the right hand side.

The terms on the right hand side are solved one by one, in the following order:

INTERACTION:

$$\frac{\partial S}{\partial t} = -\frac{\partial p}{\partial r}, \tag{C.3.1}$$

$$U = \frac{S}{D + E + p\Gamma}, \tag{C.3.2}$$

$$\frac{\partial E}{\partial t} = -p\frac{\partial \Gamma}{\partial t}, \tag{C.3.3}$$

$$\frac{\partial E}{\partial t} = -p\frac{\partial (r^2 U)}{r^2 \partial r}, \tag{C.3.4}$$

ADVECTION:

$$\frac{\partial D}{\partial t} = -\frac{\partial (r^2 D v)}{r^2 \partial r}, \tag{C.3.5}$$

$$\frac{\partial E}{\partial t} = -\frac{\partial (r^2 E v)}{r^2 \partial r}, \tag{C.3.6}$$

$$\frac{\partial S}{\partial t} = -\frac{\partial (r^2 S v)}{r^2 \partial r}. \tag{C.3.7}$$

From the physical point of view one may think that first we solve the physical interactions in the plasma, namely

- the acceleration due to radiative pressure,
- the new velocity,
- the new energy densities for the changes in velocity and pressure.

Then we solve the “advection equations” which can be thought just as a rearrangement of the densities in space. As the fluid elements move in space, the “advection equations” will just show where the fluid element located before in r_1 will be after the time iteration, to say r_2.

Using (C.2.3, C.2.4 and C.2.5), equations (C.3.1)-(C.3.4) become,

$$\frac{\partial S}{\partial t} = -\frac{\partial E/\Gamma}{3\partial r}, \tag{C.3.8}$$
$$U = \frac{S}{D + (4/3)E}, \tag{C.3.9}$$
$$\frac{\partial E}{\partial t} = -\frac{E}{3\Gamma}\frac{\partial \Gamma}{\partial t}, \tag{C.3.10}$$
$$\frac{\partial E}{\partial t} = -\frac{E}{3\Gamma}\frac{\partial (r^2 U)}{r^2 \partial r}. \tag{C.3.11}$$

C.3.1. Finite difference form of equations

Using a finite difference method to solve numerically the previous equations, we can have an iteration system in which, given initial conditions, we can solve the evolution of the variables step by step in time. We introduce the following notation:

$$\Delta t = t^n - t^{n-1}, \tag{C.3.12}$$
$$\Delta r = r_k - r_{k-1}, \tag{C.3.13}$$
$$\Delta^t G = G^n - G^{n-1}, \tag{C.3.14}$$
$$\Delta^r G = G_k - G_{k-1}, \tag{C.3.15}$$

where G represents any of the variables or functions of variables, n is a temporal step and k is a spatial step. The system of equations (C.3.5)-(C.3.11), after an adapted integration, can be expressed as:

INTERACTION:

$$\frac{\Delta^t S}{\Delta t} = -\frac{r^2}{3\Delta r}\Delta^r(E/\Gamma), \tag{C.3.16}$$
$$U = \frac{S}{D + (4/3)E}, \tag{C.3.17}$$
$$\Delta^t(lnE) = -\frac{1}{3}\Delta^t(ln\Gamma), \tag{C.3.18}$$
$$\Delta^t(lnE) = -\frac{\Delta t}{3\Gamma}\frac{\Delta^r(r^2 U)}{r^2 \Delta r}, \tag{C.3.19}$$

ADVECTION:

$$\frac{\Delta^t D}{\Delta t} = -\frac{4\pi\Delta^r(r^2 Dv)}{\Delta^r V}, \tag{C.3.20}$$

$$\frac{\Delta^t E}{\Delta t} = -\frac{4\pi\Delta^r(r^2 Ev)}{\Delta^r V}, \tag{C.3.21}$$

$$\frac{\Delta^t S}{\Delta t} = -\frac{4\pi\Delta^r(r^2 Sv)}{\Delta^r V}, \tag{C.3.22}$$

where V is the volume.

In order to solve (C.3.16)-(C.3.22), we have to give as initial condition spatial profiles for the physical variables at $t = 0$, then, by iteration method we can calculate the spatial distribution for the variables at any later time. Therefore we have to set initial profiles for: $D(t = 0, r), E(t = 0, r), \Gamma(t = 0, r)$.

We can study any kind of initial conditions changing initial velocity and initial energy to mass ratio distribution. This is the main goal of this work: we intend to study which interesting results can be found using different initial spatial distributions for E and D.

C.3.2. Numerical issues

Some important points should be kept in mind when making a hydrodynamic code, especially in relativistic case. These points influence both accuracy and stability of the scheme. In many problems in relativistic hydrodynamics strong shocks occurs. For this reason either artificial viscosity (AV) schemes or flux limiter (FL) ones are usually implemented. In our case, as we will see in the following, shocks indeed occur, but they can be resolved without AV. The FL scheme used in our code in order to avoid spurious oscillations near shocks is described in section C.3.3.

Centering

The variables have different position on the grid: some are calculated in the center of each grid cell (G_{k+1}) and some are defined in the edge of grid cells (G_k), where k is a even number (see figure C.3). Odd numbers define the center of cells and even numbers define the boundary of cells. After the discretization of the spatial grid we define the volume element as,

$$\Delta V_{k+1} = \frac{4\pi}{3}(r^3_{k+2} - r^3_k). \tag{C.3.23}$$

Variables are defined in these volume elements. Volume elements represents the smallest resolvable part of the problem. Since in a numerical problem the functions of the variables are not continuous but discretized. The volume element theoretically tends to the differential volume when its dimension tends to zero. For each one of these volume elements we give a value for these variables. Inside each volume element the variables have a constant value, this value can change just from one to another volume element.

For stability we have to define other volume elements translated spatially with respect to the above ones. Some variables have to be defined in these new volume elements (for illustration see figure C.4),

$$\Delta V_k = \frac{4\pi}{3}(r_{k+1}^3 - r_{k-1}^3). \tag{C.3.24}$$

There is no general rule, but specifically in our case variables which are not intrinsically related to motion ($\rho, \epsilon, E, D,$) are computed on the centers of grid cells, equation (C.3.23); instead, variables related to motion (v, u, γ, S) are computed in edges of grid cells, what means that the correct volume elements for these variables are the shifted ones, equation (C.3.24).

After centering one variable, we can construct the variable in the shifted volume element, for example: D is centered in the middle of the grid cells, $D \equiv D_1$; but we can construct,

$$D_k = \frac{1}{2}(D_{k+1} + D_{k-1}), \tag{C.3.25}$$

and *mutatis mutandis* for the variables centered in the edge of the grid cells. But the way to compute these shifted values should maintain the order of accuracy of the code. The equation (C.3.25) is of first order, we can do it with greater order of accuracy if needed.

To give an example, in equation (C.3.20), as mentioned before, the quantity D is calculated in the center of grid cell: D_{k+1}. So the spatial derivative will be done using the edge values of this cell (D_k, D_{k+2}). In order to give values on these edges for variables which are first computed on the center of grid cells, we use a second order interpolation, like the following algorithm:

If $v_k > 0$, then

$$D_k = D_{k-1} - \frac{1}{2}\nabla D_{k-1}(\Delta r - v_k \Delta t). \tag{C.3.26}$$

If $v_k < 0$, then

$$D_k = D_{k+1} + \frac{1}{2}\nabla D_{k+1}(\Delta r + v_k \Delta t). \tag{C.3.27}$$

And if $v = 0$ we use equation (C.3.25). The gradient ∇D_{k+1} is calculated using flux limiter.

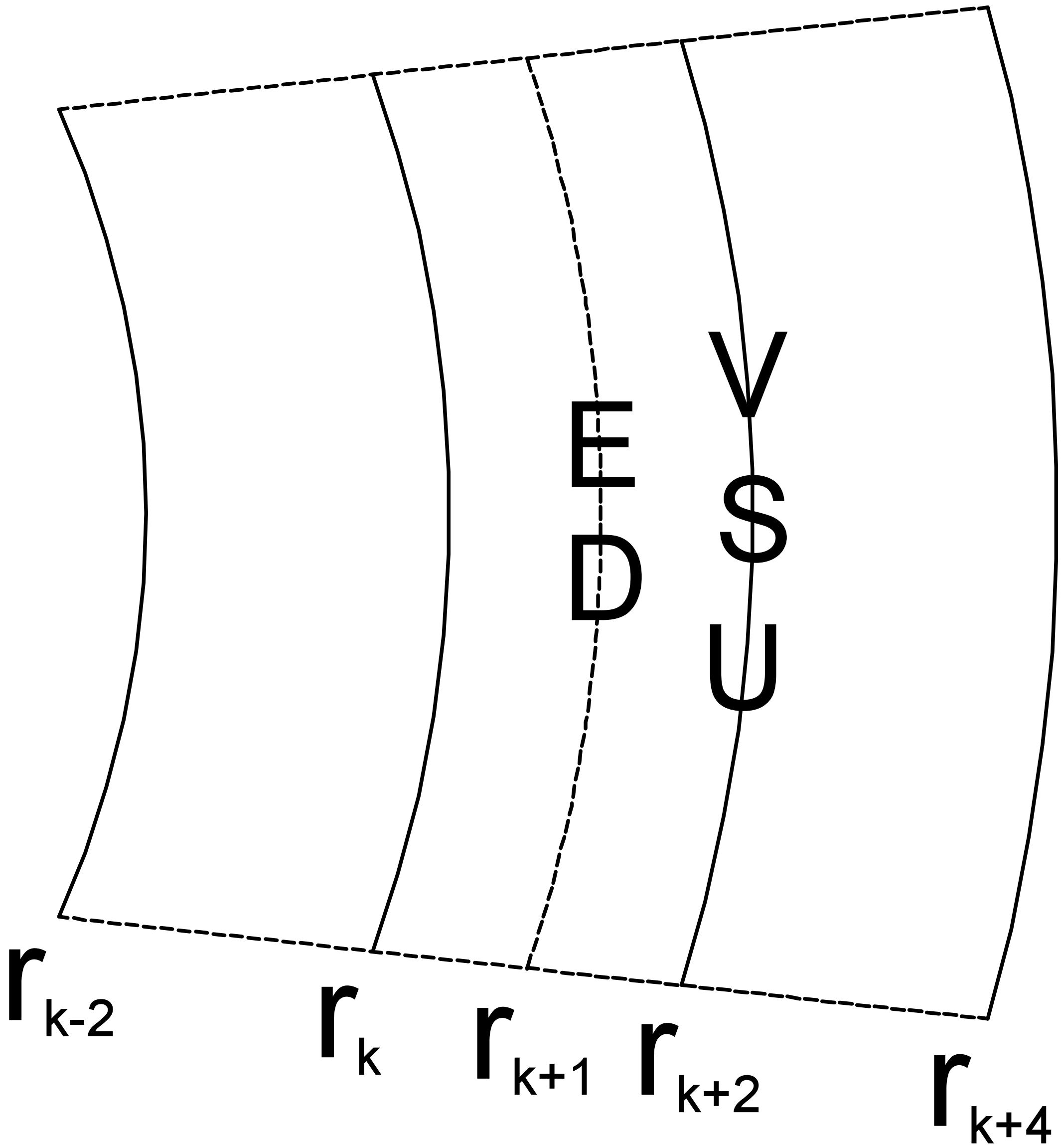

Figure C.3.: Grid cells are defined with boundaries in r_k with even k. One can see that v, S and U are defined in boundaries of cells, while E and D are define in centers of cells.

Boundary conditions

As in many finite difference methods the differentiation is approximated as:

$$\frac{\partial G_k}{\partial r} \equiv \frac{G_{k+1} - G_{k-1}}{\Delta r}, \tag{C.3.28}$$

and

$$\frac{\partial G_{k+1}}{\partial r} \equiv \frac{G_{k+2} - G_k}{\Delta r}. \tag{C.3.29}$$

The values on the right hand side are the current time step iteration (G^n)

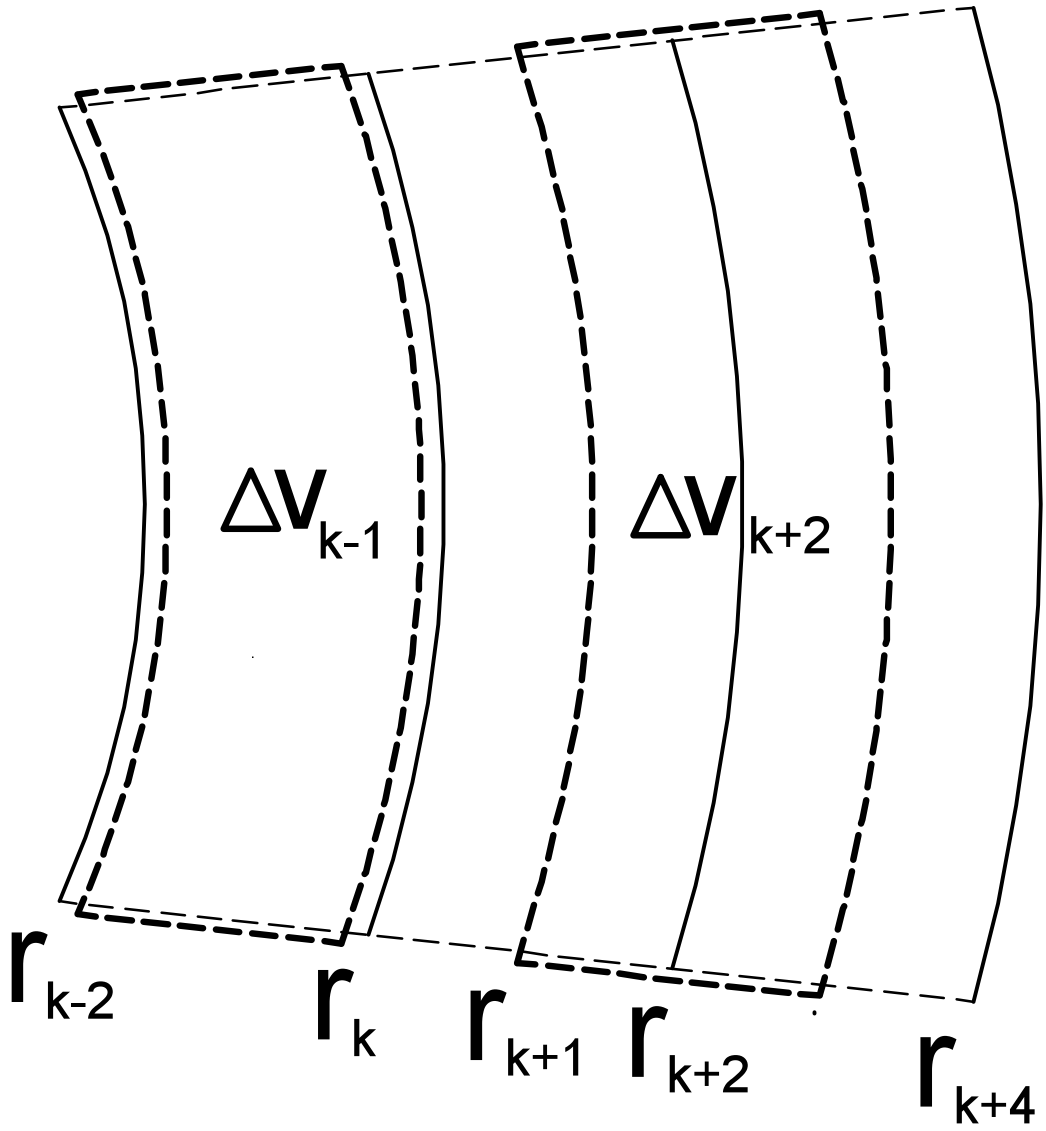

Figure C.4.: The volume elements of variables defined in boundaries of cells, are defined like ΔV_{k+2} which is centered in the boundary of cells (r_{k+2} in this case) and have as boundaries r_{k+1} and r_{k+3}. This is the volume element for S_{k+2}, for example. For variables defined in centers of cells, the volume element is defined like ΔV_{k-1}, with boundaries in r_{k-2} and r_k. This is the volume element for E_{k-1}, for example.

while those on the left hand side will be used to construct the variables at next iteration (G^{n+1}).

It means that, in the cases where the spatial differentiation appears, in order to know (G_k^{n+1}), we need the values of (G_{k-1}^n) and (G_{k+1}^n). If the initial spatial grid goes from $k_{min} - 1$ until $k_{max} + 1$, because of the spatial differentiation, at the next time step we will have just variables going from k_{min} until k_{max}

(we cannot construct the value $G^{n+1}_{k_{max}+1}$ since we do not have $G^{n}_{k_{max}+2}$). Doing so at each time step we lose the values on the edges of the grid in a way that after n iterations we will loose $2n$ points (n in the beginning of the grid and n in the end). In a massive computation, after few "time", the grid will be totally lost; to not loose the important information, one could do a grid much greater than the "really needed" one.

Example: if we need to calculate some physical variable from radius 0 until 100 meters, and we can use just 100 points in the grid to represent this, it's possible to construct a grid with 1100 points (corresponding to physical radius going from $r_{min} = -500$ meters and $r_{max} = 600$ meters), with the physical important region in the middle of the grid (from 500 to 600). With this configuration, after each iteration the points without physical interest will be lost. After the 500th iteration, the grid will be reduced to the 100 points of physical interest, if we calculate more then this, information will be lost. This can be a solution for very simple and small size problems, but it is clearly a very inefficient way.

In order to solve this problem one can use an extrapolation to set the boundary conditions. The initial grid is from $k_{min} - 1$ until $k_{max} + 1$, after each iteration, we loose the ends of the grid, so we have to reconstruct them, in order to keep the same grid size as the initial one. A linear extrapolation can be done in the following way:

$$G_{k_{max}+1} = 2G_{k_{max}-1} - G_{k_{max}-3}, \tag{C.3.30}$$

$$G_{k_{min}-1} = 2G_{k_{min}+1} - G_{k_{min}+3}, \tag{C.3.31}$$

which is nothing more than the calculation of one point in the line formed by the last two end points in the grid (at each boundary). It works in the case when the physical functions in the ends of the grid does not differs too much from a linear function.

In our case we did in a different way, we simply set to zero the end values of D, E and Γ. This is equivalent to loosing the matter (E, D) in these points. It works well when we can neglect the quantities in the end points in comparison with quantities in points we are interested in. We did (for D and E):

$$G_{k_{max}+1} = G_{k_{min}-1} = 0. \tag{C.3.32}$$

Since $K_{min} = 2$, we have

$$G_{k_{min}-1} = G_1 = 0. \tag{C.3.33}$$

Since the plasma is expanding radially to outside, from $r_{k_0} = 0$, we have $v_{k_{min}+1} > 0$ since it is on the positive part of the grid, and $v_1 < 0$ since it is on the negative part of the grid. With these velocities and the above boundary conditions this means that if the matter arrives to the ends of the grid, then it is lost to next calculations (transparent boundary conditions).

With this boundary conditions we can use a grid with almost the same size we want to study the physical evolution of the variables, avoiding using points outside the range of interest.

Reflection at the origin

The original physical problem is in three dimensions, but, assuming spherical symmetry we represent it numerically with just one dimension. In order to reproduce the spherical symmetry in one dimension we impose a reflection symmetry at the origin ($r = 0$). The same initial profile for $r > 0$ is used also for $r < 0$, with the difference that for negative radius the velocity is also negative, so, we set for initial profiles: $E(r) = E(-r)$, $D(r) = D(-r)$, $\Gamma(r) = \Gamma(-r)$, $v(r) = -v(-r)$. In figure C.5 we illustrate the reflection in the initial profile also for negative radius, as for the non relativistic case, see section C.4.4.

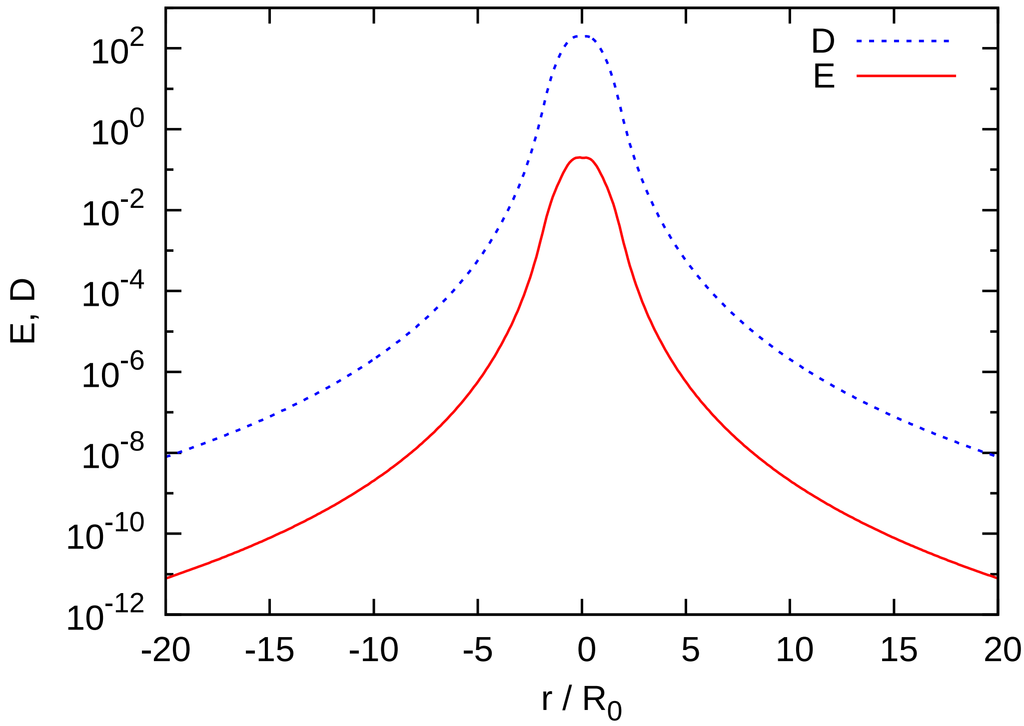

Figure C.5.: Initial profiles have a reflection in the origin, as illustrated here for the non relativistic case considered in section C.4.4.

The negative part is just a reflection of the positive part, in principal it is not of physical interest. Indeed, the negative part does not need to have the same size (in radius) as in the positive part. The positive part has to have the size which we want for the physical problem, while the negative one is just necessary to maintain the right solution in the center ($r = 0$). Remembering that the boundary conditions (C.3.32) means loss of matter, we need to choose the size in the negative part in a way that during the total evolution (in time), the loss of matter in the negative part does not become significant to affect the positive part. In more detailed way, let's call k_0 as the grid point at the center of the plasma, in which $r_{k_0} = 0$. Then, if the profiles for (D, E and Γ) in $k_0 - 1$ are equal to the profiles in $k_0 + 1$, it means that the solution is not affected by the grid size in the negative part. If the grid size in the negative part is too small and the loss of matter is too strong in a way that the values in $k_0 - 1$ and $k_0 + 1$ become different, then the solution in the positive part is affected by the grid size in the negative part.

In our simulations the grid size in the negative part is usually 10 times smaller than the grid size in the positive part, see figure C.6.

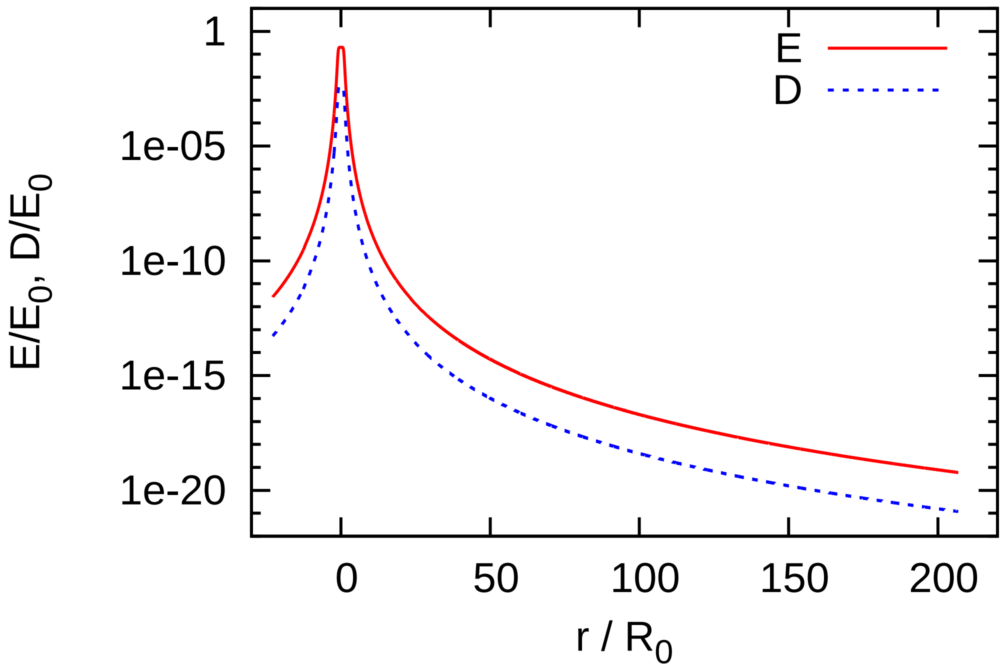

Figure C.6.: Using the boundary conditions (C.3.32), the size in the grid corresponding to negative radius can be much smaller then the grid for positive radius. In this case the negative grid is nine times smaller then the positive one.

Time step and diffusion

The steps in radial coordinate Δr and in time interval Δt are related, the results are quite sensitive to these choices, which should satisfy the Courant condition. Due to relativistic velocities it is better to set the limit for Δt, $\Delta t < \Delta r/c$, (see Wilson & Mathews Wilson and Mathews (2003)). We found that to avoid instability we can not use values near to $\Delta t = \Delta r$. So we fixed $\Delta t = \Delta r/2$ in all our simulations. If we use smaller values for Δt, for a fixed Δr, the numerical diffusion increases. But if we use smaller values for Δr, for a fixed value of $\Delta r/\Delta t$, the diffusion decreases. For this reason we used high spatial resolution with the number of spatial intervals $N_r > 10^5$.

It is necessary to use large number of spatial intervals specially in Eulerian simulations where we would like to resolve the structure of shocks occurring far alway from the source.

C.3.3. Implementation

Here we will show the implementation of the ordered equations (C.3.16)-(C.3.22). In order to maintain stability, some equations are changed when written in numerical form. The iteration indices are: k ranging from 2 to k_{max} (just even numbers), and n ranging from 1 to t_{max}.

First we set up initial profiles for E, D and Γ, and we also compute the volume elements ΔV. All these variables are given in k and $k+1$ (for all k values). Then we begin the temporal iterations, below we show all the steps in one temporal iteration.

Pressure Acceleration

The acceleration due to pressure is computed first. We solve the term of the radial moment S which is related to the spatial derivative of pressure p (recalling that $p = E/3\Gamma$). Since S is defined in boundaries of cells (k), the spatial derivative of p will use the values in the center of cells ($k+1$):

$$\frac{\Delta^t S_k}{\Delta t} = -\frac{r_k^2}{3\Delta r}\Delta^r(E/\Gamma)\big|_k = -\frac{r_k^2}{3\Delta r}\left(\frac{E}{\Gamma}\bigg|_{k+1} - \frac{E}{\Gamma}\bigg|_{k-1}\right) \quad , \tag{C.3.34}$$

which in the code becomes

$$S_k^{n+1} = S_k^n - \frac{4\pi r_k^2 \Delta t}{A^n 3\Delta V_k}\left(\frac{E_{k+1}}{\Gamma_{k+1}} - \frac{E_{k-1}}{\Gamma_{k-1}}\right), \tag{C.3.35}$$

where A^n is one variable which gives for the first iteration ($n = 1$) the value $A^1 = 1/2$, and gives $A^n = 1$ for all other iterations ($n > 1$). This is used because in the initial profile we have S computed in the same time moment as the other variables D, E and Γ, while in the other iterations we have S computed half time step after the pressure (or E and Γ). So in this first iteration we advance S just half time step from the initial profiles, and in the other iterations, we advance S also half time step in comparison with E and Γ, since we have equations (C.3.96), (C.3.99) which computes E and Γ in the end of each time iteration.

Another important point here, is the meaning of the upper indexes n and $n+1$. If we had not used the splitting method, the variables would have all the contributions being calculated in just one equation. Then it would have sense to say that the temporal variation $\Delta^t S$ means that we are computing the difference between one time S^{n+1} and the time step before S^n. But, since we use the splitting method, the contributions to a single variable appears in more then one equation, so the full contributions to S for the next time step will be computed just in the end of the total time iteration. In the above equation S_k^n means the old value of S, and S_k^{n+1} means the new value of S after the pressure acceleration contribution; but we can not say that this is the new value of S after the entire time step, since there is another equations which is also necessary to compute the total evolution of S. From now on I will omit the temporal indices. The value in the right hand side has to be thought as an old value, and the value in the left hand side as the new value after the contribution of the equation which is being computing in the case. To thought in the value of the variables S, D and E in different time steps we have to get the values just after the end of each full time iteration.

Now we apply the acceleration computed in the radial momentum in the velocities (u, v and Γ),

Velocity

$$U_k = \frac{S_k}{(D_k + (4/3)E_k)}, \tag{C.3.36}$$

$$\Gamma_k^* = \sqrt{1 + U_k^2}, \tag{C.3.37}$$

$$v_k = \frac{U_k}{\Gamma_k^*}. \tag{C.3.38}$$

(C.3.39)

Since S is defined in center of cells (k), the velocities will be computed in k, and we need also D and E computed in k. So, as said in the introduction of this section, in the initial profiles we compute E and D in the center of shells, to do this we use equation (C.3.25). Here we label the Lorentz factor as Γ^* instead of Γ because it will be used again in the end of the time iteration.

Pressure work

After the computation of new velocity caused by the acceleration due to the spatial pressure gradient, we compute the change in energy density E due to the new velocity. We solve first the term in equation for E which depends on the temporal variation in Γ, equation (C.3.18). Since E is defined in $k+1$ and we do not have any spatial derivatives in this term, all quantities are used in $k+1$,

$$\Delta^t(lnE_{k+1}) = -\frac{1}{3}\Delta^t(ln\Gamma_{k+1}) \quad . \tag{C.3.40}$$

We stress the importance to use the correct definition of the limits when solving the integral of this equation, since this is the only term in which a time derivative in the right hand side appears. In principle the time derivative in Γ should be calculated in a full time step, which means that the lower limit on the integral should be the Γ calculated in equation (C.3.36) in the previous time step ($n-1$) and the upper limit should be the Γ calculated in equation (C.3.36) in the current time step (n). But, as argued in Wilson & Mathews Wilson and Mathews (2003), it is necessary to split this term (equation (C.3.18)) and the next one (equation C.3.19) in two parts. To maintain stability, half of the change in energy due to change in velocity (equations (C.3.18), (C.3.19)) shall be computed before the advection step (as you can see in equations (C.3.41), (C.3.42)), and half of the change shall be computed after the advection step (as you can see in equations (C.3.91), (C.3.92)). In fact we had then, split these terms in two, and we use half time step in each of these computations (it is the reason why we write $\Delta t/2$ in these terms).

Then, the limits in the integral in time of Γ will not be computed in a full time step, but in a 'half' time step. In the first equation (C.3.40) we use as lower limit the Γ computed before the equation (C.3.91) (which is Γ') and as an upper limit the Γ computed before (C.3.40) (which is Γ^*). In the second part of this term (equation C.3.91) we use the opposite: as a lower limit Γ^* and as an upper limit Γ'. Since Γ' is computed just in the end of the temporal iterations, to have an initial value for it for the first iteration ($n = 1$) we set $\Gamma' = \Gamma$ before the beginning of first temporal iteration.

$$E_{k+1} = E_{k+1}\left(\frac{\Gamma'_{k+1}}{\Gamma^*_{k+1}}\right)^{(1/3)} \quad . \tag{C.3.41}$$

Now, with the new E computed in the equation above, we compute how it changes due to the spatial gradient of U:

$$\Delta^t(lnE_{k+1}) = -\frac{\Delta t/2}{3\Gamma^*_{k+1}r^2_{k+1}\Delta r}\Delta^r(r^2U)\big|_{k+1}. \tag{C.3.42}$$

Since this equation is also splitted in two, we use half time step $\Delta t/2$. In the code, instead of computing the spatial variation of U, we compute the spatial variation of $v\Gamma$, as suggested in Wilson and Mathews (2003). We compute the spatial finite differences,

$$(v\nabla\Gamma)_{k+1} = \frac{(v_k + v_{k+2})(\Gamma^*_{k+2} - \Gamma^*_k)}{2\Delta r}, \tag{C.3.43}$$

$$(\Gamma\nabla v)_{k+1} = \Gamma^*_{k+1}\frac{4\pi r^2_{k+2}v_{k+2} - 4\pi r^2_k v_k}{\Delta V_{k+1}}, \tag{C.3.44}$$

and we apply in the energy equation,

$$E_{k+1} = E_{k+1} Exp\left[-(\Delta t/6)\left(\frac{(v\nabla\Gamma)_{k+1} + (\Gamma\nabla v)_{k+1}}{\Gamma^*_{k+1}}\right)\right]. \tag{C.3.45}$$

Notice that the factor $\Delta t/6$ appears instead of $\Delta t/3$ because we use half time step.

Interpolation

To calculate the advection equations (C.3.79), (C.3.80) and (C.3.81), we need to use in the right hand side the flux of the variables in the boundaries of the volume element in which the spatial derivative is done. The calculation of these fluxes is crucial for the stability as well. In the following we illustrate the steps needed to find these fluxes.

First we calculate the average of densities in the boundaries,

$$D_k = (1/2)(D_{k+1} + D_{k-1}), \tag{C.3.46}$$

$$E_k = (1/2)(E_{k+1} + E_{k-1}). \tag{C.3.47}$$

And then, since S is defined in the boundary of cells, the volume element related to it is ΔV_k which has as boundaries $k-1$ and $k+1$, so, to calculate the fluxes of S in the boundaries of its volume element, we need the velocities in $k-1$ and $k+1$.

$$U_{k+1} = (1/2)(U_k + U_{k+2}). \tag{C.3.48}$$

$$v_{k+1} = (1/2)\left(\frac{U_k}{\sqrt{1+U_k^2}} + \frac{U_{k+2}}{\sqrt{1+U_{k+2}^2}}\right). \tag{C.3.49}$$

Flux limiter

The flux limiter is used to limit the flux of variables in boundaries of the volume elements Dönmez (2006). It will smooth the steep gradients to avoid instabilities in shocks. To compute the gradients, we calculate a minimum value between three possible choices:

- the gradient using the medium values as in equations (C.3.46) and (C.3.47),
- the gradient using the difference from the value of the variable in the point and in the previous one: $G_k - G_{k-1}$,
- and the gradient using the difference from the variable in the point and in the next one: $G_k - G_{k+1}$.

The algorithm showed bellow, illustrate the choice of the minimum gradient for each variable.

For D (For E will be equal, just changing $D \rightarrow E$):

$$
\begin{aligned}
D_{min} =& \min(\mathrm{D_{k-1}}, \mathrm{D_{k+1}}, \mathrm{D_{k+3}}), && \text{(C.3.50)}\\
D_{max} =& \max(D_{k-1}, D_{k+1}, D_{k+3}), && \text{(C.3.51)}\\
\Delta D_{min} =& \min(\mathrm{D_{max}} - \mathrm{D_{k+1}}, \mathrm{D_{k+1}} - \mathrm{D_{min}}), && \text{(C.3.52)}\\
\Delta D_{max} =& \max(\mathrm{D_{max}} - \mathrm{D_{k+1}}, \mathrm{D_{k+1}} - \mathrm{D_{min}}, |\mathrm{D_{k+2}} - \mathrm{D_k}|). && \text{(C.3.53)}
\end{aligned}
$$

If we have a point of maximum or minimum, the gradient is set to zero:
if $(D_{k+3} - D_{k+1})(D_{k+1} - D_{k-1}) < 0$ then

$$\nabla D_{k+1} = 0. \tag{C.3.54}$$

And if the difference of the averaged variables is zero, we also set the gradient to zero:
if $D_{k+2} - D_k = 0$ then

$$\nabla D_{k+1} = 0. \tag{C.3.55}$$

Otherwise, we compute the gradient,

$$\nabla D_{k+1} = \frac{\min(\Delta D_{min}, \Delta D_{max})}{(\Delta r)} \frac{D_{k+2} - D_k}{|D_{k+2} - D_k|}. \tag{C.3.56}$$

For U:

$$U_{min} = \min(U_{k-2}, U_k, U_{k+2}), \tag{C.3.57}$$
$$U_{max} = \max(U_{k-2}, U_k, U_{k+2}), \tag{C.3.58}$$
$$\Delta U_{min} = \min(U_{max} - U_k, U_k - U_{min}), \tag{C.3.59}$$
$$\Delta U_{max} = \max(U_{max} - U_k, U_k - U_{min}). \tag{C.3.60}$$

If we have a point of maximum or minimum, the gradient is set to zero:
if $(U_{k+2} - U_k)(U_k - U_{k-2}) < 0$ then

$$\nabla U_k = 0. \tag{C.3.61}$$

And if the difference of the averaged variables is zero, we set also the gradient to zero:
if $U_{k+1} - U_{k-1} = 0$ then

$$\nabla U_k = 0. \tag{C.3.62}$$

Otherwise, we compute the gradient,

$$\nabla U_k = \frac{\min(\Delta U_{min}, \Delta U_{max})}{\Delta r} \frac{(U_{k+1} - U_{k-1})}{|U_{k+1} - U_{k-1}|}. \tag{C.3.63}$$

Interpolation (continuation)

Finally we can compute the interpolated variables on boundaries. If the velocity is positive we use the computed gradients of the previous spatial grid point:
if $(v_k > 0)$ then

$$\check{D}_k = D_{k-1} - (1/2)\nabla D_{k-1}(\Delta r - v_k \Delta t), \tag{C.3.64}$$
$$\check{E}_k = E_{k-1} - (1/2)\nabla E_{k-1}(\Delta r - v_k \Delta t). \tag{C.3.65}$$

If the velocity is negative we use the computed gradients of the next spatial grid point:
if $(v_k < 0)$ then

$$\check{D}_k = D_{k+1} + (1/2)\nabla D_{k+1}(\Delta r + v_k \Delta t), \tag{C.3.66}$$
$$\check{E}_k = E_{k+1} + (1/2)\nabla E_{k+1}(\Delta r + v_k \Delta t). \tag{C.3.67}$$

And if the velocity is zero, we use the simple average:
if $(v_k = 0)$ then

$$\check{D}_k = D_k, \tag{C.3.68}$$
$$\check{E}_k = E_k. \tag{C.3.69}$$

The fluxes on the boundaries of the cells will be:

$$MD_k = \check{D}_k 4\pi r_k^2 v_k \Delta t, \quad \text{(C.3.70)}$$
$$ME_k = \check{E}_k 4\pi r_k^2 v_k \Delta t, \quad \text{(C.3.71)}$$
$$MS_k = MD_k + ME_k(4/3). \quad \text{(C.3.72)}$$

Recalling that S is defined in a different volume element, we have to compute the variables in the apposite grid places.

First we compute the interpolated four-velocity on center of grid cells. As for densities if the velocity is positive we use the computed gradients of the previous spatial grid point:

if $(v_{k+1} > 0)$ then

$$\check{U}_{k+1} = U_k + (1/2)\nabla U_k(\Delta r - v_{k+1}\Delta t). \quad \text{(C.3.73)}$$

If the velocity is negative we use the computed gradients of the next spatial grid point:

if $(v_{k+1} < 0)$ then

$$\check{U}_{k+1} = U_{k+2} - (1/2)\nabla U_{k+2}(\Delta r + v_{k+1}\Delta t). \quad \text{(C.3.74)}$$

And if the velocity is zero, we use the simple average:

if $(v_{k+1} = 0)$ then

$$\check{U}_{k+1} = U_{k+1}. \quad \text{(C.3.75)}$$

Finally the fluxes for the boundaries of S are evaluated

$$MS_{k+1} = (1/2)(MS_k + MS_{k+2}). \quad \text{(C.3.76)}$$
$$\phi_{k+1} = MS_{k+1}\check{U}_{k+1}. \quad \text{(C.3.77)}$$
$$\quad \text{(C.3.78)}$$

Advection

Now we compute how the variables will move due to the new velocity,

$$\frac{\Delta^t D_{k+1}}{\Delta t} = -\frac{1}{\Delta^r v_{k+1}} \Delta^r (r^2 D v)\big|_{k+1}, \quad \text{(C.3.79)}$$
$$\frac{\Delta^t E_{k+1}}{\Delta t} = -\frac{1}{\Delta^r v_{k+1}} \Delta^r (r^2 E v)\big|_{k+1}, \quad \text{(C.3.80)}$$
$$\frac{\Delta^t S_k}{\Delta t} = -\frac{1}{\Delta^r v_k} \Delta^r (r^2 S v)\big|_{k}, \quad \text{(C.3.81)}$$

which in the code becomes

$$D_{k+1} = \frac{D_{k+1} - (MD_{k+2} - MD_k)}{\Delta V_{k+1}}, \tag{C.3.82}$$
$$E_{k+1} = \frac{E_{k+1} - (ME_{k+2} - ME_k)}{\Delta V_{k+1}}, \tag{C.3.83}$$

$$D_k = \frac{1}{2}(D_{k+1} + D_{k-1}), \tag{C.3.84}$$
$$E_k = \frac{1}{2}(E_{k+1} + E_{k-1}), \tag{C.3.85}$$

$$S_k = S_k - \frac{(\phi_{k+1} - \phi_{k-1})}{(\Delta V_k)}. \tag{C.3.86}$$

After the advection of the variables, we compute the second part of terms (C.3.18) and (C.3.19), but before this we need to compute the new advected velocities.

Velocity:

$$U_k = S_k/(D_k + (4/3)E_k), \tag{C.3.87}$$
$$\Gamma'_k = \sqrt{1 + U_k^2}, \tag{C.3.88}$$
$$v_k = U_k/\Gamma'_k, \tag{C.3.89}$$

$$\Gamma'_{k+1} = \sqrt{(1 + (U_k^2 + U_{k+2}^2)/2)}. \tag{C.3.90}$$

Pressure work

Now we compute the second half time step of (C.3.18) and (C.3.19), which will be the same as (C.3.40) and (C.3.42), but changing Γ^* by Γ' and vice-versa.

$$\Delta^t(lnE_{k+1}) = -\frac{1}{3}\Delta^t(ln\Gamma_{k+1}), \tag{C.3.91}$$
$$\Delta^t(lnE_{k+1}) = -\frac{\Delta t/2}{3\Gamma'_{k+1}r_{k+1}^2\Delta r}\Delta^r(r^2U)\big|_{k+1}, \tag{C.3.92}$$

which in the code become,

$$(v\Gamma)_{k+1} = \frac{1}{(2\Delta r)}(v_k + v_{k+2})(\Gamma'_{k+2} - \Gamma'_k), \tag{C.3.93}$$

$$(\Gamma\nabla v)_{k+1} = \Gamma'_{k+1}\frac{(4\pi r_{k+2}^2 v_{k+2} - 4\pi r_k^2 v_k)}{\Delta V_{k+1}}, \tag{C.3.94}$$

$$(E\Gamma)_{k+1} = E_{k+1}\left(\frac{\Gamma^*_{k+1}}{\Gamma'_{k+1}}\right)^{(1/3)}, \tag{C.3.95}$$

$$E_{k+1} = (E\Gamma)_{k+1} Exp\left[-(\Delta t/6)\left(\frac{(v\Gamma)_{k+1} + (\Gamma\nabla v)_{k+1}}{\Gamma'_{k+1}}\right)\right], \tag{C.3.96}$$

$$E_k = \frac{1}{2}(E_{k+1} + E_{k-1}). \tag{C.3.97}$$

Velocity

The only quantity which remains to be updated is the pressure p. We do not need explicitly p because in our case $p = E/3\Gamma$, but for equation (C.3.34) in the next time step, we need the spatial gradient of p (or of E and Γ). We have already updated E in the full time step, so we still have to update just Γ,

$$U_k = S_k/(D_k + (4/3)E_k), \tag{C.3.98}$$

$$\Gamma_k = \sqrt{(1 + U_k^2)}, \tag{C.3.99}$$

$$v_k = U_k/\Gamma_k, \tag{C.3.100}$$

$$\Gamma_{k+1} = \sqrt{(1 + (U_k^2 + U_{k+2}^2)/2)}. \tag{C.3.101}$$

This computation of Γ is needed just to use in the place of pressure in equation (C.3.34), is not like an update to real physical velocities. With this, we complete one time step iteration.

When we need to know the values of some variables in $k = 1$ or $k = k_{max+1}$ we give the boundary conditions (for E and D),

$$E_1 = 0, \tag{C.3.102}$$

$$E_{(kmax+1)} = 0. \tag{C.3.103}$$

Let us summarize the most important points one needs to keep in mind about the code:

- in order to avoid numerical instability and maintain accuracy the sequence of solving the relativistic hydrodynamic equations has to be the one presented in this section.

- Since by the operator splitting method each term on RHS of evolution equations has to be solved separately, the presence of time derivative in equation C.2.8 allows to use the analytic solution C.3.18. However it requires the knowledge of two values of the Lorentz factor to be used in that equation.

C.4. Tests

In this section we illustrate the performance of numerical code with several test problems.

C.4.1. Advection

In order to see if the advection in the code works well (without much dispersion), we made a test using a gaussian distribution of matter moving with constant velocity in a planar geometry with

$$D(t=0,r) = 1 + e^{-(r-25)^2/0.9}, \tag{C.4.1}$$

and with initial Lorentz factor $\Gamma = 2$. Equations in the planar geometry (corresponding to equations (C.2.7) to (C.2.9), written only for matter density) are:

$$\frac{\partial D}{\partial t} = -\frac{\partial (Dv)}{\partial r}, \tag{C.4.2}$$

$$\frac{\partial S}{\partial t} = -\frac{\partial (Sv)}{\partial r} - \frac{\partial p}{\partial r}. \tag{C.4.3}$$

The result shows that the pulse has the spreading of 3% its original size, after traveling 8 times its original width. This result can be compared with the one reproduced in Bowers and Wilson (1991) using a second order monotonicity scheme with a spreading of 4% after the pulse has traveled 5 times its original width.

C.4.2. Spatial resolution

In order to avoid numerical spreading, we have to choose a very small value for the radius step. We show in figure C.7 that the larger Δr is, the more spreading appears in the pulse. The difference between the pulses widths at the end of simulations is significant. The initial profiles are:

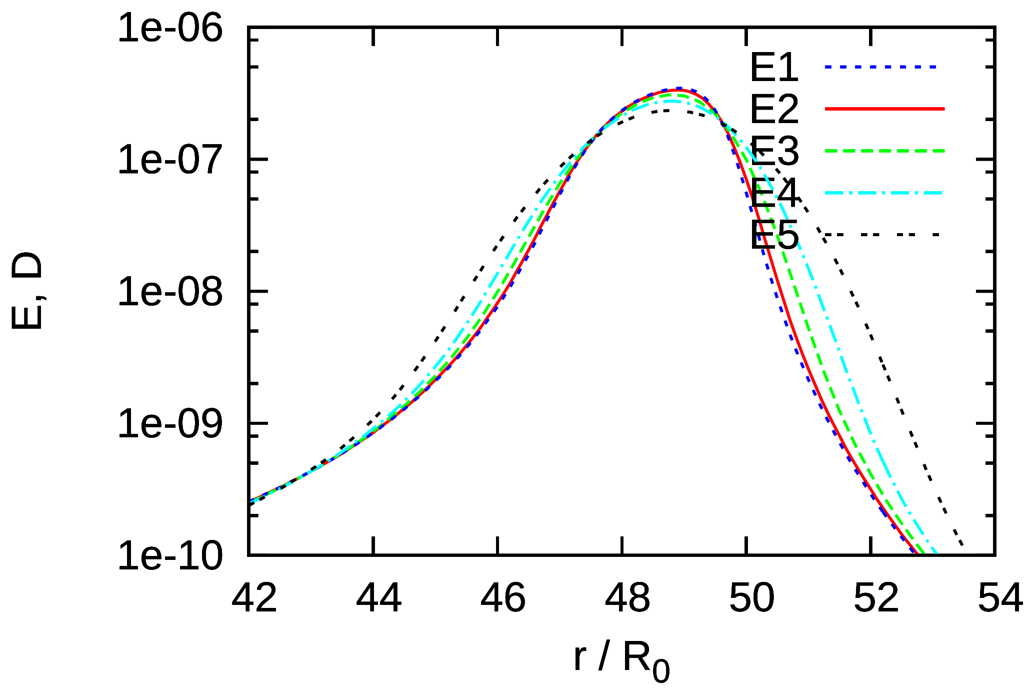

Figure C.7.: The figure shows simulations with five different values of Δr using the profiles (C.4.4), (C.4.5). The values of Δr are: $1/1000, 1/400, 1/200, 1/100, 1/50$, for simulations $E1, E2, E3, E4, E5$ respectively. In all simulations $\Delta t = \Delta r/2$. We can see significant difference between simulations 3, 4 and 5, while for simulations 1 and 2, the difference is not too much, even changing the resolution more than twice. For all simulations done in this thesis we use $\Delta r = 1/500$.

$$D(t=0,r) = \frac{\rho_0 \Gamma_0}{R_0 + r^8}, \tag{C.4.4}$$

$$E(t=0,r) = \epsilon_0 D(t=0,r) = \frac{\epsilon_0 \rho_0 \Gamma_0}{R_0 + r^8}, \tag{C.4.5}$$

with the following parameters $\epsilon_0 = 50, \rho_0 = 0.004, \Gamma_0 = 1$ and $R_0 = 1$. And for the usual hydrodynamic quantities: ρ, $\epsilon\rho$ and p,

$$\rho(t=0,r) = \frac{\rho_0}{R_0 + r^8}, \tag{C.4.6}$$

$$\epsilon(t=0,r)\rho(t=0,r) = \frac{\epsilon_0 \rho_0}{R_0 + r^8}, \tag{C.4.7}$$

$$p(t=0,r) = \frac{\epsilon_0 \rho_0}{3(R_0 + r^8)}. \tag{C.4.8}$$

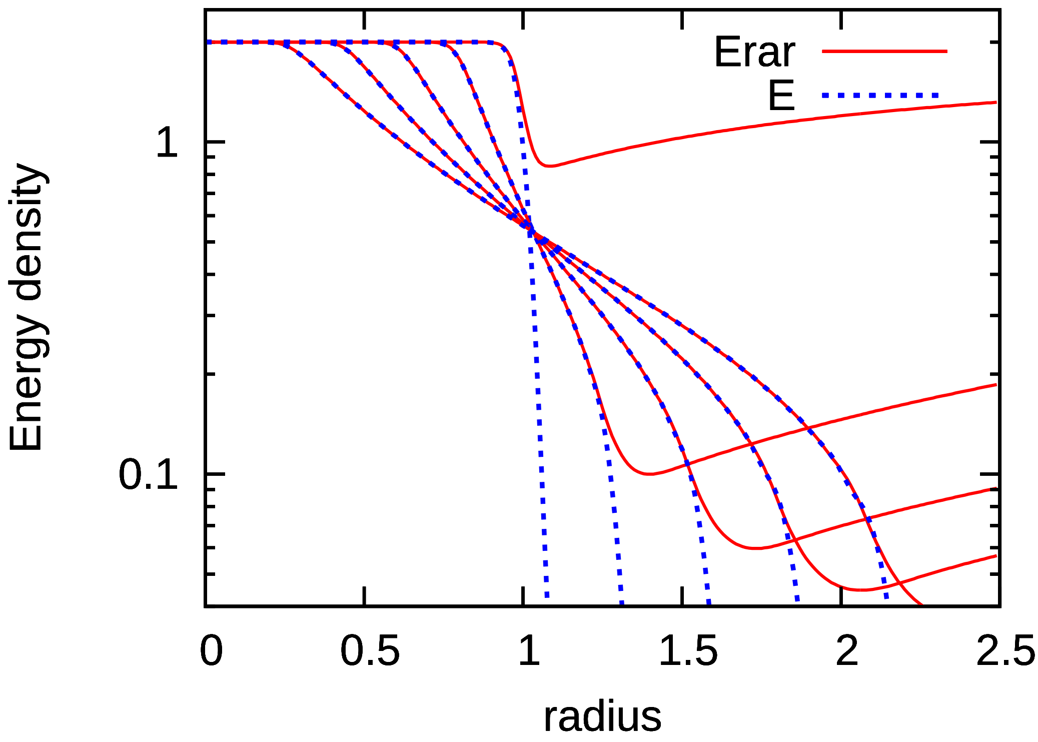

Figure C.8.: Comparison between our results and the analytical rarefaction solution from Thompson (1986).

In figure C.7 the simulations 4 and 5 have respectively $\Delta r = 1/400$ and $\Delta r = 1/1000$. We see that the difference is not significant between these two simulations. So we used $\Delta r = 1/500$ in all our simulations.

C.4.3. Rarefaction

Another test problem computed with the code is the relativistic rarefaction wave (Thompson (1986)). The solution for this problem includes the rarefaction wave itself and a shock. Just the rarefaction part is considered here. Given the values of Γ from our simulations we applied the following equations from Thompson (1986):

$$u = \sqrt{\Gamma^2 - 1}, \quad y_1 = \left(\frac{4p_0}{\rho_0}\right)^{1/2}, \quad y_2 = \frac{f(y_1)^2 - f(u)^{\sqrt{1/3}}}{2f(y_1)f(u)^{1/(2\sqrt{3})}}, \tag{C.4.9}$$

$$f(y_1) = y_1 + (1 + y_1^2)^{1/2}, \qquad f(u) = u + (1 + u^2)^{1/2}, \tag{C.4.10}$$

$$\rho = \rho_0 \left(\frac{y_1}{y_2}\right)^{-6}, \quad p = p_0 \left(\frac{\rho}{\rho_0}\right)^{4/3}, \quad D_{rar} = \rho\Gamma, \quad E_{rar} = 3p\Gamma, \tag{C.4.11}$$

where $\rho_0 = 0.002$ and $p_0 = 2/3$. Figure C.8 shows the results of numerical computation (dashed line) as well as the solutions of rarefaction equations. There is a complete agreement between analytical and numerical solutions until the point where the rarefaction solution starts to deviate from the full solution, see details in Thompson (1986).

C.4.4. Piran profiles

In this section we reproduce the results of Piran et al. (1993), as another test of the code. We performed a simulation with the same initial conditions as in that article. Initial profile for E and D with a very steep decay for $r > R_0$ were chosen, namely:

$$D(t=0,r) = \frac{\rho_0 \Gamma_0}{R_0 + r^8}, \tag{C.4.12}$$

$$E(t=0,r) = \epsilon_0 D(t=0,r) = \frac{\epsilon_0 \rho_0 \Gamma_0}{R_0 + r^8}, \tag{C.4.13}$$

where parameters are: $\epsilon_0 = 0.001, \rho_0 = 200, \Gamma_0 = 1$ and $R_0 = 1$, and we used a spatial step $\Delta r = 2 \times 10^{-3}$ and a time step $\Delta t = 1 \times 10^{-3}$ (these values are the same for all simulations). The high power in r is needed to represent a dense object with vacuum outside. The material is initially at rest, and it is never relativistic because from the beginning it is matter dominated $D(t=0,r) = 10^3 E(t=0,r)$. Plasma expands like a gas which was initially confined. It just tends to fill all the space with equal density (at infinite time), see figure C.9, in good agreement with figure 3 of Piran et al. (1993).

In the relativistic case we use also the equations (C.4.12), (C.4.13) for the initial profiles, but with parameters: $\epsilon_0 = 50, \rho_0 = 0.004, \Gamma_0 = 1$ and $R_0 = 1$. The matter is initially at rest with $\Gamma(0,r) = 1$, but due to the pressure of relativistic particles, it self accelerates reaching high bulk Lorentz factors. Because of this peculiarity practically all particles of the shell accelerate together. In contrast with the non relativistic case, in the central region inside the shell the density is very small, see figure C.10.

Notice that soon after beginning of expansion matter and energy get concentrated in a narrow shell with thickness independent on time. Piran et al. (1993) call this structure as the "frozen radial profile". It is found that this approximation is valid in the energy dominated regime, and in the beginning of the matter dominated regime. In section C.5 we show that for different initial distributions of energy and matter the resulting evolution can be also different from the one found in Piran et al. (1993).

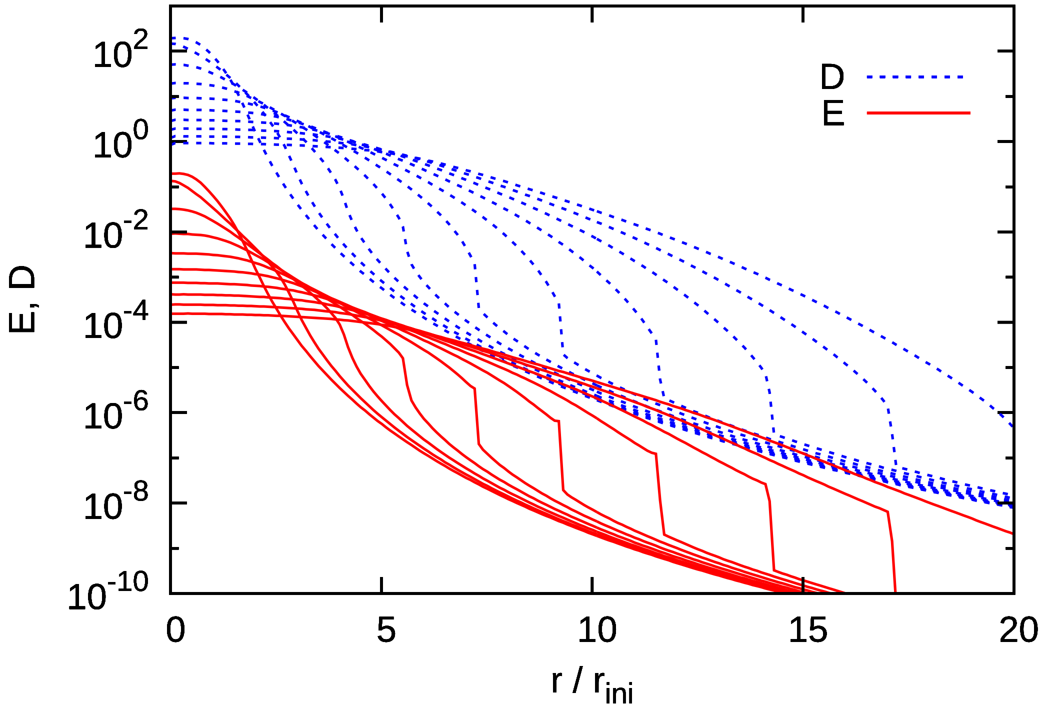

Figure C.9.: Time evolution of the energy density $E(r)$ and matter density $D(r)$ profiles for non relativistic case, with initial conditions shown in equations (C.4.12,C.4.13). All quantities are shown in laboratory frame. In this case the baryon loading parameter is $B = 10^3$.

C.4.5. Scaling laws

Here we show the analysis of the scaling laws. These laws are valid for average values in each "differential" individual radial shell in the plasma. The averages are:

$$\langle \rho \rangle = \langle nm \rangle = \frac{\int (D/\Gamma)\, r^2 dr}{\int r^2 dr}, \tag{C.4.14}$$

$$\langle \epsilon\rho \rangle = \langle em \rangle = \frac{\int (E/\Gamma)\, r^2 dr}{\int r^2 dr}, \tag{C.4.15}$$

where the limits of the integrals should be the internal and the external radius of the volume in which the average is being computed. In figure C.11 we show the evolution of baryon number density, and two curves. The curve labeled r^{-2} is a curve which scales as r^{-2} and is constructed to have the same value of n evolution in the end of the grid ($r \approx 200$). And the curve labeled r^{-3} is constructed to have the same value of n in the beginning of the grid

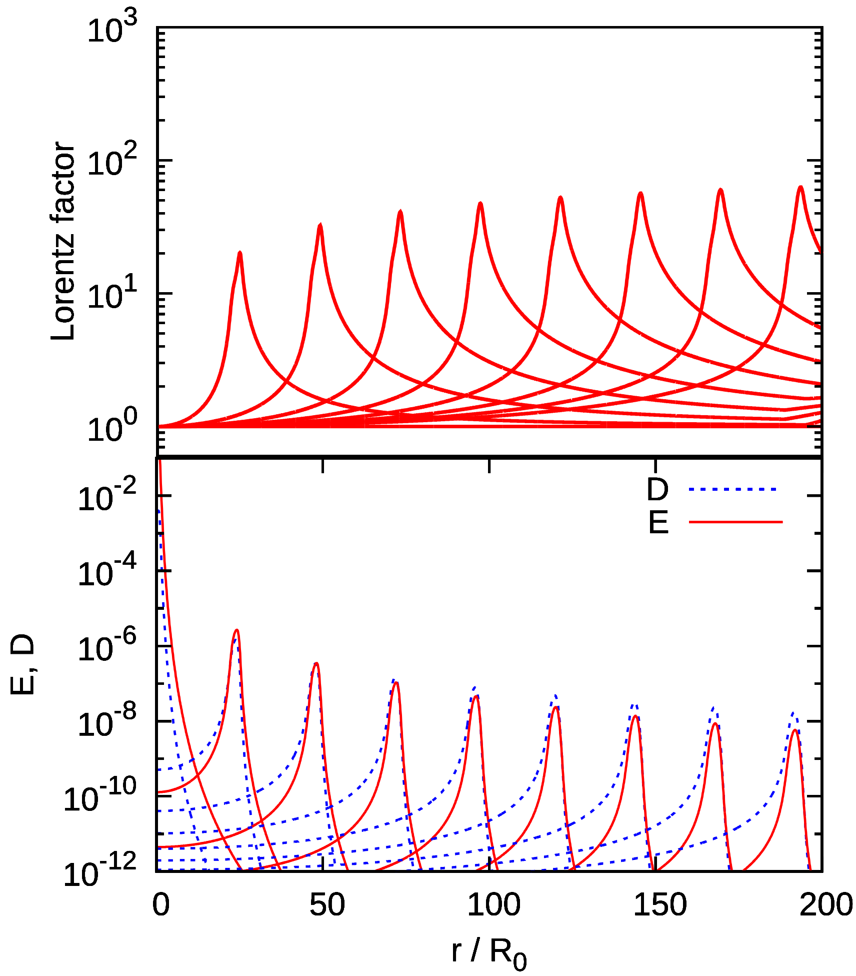

Figure C.10.: The same as in figure C.9, but for relativistic case. Here $B = 2 \times 10^{-2}$.

($r \approx 10$). We see that for very small radius ($r < 20$) the n slope is much similar to r^{-3}, and after this its slope changes, until being very similar to r^{-2} in the end of the grid. Following the above mentioned scaling laws, we did the same analysis for e, see figure C.12 were the curve which coincides in the beginning has a slope r^{-4}, and the curve which coincides in the end has a slope $r^{-8/3}$.

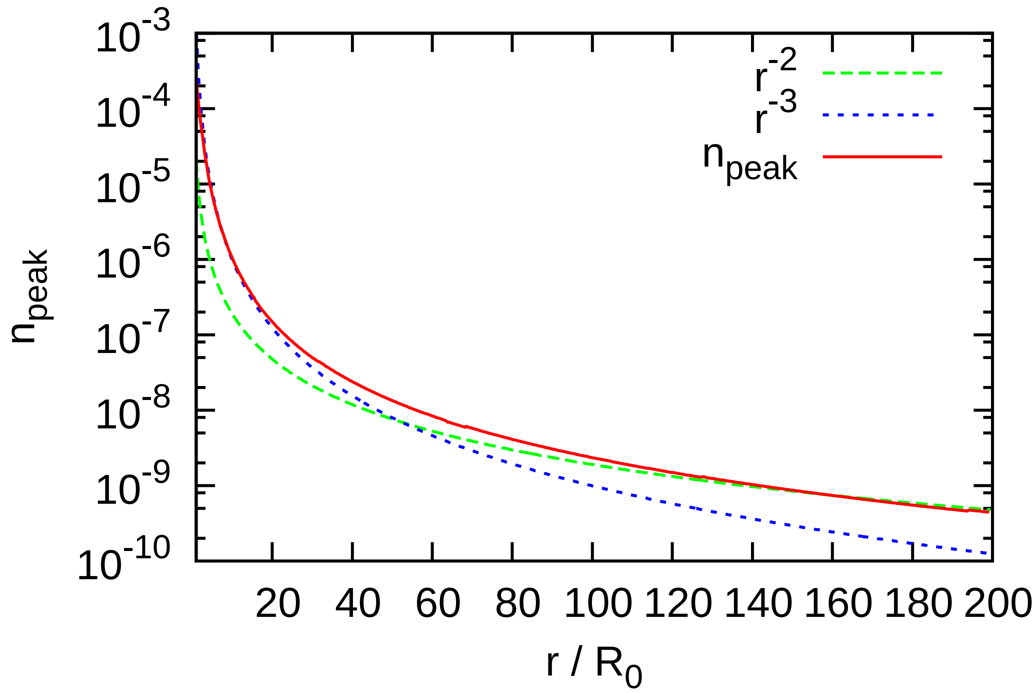

Figure C.11.: Analysis of the scaling laws of number density of baryons n. It is in a good agreement with the scaling laws found in Piran et al. (1993).

C.5. Results

In the previous section we reproduced the results obtained by Piran et al. (1993) considering the evolution of initially energy dominated plasma loaded with baryons through the energy dominated and mater dominated phases. Recall that this solution represents the expansion into vacuum. In what follows we will consider two examples of generalizations of such simple picture. In section C.5.1 we will consider the same initial energy density profile as before but different matter density profile which is chosen to be uniformly distributed. Our analysis is different from Ruffini et al. (2000) because in that paper a shell of baryons is considered located initially at some distance from the origin. Then in section C.5.2 a combination of Piran profile and the constant baryons density one is used for the initial conditions of our simulations.

C.5.1. Constant baryonic distribution profile

Consider the modification to Piran et al. (1993) spatial profile, where the matter density D and energy density E are:

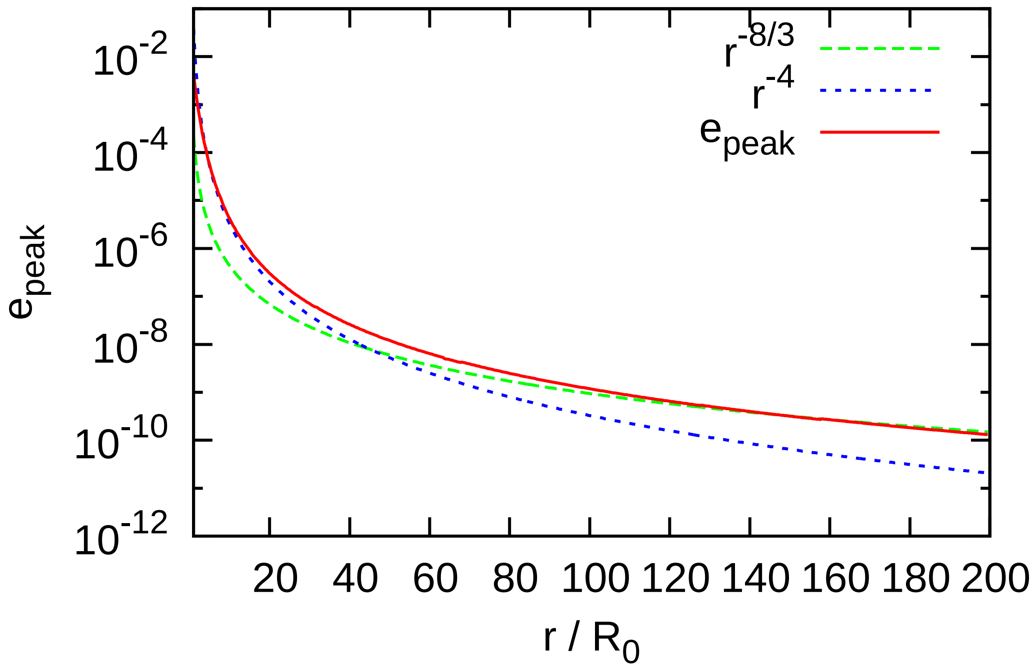

Figure C.12.: Analysis of the scaling laws of energy density e. It is in a good agreement with the scaling laws found in Piran et al. (1993).

$$D(t=0,r) = \rho_0 \Gamma_0, \tag{C.5.1}$$

$$E(t=0,r) = \epsilon(t=0,r) D(t=0,r) = \frac{\epsilon_0 \rho_0 \Gamma_0 R_0^8}{R_0^8 + r^8}, \tag{C.5.2}$$

with initial parameters: $\epsilon_0 = 0.2 \times 10^{10}$, $\Gamma_0 = 1$ and $\rho_0 = 5 \times 10^{-10} E_0$, where $E_0 = E(r=0, t=0)$. The initial profiles for usual hydrodynamic quantities, namely, matter density ρ, energy density $\epsilon\rho$ and pressure p, are:

$$\rho(t=0,r) = \rho_0, \tag{C.5.3}$$

$$\epsilon(t=0,r)\rho(t=0,r) = \frac{\epsilon_0 \rho_0 R_0^8}{R_0^8 + r^8}, \tag{C.5.4}$$

$$p(t=0,r) = \frac{\epsilon_0 \rho_0 R_0^8}{3(R_0^8 + r^8)}. \tag{C.5.5}$$

For the present section we define a modified baryon loading parameter which is more convenient to plot:

$$B' = \frac{1}{1 + \frac{1}{B}}. \tag{C.5.6}$$

Spatial profiles of E, D and Lorentz factor for selected time moments are presented in figure C.13. The plasma in spatial region dominated by the relativistic component E self accelerates like in the previous case. However, it pushes the nonrelativistic baryons which are collected in the front of the shell, creating an additional leading shell.

More details can be seen in figure C.14. It shows that soon after expansion starts two shocks are being formed: the forward shock (FS) propagating into the external medium and the reverse shock (RS) propagating back into the expanding shell. This radial structure is in some aspects similar to the one occurring during the interaction of the ultrarelativistic shell with the interstellar medium in the external shock model of GRBs.

The region between the shocks, in what follows, will be referred to as outer shell. The unshocked part of the expanding shell will be referred to as inner shell. We also notice that inside the shocked region there are two distinct regions: the energy dominated one and the matter dominated one.

This picture corresponds to the radial profiles of E, D, B' and Γ at the time moment $t = 33.2R_0$. One can see that the forward shock is located at about $r = 36.4R_0$. It should be noticed that the propagations velocity of the FS is subluminal. In our case the initial size of the energy dominated shell is given by the condition $E(t = 0) = D(t = 0)$ which is $r_{eq}(t = 0) = 15R_0$. The average Lorentz factor of the inner shell is much larger than the one of the outer shell, meaning that they should eventually merge.

The development of this structure is shown in figure C.15 for the moment $t = 93.6$ and in figure C.16 for $t = 173.6$. Comparison of figures C.14, C.15 and C.16 shows that while the inner shell is getting accelerated for larger and larger Lorentz factors, the outer shell stays mildly relativistic reaching $\Gamma \approx 10$ in the last figure. Indeed the shells approach each other with the expansion and then eventually merge as can be seen from figure C.16. Even when they merge, there still the signature of the reverse shock propagating back in the energy dominated shell, clearly visible in the Lorentz factor profile.

The parameters of the simulations and the size of the grid are chosen in such a way that the total energy exceed the total mass. It means that the amount of baryonic matter is not sufficient to decelerate the expanding shell. In other words the reverse shock never crosses entirely the expanding shell.

The deceleration phase begins when the total mass density become equal to the total initial energy density. Our simulations are done respecting this condition till the end of the simulation.

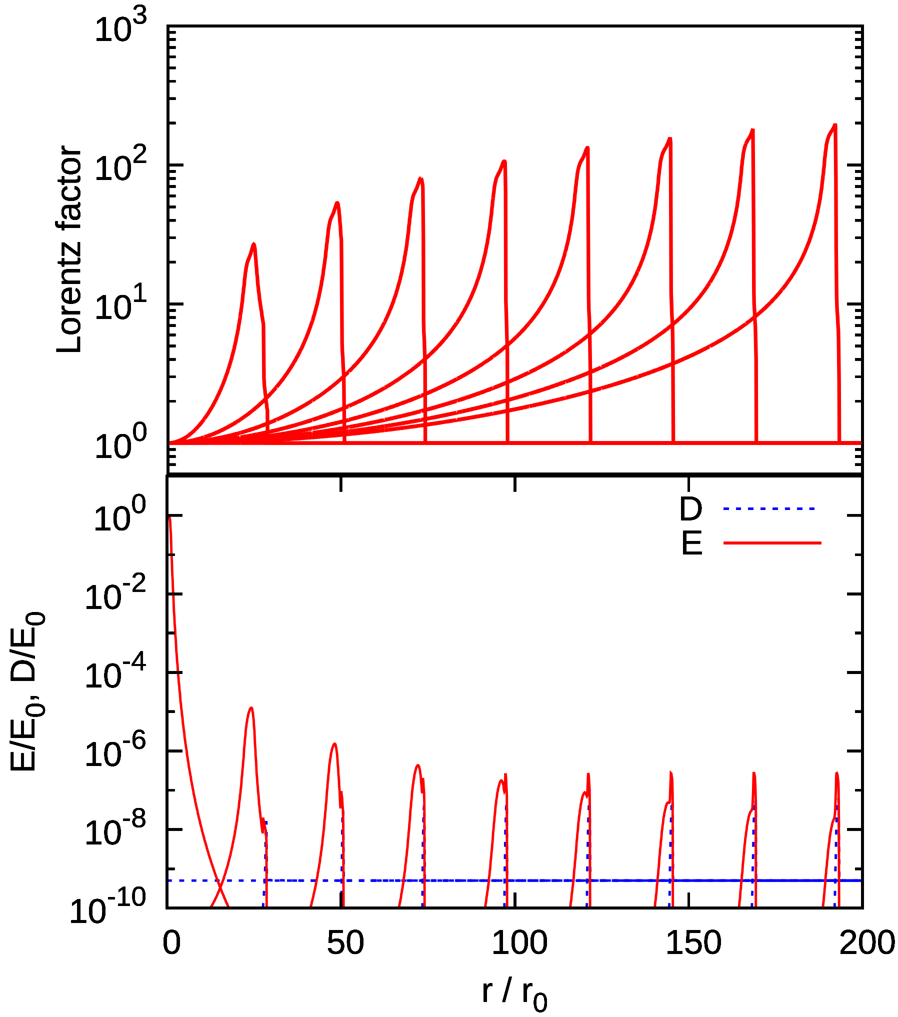

Figure C.13.: Densities and Lorentz factor evolution (at different times) in the case with a constant baryonic distribution profile, see section C.5.1.

C.5.2. Hybrid profile

Combining the profile used in section C.4.4 with the previous one, we now choose for E and D the following profiles:

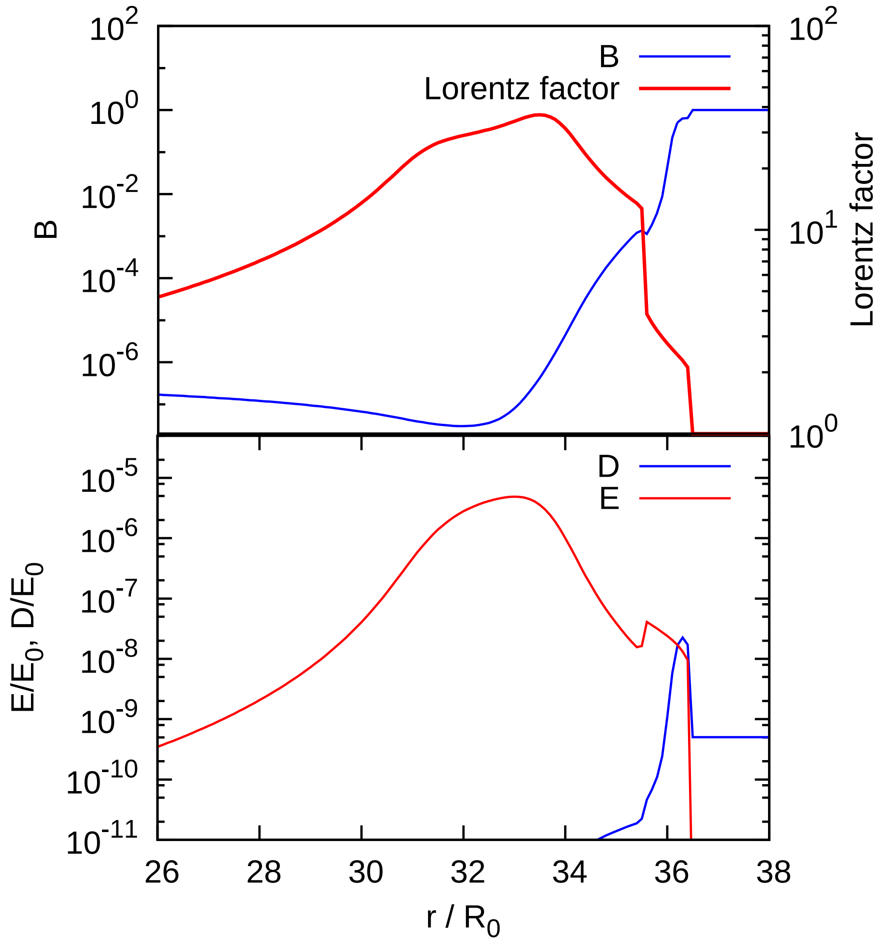

Figure C.14.: Detailed structure of the spatial distribution of Lorentz factor and baryonic loading (upper panel), energy and matter density (lower panel) is shown for the moment $t = 33.2$. The B parameter changes 8 orders of magnitude throughout the shell.

$$D(t=0,r) = \rho(t=0,r)\Gamma(t=0,r) = \frac{\rho_0 \Gamma_0 R_0^8}{(aR_0)^8 + r^8} + d, \tag{C.5.7}$$

$$E(t=0,r) = \epsilon(t=0,r)D(t=0,r) = \frac{\epsilon_0 \rho_0 \Gamma_0 R_0^8}{R_0^8 + r^8}, \tag{C.5.8}$$

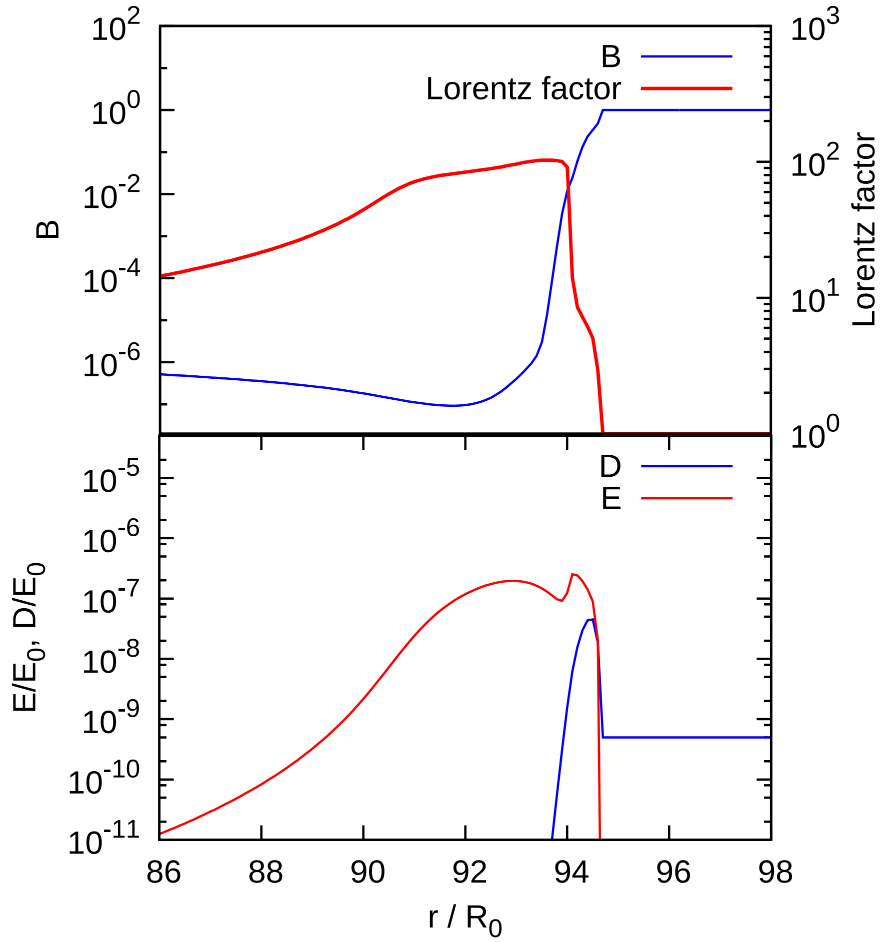

Figure C.15.: The same as in figure C.14, for the moment $t = 93.6$. The density of the outer energy dominated shell increases, and the density of the inner energy dominated one decreases.

with the parameters: $\epsilon_0 = 5 \times 10^5$, $\rho_0 = 0.2 \times 10^{-5} E_0$, $\Gamma_0 = 1$, $d = 5 \times 10^{-11} E_0$ and $a = 10^{-1/2}$, which correspond to a dense core of cold baryonic matter inside the radiation dominated region, immersed in a uniform external baryonic medium.

The initial profiles for the usual hydrodynamic quantities, matter density ρ, energy density $\epsilon\rho$ and pressure p, are:

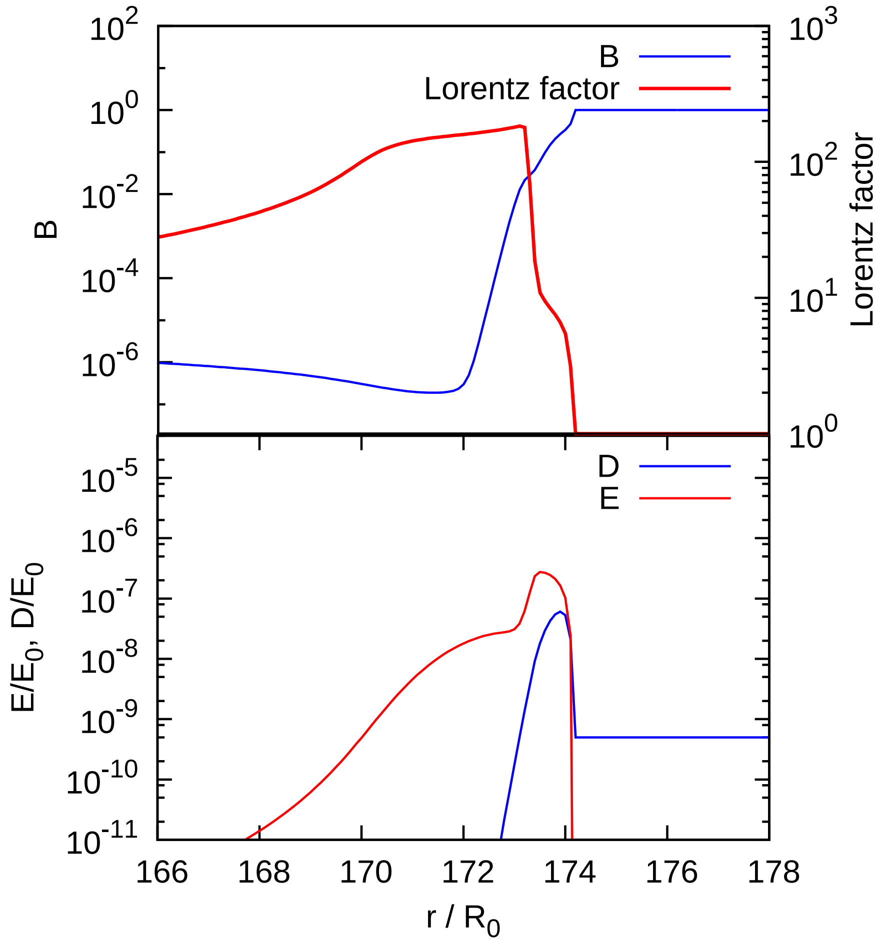

Figure C.16.: The same as in figure C.14, for $t = 173.6$.

$$\rho(t=0,r) = \frac{\rho_0 R_0^8}{(aR_0)^8 + r^8} + d, \tag{C.5.9}$$

$$\epsilon(t=0,r)\rho(t=0,r) = \frac{\epsilon_0 \rho_0 R_0^8}{R_0^8 + r^8}, \tag{C.5.10}$$

$$p(t=0,r) = \frac{\epsilon_0 \rho_0 R_0^8}{3(R_0^8 + r^8)}, \tag{C.5.11}$$

In this case we have a mixture of two previous cases. In fact, two shells

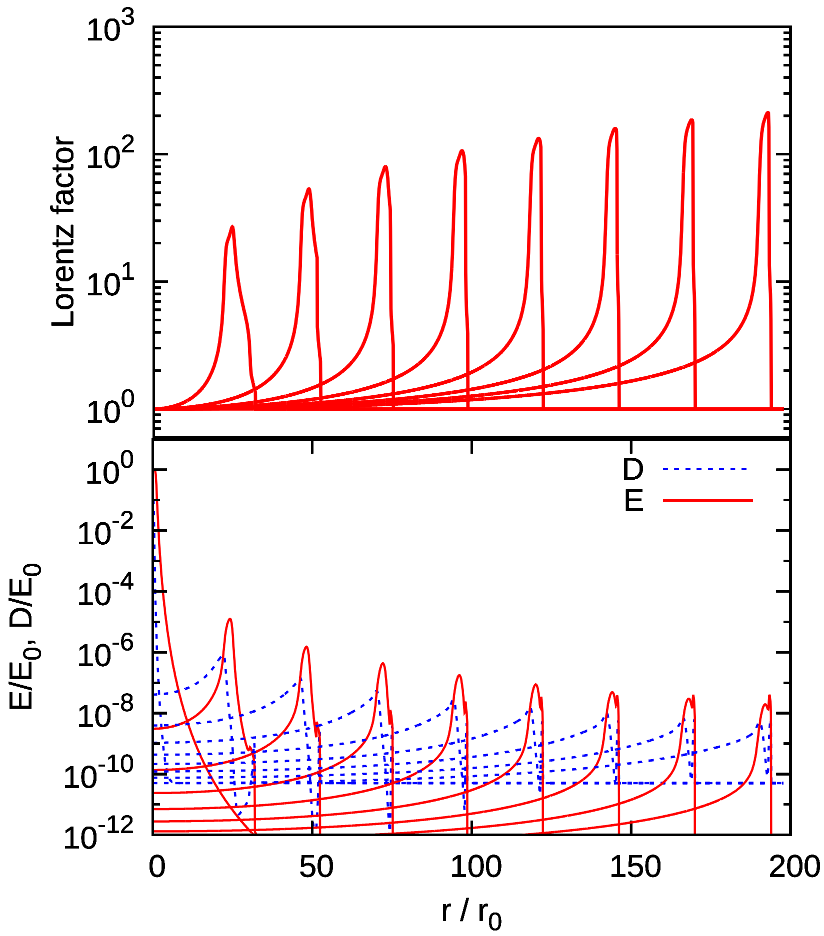

Figure C.17.: The same as in figure C.13, but for the hybrid case considered in section C.5.2. The Lorentz factor evolution presents some structure, but its shape is very similar to the case reproduced in section C.4.4. The densities profiles instead show a very different structure.

form again, see figure C.17. More details can be seen in figure C.18. The spatial profiles of energy density and Lorentz factor are similar to previous case, see figure C.14, the difference between these to figures is the presence of accelerated baryonic matter in the inner shell. These are baryons located initially in the center which are carried together with the inner energy dominated shell.

The development of the structure is shown in figure C.19. The separation between the inner and outer shell decreases with time, similar to the previous case, due to the difference of their average Lorentz factors. Notice that the

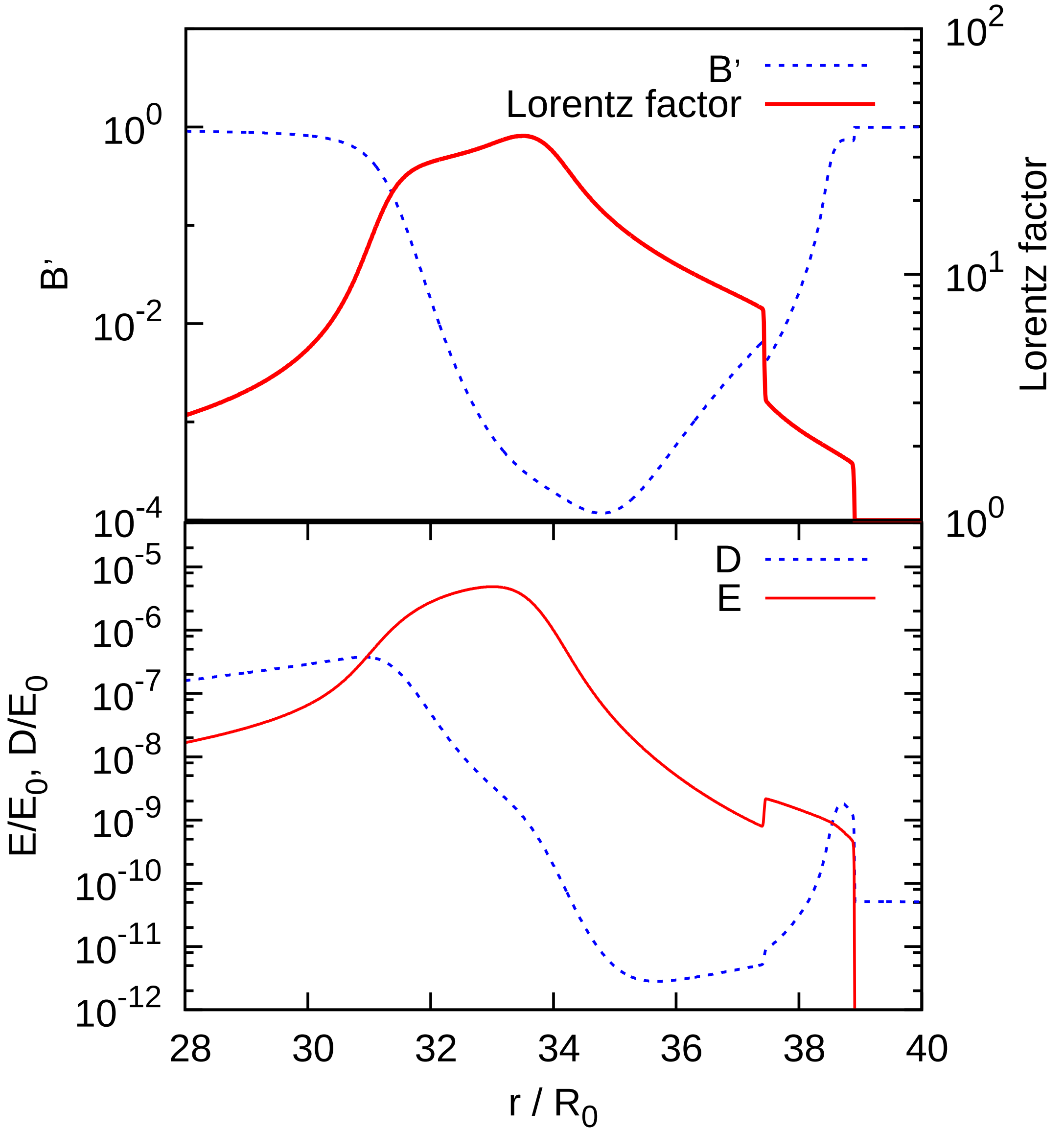

Figure C.18.: The same as in figure C.14, for the hybrid case, with $t = 32.8$.

"frozen radial profile" is valid for the inner E-shell.

The presence of the double peak structure in the D profile is crucial here since the transparency condition is determined by the number density of baryons. Such double peak structure may then be visible in the light curve of the radiation emitted at transparency provided that: a) the amplitude of both peaks is similar b) there is a separation between the peaks. For this reason we performed different simulations with this hybrid profile changing the value of d for fixed values of a, ϵ_0 and ρ_0, assuming that the external medium density does not change up to transparency radius defined by the condition $\tau(r_{tr}) = 1$. We analyzed the E and the D profiles and we found the relation

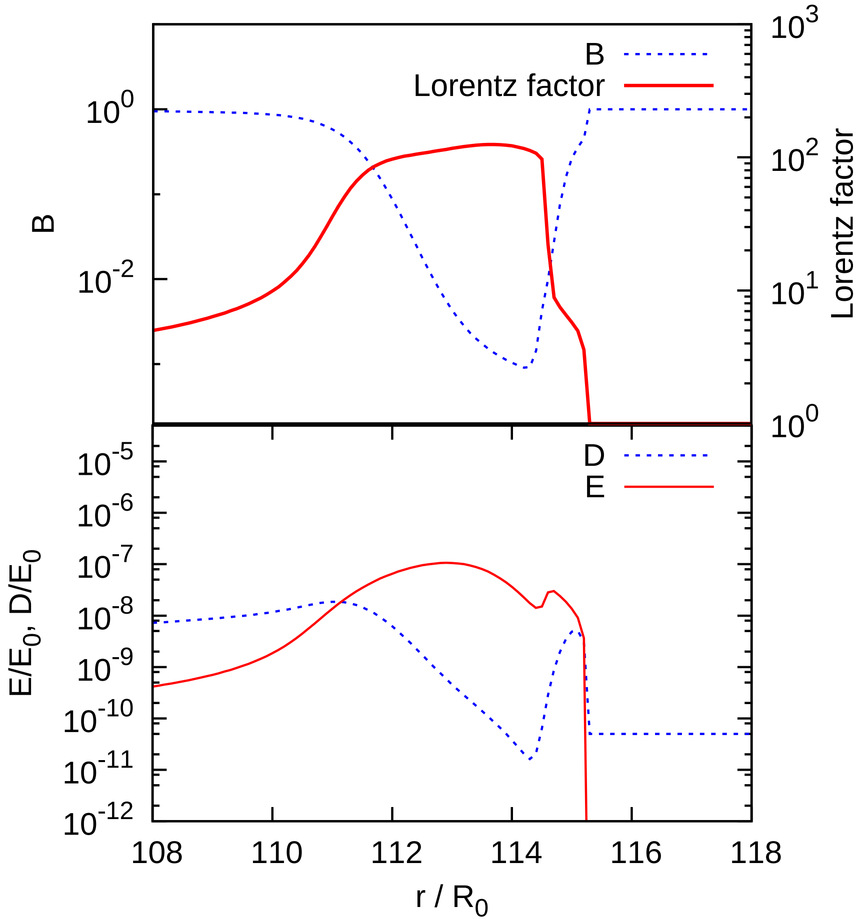

Figure C.19.: The same as in figure C.14, with $t = 112.8$. Now we can see two shells for both densities E and D.

between the value of the ratio d/E_0 and the ratio of the radius in which the amplitude of two peaks discussed above (showed in figure C.19) coincides and R_0. Numerically we determined the following relations:

$$\left(\frac{r_{eqE}}{R_0}\right) \approx 0.49 \left(\frac{d}{E_0}\right)^{-0.24}, \tag{C.5.12}$$

$$\left(\frac{r_{eqD}}{R_0}\right) \approx 0.039 \left(\frac{d}{E_0}\right)^{-0.35}, \tag{C.5.13}$$

where r_{eqE}/R_0 and r_{eqD}/R_0 correspond to the radius of equality of amplitudes in E and D profiles respectively.

Assuming for the radius of transparency

$$10^3 < \frac{r_{tr}}{R_0} < 10^6, \tag{C.5.14}$$

from (C.5.13) and (C.5.14) we then have

$$10^{-23} < \frac{d}{E_0} < 10^{-13}. \tag{C.5.15}$$

or expressed in physical units, assuming $E_0 = 10^{26}$ erg/cm^3 (corresponding to the temperature of plasma of 1 MeV)

$$10^{-18} < d < 10^{-8}\mathrm{g/cm}^3. \tag{C.5.16}$$

If we consider that the baryonic matter is represented just by protons we have

$$10^6 < d < 10^{16}\,\#/\mathrm{cm}^3. \tag{C.5.17}$$

C.6. Discussion of the results

Motivated by the recent observations of structured P-GRBs in this Chapter we performed the analysis of the accelerating phase of electron-positron plasma expansion. We examined the possibility that the structure seen in P-GRBs light curves originates from the structure of matter and energy distribution in the sources of GRBs. For this reason we were looking for possible deviations from the frozen radial profile of Piran et al. (1993).

We developed a hydrodynamic code based on the operator splitting technique, following Bowers and Wilson (1991) and Wilson and Mathews (2003). The same code was used earlier in Ruffini et al. (2000), who also considered expansion of electron-positron plasma assuming that baryons are engulfed during the acceleration phase of expansion. The difference between the initial conditions adopted in Ruffini et al. (2000) and ours is that we are considering continuous engulfment of baryons uniformly distributed in space while they considered baryons located in a thin shell at a certain radial distance from the source of the e^+e^- plasma. Similarly to Ruffini et al. (2000) we also find that the thickness of the unshocked part of the expanding shell is constant in time. The main difference is that our initial conditions result in the formation of long living shocks propagating both in the external medium (FS) and in the expanding shell (RS). The shocked region located in between is the new feature of our solution.

Appearance of shocks caused by the interaction of the relativistic shells with external medium is not new in the literature. Similar situation occurs for example in the external shock model of GRBs (Rees and Meszaros (1992)) where the forward shock is propagating in the interstellar medium. There is however an essential difference: the expanding shell playing the role of a piston is always energy dominated in our case, unlike the called ultrarelativistic shell considered in the external shock model. This point is crucial since in our case both forward and reverse shocks are formed at the acceleration phase of the shell expansion and not in the deceleration phase as in the case of external shock model.

In the external shock model the deceleration of the expanding shell occurs when the reverse shock crosses the entire shell. In our case instead we are interested in the acceleration of the expanding shell.

Its important to stress our assumption that at any time moment the inner shell is not affected by the presence of the external medium since the reverse shock did not reach it yet. For this reason the asymptotic Lorentz factor attained by the inner shell is given by the relation

$$\Gamma_{asym} \approx B_0^{-1}, \tag{C.6.1}$$

where B_0 is given by

$$B_0 = \int_0^{R_{eq}} \frac{D(r)r^2dr}{E(r)r^2dr}, \tag{C.6.2}$$

and R_{eq} is determined from the equality

$$D(t=0, R_{eq}) = E(t=0, R_{eq}). \tag{C.6.3}$$

Our assumption will be valid if the radius at which the reverse shock crosses entirely the inner shell (the deceleration radius R_{dec}, see Mészáros et al. (1993)) is larger than the radius $R_c = \Gamma_{asym} R_0$. The deceleration radius is defined by the condition that total energy of baryons located in both shells is equal to the initial energy released in the source of GRB. Moreover we also assume that the transparency is reached before the deceleration begins. In other words we require

$$R_c < R_{dec}, \tag{C.6.4}$$

$$R_{tr} < R_{dec}, \tag{C.6.5}$$

where R_{tr} is the radius at transparency.

Its is our main finding that in the acceleration phase the reverse shock does not propagate in the expanding shell and the width of the shocked region (outer shell) does not increase in the laboratory frame. This means that the inner shell indeed remains unaffected by the external medium, provided that the acceleration is not saturated.

As we discussed in section C.5.2 the double peak structure is formed in the $D(r)$ profile in the hybrid case: the outer peak corresponds to the shocked region containing the swept up baryons heated by the forward shocks; the inner one is due to the baryons carried together with the accelerating e^+e^- plasma.

We found a relation between the parameter which determines the radius at which the amplitudes of both peaks in the double peak profile coincide. By extrapolating this relation to the transparency radius we found the admissible range of external baryon densities.

The appearance of this double peak structure requires also the separation between the two shells (outer and inner ones), depending mainly on three parameters:

- the relative value of external constant baryonic matter density d/E_0 which is responsible to the formation of the outer shell (front of the forward shock);
- the ratio a of the width of the internal baryonic shell and the width of the E shell;
- the value of the ratio between D and E in the beginning at $r = 0$, ρ_0/E_0.

Such structure, if survives until the transparency moment will give rise to two shells, moving ballistically with different Lorentz factors. Since the Lorentz factor of the outer shell is smaller than the one of the inner shell, they will eventually collide and interact in the collisionless regime. This brings some similarities with the internal shock model of GRBs (Narayan et al. (1992); Rees and Meszaros (1994)), where the existence of multiple shells having different Lorentz factors is postulated. In our case the appearance of two shells with different Lorentz factors is the natural consequence of the interaction of the expanding shell with the external medium in the optically thick phase.

The simulation of the hybrid profile containing only one initial internal shell of baryons immersed in a uniformly distributed baryonic matter, can be considered as a toy model for a more refined scenario. In principle more complex structure of initial matter and energy distribution can give at transparency more complex light curves. In the same way a more complex distribution of external medium can generate multiple shocks propagating both in the external medium and in the expanding shells. Such shocks will result in shells having different Lorentz factors left to interact after transparency occurred.

It is also important that part of kinetic energy of baryons is used to hit up the baryons swept up from the external medium (by the reverse shock). Thus the energy budget of photons emitted at transparency versus kinetic energy of remaining baryons will be affected by this solution as contrasted to the "frozen radial profile" one.

In principle if this scenario will be confirmed by the observations it will open an interesting possibility to get information from the structure of the P-GRB and the different Lorentz gamma factors in the spatial distribution of accelerated baryons left over at transparency, to infer the information about the matter distribution during the process of the gravitational collapse to a black hole.

D. On the thermal spreading of the fireshell

D.1. Introduction

Optically thick pair plasma with baryon loading is assumed to power GRBs in many models, considered in the literature, see e.g. Piran (1999); Ruffini et al. (1999, 2000). Such plasma is self accelerated to large bulk Lorentz factors before it becomes transparent to Compton scattering. At the moment of transparency a pulse of radiation is expected to be formed. In the fireshell model (e.g. Ruffini et al. (2009)) this photospheric emission is called the Proper GRB (P-GRB).

Hydrodynamical analytical and numerical results show that during expansion from the initial size of plasma r_0 up to transparency the thickness of the fireshell $\Delta r \sim r_0$ does not increase substantially. This fact has been used in the development of the fireshell model and it termed constant thickness approximation, c.f. Ruffini et al. (2000). Due to relativistic beaming it is believed that the duration of the P-GRB is of order of $\Delta r/c$.

In 1993 Mészáros, Laguna and Rees (Mészáros et al. (1993)) suggested a mechanism of the shell expansion based on thermal spreading. The presence of nonzero thermal velocity dispersion δv_r leads to expansion of the shell. Taking dispersion $\Delta v_r/c \sim 1/\Gamma^2$ for the shell moving with bulk Lorentz factor Γ, this spreading will be of order $\Delta r \sim \Delta v_r\, t \sim r/\Gamma^2$. During the matter-dominated stage of GRB $\Gamma \sim const$ is approximately equal to the inverse of the baryonic loading B, which represents the ratio between baryonic rest mass and the total energy of pairs. Therefore when the fireshell reaches the radius of transparency r_{tr} (see (D.4.6) below) we have $\Delta r \sim r_{tr} B^2$ or

$$\Delta r/c \sim 3.42 \left(\frac{B}{10^{-2}}\right)^{5/2} \left(\frac{E_{e^+e^-}}{10^{54}\,\mathrm{erg}}\right)^{1/2} \mathrm{sec}, \tag{D.1.1}$$

where $E_{e^+e^-}$ is the initial energy deposition of the fireshell. As a result the amount of thermal spreading, and not the initial size of of the shell, determines the duration of P-GRB. This statement is usually noncritically repeated in reviews, see e. g. Piran (1999); Meszaros (2006).

In what follows we argue that the treatment of Mészáros et al. (1993) drastically overestimates the value of the spreading, since thermal velocity dispersion is taken there as independent on the temperature. In order to show this, and to compute the real spreading of the fireshell we determine particle velocity spread as a function of comoving temperature and bulk Lorentz factor for relativistic Maxwellian distribution and then apply the result to compute the spreading of the fireshell during expansion.

D.2. Problem

We assume that each layer of the expanding shell is in local thermodynamical equilibrium. It is a reasonable assumption for the hydrodynamic stage of expansion due to large optical depth of the shell. Then the distribution of particles in the momentum space (p'_x, p'_y, p'_z) in the rest frame of plasma is relativistic Maxwellian one

$$f(p'_x, p'_y, p'_z) = A \exp\left[-\frac{mc^2}{kT}\sqrt{1+\left(\frac{p'_x}{mc}\right)^2+\left(\frac{p'_y}{mc}\right)^2+\left(\frac{p'_z}{mc}\right)^2}\right], \quad \text{(D.2.1)}$$

where A is a normalization constant determined by the particle density, m is the mass of particles, c is the speed of light, T is the local temperature and k is Boltzmann constant. Then in the laboratory frame this distribution will be transformed to Lorentz-boosted Maxwellian

$$f(p_x, p_y, p_z) = A \exp\Bigg(-\frac{c}{kT}\Bigg[m^2c^2+$$
$$\left(\Gamma p_x - \sqrt{(\Gamma^2-1)(m^2c^2+{p_x}^2+{p_y}^2+{p_z}^2)}\right)^2 + {p_y}^2+{p_z}^2\Bigg]^{1/2}\Bigg), \quad \text{(D.2.2)}$$

where we assumed that the relative motion of the frames is along their x-axes.

Velocity dispersion in the x-direction will be

$$D(v_x) = M(v_x^2) - M^2(v_x), \quad \text{(D.2.3)}$$

where $M(\chi)$ denotes average value of χ, which can be found by convolution with distribution function

$$M(\chi) = \frac{\int_{-\infty}^{+\infty} dp_x \int_{-\infty}^{+\infty} dp_y \int_{-\infty}^{+\infty} dp_z\, \chi(p_x, p_y, p_z) f(p_x, p_y, p_z)}{\int_{-\infty}^{+\infty} dp_x \int_{-\infty}^{+\infty} dp_y \int_{-\infty}^{+\infty} dp_z\, f(p_x, p_y, p_z)}. \quad \text{(D.2.4)}$$

In what follows we use the dimensionless velocity $\beta = v/c$. The above written integrals cannot be computed analytically, but their numerical approximations can be found after the following convenient change of variables

$$p_x = mc\, p_r, \qquad p_y = mc\, p_p \cos\phi, \qquad p_z = mc\, p_p \sin\phi \tag{D.2.5}$$

so that for χ with axial symmetry around x-axis

$$M(\chi) = \frac{\int_{-\infty}^{+\infty} dp_r \int_0^{+\infty} dp_p\, \chi(p_r, p_p) \exp\left(-\frac{mc^2}{kT}\sqrt{1+(\Gamma p_r - \sqrt{\Gamma^2-1}\sqrt{1+p_r^2+p_p^2})^2+p_p^2}\right)}{\int_{-\infty}^{+\infty} dp_r \int_0^{+\infty} dp_p\, \exp\left(-\frac{mc^2}{kT}\sqrt{1+(\Gamma p_r - \sqrt{\Gamma^2-1}\sqrt{1+p_r^2+p_p^2})^2+p_p^2}\right)}. \tag{D.2.6}$$

Numerical issues in the velocity dispersion calculations by (D.2.3) arise from the fact that for high Γ we need to subtract two numbers $M(\beta_r^2)$ and $M^2(\beta_r)$ which are very close to each other and to unity. This leads to substantial reduction of accuracy. A different formula for dispersion

$$D(v_x) = M([v_x - M(v_x)]^2) \tag{D.2.7}$$

proves to be more convenient for numerical reasons. The spread of particle velocities then will be $\Delta v = c\sqrt{D(\beta_r)}$.

D.3. Velocity spread

Results of the numerical integration are illustrated by fig. D.1–D.4. For non-relativistic comoving temperatures the correct asymptotics is (see fig. D.1)

$$\frac{\Delta v_r}{c} = \Gamma^{-2}\sqrt{\frac{kT}{mc^2}}, \tag{D.3.1}$$

but not $\Delta v_r/c = \Gamma^{-2}$. This behavior can be understood easily with the following argument: when the initial spread of velocities is small compared to the bulk velocity, then by the velocity transformation formula we can approximate new spread as

$$\Delta v \simeq \Delta v' \left.\frac{d}{dv'}\frac{V+v'}{1+\frac{Vv'}{c^2}}\right|_{v'=0} = \Delta v'\left(1-\frac{V^2}{c^2}\right), \tag{D.3.2}$$

that gives us exactly the result obtained numerically.

The case of highly relativistic comoving temperature ($\frac{kT}{mc^2} \gg 1$) is more interesting. Starting from almost maximal value $1/\sqrt{2}$, $\Delta v/c$ for not-so-high bulk Lorentz factors (intermediate region $10 \lesssim \Gamma \lesssim \frac{kT}{mc^2}$) reaches approximately (see fig. D.2)

$$\frac{\Delta v_r}{c} \simeq \Gamma^{-3/2}, \tag{D.3.3}$$

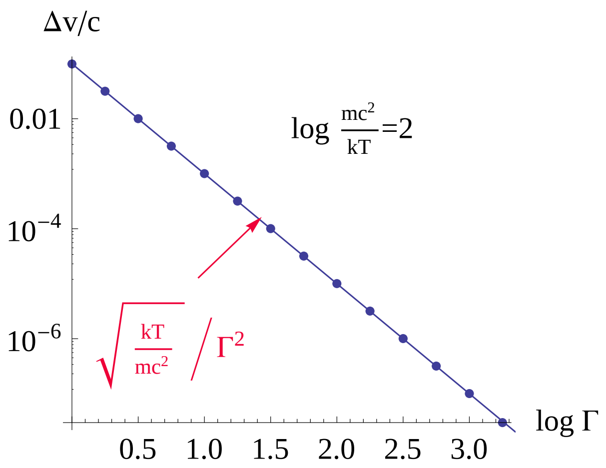

Figure D.1.: The velocity dispersion along the direction of bulk motion for nonrelativistic comoving temperature shown as a function of the bulk Lorentz factor.

which means that the dispersion is independent on the temperature, but for fast motion $\Gamma \gg \frac{kT}{mc^2}$ the asymptotics (D.3.1) is restored just up to a multiplier close to unity (see fig. D.4)

$$\frac{\Delta v_r}{c} \simeq 1.16\,\Gamma^{-2}\sqrt{\frac{kT}{mc^2}}. \tag{D.3.4}$$

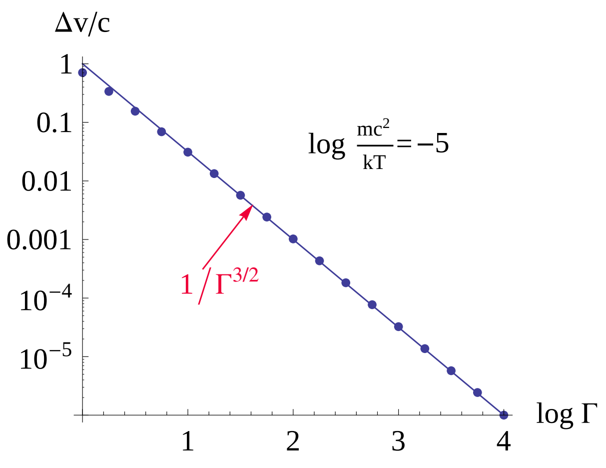

Figure D.2.: The velocity dispersion along the direction of bulk motion for highly relativistic comoving temperature as a function of the bulk Lorentz factor in intermediate regime $10 \lesssim \Gamma \lesssim \frac{kT}{mc^2}$.

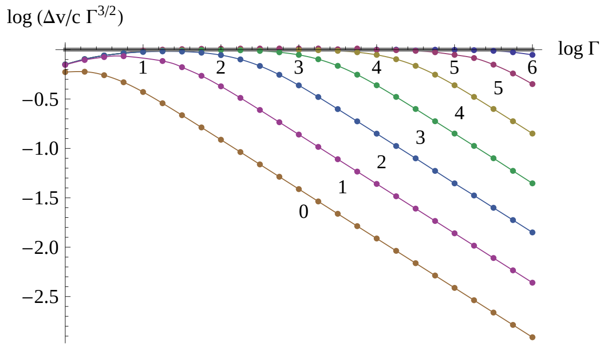

Figure D.3.: The asimptotic velocity dispersion along the direction of bulk motion for highly relativistic comoving temperature as a function of the bulk Lorentz factor in intermediate regime. Six sets of dots presented on the figure correspond to values of $\log \frac{kT}{mc^2}$ from 0 (lowest curve) to 6 (highest curve) in steps of 1. Thick gray line is the asymptotic value (D.3.3).

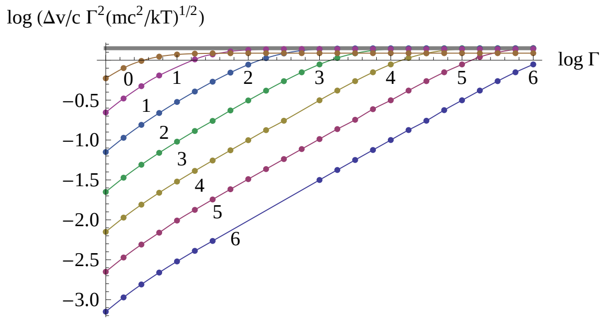

Figure D.4.: The asimptotic velocity dispersion along the direction of bulk motion for highly relativistic comoving temperature as a function of the bulk Lorentz factor in high-Γ regime. Six sets of dots presented on the figure correspond to values of $\log \frac{kT}{mc^2}$ from 0 (highest curve) to 6 (lowest curve) in steps of 1. Thick gray line is the asymptotic value (D.3.4).

D.4. Implications for PGRB

Now we apply these results to the problem of the fireshell spreading. Hydrodynamical simulations show that expansion up to transparency can be roughly divided into two stages: the energy dominated regime with accelerated expansion so that $\Gamma \propto t$, and the matter dominated regime when $\Gamma \simeq const$. At very low baryonic loadings the second stage does not occur and acceleration continues up to transparency of plasma. At both stages temperature decreases as inverse to radius $T \simeq T_0 r_0 / r$. Now we compute the fireshell spreading at both stages, and then sum them up to obtain overall spreading.

For the first stage the reasonable approximation of Lorentz factor, giving correct asimptotics in small and large times, is

$$\Gamma(t) \simeq \sqrt{1+\left(\frac{ct}{R}\right)^2},$$

where R is related to the initial size of plasma $R \simeq r_0$. Due to the nature of Lorentz transformations in constantly accelerated frame (as in the case of hyperbolic motion), the final spreading of the shell $\Delta r_1 = \int_0^t \Delta v\, dt$ appears to be finite even if we extend this stage infinitely in time. The main part of the spreading is connected with initial part of motion with relatively small Γ, that justifies application of Eq. (D.3.3) for velocity spread under the assumption of ultrarelativistic initial temperature T_0

$$\Delta r_1 = \int_0^{t_1} \Delta v(t) dt \lesssim \int_0^{\infty} c\Gamma(t)^{-3/2} dt \simeq 2.6 r_0, \tag{D.4.1}$$

while for nonrelativistic initial temperatures the spread is given by (D.3.1) that leads to even smaller spread values

$$\Delta r_1 \lesssim 2.2\sqrt{\frac{kT_0}{mc^2}} r_0. \tag{D.4.2}$$

At the second stage of expansion $\Gamma \sim const$ and temperature is nonrelativistic $T(t) \simeq T_0 \frac{r_0}{ct}$ ($r \simeq ct$) so the maximal spread of the shell is of the order

$$\Delta r_2 = \int_{t_1}^{t_{tr}} \Delta v(t) dt = \int_{t_1}^{t_{tr}} c\Gamma^{-2}\sqrt{\frac{kT_0 r_0}{mc^2 ct}} dt \simeq \Gamma^{-2}\sqrt{\frac{kT_0}{mc^2}}\sqrt{r_0 c t_{tr}}, \tag{D.4.3}$$

when $t_{tr} \gg r_0$. The radius at which the shell becomes transparent for photons is

$$r_{tr} = \left(\frac{3}{4\pi} N_b \sigma_T\right)^{1/2} \tag{D.4.4}$$

where N_b is the number of baryons, and σ_T is Thompson cross-section. By the definition of baryonic loading

$$B = \frac{M_b c^2}{E_{e^+e^-}} = \frac{N_b m_p c^2}{E_{e^+e^-}} \tag{D.4.5}$$

we then find

$$r_{tr} = \left(\frac{3}{4\pi} \frac{\sigma_T}{m_p c^2} B E_{e^+e^-}\right)^{1/2}, \tag{D.4.6}$$

so assuming that the temperature is determined by e^+e^- pairs only

$$\frac{E_{e^+e^-}}{V_0} = \frac{3E_{e^+e^-}}{4\pi r_0^3} = aT_0^4 \tag{D.4.7}$$

we get

$$\frac{kT_0}{m_e c^2} \simeq \frac{k}{m_e c^2}\left(\frac{3E_{e^+e^-}}{4\pi r_0^3 a}\right)^{1/4}. \tag{D.4.8}$$

Combining everything together we arrive to

$$\frac{\Delta r_2}{r_0} \simeq 0.79\left(\frac{\hbar}{m_e c r_0}\right)^{7/8}\left(\frac{E_{e^+e^-}}{M_\odot c^2}\right)^{3/8}\left(\frac{m_{pl}}{m_p}\right)^{9/8} B^{9/4}. \tag{D.4.9}$$

With the numbers $r_0 = 10^8$cm, $B = 10^{-2}$, $E_{e^+e^-} = M_\odot c^2 \simeq 10^{54}$ erg we get

$$\Delta r_2 \simeq 5r_0, \tag{D.4.10}$$

and total spreading of the fireshell in the first and second stage is $\Delta r_{tot} = \Delta r_1 + \Delta r_2 \lesssim 8r_0$. It should be noted that numbers taken above are somewhat extreme, for example, if we take $B = 10^{-3}$ then spreading on this stage will be really negligible, $\Delta r_2 \simeq 0.03 r_0$.

D.5. Conclusions

In this paper we determined the velocity dispersion of the relativistic fluid depending on its temperature and the Lorentz factor of the bulk motion. We then applied these results to the fireshell model and determined the value of the thermal spreading of the fireshell which occurs before it reaches transparency. The spreading appears to be significant and gives about a tenfold increase compared to the initial size of the fireshell. It implies that the duration of the P-GRB is not determined by the initial size of the plasma r_0/c, but by the value of the thermal spreading $\Delta r_{tot}/c \simeq 8r_0/c$.

Our results show that the results of authors in Mészáros et al. (1993) are not valid, in particular their Eqs. (3.5-3.9). Their results are based on the assumption that the velocity dispersion is independent on the temperature, which is not the case. Thus the paper Mészáros et al. (1993) overestimates the value of thermal spreading.

E. Dark Matter Candidates

Understanding the nature of dark matter (DM) and its origin represents one of the longest-standing challenges in particle cosmology. We know from cosmological observations Spergel et al. (2007); Tegmark et al. (2006b) that only $\sim 5\%$ of the Universe's energy content is accounted for by normal, baryonic matter while the remaining is in the form of dark matter ($\sim 25\%$) and of a similarly elusive energy component, dubbed dark energy ($\sim 70\%$).

E.1. The Majoron

Historically, the neutrino was at first seen as a natural dark matter candidate due to its weak interaction with ordinary matter. However, it soon became evident that the high velocity dispersion of relativistic neutrinos would erase all density perturbations below a critical scale of some tens of megaparsecs (Bond et al., 1980), thus completely spoiling the whole process of structure formation. This critical scale is called the free-streaming length; dark matter candidates with a large free streaming length, like the neutrino, are classified as Hot Dark Matter (HDM). Nowadays, although we know from neutrino oscillation experiments that neutrinos do have mass (Maltoni et al., 2004), recent cosmological data (Lesgourgues and Pastor, 2006), as well as searches for distortions in beta (Drexlin, 2005) and double beta decay spectra (Klapdor-Kleingrothaus et 2004), place a stringent limit on the absolute scale of the neutrino mass and precludes neutrinos from being viable dark matter candidates (Gelmini et al., 1984) and from playing a *direct* role in structure formation.

Many candidates for the dark matter particle are presently under consideration: among the most popular are the supersymmetric neutralino, and the Kaluza-Klein particles [see Bertone et al. (2005) and references therein]. Most of these candidates share the property of being Cold Dark Matter (CDM) particles because their velocity dispersion and consequently their free-streaming length are so small as to be practically irrelevant for cosmological structure formation. This avoids the problem of small-scale damping of HDM models; in fact, CDM models agree well with observations down to scales of several Mpc, once mildly non-linear effects are taken into account (Tegmark et al., 2006b). However, it seems that the CDM scenario is unable to reproduce the matter distribution on the smallest scales, i.e, on Mpc scales and below [see Ostriker and Steinhardt (2003) and references therein]. First, it predicts a number of dwarf galaxies much larger than observed. Secondly, numerical simulations produce DM halos with very high density cores, but this cuspiness is not actually observed in real galactic cores. It is still unclear if these are shortcomings of the model itself or instead come from our poor understanding of astrophysical processes important at the scale of interest, or even from numerical issues related to the high non-linearity of the phenomena under consideration. The problem with the CDM scenario is in some sense opposite that with to the HDM scenario in that the latter predicts too little power in the small-scale fluctuations while the former predicts too much. In other words, a HDM Universe is too smooth with respect to the observed one while a CDM Universe is too clumpy.

Between the two limiting cases of hot and cold dark matter lies the so-called Warm Dark Matter (WDM). Examples of WMD candidates include the sterile neutrino (Dodelson and Widrow, 1994) and the light gravitino (Pagels and Primack, 1982). The free-streaming length of WDM particles is in the Mpc range, thus being quite small with respect to the typical HDM value (hence the name). This is appealing because it suggest the possibility of keeping the successful predictions of the CDM scenario at the intermediate and large scales while the same time alleviating (and hopefully eliminating) the small-scale inconsistencies of the model (Bode et al., 2001). Here we describe, our recent proposal for a WDM candidate linking the problem of dark matter with the issue of the origin of neutrino masses (Lattanzi and Valle, 2007; Lattanzi, 2010).

If neutrinos are Majorana particles, then lepton number is necessariliy broken. The (spontaneous) symmetry breakdown can be either global or local. If neutrino masses arise from a spontaneous violation of ungauged lepton number, there must exist a pseudoscalar gauge singlet Nambu-Goldstone boson, the majoron (Chikashige et al., 1981; Schechter and Valle, 1982). We shall now briefly show how the majoron arises from this global symmetry breakdown in a simple one-generation model, following Chikashige et al. (1981). Let us assume that, in addition to the ordinary, left-handed neutrinos (arranged in left-handed doublets, together with the charged leptons), a SU(2)⊗U(1) singlet, right-handed neutrino exists. We also assume that the neutrinos have both Majorana and Dirac mass terms. The diagonalization of the neutrino mass matrix yields two Majorana neutrino fields: one that we denote as D_L is part of the doublet $\psi_L = (D_L, e_L^-)^T$ while the other, S_R, is a singlet. Their charge conjugate partners are D_R^c and S_L^c. We consider two different Yukawa couplings to a doublet, Φ, and a singlet, ϕ, Higgs field:

$$\mathcal{L}_1 = -h_1 \left(\bar{\psi}_L \Phi S_R + \bar{S}_R \Phi^+ \psi_L \right) , \tag{E.1.1}$$

$$\mathcal{L}_2 = -h_2 \left(\phi \bar{S}_L^c S_R + \phi^+ \bar{S}_R S_L^c \right) . \tag{E.1.2}$$

When Φ acquires a non-zero vacuum expectation value, a Dirac mass term ensues; however when $\langle\phi\rangle \neq 0$, a Majorana mass term ensues. Then one has:

$$\mathcal{L}_{\text{mass}} = -\left[(\bar{D}_L, \bar{S}^c_L)\begin{pmatrix}0 & m\\ m & M\end{pmatrix}\begin{pmatrix}D^c_R\\ S_R\end{pmatrix} + (\bar{D}^c_R, \bar{S}_R)\begin{pmatrix}0 & m\\ m & M\end{pmatrix}\begin{pmatrix}D_L\\ S^c_L\end{pmatrix}\right], \tag{E.1.3}$$

where m and M are the Dirac and the Majorana masses, respectively. If $M \gg m$, the mass eigenstates have approximate eigenvalues M and m^2/M. The physical states are

$$\nu_L \simeq D_L - \frac{m}{M}S^c_L, \qquad \nu^c_R \simeq D^c_R - \frac{m}{M}S_R, \tag{E.1.4}$$

with mass $m_\nu \sim m^2/M$, and

$$\eta_R \simeq S_R + \frac{m}{M}D^c_R, \qquad \eta^c_L \simeq S^c_L + \frac{m}{M}D_L, \tag{E.1.5}$$

with mass $m_\eta \sim M$.

The physical fields ν and η are coupled to the Higgs field ϕ whose spontaneus breakdown violates lepton number. We can split the ϕ field into a scalar and a pseudoscalar field; i.e.,

$$\phi = \frac{1}{\sqrt{2}}(\langle\phi\rangle + \rho + iJ). \tag{E.1.6}$$

The fields ρ and J are, respectively, a massive and a massless field with zero vacuum expectation value. The field J is the majoron. Although massless, it may pick up a mass from non-perturbative gravitational effects that explicitly break global symmetries (Coleman, 1988).

The coupling of the majoron to neutrinos and ordinary matter is given by

$$\mathcal{L}_{J\nu} = -\frac{ih_2}{\sqrt{2}}J\left[\bar{\eta}\gamma_5\eta - \left(\frac{m_\nu}{M}\right)^{1/2}(\bar{\eta}\gamma_5\nu + \bar{\nu}\gamma_5\eta) + \frac{m_\nu}{M}\bar{\nu}\gamma_5\nu \right.$$
$$\left. + \frac{G_F}{8\sqrt{2}\pi^2}m_\nu m_f g_f(\bar{f}\gamma_5 f)\right]. \tag{E.1.7}$$

The coupling to neutrinos is quite small, being suppressed by a factor m_ν/M. The coupling to the matter fields is even weaker. The only sizeable coupling is the one to the heavy neutrino η, but these particles are unstable because they rapidly decay into a majoron and a light neutrino.

The coupling of the majoron to leptons leads to the possibility of $J \to \gamma\gamma$ decays, mediated, for example, by triangle loops. Actually, in the most general case, the current connected with the spontaneously-violated global symmetry is anomalous, and the majoron is coupled to photons through the electromagnetic anomaly of this symmetry.

E.1.1. Majoron dark matter

Despite the fact that the majorons produced at the corresponding spontaneous L–violation phase will decay, mainly to neutrinos, they could still provide a sizeable fraction of the dark matter in the Universe because their couplings are rather tiny. This scenario was first considered by Berezinsky and Valle (1993); however, since then, there have been important observational developments that must be taken into account in order to assess its viability, most notably the recent cosmological microwave observations from the Wilkinson Microwave Anisotropy Probe (WMAP) (Spergel et al., 2007).

In the following, we consider the majoron decaying dark matter (DDM) idea in a modified Lambda Cold Dark Matter (ΛCDM) cosmological model in which the dark matter particle is identified with the weakly interacting majoron, J, with a mass in the keV range. A keV weakly interacting particle could provide a sizeable fraction of the critical density $\rho_{cr} = 1.88 \times 10^{-29} h^2$ g/cm^3 and possibly play an important role in structure formation, because the associated Jeans mass, $m_{Jeans} \sim m_{Pl}^3/m_J^2$, lies in the relevant range.

The majoron is, however, not stable, but decays non-radiatively with a small decay rate Γ. In this DDM scenario, the anisotropies of the cosmic microwave background (CMB) can be used to constrain the lifetime, $\tau = \Gamma^{-1}$, and the present abundance, Ω_J, of the majoron; here, we show that the cosmological constraints on DDM majorons not only can be fulfilled but also can easily fit into a comprehensive global picture for neutrino mass generation with spontaneous violation of lepton number.

Majoron Abundance

Although majorons could result from a phase transition, we first consider them to be produced thermally and in equilibrium with photons in the early Universe. In this case, the majoron abundance, n_J, at the present time, t_0, will be, owing to entropy conservation and the finite lifetime,

$$\frac{n_J(t_0)}{n_\gamma(t_0)} = \frac{43/11}{N_D} \frac{n_J(t_D)}{n_\gamma(t_D)} \, e^{-t_0/\tau}, \tag{E.1.8}$$

where t_D is the time of majoron decoupling, and N_D denotes the number of quantum degrees of freedom at that time. The exponential factor accounts for majoron decay. If $T(t_D) \gtrsim 170$ GeV, then $N_D = 427/4 = 106.75$ for the particle content of the standard model, while in the context of a supersymmetric extension of the SM, there would possibly be, at sufficiently early times, about twice that number of degrees of freedom. Finally, in thermal equilibrium the majoron-to-photon ratio, $f \equiv n_J(t_D)/n_\gamma(t_D)$, is equal to 1/2. The present density parameter of majorons is then, by using $N_D = 106.75$, given by

$$\Omega_J h^2 = \frac{m_J}{1.25\,\mathrm{keV}} e^{-t_0/\tau}. \tag{E.1.9}$$

Another possibility is that majorons were already produced out of equilibrium. In this case, there is a range of possible models, which we can write generically as

$$\Omega_J h^2 = \beta \frac{m_J}{1.25\,\mathrm{keV}} e^{-t_0/\tau}, \tag{E.1.10}$$

where the quantity β parametrizes our ignorance about both the exact production mechanism and the exact value of N_D. When $\beta = 1$, we recover the scenario described above, with $f = 1/2$ and $N_D = 427/4$.

Effects of Majoron DM on the CMB

Clearly, if the majoron has to survive as a dark matter particle, it must be long-lived, $\tau \geq t_0$. However, a more stringent bound follows by studying the effect of a finite majoron lifetime on the cosmological evolution and, in particular, on the CMB anisotropy spectrum. In the DDM scenario, due to particle decays, the dark matter density is decreasing faster than it is in the standard cosmological picture. This changes the time, t_{eq}, of radiation-matter equality. This means that, for a fixed Ω_J, there will be more dark matter at early times, and the equality will take place earlier, as illustrated in Fig. E.1. The present amount of dark matter is $\Omega_{DM} = 0.25$ for both models; $\Gamma^{-1} = 14\,\mathrm{Gyr}$ in the DDM model. Other relevant parameters are $\omega_b = 2.23 \times 10^{-2}$ and $h = 0.7$. The time at which the blue and the red lines cross is the time of matter-radiation equality; for fixed Ω_{DM}, it shifts to earlier times as the majoron lifetime decreases. Another effect of the majoron having a finite lifetime is the increase in radiation density close to the present time.

The time of matter-radiation equality has a direct effect on the CMB power spectrum. The gravitational potentials are decaying during the radiation-dominated era; this means that photons will receive an energy boost after crossing potential wells. This so-called early integrated Sachs-Wolfe (EISW) effect ceases when matter comes to dominate the Universe because the potentials are constant during matter domination. The overall effect is to increase the power around the first peak of the spectrum as the equality moves to later times. On the other hand, since $\tau \gtrsim t_0$, we expect a large production of relativistic particles (specifically, neutrinos) at low redshifts. This can be seen in Fig. E.1; it is the rise in radiation density occurring close to $a = 1$, so that the universe is not completely matter dominated. Thus, majoron decays cause the gravitational potentials to vary again in the late stage of the cosmological evolution. This will induce an effect similar to the one described above, only affecting larger scales due to the increased horizon size. Thus, late integrated Sachs-Wolfe (LISW) effect results in an excess of power at small multipoles.

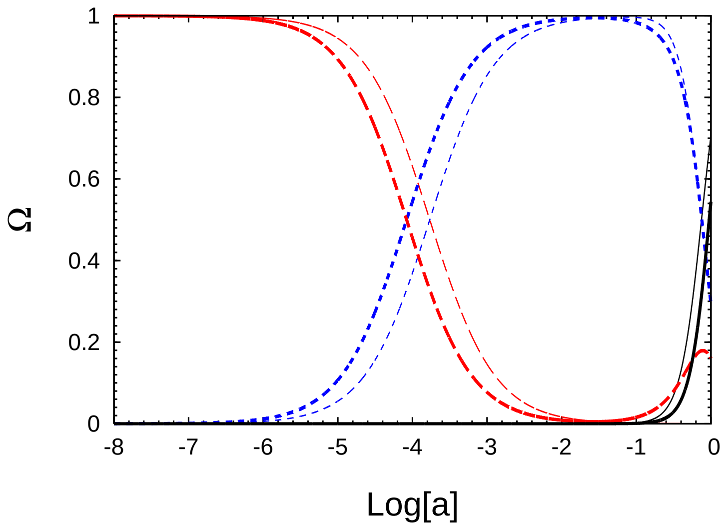

Figure E.1.: Evolution of the abundances in the standard (thin lines) and in the DDM (thick lines) Universe scenario: blue/short dashed, red/long dashed, and black/solid correspond to the matter, the radiation and the Λ components, respectively.

Evolution of Perturbations in DDM models

Both the above effects can be used in principle to constrain the majoron lifetime and cosmological abundance. In order to carry out a quantitative analysis, we have developed a modified version of the `CAMB` code (Lewis et al., 2000), which enables us to compute the CMB anisotropy spectrum once the majoron lifetime and abundance are given in addition to the standard ΛCDM model parameters.

We stress the fact that even if a keV majoron constitutes a warm dark matter particle, it actually behaves as cold dark matter insofar as the calculation of its effect on the CMB spectrum is concerned because CMB measurements cannot discriminate between cold and warm dark matter. The latter behaves differently from the former on scales smaller than its free-streaming length λ_{fs}. For a particle mass in the keV range, we have $\lambda_{fs} \sim 1\,\text{Mpc}$, which corresponds in the CMB to a multipole $\ell \sim$ few thousands.

The formalism needed to account for the cosmological evolution of an unstable relic and its light decay products has been developed for example by Kaplinghat et al. (1999) and Ichiki et al. (2004), including the modifications in both the background quantities and the perturbation evolution. We report here the necessary changes to the evolution equations, using the formalism introduced in by Ma and Bertschinger (1995). The subscript J denotes the majoron dark matter component while the subscript DP denotes the majoron relativistic decay products.

Background equations The equations for the time evolution of the dark matter and decay products energy density are

$$\dot{\rho}_J + 3\frac{\dot{a}}{a}\rho_J = -a\Gamma\rho_J, \tag{E.1.11a}$$

$$\dot{\rho}_{DP} + 4\frac{\dot{a}}{a}\rho_{DP} = a\Gamma\rho_J, \tag{E.1.11b}$$

where a is the cosmological scale factor, and the dot denotes the derivative with respect to the conformal time (hence, the extra a factor on the right-hand side). Note that the source term for the decay products involves the dark matter density, thus effectively coupling the two equations.

Perturbation equations The perturbations in the dark matter and the decay products components evolve according to the following set of equations [see Ma and Bertschinger (1995) for the meaning of the symbols]:

Background equations

$$\dot{\delta}_J = -\frac{\dot{h}}{2}, \tag{E.1.12}$$

Decay products

$$\dot{\delta}_{DP} = -\frac{2}{3}\left(\dot{h} + 2\theta_{DP}\right) + \frac{\dot{r}}{r}\left(\delta_J - \delta_{DP}\right), \tag{E.1.13a}$$

$$\dot{\theta}_{DP} = k^2\left(\frac{\delta_{DP}}{4} - \sigma_{DP}\right) - \frac{\dot{r}}{r}\theta_{DP}, \tag{E.1.13b}$$

$$\dot{\sigma}_{DP} = \frac{2}{15}\left(2\theta_{DP} + \dot{h} + 6\dot{\eta}\right) - \frac{3}{10}kF_{DP,3} - \sigma_{DP}\frac{\dot{r}}{r}, \tag{E.1.13c}$$

$$\begin{aligned}\dot{F}_{DP,\ell} = {} & \frac{k}{2\ell+1}\left[\ell F_{DP,\ell-1} - (\ell+1)F_{DP,\ell+1}\right] \\ & - F_{DP,\ell}\frac{\dot{r}}{r}, \qquad \ell \geq 3,\end{aligned} \tag{E.1.13d}$$

where r denotes the ratio of DP to photon energy densities, i.e., $r \equiv \rho_{DP}/\rho_\gamma$ (any fiducial density scaling as a^{-4} will actually do the job). The presence of the dark matter density perturbation δ_J on the right-hand side of Eq. (E.1.13a) again couples the two sets of equations.

E.1.2. Statistical analysis

Parametrization

Two distinct mechanisms effective at very different times characterize the effect of the DDM on the CMB. It is, therefore, convenient to choose a parametrization that can take advantage of this fact. In particular, the "natural" parametrization (Ω_J, Γ) has the drawback that both parameters affect the time of matter-radiation equality. It is more convenient to define the quantity

$$Y \equiv \left.\frac{\rho_J}{\rho_b}\right|_{t=t_{\rm early}}, \tag{E.1.14}$$

where ρ_b is the energy density of baryons, and $t_{\rm early} \ll t_0 \lesssim \tau$. As long as this condition is fulfilled, the value of Y does not depend on the particular choice of $t_{\rm early}$ beacuse the ratio ρ_J/ρ_b is asymptotically constant at small times. Given that $t_{eq} \ll \tau$, we can use the value of Y to parametrize the relative abundance of majorons at matter-radiation equality. In order to simplify notation, let us also define $\Gamma_{18} \equiv \Gamma/(10^{-18}\text{sec}^{-1})$; in this way, $\Gamma_{18} = 1$ corresponds to a lifetime $\tau \simeq 30\,\text{Gyr}$. The advantage of using the parametrization (Y, Γ) is that, when all other parameters are fixed, the time of matter-radiation equality is uniquely determined by Y while the magnitude of the LISW effect is largely determined by Γ.

We show in Fig. E.2 how the two physical effects are nicely separated in this parametrization. We start from a fiducial model with $\Gamma_{18} = 0$ and $Y = 4.7$; all other parameters are fixed to their WMAP best-fit values. The values of Γ_{18} and Y are chosen in such a way to give $\Omega_J h^2 = 0.10$ so that this fiducial model reproduces exactly the WMAP best-fit. At a larger majoron decay rate of $\Gamma_{18} = 1.2$, i.e., $\Gamma^{-1} \simeq 27\,\text{Gyr}$, the LISW effect causes, as expected, the power at small multipoles to increase while the shape of the spectrum around the first peak does not change, because the abundance of matter at early times does not change. Finally, if Y is increased by 20%, the height of the first peak decreases accordingly while the largest angular scales (small ℓs) are nearly unaffected. A small decrease in power in this region is actually observed and can be explained by noticing that increasing the matter content delays the onset of the Λ-dominated era, reducing the Λ contribution to the LISW effect. Another advantage of using the above parametrization is that Y is directly related to the majoron mass through

$$Y = 0.71 \times \left(\frac{m_J}{\text{keV}}\right)\left(\frac{\beta}{\Omega_b h^2}\right). \tag{E.1.15}$$

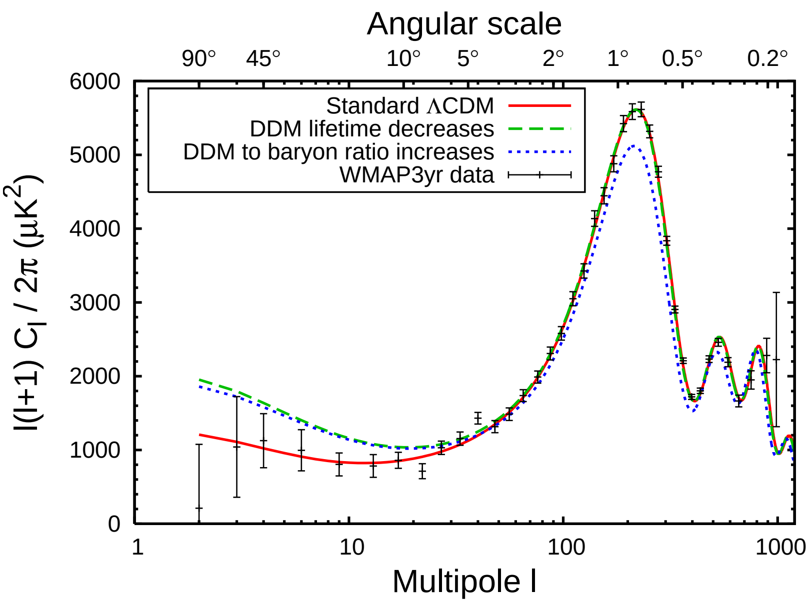

Figure E.2.: Effect of DDM parameters on the CMB anisotropy spectrum. The values of the parameters are as follows: red/solid: fiducial model $(\Gamma_{18}, \Upsilon) = (0, 4.7)$; Green/dashed: $(\Gamma_{18}, \Upsilon) = (1.2, 4.7)$; Blue/dotted: $(\Gamma_{18}, \Upsilon) = (1.2, 5.6)$. See text.

E.1.3. Results and Discussion

We are now ready to compute the constraints that CMB observations put on the majoron abundance and lifetime. As seen from Fig. E.2, even a lifetime twice as long as the present age of the Universe, is quite at variance with respect to the WMAP data. However, one must take into account the fact that the values of other cosmological parameters can be arranged in such a way as to reduce or even cancel the conflict with observation; i. e., degeneracies may be present in parameter space. In order to obtain reliable constraints for the majoron mass and lifetime, we perform a statistical analysis allowing for the variation of all parameters. This is better accomplished using a Markov-chain Monte Carlo approach; we used for this purpose the widely-known `COSMOMC` code.

In our modified flat ($\Omega = 1$) ΛCDM model, all the dark matter is composed of majorons. This means that no stable cold dark matter is present.[1] The 7-dimensional parameter space we explore, therefore, includes the two parameters (Υ, Γ) defined above, in addition to the five standard parameters: namely, the baryon density $\Omega_b h^2$, the dimensionless Hubble constant h, the reionization optical depth τ_{re}, the amplitude A_s, and spectral index n_s of the primordial density fluctuations. The cosmological constant den-

[1]This happens, e. g., in models where supersymmetry with broken R parity is the origin of the neutrino mass (Hirsch and Valle, 2004; Hirsch et al., 2000).

sity Ω_Λ depends on the values of the other parameters due to the flatness condition. We compare the theoretical prediction obtained with `CAMB` with the temperature and polarization data from the following CMB experiments: WMAP (Hinshaw et al., 2007; Page et al., 2007), ACBAR (Kuo et al., 2007), BOOMERANG (Piacentini et al., 2006; Jones et al., 2006), CBI (Readhead et al., 2004), and VSA (Dickinson et al., 2004). Once the full probability distribution function for the seven base parameters has been obtained in this way, the probability densities for derived parameters, such as the majoron mass m_J, can be consequently calculated.

We start by discussing the results concerning the majoron parameters. The 68% and 95% confidence contours in the (m_J, Γ) plane, for the case $\beta = 1$, i.e., thermal majoron production and $N_D = 427/4$, are shown in Fig. E.3. It can be understood from this figure that the parameters are not degenerate with one another, so the respective constraints are independent. The marginalized 1-dimensional limits for Γ and m_J are

$$\Gamma < 1.2 \times 10^{-19} \mathrm{sec}^{-1}, \tag{E.1.16}$$

$$0.13\,\mathrm{keV} < m_J < 0.17\,\mathrm{keV}. \tag{E.1.17}$$

Expressed in terms of the majoron lifetime, our result implies $\tau > 250\,\mathrm{Gyr}$, nearly a factor 20 improvement with respect to the naive limit $\tau > t_0 \simeq 14$ Gyr, illustrating the power of CMB observations in constraining particle physics scenarios.

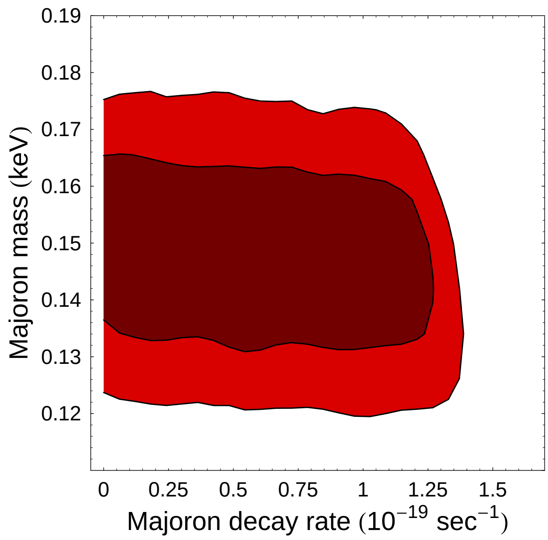

Figure E.3.: Contours of the 68% (dark) and the 95% (light) confidence regions in the (Γ_J, m_J) plane.

Let us comment on the possibility that $\beta \neq 1$. From Eq. E.1.10, it can be seen that this amounts to the transformation $m_J \to \beta m_J$. For example, as we have already pointed out, N_D can be as large as $427/2 \simeq 200$ so that the above limit would read $0.24\,\text{keV} < m_J < 0.34\,\text{keV}$. In general, if we allow for the possibility of extra degrees of freedom in the early Universe, we always have $\beta < 1$ and then $m_J > 0.12\,\text{keV}$. If instead majorons are produced non-thermally, one will in general have $\beta > 1$.

The posterior probability distributions for all the parameters in the model are shown in Fig. E.4, again for the case $\beta = 1$. We show the posterior for the following combinations of parameters: ($\Omega_b h^2$, H_0, τ_{re}, n_s, $\log(10^{10}A)$, Ω_{DM}, Γ, m_J). These are eight parameters, but only seven of them are independent because the dark matter density, $\Omega_{DM} = \Omega_J$, is determined through Eq. (E.1.9) once H_0, m_J, and Γ are fixed. This is included because in this way, the first six parameters that appear in Fig. E.4 correspond to the parameters used to describe a standard ΛCDM model. The plots on the diagonal of the figure show the one-dimensional posterior distribution for each of the parameters. It can be noticed that for the standard parameters, there is no significant deviation from the WMAP best estimate (Spergel et al., 2007). The results for the additional majoron parameters were discussed above. The off-diagonal plots show the two-dimensional posterior distributions for pairs of parameters. It can be seen that Γ is not degenerated with any of the other parameters. A degeneracy exists between the present value of the Hubble constant H_0 and the majoron mass m_J due to the fact that the CMB spectrum actually constrains the dark matter density Ω_J through the position of the first peak. Then, it can be clearly seen by Eq. (E.1.9) that m_J and h^2 must be anticorrelated.

A recent analysis of the Lyman-α forest data (Seljak et al., 2006) suggests that the mass of the warm dark matter particle should be larger than at least 1 keV (maybe even an order of magnitude more), the exact result depending on the candidate under consideration, on the data used, and on the analysis pipeline. Taken at face value, these results, combined with the limits we obtain from the CMB, seem to exclude the majoron as a viable dark matter candidate. However, care should be taken in naively applying these results to the model presented here. First, the limits on the mass of the WDM particle have been obtained in the case of a stable particle. The effect of the decay on the growth of density fluctuations should be taken into account to reliably compare the predicted matter power spectrum to the observations. Second, the results of the Lyman-α forest analysis actually depend on the phase space distribution of the particles at the time of decoupling and then ultimately on the production mechanism. To the contrary, our results, when quoted in terms of the quantity βm_J, are completely independent of the production mechanism due to the fact that, as we commented above, it is a good approximation to consider that the thermal velocities of majorons are negligible, as far as the CMB is concerned. This means that the particle mass never enters directly into the perturbation equations; instead, it only enters indirectly through the background quantity $\Omega_J \propto \beta m_J$, and this should be regarded as the quantity that is really constrained by CMB observations. A production mechanism resulting in a "sub-thermal" (i.e., $\beta < 1$) majoron abundance will result in the same dark matter energy density being shared between a smaller number of particles and in a larger particle mass. The same result of a larger mass for fixed Ω_J can be achieved if the number of quantum degrees of freedom at decoupling is substantially larger than the standard model value of 106.75, for example in theories with larger gauge groups and representations. Finally, we should remember that there is still no consensus on whether the Lyman-α data can be considered fully reliable due the various systematics that are involved in the analysis pipeline.

We now briefly comment on the particle physics model. The simplest possibility is that neutrino masses arise *a la seesaw* (Valle, 2006). In the basis ν, ν^c (where ν denotes ordinary neutrinos, while ν^c are the SU(2) $\otimes$ U(1) singlet "right-handed" neutrinos), the full neutrino mass matrix is given as

$$\mathcal{M}_\nu = \begin{pmatrix} Y_3 v_3 & Y_\nu v_2 \\ {Y_\nu}^T v_2 & Y_1 v_1 \end{pmatrix}, \tag{E.1.18}$$

and involves, in addition to the singlet, a Higgs triplet contribution (Schechter and Valle, 1980) whose vacuum expectation value obeys a "vev seesaw" relation of the type $v_3 v_1 \sim v_2^2$. The Higgs potential combines spontaneous breaking of lepton number and electroweak symmetry. The properties of the seesaw majoron and its couplings follow from the symmetry properties of the potential were extensively discussed by Schechter and Valle (1982). Here we assume, in addition, that quantum gravity effects (Coleman, 1988) produce non-renormalizable Planck-mass-suppressed terms, which explicitly break the global lepton number symmetry and provide the majoron mass, which we can not reliably compute, but we assume that it lies in the cosmologically interesting keV range.

In all such models, the majoron interacts mainly with neutrinos in proportion to their mass (Schechter and Valle, 1982), leading to

$$\tau(J \to \nu\nu) \approx \frac{16\pi}{m_J} \frac{v_1^2}{m_\nu^2}. \tag{E.1.19}$$

The limits obtained above from the WMAP data can be used to roughly constrain the lepton number breaking scale as $v_1^2 \gtrsim 3 \times \left(10^6\,\mathrm{GeV}\right)^2$ for $m_\nu \simeq 1\mathrm{eV}$.

The massive majoron also has a sub-leading radiative decay mode, $J \to \gamma\gamma$, making our DDM scenario potentially testable through studies of the diffuse photon spectrum in the far ultraviolet (Bazzocchi et al., 2008). A more extended investigation of these schemes will be presented elsewhere, including other cosmological data, such as the large-scale structure data from the Sloan

Digital Sky Survey (SDSS). In contrast, we do not expect the data from upcoming CMB experiments like Planck to substantially improve our bounds on the majoron decay rate because they mainly affect the large angular scales where the error bars have already reached the limit given by the cosmic variance. We also note that direct detection of a keV majoron is possible in a suitable underground experiment (Bernabei et al., 2006). Another interesting possibility is that the entropy production and bulk viscosity associated with the late decay of the dark matter particle could explain the observed acceleration of the Universe (Mathews et al., 2008), although the decay rate needed to accomplish this seems to be too large with respect to the limit found in our analysis of the CMB data.

E.2. The Barbero-Immirzi Axion

According to the Standard Model, two terms contribute to the strong *CP* violation. Specifically, the non-hermitian quark mass matrix M introduces a *CP* violation term proportional to $\text{Arg}\det M$. This sums up to the vacuum angle of QCD, θ, generating a *CP* violating interaction that depends on the parameter $\tilde{\theta} = \theta + \text{Arg}\det M$. By measuring the electric dipole moment of the neutron, an extremely small upper limit can be fixed for $\tilde{\theta}$, which turns out to be smaller than 10^{-10}. Such a small value implies an extremely precise compensation between two completely uncorrelated parameters: one associated to the global structure of the $SU(3)$ gauge group and the other related to the $SU(2) \times U(1)$ breaking symmetry. The unnaturalness of this "fine tuning" goes under the name of *strong CP problem*.

Peccei and Quinn proposed a dynamical mechanism to solve the strong *CP* problem (Peccei and Quinn, 1977a,b). They postulated the existence in the Standard Model of an additional $U(1)$ axial symmetry, often denoted as $U(1)_{PQ}$. On the one hand, if this symmetry were exact, the *CP* violating interaction could be eliminated through a chiral rotation. On the other hand, we expect that the $U(1)_{PQ}$ is spontaneously broken by the chiral anomaly. Interestingly enough, the Peccei–Quinn (PQ) mechanism allows us to solve the strong *CP* problem, even though the $U(1)_{PQ}$ additional symmetry is not preserved by quantization.

In order to briefly describe how the PQ mechanism works, it is worth recalling that the spontaneous breaking of the $U(1)_{PQ}$ symmetry generates a (pseudo) Nambu–Goldstone boson, called *axion* (Weinberg, 1978; Wilczek, 1978), a possible cold dark matter (CDM) candidate (Kolb and Turner, 1990).

The axion interacts with matter through the following effective action [2].

$$S_{\text{Eff}} = S\left[A\right] + S_{\text{Dir}}\left[\psi, \bar{\psi}, A\right] + S_{\text{matt}}\left[\frac{da}{f_a}, \psi, \bar{\psi}\right] \\ + \frac{1}{2}\int \star da \wedge da - \frac{g_s^2}{8\pi^2}\int \left(\tilde{\theta} + \frac{a}{f_a}\right) \text{tr}G \wedge G\,, \quad \text{(E.2.1)}$$

where f_a denotes the scale of the $U(1)_{PQ}$ symmetry breaking. $G = dA + ig_s A \wedge A$ is the curvature 2-form associated to the $SU(3)$ valued connection 1-form $A = A^I \lambda^I$, λ^K being the generators of the group, and g_s the strong coupling constant. With the collective symbols ψ and $\bar{\psi}$ we denoted fermion matter fields, interacting with the axion through a derivative coupling term, S_{matt}.

The CP violating $\tilde{\theta}$-term combines with the anomaly-induced interaction between the axion and the gluon fields; the possible observables of the theory now depend on the effective vacuum angle $\theta(x) = \tilde{\theta} + \frac{a(x)}{f_a}$, sometimes referred as *misalignment angle*. The effective interaction, $\theta(x)\text{tr}G \wedge G$, represents a non-trivial potential for the axion field, which selects a particular vacuum expectation value. In particular, the periodicity of the potential in the effective vacuum angle, $\theta(x)$, implies that it has a non-trivial minimum corresponding to $\theta(x) = 0$ (Peccei, 1998), so that $\langle a(x) \rangle = -f_a \tilde{\theta}$. Consequently, the gluons effectively interact only with the physical axion $a_{\text{Phys}}(x) = a(x) - \langle a(x) \rangle$, preserving the theory from the strong CP violation [3].

The physical features of the axion, as, e.g., its mass and the strength of its interactions with ordinary matter, strictly depend on the scale of the PQ symmetry breaking, f_a, which remains a completely free parameter, not fixed by the theory. The scope of this letter is to present a new model that allows us to solve the strong CP problem *à la* Peccei–Quinn, with the remarkable advantage that the parameter f_a turns out to be fixed by the theory. This provides a completely determined dynamics, so that the contribution of such an axion field to CDM can be estimated as function of the initial misalignment angle.

Even more interestingly, the model predicts the production of isocurvature fluctuations during inflation, allowing us to fix a tight upper limit to the tensor-to-scalar ratio, r. This represents an experimentally testable prediction that can, eventually, rule out the model.

[2]The signature throughout this section is $(+,-,-,-)$ with $\epsilon_{0123} = 1$. For convenience, we set $\hbar = c = k_B = 1$ and $8\pi G = k$.

[3]It is worth remarking that, even postulating the existence of an additional $U(1)_{PQ}$ chiral symmetry, the electroweak CP violating effects prevent $\tilde{\theta}$ from vanishing exactly. Nevertheless, these electroweak effects induce a CP violation well within the experimental limit discussed above, i.e. $\tilde{\theta}_{\text{ew}} \approx 10^{-15}$.

Let us start by considering a generic space-time with torsion. The chiral rotation of the fermionic measure in the Euclidean path-integral generates, besides the usual Pontryagin class, a Nieh–Yan term (Nieh and Yan, 1982), which diverges as the square of the regulator (Chandia and Zanelli, 1997; Obukhov et al., 1997; Soo, 1999; Chang and Soo, 1999) [see also Kreimer and Mielke (2001); Chandia and Zanelli (2001)], i.e.

$$\delta\psi\delta\overline{\psi} \to \delta\psi\delta\overline{\psi}\exp\left\{\frac{i}{8\pi^2}\int\alpha\Big[R_{ab}\wedge R^{ab} + 2M^2\big(T_a\wedge T^a - e_a\wedge e_b\wedge R^{ab}\big)\Big]\right\}. \quad \text{(E.2.2)}$$

Above, M denotes the regulator, while α is the parameter of the transformation [4]. In order to avoid the appearance of this divergence, one of us has recently proposed to introduce a field, $\beta(x)$, interacting with gravity through the Nieh–Yan density (Mercuri, 2009), namely

$$S_{\text{Tot}}\left[e,\omega,\psi,\overline{\psi},\beta\right] = S_{\text{HP}}\left[e,\omega\right] + S_{\text{D}}\left[e,\omega,\psi,\overline{\psi}\right] + \chi\int\beta(x)\left(T^a\wedge T_a - e_a\wedge e_b\wedge R^{ab}\right), \quad \text{(E.2.3)}$$

where χ is a generic coupling constant with the dimension of energy. According to this proposal, we assume that (E.2.3) is the fundamental action for gravity and matter [5].

In order to clarify some aspects related to the proposed modification, we write below the resulting semi-classical effective action (Mercuri, 2009; Mercuri and Taveras, 2009):

$$\begin{aligned} S_{\text{eff}} = {} & S_{\text{HP}}\left[e\right] + S[A] + S_{\text{Dir}}\left[e,\psi,\overline{\psi}\right] + \frac{1}{2}\int\star d\tilde{\beta}\wedge d\tilde{\beta} \\ & + \frac{1}{8f_{\tilde{\beta}}}\int\star J_{(A)}\wedge J_{(A)} - \frac{1}{2f_{\tilde{\beta}}}\int\star J_{(A)}\wedge d\tilde{\beta} \\ & - \frac{1}{8\pi^2}\int\left[\left(\tilde{\Theta}+\frac{\tilde{\beta}}{2f_{\tilde{\beta}}}\right)R\wedge R + \left(\tilde{\theta}+\frac{\tilde{\beta}}{2f_{\tilde{\beta}}}\right)G\wedge G\right], \end{aligned} \quad \text{(E.2.4)}$$

where we have defined the new field $\tilde{\beta}(x) = \sqrt{6k}\chi\beta(x)$ and introduced the constant $f_{\tilde{\beta}} = \frac{2}{\sqrt{6k}} \simeq 1.98\times 10^{18}$GeV. An $SU(3)$ valued connection 1-form A,

[4] The imaginary unit i disappears in Minkowski space.

[5] The field β is usually referred as Barbero–Immirzi (BI) field, see Taveras and Yunes (2008); Calcagni and Mercuri (2009). See also Leigh et al. (2009) and Cianfrani and Montani (2009) for different approaches).

representing the strong interaction, has been considered as well; G being its curvature. In the last line, a trace over internal indexes is understood.

Some comments are now in order. The pure gravitational sector of the effective theory is reminiscent of the so-called Chern–Simons modified gravity, vastly studied in the Literature (see the interesting and complete review by Alexander and Yunes (2009)). So, from an effective point of view, the modification of the gravitational action proposed in Eq. (E.2.3) reduces to a well known theory of gravity, originating from String Theory and featuring some interesting dynamical effects, well within the presently available experimental limits (Yunes and Pretorius, 2009), thus persuading us to take it seriously. The resulting semi-classical effective theory does not depend on the free coupling constant χ and shares many common features with that postulated by Peccei and Quinn. It is worth noting that in fact, in the case of massless fermions, the full action with the Nieh–Yan modification presents an additional $U(1)_A$ symmetry, which is broken at an effective level by the interaction between the $\beta(x)$ field and the fields strength in the last line of (E.2.4) [6]; exactly analogous to the $U(1)_{PQ}$ introduced above. The presence of these interaction terms reflects the existence of the chiral anomaly, which, in fact, spontaneously breaks the $U(1)_A$ symmetry at the energy scale $f_{\tilde{\beta}}$, naturally determined by the theory; in striking contrast with the Peccei–Quinn scenario, where f_a is a free parameter of the theory.

Let us now assume that the system evolves in a symmetric space-time, characterized by a vanishing $R^{ab} \wedge R_{ab}$ term, as the unperturbed Friedmann–Robertson–Walker (FRW) cosmological model. In this hypothesis, comparing action (E.2.4) with (E.2.1), one can appreciate the functional analogy of the two effective theories. This analogy strongly suggests to identify the field $\tilde{\beta}$ with the axion field a (see also Gates et al. (2009) for a supersymmetric analogous identification); this is the essence of our proposal, which represents the main novelty of this model, whereas, in some previous papers (Mercuri, 2009; Mercuri and Taveras, 2009), the possible coexistence of the $\tilde{\beta}(x)$ field and the standard axion, $a(x)$ was addressed.

The term in the last line of (E.2.4) represents a non-trivial potential for the BI-axion field, selecting a particular CP preserving vacuum state. So, by implementing a mechanism analogous to the Peccei–Quinn one, we can solve the strong CP problem via the BI-axion field.

As was noted above, in this model the symmetry breaking energy scale $f_{\tilde{\beta}}$ is fixed by the theory, allowing us to estimate the expected zero-temperature mass of the BI-axion field, which, as for the standard axion, is generated by

[6] It is worth remarking that the BI field turns out to be a pseudo-scalar as suggested by its contribution to the irreducible torsion components Mercuri (2009) and confirmed by its equations of motion Mercuri and Taveras (2009).

instantontic effects (Peccei, 1998). We obtain,

$$
{}^{0}m_{\tilde{\beta}} = \frac{f_{\pi}}{f_{\tilde{\beta}}} m_{\pi} \frac{\sqrt{m_u m_d}}{m_u + m_d} \simeq 3.04 \times 10^{-12}\,\mathrm{eV}\,, \tag{E.2.5}
$$

where we used the value of the pion decay constant, $f_{\pi} = 93\,\mathrm{MeV}$, measured in the decay process $\pi^{+} \rightarrow \mu^{+} + \nu_{\mu}$. As is well known, instantonic effects depend on the temperature, in particular, we expect that the greater the temperature, the smaller the mass of the BI-axion field becomes; according to the standard Literature, we have that (Gross et al., 1981; Turner, 1986)

$$
m_{\tilde{\beta}}(T) = \begin{cases} {}^{0}\bar{m}_{\tilde{\beta}} b \left(\frac{\Lambda}{T}\right)^{4} & T \gtrsim \Lambda\,, \\ {}^{0}\bar{m}_{\tilde{\beta}} & T \lesssim \Lambda\,, \end{cases} \tag{E.2.6}
$$

where we have assumed $b = 0.018$ and color anomaly index equal to 1. $\Lambda \simeq 200\,\mathrm{MeV}$ is the QCD scale.

So, in this model, the physical parameters, namely the mass of the field and the magnitude of its interaction with matter, are fixed by the theory. Remarkably, this allows us to reduce the parameter space of the theory and extract strong predictions from the cosmological scenario we are going to study.

In general, when dealing with axion scenarios, there are two possibilities. The first one is that the PQ symmetry is restored after inflation, and then broken again after the Universe cools down. This happens if the reheating temperature T_{RH} is larger than the energy scale at which the symmetry is broken. The second possibility is that the PQ symmetry is broken during inflation and never restored afterwards. In order for the symmetry to be broken during inflation, the scale f_{PQ} has to be larger than the Gibbson-Hawking temperature $T_{GH} = H_I/2\pi$ associated to the cosmological horizon (here H_I is the value of the Hubble expansion rate during inflation) (Lyth and Stewart, 1992); furthermore, in order for the symmetry to stay broken after inflation, the reheating temperature has to be smaller than f_{PQ}. The inflationary expansion rate is constrained by the WMAP observations (Komatsu et al., 2009) to be $H_I \leq 6.29 \times 10^{14}\mathrm{GeV}$. The reheating temperature is poorly constrained by the observations and could be anywhere in the range $1\,\mathrm{MeV} - 10^{16}\mathrm{GeV}$. However in the context of the model presented here, the relevant energy scale $f_{\tilde{\beta}} \sim 10^{18}\mathrm{GeV}$ is so large that we will always have to deal with the second scenario, i.e., the symmetry remains broken after inflation. Nevertheless, we will also briefly take into account the possibility that inflation never occurred.

The fact that the PQ symmetry stays broken after the end of inflation, has two important consequences. The first is that the initial misalignment angle of the BI field is practically constant within the region corresponding to our present horizon, and can take any value between $-\pi$ and π. The second is that isocurvature perturbations are produced in the BI field.

The cosmological limits on axion properties have been recently reassessed in light of the 5-year WMAP data (Visinelli and Gondolo, 2009; Hamann et al., 2009). Here we will do the same for the BI-axion. Axions can be produced in the early Universe through two distinct mechanisms (thermal production is excluded by astrophysical constraints), namely coherent production due to the initial misalignment of the axion field, and the decay of axionic strings. The latter is relevant only if the symmetry breaking happens after the end of inflation, then, here, we will be only concerned with the misalignment production. The basic idea is that, when the axion field is created, the initial value θ_i of the misalignment angle θ is displaced from zero, since no preferred value of θ exists. Since the axion field is created during inflation, our present Hubble volume corresponds to a small patch at the time of creation, where the value of θ_i can be assumed to be spatially constant.

In a flat FRW Universe, the zero mode of the dynamical field $\theta(x)$ evolves according to:

$$\ddot{\theta} + 3H\dot{\theta} + \frac{1}{f_{\tilde{\beta}}^2}\frac{\partial V(\theta)}{\partial \theta} = 0, \tag{E.2.7}$$

where a dot denotes the derivative with respect to cosmological time, H is the Hubble parameter, and the potential $V(\theta) = m_{\tilde{\beta}}^2(T) f_{\tilde{\beta}}^2 (1 - \cos\theta)$ [7]. It is clear from Eq. (E.2.6) that in the high temperature limit $T \gg \Lambda$ the BI-axion is effectively massless. Then $V(\theta) = 0$ and $\theta = \text{const}$ is a solution of the equation of motion and the misalignment field is frozen to its initial value, θ_i, until the mass becomes comparable to the expansion rate of the Universe, i.e. $H \sim T$, and the field starts oscillating around $\theta = 0$. For the value of the mass considered here, this happens at $T \simeq 52\,\text{MeV}$. We have numerically integrated the Klein-Gordon Eq. (E.2.7) down to a temperature well below the onset of oscillations and used entropy conservation to obtain the present number density. In the limit of small θ_i, this procedure yieds:

$$n_{\tilde{\beta}}(T_0) \simeq 2.8 \times 10^{22} \theta_i^2 \frac{\text{axions}}{\text{cm}^3}, \tag{E.2.8}$$

corresponding to an energy density $\rho_{\tilde{\beta}}(T_0) \simeq 85\,\theta_i^2 \text{GeV/cm}^3$. What is remarkable about this result is that, since the energy scale at which the symmetry breaking occurs is fixed by the theory, the present day energy density of the BI-axion depends only on the initial misalignment angle. Given that the present critical density of the Universe is $\rho_c \sim 10^{-5}\text{GeV/cm}^3$, the above formula points to the necessity of having $\theta_i \ll 1$. In particular, we know from the recent measurements of the WMAP satellite (Komatsu et al., 2009) that the present dark matter density is $\Omega_{\text{dm}} h^2 = 0.1131 \pm 0.0034$ at 68% CL, where

[7] According to the standard Literature (Gross et al., 1981; Turner, 1986), the form of the potential is motivated by the expected periodicity in the misalignment angle, once the gravitational instantons, depressed by the symmetries, have been neglected.

$\Omega_{\rm dm} \equiv \rho_{\rm dm}/\rho_c$ is the density in units of the critical density, and h is the Hubble parameter in units of 100 km sec^{-1} Mpc^{-1}. Then assuming that BI-axions make up all the dark matter ($\Omega_{\tilde{\beta}} = \Omega_{\rm dm}$) the initial misalignment angle has to be very small: $\theta_i \simeq 1.2 \times 10^{-4}$. Larger values of the initial misalignment angle lead to a present axion density too large with respect to the WMAP value, so, in general, one should require that $\theta_i \leq 1.2 \times 10^{-4}$. The axion density would be diluted, and then the limits on θ_i relaxed, in the presence of a significant entropy production at a temperature below the QCD scale. This could be the case if the reheating temperature $T_{RH} < \Lambda$ (Giudice et al., 2001).

Let us also examine the possibility that inflation never occurred [8]. In this case, the initial misalignment angle would be a function of the spatial coordinates and should be replaced with its average over $[-\pi, \pi]$, i.e. $\langle \theta_i^2 \rangle = \pi^2/3$. Consequently, the present axion energy density would be completely fixed, leading to a density parameter $\Omega_{\tilde{\beta}} h^2 \sim 10^8$, clearly overshooting the observed value by 9 orders of magnitude [9].

Another prediction of the model examined here is the production of axion isocurvature perturbations. As it happens for the inflaton field, de Sitter-induced quantum fluctuations in the BI-axion field are generated during inflation. The corresponding energy density fluctuations have an amplitude proportional to $H_I/(\theta_i f_{\tilde{\beta}})$ and are completely uncorrellated to those in the other components (radiation and matter) since axions were not in thermal equilibrium with photons during inflation. Moreover, since axions made a negligible contribution to the energy budget of the Universe at that time, the fluctuations in their energy density did not produce a corresponding perturbation in the curvature, hence the name "isocurvature". The amplitude of primordial isocurvature perturbations can be constrained by observations of the CMB anisotropies; in fact, an analysis of the WMAP data yields the constraint $H_I/\theta_i < 4.3 \times 10^{-5} f_{\tilde{\beta}} = 8.25 \times 10^{13}$GeV (Visinelli and Gondolo, 2009; Hamann et al., 2009). This bound can be combined with the constrain $\theta_i < 1.2 \times 10^{-4}$ to obtain the allowed region in the (H_I, θ_i) parameter space as shown in Fig. E.5. In particular, the two constraints together imply $H_I \lesssim 10^{10}$GeV. This low value leads to an interesting prediction of the model. Since the amount of gravitational waves (corresponding to tensor perturbation modes) produced during inflation is also proportional to H_I, the model yields an upper bound to the amplitude of tensor modes. In particular, in terms of the tensor-to-scalar ratio r, we get the very tight upper bound $r < 1.4 \times 10^{-9}$. This means that a detection of even a very small amount of primordial gravitational waves by one of the upcoming CMB experiments would rule out the model proposed here. This would be the case, in particu-

[8] Although this is unlikely, it cannot be ruled out since other possible scenarios can avoid the shortcomings of the standard model and generate the primordial fluctuations.

[9] One should take into account the axion production via the decay of axionic strings as well, but this would only make our point stronger.

lar, if tensor modes are detected by Planck, since it is expected to be sensitive to $r \gtrsim 0.05$.

Finally, let us briefly discuss the astrophysical constraints on the BI-axion. In the case of the standard axion, the astrophysical constraints mainly depend on the strength of its interaction with ordinary matter, since this controls the rate at which the nuclear energy generated in the core of a star is carried away in the form of axions, thus modifying the standard stellar evolution. In order to evade these constraints, the axion couplings have to be either small enough so that few axions are produced as a by-product of the nuclear reactions, or large enough in order to keep the mean free path of axions well inside the radius of the star. However, the computation of the couplings of the axion is completely general, so that the standard results also hold for the BI-axion. In particular, one has that the couplings are inversely proportional to $f_{\tilde{\beta}}$, so that we can expect them to be extremely small [10]. In fact, this implies that the BI-axion is, as long as astrophysical limits are concerned, roughly equivalent to a DFSZ axion with a mass $m_a \simeq 3 \times 10^{-12}$eV. The most stringent astrophysical upper limit on the axion mass comes from the observations of SN 1987A and states that $m_a \lesssim 10^{-3}$eV (or, equivalently, $f_a \gtrsim 6 \times 10^9$GeV). Thus we conclude that astrophysical observations cannot rule out the existence of a BI-axion.

[10] A remarkable difference with respect to the PQ model lies is the fact that while, on the one hand, the $U(1)_{PQ}$ charges of the SM particles are not given by the theory, and thus have to experimentally measured, on the other hand the Nieh-Yan "charges" $X_i^{(NY)}$ associated to the $U(1)_A$ symmetry of our model can be calculated exactly from the theory. In particular, as it can be inferred from the effective action (E.2.4), the charges of the fundamental fermionic fields (leptons and quarks) all turn out to be equal to unity. This universality is a direct consequence of the geometrical nature of the interaction. We would also like to remark that this completely fixes the BI-axion couplings g_{aii}, since these depend, other than from the X_i's and from known quantities, only on the BI-axion mass.

Figure E.4.: One- and two- dimensional posterior distributions for the parameters of the model, using the CMB data. In the 1D plots, the solid line is the marginalized posterior while the dotted line is the mean likelihood. In the 2D plots, the lines bound the 68% and 95% confidence regions; the gray shading indicates regions of high (dark) and low (light) mean likelihood. See the text for a discussion.

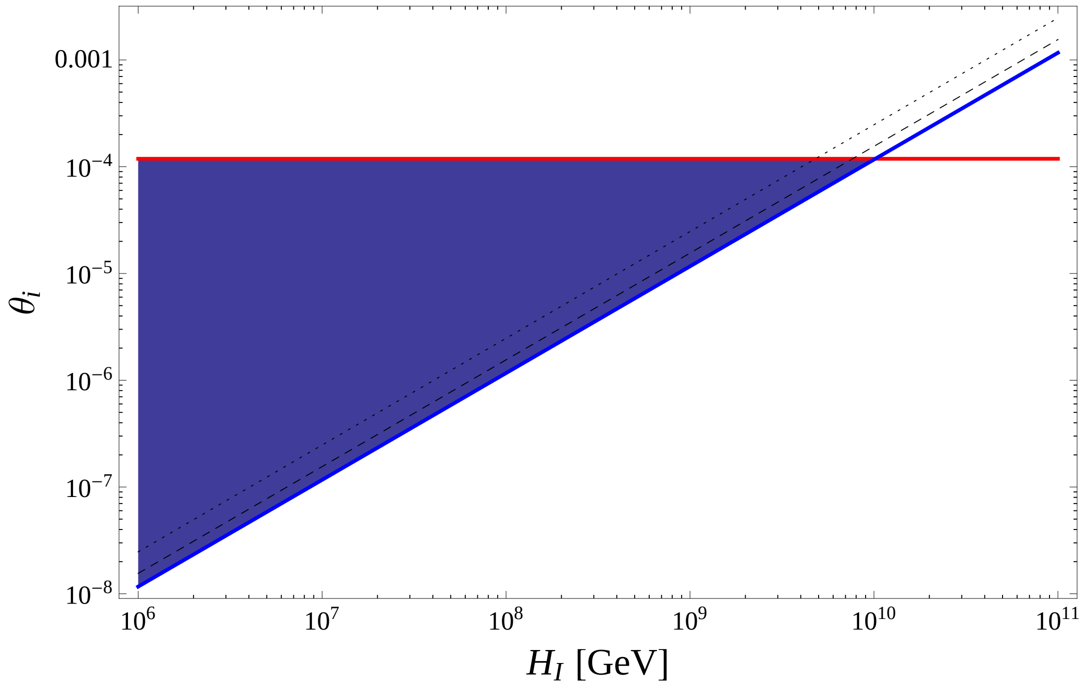

Figure E.5.: Constraints for the BI-axion in the (H_I, θ_i) plane. The horizontal line corresponds to the BI-axion making all the dark matter in the Universe (namely $\theta_i \simeq 1.2 \times 10^{-4}$). The diagonal line comes from the constraints on the isocurvature fluctuations ($H_I/\theta_i < 8.25 \times 10^{13}$GeV). The shaded area shows the allowed parameter region. The dashed and dotted diagonal lines corresponds to the expected improvement of the bound on isocurvature fluctuations from the measurements of the Planck satellite and from an ideal, cosmic variance limited CMB experiment, respectively [see Visinelli and Gondolo (2009); Hamann et al. (2009) for details].

F. Indirect Detection of Dark Matter

F.1. Boosting the WIMP annihilation through the Sommerfeld enhancement

The motivation for studying dark matter annihilation signatures (see e.g. (Bertone et al., 2005)) has received considerable recent attention following reports of a 100 GeV excess in the PAMELA data on the ratio of the fluxes of cosmic ray positrons to electrons (Adriani et al., 2009). In the absence of any compelling astrophysical explanation, the signature is reminiscent of the original prediction of a unique dark matter annihilation signal (Silk and Srednicki, 1984), although there are several problems that demand attention before any definitive statements can be made. By far the most serious of these is the required annihilation boost factor. The remaining difficulties with a dark matter interpretation, including most notably the gamma ray signals from the Galactic Centre and the inferred leptonic branching ratio, are, as we argue below, plausibly circumvented or at least alleviated. Recent data from the ATIC balloon experiment provides evidence for a cut-off in the positron flux near 500 GeV that supports a Kaluza-Klein-like candidate for the annihilating particle (Chang et al., 2008) or a neutralino with incorporation of suitable radiative corrections (Bergstrom et al., 2008).

In a pioneering paper, it was noted (Profumo, 2005) that the annihilation signal can be boosted by a combination of coannihilations and Sommerfeld corrrection. We remark first that the inclusion of coannihilations to boost the annihilation cross-section modifies the relic density, and opens the 1-10 TeV neutralino mass window to the observed (WMAP5-normalised) dark matter density. As found by Lavalle et al. (2008), the outstanding problem now becomes that of normalisation. A boost factor of around 100 is required to explain the HEAT data in the context of a 100 GeV neutralino. The flux is suppressed by between one and two powers of neutralino mass, and the problem becomes far more severe with the 1-10 TeV neutralino required by the PAMELA/ATIC data (Cirelli et al., 2009b), a boost of 10^4 or more being required. These latter authors included a Sommerfeld correction appropriate to our $\beta \equiv v/c = 0.001$ dark halo and incorporated channel-dependent boost factors to fit the data, but the required boosts still fell short of plausible values by at least an order of magnitude.

Here we propose a solution to the boost problem via Sommerfeld correction in the presence of a model of substructure that incorporates a plausible phase space structure for cold dark matter (CDM). We reassess the difficulty with the leptonic branching ratio and show that it is not insurmountable for supersymmetric candidates. Finally, we evaluate the possibility of independent confirmation via photon channels.

Substructure survival means that as much as 10% of the dark matter is at much lower β. This is likely in the solar neighbourhood and beyond, but not in the inner galaxy where clump destruction is prevalent due to tidal interactions. Possible annihilation signatures from the innermost galaxy such as the WMAP haze of synchrotron emission and the EGRET flux of diffuse gamma rays are likely to be much less affected by clumpy substructure than the positron flux in the solar neighbourhood. We show in the following section that incorporation of the Sommerfeld correction means that clumps dominate the annihilation signal, to the extent that the initial clumpiness of the dark halo survives.

F.1.1. The Sommerfeld enhancement

Dark matter annihilation cross sections in the low-velocity regime can be enhanced through the so-called "Sommerfeld effect" (Sommerfeld, 1931; Hisano et al., 2004, 2005; Cirelli et al., 2007; March-Russell et al., 2008; Arkani-Hamed et al., 2009; Pospelov and Ritz, 2009). This non-relativistic quantum effect arises because, when the particles interact through some kind of force, their wave function is distorted by the presence of a potential if their kinetic energy is low enough. In the language of quantum field theory, this correspond to the contribution of "ladder" Feynman diagrams like the one shown in Fig. F.1 in which the force carrier is exchanged many times before the annihilation finally occurs. This gives rise to (non-perturbative) corrections to the cross section for the process under consideration. The actual annihilation cross section times velocity will then be:

$$\sigma v = S\,(\sigma v)_0 \tag{F.1.1}$$

where $(\sigma v)_0$ is the tree level cross section times velocity, and in the following we will refer to the factor S as the "Sommerfeld boost" or "Sommerfeld enhancement" [1].

In this section we will study this process in a semi-quantitative way using a simple case, namely that of a particle interacting through a Yukawa potential. We consider a dark matter particle of mass m. Let $\psi(r)$ be the reduced two-body wave function for the s-wave annihilation; in the non-relativistic limit,

[1] In the case of repulsive forces, the Sommerfeld "enhancement" can actually be $S < 1$, although we will not consider this possibility here.

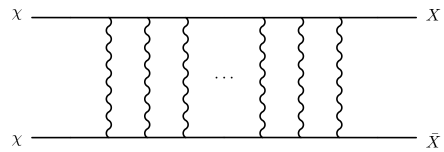

Figure F.1.: Ladder diagram giving rise to the Sommerfeld enhancement for $\chi\chi \to X\bar{X}$ annihilation, via the exchange of gauge bosons.

it will obey the radial Schrödinger equation:

$$\frac{1}{m}\frac{d^2\psi(r)}{dr^2} - V(r)\psi(r) = -m\beta^2\psi(r), \tag{F.1.2}$$

where β is the velocity of the particle and $V(r) = -\frac{\alpha}{r}e^{-m_\mathrm{V}r}$ is an attractive Yukawa potential mediated by a boson of mass m_V.

The Sommerfeld enhancement S can be calculated by solving the Schrödinger equation with the boundary condition $d\psi/dr = im\beta\psi$ as $r \to \infty$. Eq. (F.1.2) can be easily solved numerically. It is however useful to consider some particular limits in order to gain some qualitative insight into the dependence of the Sommerfeld enhancement on particle mass and velocity. First of all, we note that for $m_\mathrm{V} \to 0$, the potential becomes Coulomb-like. In this case the Schrödinger equation can be solved analytically; the resulting Sommerfeld enhancement is:

$$S = \frac{\pi\alpha}{\beta}(1 - e^{-\pi\alpha/\beta})^{-1}. \tag{F.1.3}$$

For very small velocities ($\beta \to 0$), the boost $S \simeq \pi\alpha/\beta$: this is why the Sommerfeld enhancement is often referred as a $1/v$ enhancement. On the other hand, $S \to 1$ when $\alpha/\beta \to 0$, as one would expect.

It should however be noted that the $1/v$ behaviour breaks down at very small velocities. The reason is that the condition for neglecting the Yukawa part of the potential is that the kinetic energy of the collision should be much larger than the boson mass m_V times the coupling constant α, i.e., $m\beta^2 \gg \alpha m_\mathrm{V}$, and this condition will not be fulfilled for very small values of β. This is also evident if we expand the potential in powers of $x = m_\mathrm{V}r$; then, neglecting terms of order x^2 or smaller, the Schrödinger equation can be written as (the prime denotes the derivative with respect to x):

$$\psi'' + \frac{\alpha}{\varepsilon}\frac{\psi}{x} = \left(-\frac{\beta^2}{\varepsilon^2} + \frac{\alpha}{\varepsilon}\right)\psi, \tag{F.1.4}$$

having defined $\varepsilon = m_\mathrm{V}/m$. The Coulomb case is recovered for $\beta^2 \gg \alpha\varepsilon$, or exactly the condition on the kinetic energy stated above. It is useful to define $\beta^* \equiv \sqrt{\alpha m_\mathrm{V}/m}$ such that $\beta \gg \beta^*$ is the velocity regime where the Coulomb approximation for the potential is valid.

Another simple, classical interpretation of this result is the following. The range of the Yukawa interaction is given by $R \simeq m_V^{-1}$. Then the crossing time scale is given by $t_{cross} \simeq R/v \simeq 1/\beta m_V$. On the other hand, the dynamical time scale associated to the potential is $t_{dyn} \simeq \sqrt{R^3 m/\alpha} \simeq \sqrt{m/\alpha m_V^3}$. Then the condition $\beta \gg \beta^*$ is equivalent to $t_{cross} \ll t_{dyn}$, i.e., the crossing time should be much smaller than the dynamical time-scale. Finally, we note that since in the Coulomb case $S \sim 1/\beta$ for $\alpha \gg \beta$, the region where the Sommerfeld enhancement actually has a $1/v$ behaviour is $\beta^* \ll \beta \ll \alpha$. It is interesting to notice that this region does not exist at all when $m \lesssim m_V/\alpha$.

The other interesting regime to examine is $\beta \ll \beta^*$. Following the discussion above, this corresponds to the potential energy dominating over the kinetic term. Referring again to the form (F.1.4) for $x \ll 1$ of the Schrödinger equation, this becomes:

$$\psi'' + \frac{\alpha}{\varepsilon}\frac{\psi}{x} = \frac{\alpha}{\varepsilon}\psi. \tag{F.1.5}$$

The positiveness of the right-hand side of the equation points to the existence of bound states. In fact, this equation has the same form as the one describing the hydrogen atom. Then bound states exist when $\sqrt{\alpha/\varepsilon}$ is an even integer, i.e. when:

$$m = 4 m_V n^2/\alpha, \qquad n = 1, 2, \ldots \tag{F.1.6}$$

From this result, we expect that the Sommerfeld enhancement will exhibit a series of resonances for specific values of the particle mass spaced in a 1 : 4 : 9 : ... fashion. The behaviour of the cross section close to the resonances can be better understood by approximating the electroweak potential by a well potential, for example: $V(r) = -\alpha m_V \theta(R - r)$, where $R = m_V^{-1}$ is the range of the Yukawa interaction, and the normalization is chosen so that the well potential roughly matches the original Yukawa potential at $r = R$. The external solution satisfying the boundary conditions at infinity is simply an incoming plane wave, $\psi_{out}(r) \propto e^{ik_{out}r}$, with $k_{out} = m\beta$. The internal solution is: $\psi_{in}(r) = Ae^{ik_{in}r} + Be^{-ik_{in}r}$, where $k_{in} = \sqrt{k_{out}^2 + \alpha m m_V} \simeq \sqrt{\alpha m m_V}$ (the last approximate equality holds because $\beta \ll \beta^*$). The coefficients A and B are as usual obtained by matching the wave function and its first derivative at $r = R$; then the enhancement is found to be:

$$S = \left[\cos^2 k_{in}R + \frac{k_{out}^2}{k_{in}^2}\sin^2 k_{in}R\right]^{-1}. \tag{F.1.7}$$

When $\cos k_{in}R = 0$, i.e., when $\sqrt{\alpha m/m_V} = (2n+1)\pi/2$, the enhancement assumes the value $k_{in}^2/k_{out}^2 \simeq \beta^{*2}/\beta^2 \gg 1$. This is however cut off by the finite width of the state.

In summary, the qualitative features that we expect to observe are

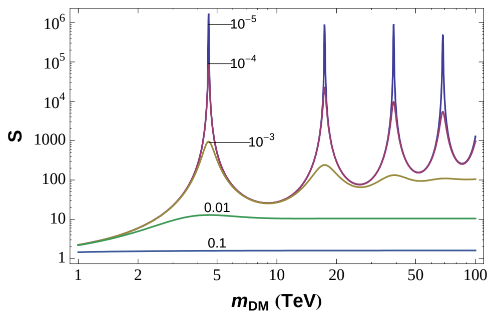

Figure F.2.: Sommerfeld enhancement S as a function of the dark matter particle mass m, for different values of the particle velocity. Going from bottom to top $\beta = 10^{-1}$, 10^{-2}, 10^{-3}, 10^{-4}, 10^{-5}.

i) at large velocities ($\beta \gg \alpha$) there is no enhancement, $S \simeq 1$;
ii) in the intermediate range $\beta^* \ll \beta \ll \alpha$, the enhancement goes like $1/v$: $S \simeq \pi\alpha/\beta$, this value being independent of the particle mass;
iii) at small velocities ($\beta \ll \beta^*$), a series of resonances appear, due to the presence of bound states. Close to the resonances, $S \simeq (\beta^*/\beta)^2$. In this regime, the enhancement strongly depends on the particle mass, because it is this that determines whether we are close to a resonance or not. Similar results have been independently obtained in Ref. (March-Russell and West, 2009).

We show the result of the numerical integration of Eq. (F.1.2) in Figure F.2, where we plot the enhancement S as a function of the particle mass m, for different values of β. We choose specific values of the boson mass $m_V =$ 90 GeV and of the gauge coupling $\alpha = \alpha_2 \simeq 1/30$. These values correspond to a particle interacting through the exchange of a Z boson.

We note however that, as can be seen by the form of the equation, the enhancement depends on the boson mass only through the combination $\varepsilon = m_V/m$, so that a different boson mass would be equivalent to rescaling the abscissa in the plot. Moreover, the evolution of the wave function only depends on the two quantities α/ε and β/ε, so that a change $\alpha \to \alpha'$ in the gauge coupling would be equivalent to: $\beta \to \beta' = \frac{\alpha'}{\alpha}\beta$, $\varepsilon \to \varepsilon' = \frac{\alpha'}{\alpha}\varepsilon$. This shows that Fig. F.2 does indeed contain all the relevant information on the behaviour of the enhancement S.

We see that the results of the numerical evaluation agree with our qualitative analysis above. When $\beta = 10^{-1}$ (bottom curve), we are in the $\beta > \alpha \simeq 3 \times 10^{-2}$ regime and there is basically no enhancement. The next curve $\beta = 10^{-2}$ is representative of the $\beta \gtrsim \beta^*$ regime, at least for m larger than a few TeV. The enhancement is constant with the particle mass and its value agrees well with the expected value $\pi\alpha/\beta \simeq 10$. The drop of the enhancement in the mass region below ~ 3 TeV is due to the fact that here $\beta \lesssim \beta^*$,

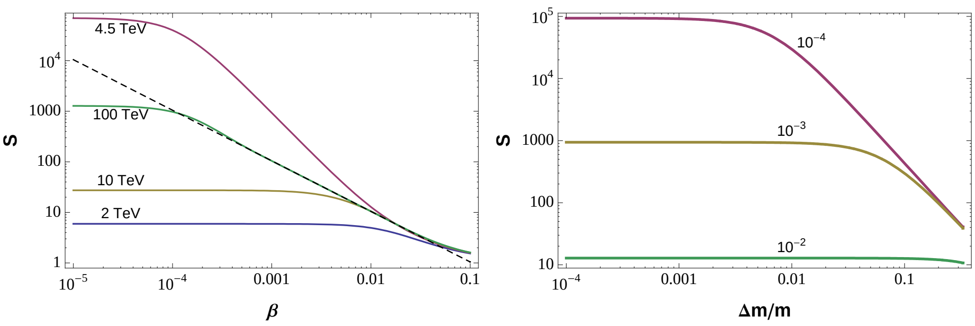

Figure F.3.: Top panel: Sommerfeld enhancement S as a function of the particle velocity β for different values of the dark matter mass. From bottom to top: $m = 2$, 10, 100, 4.5 TeV, the last value corresponding to the first resonance in Fig. F.2. The black dashed line shows the $1/v$ behaviour that is expected in the intermediate velocity range (see text for discussion). Bottom panel: Sommerefeld enhancement S as a function of the relative distance from the first resonance shown in Fig. F.2, occurring at $m \simeq 4.5\,\text{TeV}$, for different values of β. From top to bottom: $\beta = 10^{-4}$, 10^{-3}, 10^{-2}.

and that there are no resonances for this value of the mass. Decreasing β again (top three curves, corresponding to $\beta = 10^{-3}$, 10^{-4}, 10^{-5} from bottom to top) we observe the appearance of resonance peaks. The first peak occurs for $m = \bar{m} = 4.5\,\text{TeV}$, so that expression (F.1.6) based on the analogy with the hydrogen atom overestimates the peak position by a factor 2. However, the spacing between the peaks is as expected, going like n^2, as the next peaks occur roughly at $m = 4, 9, 16\,\bar{m}$. The height of the first peak agrees fairly well with its expected value of $(\beta^*/\beta)^2$. The other peaks are damped; this is particularly evident for $\beta = 10^{-3}$, and in this case it is due to the fact that β^* decreases as m increases, so that for $m \sim 100\,\text{TeV}$ we return to the non-resonant, $1/\beta$ behaviour, and the enhancement takes the constant value $\pi\alpha/\beta \simeq 100$.

Complementary information can be extracted from the analysis of the upper panel of Fig. F.3, where we plot the Sommerfeld enhancement as a function of β, for different values of the particle mass. Far from the resonances, the enhancement factor initially grows as $1/\beta$ and then saturates to some constant value. This constant value can be estimated by solving the Schrödinger equation with $\beta = 0$. We find that a reasonable order of magnitude estimate is given by $S_{max} \sim 6\alpha/\varepsilon$; the corresponding value of $\beta \sim 0.5\varepsilon$. The $1/\beta$ behaviour holds down to smaller velocities for larger particle masses, leading to larger enhancement factors. However, when the particle mass is close to a resonance, S initially grows like $1/\beta$ but at some point the $1/\beta^2$ behaviour "turns on", leading to very large values of the boost factor, until this also saturates to some constant value.

It is clear from the discussion until this point that the best hope for obtaining a large enhancement comes from the possibility of the dark matter mass lying close to a resonance; for the choice of parameter used above this would mean $m \simeq \bar{m} \simeq 4.5\,\text{TeV}$. However, one could be interested in knowing how close the mass should be to the center of the resonance in order to obtain a sizeable boost in the cross-section. In order to understand this, we show in Fig. F.3 the enhancement as a function of $\mu \equiv |m - \bar{m}|/m$, i.e., of the fractional shift from the center of the resonance. Clearly, for $\beta \leq 10^{-3}$, a boost factor of $\gtrsim 100$ can be obtained for $\mu \lesssim 0.2$, i.e., for deviations of up to 20% from $\bar{m}$, corresponding to the range between 3.5 and 5.5 TeV. This is further reduced to the 4 to 5 TeV range if one requires $S \gtrsim 10^3$.

F.1.2. The leptonic branching ratio

The relevance of the Sommerfeld enhancement for the annihilation of supersymmetric particles was first pointed out in Refs (Hisano et al., 2004, 2005), in the context of the minimal supersymmetric standard model where the neutralino is the lightest supersymmetric particle. A wino-like or higgsino-like neutralino would interact with the W and Z gauge bosons due to its $SU(2)_L$ nonsinglet nature. In particular, the wino $\tilde{W}^0$ is the neutral component of a $SU(2)_L$ triplet , while the higgsinos $(\tilde{H}_1^0, \tilde{H}_2^0)$ are the neutral components of two $SU(2)_L$ doublets. The mass (quasi-) degeneracy between the neutralino and the other components of the multiplet leads to transitions between them, mediated by the exchange of weak gauge bosons; this gives rise to a Sommerfeld enhancement at small velocities. On the other hand, the bino-like neutralino being a SU(2) singlet, would not experience any Sommerfeld enhancement, unless a mass degeneracy with some other particle is introduced into the model.

The formalism needed to compute the enhancement when mixing among states is present is slightly more complicated than the one described above, but the general strategy is the same. As shown in the paper by Hisano et al. (Hisano et al., 2005) through direct numerical integration of the Schrödinger equation, the qualitative results of the previous section still hold: for dark matter masses $\gtrsim 1\,\text{TeV}$, a series of resonances appear, and the annihilation cross section can be boosted by several order of magnitude.

An interesting feature of this "multi-state" Sommerfeld effect is the possibility of boosting the cross section for some annihilation channels more than others. This happens when one particular annihilation channel is very suppressed (or even forbidden) for a given two-particle initial state, but not for other initial states. This can be seen as follows. The general form for the total annihilation cross section after the enhancement has been taken into account is

$$\sigma v = N \sum_{ij} \Gamma_{ij} d_i(v) d_j^*(v), \tag{F.1.8}$$

where N is a multiplicity factor, Γ_{ij} is the absorptive part of the action, responsible for the annihilation, the d_i are coefficients describing the Sommerfeld enhancement, and the indices i, j run over the possible initial two-particle states. Let us consider for definiteness the case of the wino-like neutralino: the possible initial states are $\{\chi^0\chi^0, \chi^+\chi^-\}$. The neutralino and the chargino are assumed to be quasi-degenerate, since they are all members of the same triplet. What we will say can anyway be easily generalized to the case of the higgsino-like neutralino. Let us also focus on two particular annihilation channels: the W^+W^- channel and the e^+e^- channel. It can be assumed that, close to a resonance, $d_1 \sim d_2$. This can be inferred for example using the square well approximation as in Ref. (Hisano et al., 2005), where it is found that, in the limit of small velocity, $d_1 \simeq \sqrt{2}(\cos\sqrt{2}p_c)^{-1} - \sqrt{2}(\cosh p_c)^{-1}$ and $d_2 \simeq (\cos\sqrt{2}p_c)^{-1} + 2(\cosh p_c)^{-1}$, where $p_c \equiv \sqrt{2\alpha_2 m/m_W}$. The elements of the Γ matrix for the annihilation into a pair of W bosons are $\sim \alpha_2^2/m_\chi^2$, so that we can write the following order of magnitude estimate:

$$\sigma v(\chi^0\chi^0 \to W^+W^-) \sim |d_1|^2 \frac{\alpha_2^2}{m_\chi^2}. \tag{F.1.9}$$

On the other hand, the non-enhanced neutralino annihilation cross section to an electron-positron pair $\Gamma_{22} \sim \alpha_2^2 m_e^2/m_\chi^4$, so that it is suppressed by a factor $(m_e/m_\chi)^2$ with respect to the gauge boson channel. This is a well-known general feature of neutralino annihilations to fermion pairs and is due to the Majorana nature of the neutralino. The result is that all low velocity neutralino annihilation diagrams to fermion pairs have amplitudes proportional to the final state fermion mass. The chargino annihilation cross section to fermions, however, does not suffer from such an helicity suppression, so that it is again $\Gamma_{11} \sim \alpha_2^2/m_\chi^2 \gg \Gamma_{22}$. Then:

$$\sigma v(\chi^0\chi^0 \to e^+e^-) \sim |d_1|^2 \frac{\alpha_2^2}{m_\chi^2}. \tag{F.1.10}$$

Then we have that, after the Sommerfeld correction, the neutralino annihilates to W bosons and to e^+e^- pairs (and indeed to all fermion pairs) with similar rates, apart from $O(1)$ factors. This means that while the W channel is enhanced by a factor $|d_1|^2$, the electron channel is enhanced by a factor $|d_1|^2 m_\chi^2/m_e^2$. The reason is that the annihilation can proceed through a ladder diagram like the one shown in Fig. F.4, in which basically the electron-positron pair is produced by annihilation of a chargino pair close to an on-shell state. This mechanism can be similarly extended to annihilations to other charged leptons, neutrinos or quarks.

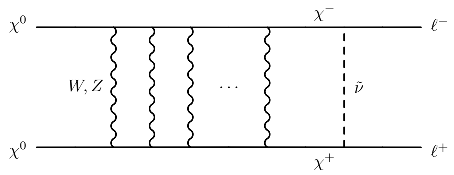

Figure F.4.: Diagram describing the annihilation of two neutralinos into a charged lepton pair, circumventing helicity suppression.

F.1.3. CDM substructure: enhancing the Sommerfeld boost

There is a vast reservoir of clumps in the outer halo where they spend most of their time. Clumps should survive perigalacticon passage over a fraction (say ν) of an orbital time-scale, $t_d = r/v_r$, where v_r is the orbital velocity (given by $v_r^2 = GM/r$). It is reasonable to assume that the survival probability is a function of the ratio between t_d and the age of the halo t_H, and that it vanishes for $t_d \to 0$. Thus, at linear order in the (small) ratio t_d/t_H, a first guess at the clump mass fraction as a function of galactic radius would be $f_{clump} \propto t_d$. We conservatively adopt the clump mass fraction $\mu_{cl} = \nu r v_r^{-1} t_H^{-1}$ with $\nu = 0.1 - 1$. This gives a crude but adequate fit to the highest resolution simulations, which find that the outermost halo has a high clump survival fraction, but that near the sun only 0.1-1 % survive (Springel et al., 2008b). In the innermost galaxy, essentially all clumps are destroyed.

Suppose the clump survival fraction $S(r) \propto f_{clump} \propto r^{3/2}$ to zeroth order. The annihilation flux is proportional to $\rho^2 \times$ Volume $\times\, S(r) \propto S(r)/r$. This suggests we should expect to find an appreciable gamma ray flux from the outer galactic halo. It should be quasi-isotropic with a $\sim$10% offset from the centre of the distribution. The flux from the Galactic Centre would be superimposed on this. High resolution simulations demonstrate that clumps account for as much luminosity as the uniform halo (Diemand et al., 2008), (Springel et al., 2008a). However much of the soft lepton excess from the inner halo will be suppressed due to the clumpiness being much less in the inner galaxy.

We see from the numerical simulations of our halo, performed at a mass resolution of $1000\mathrm{M}_\odot$ that the subhalo contribution to the annihilation luminosity scales as $M_{min}^{-0.226}$ (Springel et al., 2008a). For $M_{min} = 10^5 M_\odot$, this roughly equates the contribution of the smooth halo at $r = 200$ kpc from the center. This should continue down to the minimum subhalo mass. We take the latter to be $10^{-6}\mathrm{M}_\odot$ clumps, corresponding the damping scale of a bino-like neutralino (Hofmann et al., 2001; Loeb and Zaldarriaga, 2005). We consider this as representative of the damping scale of neutralino dark matter, although it should be noted that the values of this cutoff for a general weakly interacting massive particle (WIMP) candidate can span several orders of magnitude, depending on the details of the underlying particle physics model (Profumo et al., 2006; Bringmann, 2009). It should also be taken into account that the substructure is a strong function of galactic radius. Since the dark matter density drops precipitously outside the solar circle (as r^{-2}), the clump contribution to boost is important in the solar neighbourhood. However absent any Sommerfeld boost, it amounts only to a factor of order unity. Incidentally the simulations show that most of the luminosity occurs in the outer parts of the halo (Springel et al., 2008a) and that the boost here due to substructure is large, typically a factor of 230 at r_{200}.

However there is another effect of clumpiness, namely low internal velocity dispersion. In fact, the preceding discussion greatly underestimates the clump contribution to the annihilation signal. This is because the coldest substructure survives clump destruction albeit on microscopic scales. Within the clumps, the velocity dispersion σ initially is low. Thus, the annihilation cross section is further enhanced by the Sommerfeld effect in the coldest surviving substructure. We now estimate that including this effect results in a Sommerfeld-enhanced clumpiness boost factor at the solar neighborhood of 10^4 to 10^5.

To infer σ from the mass M of the clump is straightforward. The scalings can be obtained by combining dynamically self-consistent solutions for the radial dependence of the phase space density in simulated CDM halos (Dehnen and McLaughlin, 2005) as well as directly from the simulations (Vass et al., 2009) $\rho/\sigma^{\epsilon} \propto r^{-\alpha}$, combined with our ansatz about clump survival that relates minimum clump mass to radius and the argument that marginally surviving clumps have density contrast of order unity. With $\epsilon = 3$ and $\alpha = 1.875$ (Navarro et al., 2008), we infer (for the isotropic case) that $\sigma \propto \rho^{1/\epsilon} r^{\alpha/\epsilon} \overset{\propto}{\sim} M^{1/4}$. This is a compromise between the two exact solutions for nonlinear clumps formed from hierarchical clustering of CDM: spherical ($M \propto r^3$) or Zeldovich pancakes ($M \propto r$), and is just the self-similar scaling limiting value. The numerical simulations of Springel et al. (2008b) suggest a scaling $M_{sub} \propto v_{max}^{3.5}$ down to the resolution limit of $\sim 10^3 \mathrm{M}_{\odot}$, somewhat steeper than self-similar scaling.

So one can combine this result with the previous scaling to compute the total boost, i.e., taking into account both the clumpiness and the Sommerfeld enhancement. We know from the analysis of Springel et al. (Springel et al., 2008a) that for a minimum halo mass of $10^{-6}\, M_{\odot}$ the luminosity of the subhalo component should more or less equate to that of the smooth halo at the galactocentric radius, i.e. $L^0_{sh} \simeq L^0_{sm}$ at $r = 8\,\mathrm{kpc}$, where the superscript 0 stands for the luminosity in the absence of any Sommerfeld correction. Thus the boost factor with respect to a smooth halo is of order unity, after the presence of subhalos is taken in consideration. Next we take into account the Sommerfeld enhancement. The velocity dispersion in the halo is $\beta \sim 10^{-3}$, while the velocity dispersion in the subhalos is $\beta \sim 10^{-5}$ for a $10^5\, M_{\odot}$ clump, and can be scaled down to smaller clumps using the $\sigma \overset{\propto}{\sim} M^{1/4}$ relation. From the discussion in sec. F.1.1 and in particular from Figs. F.2 and F.3 it appears that, if the dark matter mass is $\lesssim 10\,\mathrm{TeV}$ and far from the resonance occurring for $m \simeq 4.5\,\mathrm{TeV}$: (1) the Sommerfeld enhancement is the same for the halo and for the subhalos, since it has already reached the saturation regime; (2) it is of order 30 at most, so that the resulting boost factor still falls short by at least one order of magnitude with respect to the value needed to explain the PAMELA data. On the other hand, if the dark matter mass is close to its resonance value, then a larger value of the boost can be achieved inside the cold clumps, since (1) the enhancement is growing like $1/v^2$ and (2) it is saturating at a small value of β. Referring for definiteness to the top curve in the top panel of Fig. F.3 ($m = 4.5\,\mathrm{TeV}$), one finds $S \simeq 10^4 - 10^5$ for all clumps with mass $M \lesssim 10^9\,M_\odot$ (that is roughly the mass of the largest clumps) while the smooth halo is enhanced by a factor 1000. Then the net result is that the boost factor is of order $10^4 - 10^5$ and is mainly due to the Sommerfeld enhancement in the cold clumps (the enhancement in the diffuse halo only contributing a fraction 1-10%). Of course the details will be model dependent; it should also be stressed that the enhancement strongly depends on the value of the mass when this is close to the resonance.

F.1.4. Discussion

In the previous section we have shown how it is possible to get a boost factor of order $10^4 - 10^5$ for a dark matter particle mass of order 4.5 TeV. This is tantalizing because this is roughly the value one needs to explain the PAMELA data for a dark matter candidate with this given mass, as can be inferred by analysis of Fig. 9 of Ref (Cirelli et al., 2009b). Although we have made several approximations concerning the clump distribution and velocity, it should be noted that our results still hold as long as the majority of the clumps are very cold ($\beta \lesssim 10^{-4}$) because this is the regime in which the enhancement becomes constant. The saturation of the Sommerfeld effect also plays a crucial role in showing that the very coldest clumps are unable to contribute significantly to the required boost factor if the dark matter mass is not close to one of the Sommerfeld resonances. Because of saturation below $\beta \sim 10^{-4}$, the Sommerfeld boost is insensitive to extrapolations beyond the currently resolved scales in simulations. Note however that the precise value for the dark matter particle mass is uncertain because of such model-dependent assumptions as the adopted mass-splitting, the multiplet nature of the supersymmetric particles, and the possibility of different couplings, weaker than weak.

The model presented here does not pose any problem from the point of view of the high energy gamma-ray emission from the centre of the galaxy, since very few clumps are presents in the inner core and thus there is no Sommerfeld enhancement. Thus there is no possibility of violating the EGRET or HESS observations of the galactic center or ridge, contrary to what is argued in Ref. (Bertone et al., 2009). There is a potential problem however with gamma ray production beyond the solar radius out to the outer halo. From (Springel et al., 2008a), the simulations are seen to yield an additional enhancement due to clumpiness alone above $10^5 M_\odot$ of around 80% at r_{200} in the annihilation luminosity. Extrapolating to earth mass clumps, the enhancement is 230 in the annihilation luminosity at the same radius. This is what a distant observer would see. The incorporation of the Sommerfeld factor would greatly amplify this signal by $S \sim 10^4 - 10^5$.

The expected flux that would be observed by looking in a direction far from the galactic center can be readily estimated. Assuming an effective cross section $\sigma v = 3 \times 10^{-22}$ cm^3 s^{-1}, corresponding to a Sommerfeld boost of 10^4 on top of the canonical value of the cross section times velocity, the number of annihilations on the line of sight is roughly $4 \times 10^{-9} (m/\mathrm{TeV})^{-2}$ cm^{-2} s^{-1}. We have assumed a Navarro-Frenk-White (NFW) profile. The effect of the clumpiness is still not included in this estimate. Following the results of the simulation in Ref. (Springel et al., 2008a), this value should be multiplied by a factor ~ 200. Convolving with the single annihilation spectrum of a 5 TeV dark matter particle yields the flux shown in Fig. F.5. There we show the spectrum that would be produced if the dark matter particle would annihilate exclusively either to W bosons, b quarks or τ leptons (blue, red and green curves, respectively). We also consider a candidate that annihilates to τ leptons 90% of the time and to Ws the remaining 10% of the time (model "Hyb1") and a candidate that annihilates only to quarks and leptons, with the same cross section apart from color factors (model "Hyb2").

The gamma ray signal mostly originates from the outer halo and should be detectable as an almost isotropic hard gamma-ray background. Candidates annihilating to heavy quarks or to gauge bosons seem to be excluded by EGRET. On the other hand, a dark matter particle annihilating to τ leptons is compatible with the measurements of EGRET at these energies (Strong et al., 2004), and within the reach of FERMI.

There are however at least two reasons that induce significant uncertainty into any estimates. Firstly, the halo density profile in the outer galaxy may be substantially steeper than is inferred from an NFW profile, as current models are best fit by an Einasto profile (Gao, 2008), $\rho(r) \propto \exp[(-2/\alpha((r/r_s)^\alpha - 1)]$, as opposed to the asymptotic NFW profile $\rho(r) \propto r^{-3}$. Using the Einasto profile yields at least a 10% reduction. Another possibility is to use a Burkert profile (Burkert, 1996), that gives a better phenomenological description of the dark matter distribution inside the halo, as it is inferred by the rotation curves of galaxies (Gentile et al., 2004; Salucci et al., 2007). Using a Burkert profile, the flux is reduced by a factor 3. Secondly, and more importantly, the subhalos are much less concentrated at greater distances from the Galactic Centre (Diemand et al., 2007). These effects should substantially reduce the gamma ray contribution from the outer halo. A future application will be to evalu-

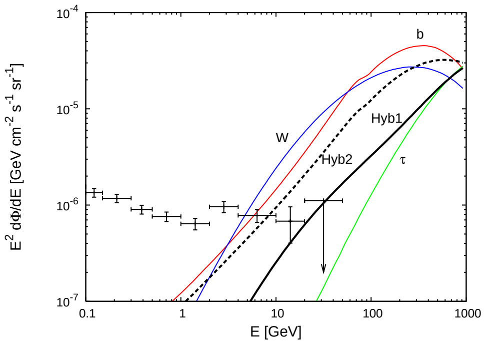

Figure F.5.: Contribution to the diffuse galactic photon background from the annihilation of a 5 TeV dark matter particle, for different channels, when both clumpiness and the Sommerfeld enhancement in cold clumps are taken into account, compared with the measurements of the diffuse gamma background from EGRET (Strong et al., 2004). The label "Hyb1" (solid black line) stands for a hybrid model in which the dark matter annihilates to τ leptons 90% of the time and to W pairs the rest of the time. The label "Hyb2" (dashed black line) stands for a model in which the dark matter annihilates to leptons and quarks only, with the same cross-section apart from color factors. The latter could be realized through the circumvention of helicity suppression.

ate the extragalactic diffuse gamma ray background where the evolution of clumpiness with redshift should play an interesting role in producing a possible spectral feature in the isotropic component. Note that the annihilation rate originating from very high redshift subhalo substructure and clumpiness near the neutralino free-streaming scale (Kamionkowski and Profumo, 2008) is mostly suppressed due to the saturation of the Sommerfeld effect that we described above.

Because of the saturation of the Sommerfeld boost, it should be possible to focus future simulations on improved modelling of the radial profiles and concentrations of substructures in the outer halo. It is these that contribute significantly to the expected diffuse gamma if our interpretation of the PAMELA and the ATIC data, and in particular the required normalisation and hence boost, is correct. Of course, there are other possible explanations of the high energy positron data, most notably the flux from a local pulsar (Aharonian et al., 1995; Yuksel et al., 2009; Hooper et al., 2009a) that has recently been detected as a TeV gamma ray source.

An interesting consequence of the model proposed here is the production of synchrotron radiation emitted by the electrons and positrons produced in the dark matter annihilations, similar to the one that is possibly the cause of the observed "WMAP haze" (Hooper et al., 2007; Cumberbatch et al., 2009). For a TeV candidate, this synchrotron emission would be visible in the $\nu \gtrsim$ 100 GHz frequency region. This region will be probed by the Planck mission; the synchrotron radiation would then give rise to a galactic foreground "Planck haze" in the microwave/far infrared part of the spectrum. This quasi-isotropic high frequency synchrotron component will be an additional source of B-mode foregrounds that will need to be incorporated into proposed attempts to disentangle any primordial B-mode component in the cosmic microwave background. Another interesting application would be to look at the gamma-ray emission from specific objects, like the Andromeda Galaxy (M31). M31 has been observed in the relevant energy range by the CELESTE and HEGRA atmospheric Cherenkov telescopes, and limits on the partial cross section to photons, in the absence of boost, were obtained by Mack et al. (2008).

Finally, we note that in Sec. F.1.2 we have described a mechanism that can enhance the production of leptons (especially light leptons) in neutralino dark matter annihilations, making the leptonic channel as important as the gauge boson channel. A dark matter candidate annihilating mainly into leptons can simultaneously fit the PAMELA positron and antiproton data, owing to the fact that no antiproton excess is produced. The enhancement of the lepton branching ratio can possibly alleviate the problem of antiproton production following neutralino annihilation into a pair of gauge bosons. It should however be noted that the mechanism in question also enhances the quark channel in a similar way, thus introducing an additional source of antiprotons. It would thus be desirable to suppress in some way the quark annihilation channel. This could be realised in a variation of the above mentioned mechanism, if the lightest neutralino is quasi-degenerate in mass with the lightest slepton $\tilde{l}$; this is what happens for example in the $\tilde{\tau}$ coannihilation region. In this case, the Sommerfeld enhancement would proceed through the creation of an intermediate $\tilde{l}^+\tilde{l}^-$ bound state that would subsequently annihilate to the corresponding standard model lepton pair, without producing any (tree-level) quark. This points to the necessity of further investigating different models in order to assess if the boost in the leptonic branching ratio is indeed compatible with the PAMELA data.

F.2. Constraining the dark matter annihilation cross-section with Cherenkov telescope observations of dwarf galaxies

F.2.1. Introduction

Detection of a rise in the high energy cosmic ray e^+ fraction by the PAMELA satellite experiment (Adriani et al., 2009) and of a possible peak in the $e^+ + e^-$ flux by the ATIC balloon experiment (Chang et al., 2008) has stimulated considerable recent theoretical activity in indirect detection signatures of particle dark matter via annihilations of the Lightest Supersymmetric Particle (LSP) and other massive particle candidates (Bergstrom et al., 2008; Cirelli and Strumia, 2008; Cholis et al., 2008; Liu et al., 2009b; Hooper et al., 2009b; Grajek et al., 2009; Donato et al., 2009; de Boer, 2009; Hooper and Zurek, 2009). Several hurdles must be surmounted if these signals are to be associated with dark matter annihilations. Firstly, a high boost factor $(10^3 - 10^4)$ is needed within a kiloparsec of the solar circle (Cirelli et al., 2008). Secondly, the boost factor must be suppressed in the inner galaxy to avoid excessive γ-ray and synchrotron radio emission (Bertone et al., 2009). Thirdly, the annihilation channels must be largely lepton–dominated to avoid $\bar{p}$ production (Cirelli et al., 2009b). Finally, account must be taken of the FERMI/HESS observations of electron/positron fluxes that do not reproduce part of the ATIC data (Abdo et al., 2009; Aharonian, 2009).

The third of these requirements is addressed in various particle physics models for the dark matter candidate (Cirelli et al., 2009b). Here we explore the implications of the first two requirements, and comment on the implications of the newest data on particle fluxes. The higher annihilation cross-section needed for the interpretation of the positron excess in terms of dark matter annihilations can be obtained via the Sommerfeld effect (Arkani-Hamed et al., 2009; Lattanzi and Silk, 2009). This effect occurs only at low relative velocities of the annihilating particles, and does not change the thermal cross-section required by cosmological measurements. Robertson and Zentner (2009) examined possible signatures of the Sommerfeld enhancement arising from the non-trivial dependence of the DM velocity distribution upon position within a DM halo. Here we consider the Sommerfeld enhancement in the substructures of our galaxy, where the velocity dispersion is as low as $10\,\mathrm{km\,s^{-1}}$ in the dwarf galaxies and becomes even lower for smaller subhalo masses. The boost, which is inversely proportional to the particle velocity, is especially relevant on the smallest scales that are unresolved by numerical simulations (Springel et al., 2008a). Throughout this paper, we will not consider the full velocity distribution function but will take the central values as a reference for computing the boost.

The second requirement can be understood because the unresolved substructures that dominate the local boost are likely to be tidally disrupted in the inner galaxy (Lattanzi and Silk, 2009). The predictions for signals coming from the Galactic Center (GC) are also reduced by adopting a shallower DM profile. We note that these effects also lower the local $\bar{p}$ contribution.

In this paper, we focus on the γ-ray signal coming from the Draco dwarf galaxy. We choose Draco because its DM density profile is determined in detail (Walker et al., 2009) and because it has been observed by the MAGIC Cherenkov Telescope (Albert et al., 2008). Our aim is to constraint the Sommerfeld enhancement through such a measurement. We will show how the constraints depend sensitively on the astrophysical uncertainties due to both numerical simulations and astronomical measurements. Moreover, we will show how the result is mainly dominated by the smooth DM halo of the dwarf galaxy, so that it is almost independent of the sub-substructure model used. We also derive exclusion plots for the effective annihilation cross-section obtained with the available measurements, as well as for the sensitivities achievable with future detectors. We apply our results to the case of the Sagittarius dwarf galaxy, which has also been observed with the HESS Cherenkov Telescope (Aharonian, 2008). This galaxy, much closer to us than Draco, would give a higher γ-ray flux and thus sets the greatest constraint. Unfortunately, the tidal stripping of Sagittarius because of its proximity to the GC makes it difficult to model the DM profile. In this paper we will assume that its mass profile can be modeled in the same way as Draco, by adopting the universality of mass profiles in the dwarf galaxies found in Walker et al. (2009). Since neither MAGIC nor HESS have observed any signal along the direction of the targets, we therefore set 95% CL upper limits on the γ-ray coming from these sources.

The paper is organized as follows: in Sec.F.2.2 we model the particle physics scenarios where the Sommerfeld enhancement is largest, as well as the astrophysical uncertainties in the determination of the γ-ray flux; in Sec.F.2.3 we derive the constraints on the effective cross-section set with the available Cherenkov Telescope measurements, and give exclusion plots achievable with the next generation of experiments that make use of Cherenkov Telescope technology, namely the proposed Cherenkov Telescope Array (CTA). We give our conclusions in Sec. F.2.4.

F.2.2. γ-ray flux from Dark Matter annihilation in Draco and Sagittarius

The observed photon flux from DM annihilations inside a halo can be factorized into two terms:

$$\frac{d\Phi_\gamma}{dE_\gamma}(M, E_\gamma, M_h, \mathbf{r}, d, \theta) = \frac{d\Phi_{PP}}{dE_\gamma}(M, E_\gamma) \times LOS(M_h, \mathbf{r}, d, \theta) \tag{F.2.1}$$

where M denotes DM particle mass, E_γ is photon energy, M_h halo mass, $\mathbf{r}$ the position inside the halo, d the distance from the observer and θ the angular resolution of the instrument ($\theta \sim 0.1^\circ$ for the Cherenkov Telescopes). The first term depends on the nature of the DM and describes the yields of photons in a single annihilation:

$$\frac{d\Phi_{PP}}{dE_\gamma}(M, E_\gamma) = \frac{1}{4\pi}\frac{(\sigma v)_0}{2M^2} \cdot \sum_f \frac{dN_\gamma^f}{dE_\gamma} B_f. \tag{F.2.2}$$

Here, dN_γ^f/dE_γ is the differential photon spectrum per annihilation relative to the final state f, which is produced with branching ratio B_f, and $(\sigma v)_0$ denotes the tree level s-wave annihilation cross section, which we assume to be equal to its thermal value necessary for reproducing the observed cosmological abundance today: $(\sigma v)_0 = 3 \times 10^{-26}\,\mathrm{cm}^3\,\mathrm{s}^{-1}$. The second term in Eq. F.2.1 is the line of sight integral of the DM density squared which describes the number of the annihilations which happen along the cone of view defined by the instrument:

$$LOS(M_h, \mathbf{r}, d, \theta) = \int\int_{\Delta\Omega} d\theta d\phi \int_{\mathrm{los}} d\lambda \left[\frac{\rho_{DM}^2(M_h, c, \mathbf{r}(\lambda, \psi, \theta, \phi))}{d^2} J(x, y, z|\lambda, \theta, \phi)\right] \tag{F.2.3}$$

Here, ρ_{DM} is the DM density profile inside the halo, c being the concentration parameter of the halo, defined as the ratio between virial radius and scale radius and computed following the prescriptions of Bullock et al. (2001); $\mathbf{r}$ is the galactocentric distance, which, inside the cone, can be written as a function of the line of sight λ, the angular coordinates θ and ϕ coordinates and the pointing angle with respect to the observed ψ through the relation $r = \sqrt{\lambda^2 + R_\odot{}^2 - 2\lambda R_\odot C}$, where $R_\odot$ is the distance of the Sun from the GC ($R_\odot = 8.5$kpc) and $C = \cos(\theta)\cos(\psi) - \cos(\phi)\sin(\theta)\sin(\psi)$; finally, inside the cone, $d = \lambda$ and $J(x, y, z|\lambda, \theta, \phi)$ is the Jacobian determinant from cartesian to polar coordinates. The presence of the Sommerfeld effect is reflected by setting $\sigma v = S(\beta(M_h, \mathbf{r}), M)(\sigma v)_0$. The Sommerfeld enhancement S now enters the line of sight integral of Eq. F.2.3.

The particle physics sector

The dark matter annihilation cross section can be enhanced, with respect to its primordial value, in the presence of the so-called Sommerfeld effect. This is a (non-relativistic) quantum effect occurring when the slow-moving annihilating particles interact through a potential (Sommerfeld, 1931). The idea that the gamma-ray flux from dark matter annihilations can be enhanced in this way was first proposed in a pioneering paper by Hisano et al. (2004) (see also Hisano et al., 2005). Recently, the possibility of explaining the large boost factor required by PAMELA using this mechanism has stimulated several studies of this effect (see for example Cirelli et al., 2007; March-Russell et al., 2008; Arkani-Hamed et al., 2009; Pospelov and Ritz, 2009; Lattanzi and Silk, 2009; March-Russell and West, 2009).

As already noticed, in the presence of the enhancement, the effective s-wave annihilation cross section times velocity can be written as:

$$\sigma v = S(\beta, M)\,(\sigma v)_0\,, \tag{F.2.4}$$

where $(\sigma v)_0$ is the tree level s-wave annihilation cross section, and the Sommerfeld enhancement S depends (for a given interaction potential) on the annihilating particle mass M and velocity $\beta = v/c$.

The enhancement is effective in the low-velocity regime, and disappears ($S = 1$) in the limit $\beta \to 1$. In general, one can distinguish two distinct behaviours, resonant and non-resonant, depending on the value of the annihilating particle mass. In the non-resonant case, the cross section grows like $1/\beta$ before saturation occurs at a certain value $S_{\max}$ of the enhancement. In the resonant case, occurring for particular values of M, the cross-section first grows like $1/\beta$ (as in the non-resonant case), then at some point it grows like $1/\beta^2$ before saturating. The Sommerfeld boost can reach very large values. Both in the resonant and non-resonant case, the values of β and S for which the saturation occurs depend, other than on the particle mass, on the parameters of the interaction potential, namely the coupling constant α and the mass of the exchange boson m_V.

In this paper, we will consider two different particle physics scenarios. In the first, we consider a weakly interacting massive particle (WIMP) dark matter candidate. In this case the Sommerfeld effect is caused by the standard model weak interaction, mediated by W and Z bosons, so that $m_V = 90$ GeV and $\alpha = 1/30$. If the dark matter is a Majorana particle, such as for example the supersymmetric neutralino, its annihilation into a fermionic final state f is helicity-suppressed by a factor $(m_f/M)^2$. For a dark matter particle in the 1 to 10 TeV range, this is a factor $10^{-2} \div 10^{-4}$ even for the heaviest possible final state, i.e. the top quark. Thus we are naturally led to consider a candidate that annihilates mainly to weak gauge bosons. However, for completeness we have also considered the heavy quark and lepton annihilation channels. The differential photon spectra per annihilation dN_γ^f/dE_γ for the various final states have been computed using PYTHIA (Sjostrand et al., 2001), including also the contribution from final state radiation.

We consider the following values for the mass of the particle: $M = (4.3, 4.45, 4.5, 4.55\,\mathrm{TeV})$. This values are chosen because, in the case of a weak interaction potential, a resonance in the Sommerfeld-enhanced cross section occurs for $M \simeq 4.5$TeV (Lattanzi and Silk, 2009). Being so close to the resonance, even a relatively small change in the mass of the particle can produce order of magnitude changes in the Sommerfeld boost. In fact, the maximum achievable boost goes from $S \simeq 1.5 \times 10^3$ for $M = 4.3$ TeV to $S \simeq 4 \times 10^5$ for $M = 4.55$ TeV.

The second scenario we consider has been introduced by Arkani-Hamed et al. (2009) [AH]. In this model, a new force with a coupling constant $\alpha \sim 10^{-2}$ is introduced in the dark sector, mediated by a boson ϕ having a mass $m_V =$

Mass (TeV)	m_V(GeV)	α	S_{max}	$\bar{\beta}$
4.3	80	1/30	1.5×10^3	8.0×10^{-4}
4.45	80	1/30	1.2×10^4	2.8×10^{-4}
4.5	80	1/30	7.0×10^4	1.1×10^{-4}
4.55	80	1/30	4.2×10^5	4.7×10^{-5}
0.7	1	10^{-2}	750	2.4×10^{-5}
0.7	0.1	10^{-2}	750	8.5×10^{-6}

Table F.1.: Values of the maximum possible boost S_{max} and of the saturation velocity $\bar{\beta}$, for different dark matter models. Each model is defined by the value of the dark matter particle mass M, and by the parameters of the Yukawa potential responsible for the enhancement, namely the mass m_V of the exchange boson and the coupling constant α.

$m_\phi \lesssim 1$ GeV. It is this new force that is responsible for the Sommerfeld enhancement. In this case, it is found that the large boosts required to explain the PAMELA and ATIC data can be obtained for a dark matter particle of mass $M \simeq 700$ GeV. In AH models, the dark matter annihilates mainly to ϕ bosons, that in turn decay into electrons or muons (depending on the mass of the ϕ). The gamma rays are produced in the decay of the ϕ as final state radiation (Bergstrom et al., 2009). We consider two particular realisations of this scenario: we take the dark matter mass to be $M = 700\,\text{GeV}$ in both, and m_ϕ equal to either 100 MeV or 1 GeV. We note that the dark matter interaction cross section in the first case is only one order of magnitude away from the upper bound coming from observations of the mass distribution inside clusters of galaxies (Miralda-Escudé, 2002).

The enhancement as a function of velocity in the models considered is depicted in Fig. F.6. The main properties of the enhancement, i.e. the maximum value S_{max} and the saturation velocity $\bar{\beta}$, are summarised in Table F.1 for the different models, together with the parameters of the interaction potential that is responsible for the Sommerfeld boost. We point out that, in the case of dwarf galaxies and their subhalos, the dispersion velocity is of the order of $10\,\text{km}\,\text{s}^{-1}$, which means that we are always in the saturation regime, and the enhancement is always maximum, and equal to S_{max}. As we show in the next sections, these large boost factors can be tested through Cherenkov telescope observations of dwarf galaxies.

The astrophysical sector: smooth dark matter halo

We discuss here the modeling of the dark matter inside the Draco dwarf galaxy. Walker et al. (2009) have recently demostrated the existence of a universal mass profile for the dwarf spheroidal galaxies of the Local Group, find-

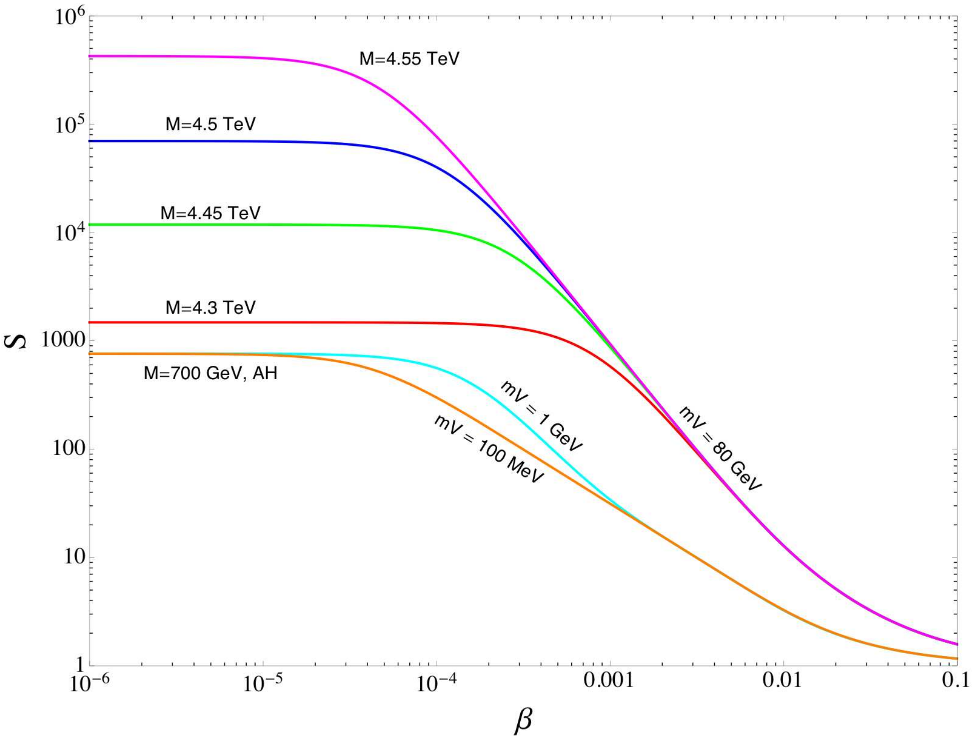

Figure F.6.: Sommerfeld enhancement S as a function of the particle velocity β for different values of the dark matter mass close to the resonance in our model with α= 1/30 and $m_V = 80$ GeV, as well as for a model with $\alpha = 10^{-2}$ and $m_V = 1$ GeV and 100 MeV (labeled AH).

ing that the enclosed mass at the half-light radius is well constrained and robust within a wide range of halo models and velocity anisotropies and that the dwarfs can be characterized by a "universal" dark matter halo of fixed shape and narrow range in normalization. The Draco galaxy lies about 80 kpc away from us, almost at the zenith with respect to the GC ($\psi_D \sim 85°$). Walker et al. (2009) found that a cuspy NFW halo:

$$\rho_{DM}(r) = \frac{\rho_s}{\left(\frac{r}{rs}\right)\left(1+\frac{r}{rs}\right)^2} \tag{F.2.5}$$

with scale radius $r_s \sim 1$kpc is the best fit to the data on the stellar velocity dispersions, although a cored universal halo:

$$\rho_{DM}(r) = \frac{\rho_s}{\left(1+\frac{r}{rs}\right)^3} \tag{F.2.6}$$

with scale radius $r_s \sim 200\,$pc is not yet ruled out. The scale density ρ_s is fixed by requiring that the mass embedded in the inner 300 pc equals the measured value of $M_{300} = 1.9 \times 10^7\,\mathrm{M}_\odot$. In Table F.2 we list the central values as well as the 95 % CL ones for the scale radius as universally found for the dwarfs by Walker et al. (2009). We note the King radius of Draco is $\sim 650\,$pc (Armandroff et al., 1995), which roughly corresponds to the scale for the mass universality in the dwarf galaxy (600 pc). The mass measured within 600 pc in the case of Draco is about $7 \times 10^7\,\mathrm{M}_\odot$, and the mass enclosed by the maximum radius with stellar velocity dispersion measurements is $\sim 9 \times 10^7\,\mathrm{M}_\odot$, while the virial mass is estimated to be $4 \times 10^9\,\mathrm{M}_\odot$ with a concentration parameter $c_{NFW} \sim 18$ (Walker et al., 2007).

The satellites, or subhalos, of our Galaxy suffer from external tidal stripping due to the interaction with the Milky Way. To account for gravitational tides, we follow Hayashi et al. (2003) and assume that all the mass beyond the subhalo tidal radius is lost in a single orbit without affecting its central density profile. The tidal radius is defined as the distance from the subhalo center at which the tidal forces of the host potential equal the self-gravity of the subhalo. In the Roche limit, it is expressed as:

$$r_{tid}(r) = \left(\frac{M_{sub}}{2M_{host}(<r)}\right)^{1/3} r \tag{F.2.7}$$

where r is the distance from the halo center, M_{sub} the subhalo mass and $M_{host}(<r)$ the host halo mass enclosed in a sphere of radius r.
In our case, the host halo is the Milky Way (MW), which we model after the recent high resolution N-body simulations *Aquarius* (Springel et al., 2008a,b) and *Via Lactea II* (Diemand et al., 2008): while the latter describes the MW with an NFW profile ($M_h \sim 1.9 \times 10^{12}\,\mathrm{M}_\odot$, $r_s = 21$kpc, $\rho_s = 8.09 \times 10^6\,\mathrm{M}_\odot\mathrm{kpc}^{-3}$),

the former finds a shallower profile in the inner regions. We have checked that the difference between the two profiles are irrelevant for our analysis. At the distance of Draco, we find $r_{tid} = 11.2$kpc. We note that the condition $r_{tid} > r_s$ holds, which guarantees that the binding energy is negative and the system is not dispersed by tides. The value of r_{tid} found making use of the Roche criterium is indeed an upper limit since it has been computed in the pointlike approximation.
The LOS integral for the Draco galaxy is computed by numerically integrating Eq. F.2.3, assuming that the integral is different from zero only in the interval $[d - r_{tid}, d + r_{tid}]$.

In the case of the dwarf galaxies, their mass and therefore the masses of the sub-subhalos lie in the region at low β where the Sommerfeld enhancement saturates. This is true for every DM mass except for the one which lies closest to the resonance (in our model, $M = 4.55$TeV). In this case, however, the radial dependence of the enhancement produces a variation of a few percent, so that as a good approximation, the Sommerfeld enhancement S can be considered constant and taken out of the LOS integral. The result of the computation of the LOS integral ($S = 1$) according to Eq.F.2.3 in the case of Draco is depicted in Fig.F.7 as a function of the angle of view ψ with respect to the center of Draco. Only the LOS relative to the central value for the NFW fit to the data is shown.

In view of the dark matter profile universality, we model the inner regions of the closer Sagittarius galaxy using the same profile parameters as in the case of Draco (see also Evans et al. (2004) for a comparison between the Draco and Sagittarius inner DM profiles), although there is no direct evidence of the shape of its DM halo. The Sagittarius dwarf galaxy is located at a distance of about 24 kpc from us, at low latitudes $\psi_S = 15°$. Its vicinity to the Galactic Center causes significant tidal stripping due to the interaction with the gravitational potential of the Milky Way. Yet the surviving stellar component suggests that its inner dark matter halo also survives. Moreover, the observations show that Sagittarius is indeed dark matter-dominated with a central stellar velocity dispersion of about 10 km s^{-1} (Ibata et al., 1997), similar to the one observed in Draco. At the distance of Sagittarius, the tidal radius is $r_{tid} = 4$kpc, still larger than the scale radius.

The results of the line of sight integral towards the center of each dwarf galaxy are shown in Table F.2, for the central value and the 95 % CL values of both the best fit NFW and the cored profile obtained by Walker et al. (2009).

In Table F.3 we list the values of the LOS computed for the smooth component of the MW in the direction of the dwarf galaxies, which will provide a foreground for the detection of the dwarfs themselves. We do not describe in this paper the details of these computations, which are studied extensively in Pato et al. (2009) and Pieri, Bertone & Branchini (in preparation). We observe

Draco fit	r_s(kpc)	$LOS^D_{\psi_D=0}$	$LOS^S_{\psi_S=0}$
NFW	0.795	1.05×10^{-3}	4.43×10^{-3}
NFW $+2\sigma$	3.0	7.85×10^{-4}	2.8×10^{-3}
NFW -2σ	0.3	1.91×10^{-3}	9.8×10^{-3}
Core	0.15	7.5×10^{-4}	2.17×10^{-3}
Core $+2\sigma$	0.3	5.2×10^{-4}	9.4×10^{-4}
Core -2σ	0.085	1.54×10^{-3}	6.9×10^{-3}

Table F.2.: Line of sight integral for the smooth halo of the dwarf galaxies. First column: models reflecting the astronomical uncertainties from a fit to the Draco stellar velocity dispersion. Second column: scale radius for each model. Third column: values for the LOS integral toward the center of Draco. Fourth column: values for the LOS integral toward the center of Sagittarius.

MW model	$LOS_{\psi_{MW}=\psi_D}$	$LOS_{\psi_{MW}=\psi_S}$
VL2	1.18×10^{-5}	2.73×10^{-4}
Aquarius	1.13×10^{-5}	4×10^{-4}

Table F.3.: Line of sight integral for the smooth component of the Milky Way integrated along a direction pointing towards the center of the dwarf galaxies. First column: MW model from numerical simulation. Second column: line of sight integral towards the center of Draco. Third column: line of sight integral towards the center of Sagittarius.

that, both for Draco and for Sagittarius, the dwarf center is brighter in γ-ray than the MW foreground.

The astrophysical sector: substructures

The recent *Aquarius* and the *Via Lactea II* simulations have succeeded in determining the properties of the subhalos and sub-subhalos such as spatial and mass distribution, density profiles and spatial dependence of the concentration parameter. We therefore study the effects on the expected γ-ray flux of a population of sub-subhalos inside the dwarfs according to the recent findings of numerical simulations, although we do not expect a significant impact on the expected flux towards the center of the dwarf, where the smooth halo flux is larger (Giocoli et al., 2008, 2009). We populate Draco with sub-subhalos with masses as small as $10^{-6}M_{\odot}$, corresponding to the damping scale of a typical DM candidate with $M = 100$GeV (Hofmann et al., 2001; Green et al., 2004, 2005; Loeb and Zaldarriaga, 2005). It should howevere be noted that such a minimum mass may vary between 10^{-12} and $10^{-4}M_{\odot}$ depending on the particle physics model considered (Profumo et al., 2006).

We follow the results of *Via Lactea II* to model the population of sub-substructures:

$$\rho_{sh}(M_h, M_{sub}, r) = \frac{A M_{sub}^{-\alpha}}{\left(1 + \frac{r}{r_s^h}\right)^2} \, \mathrm{M}_\odot{}^{-1} \mathrm{kpc}^{-3} \tag{F.2.8}$$

where r_s^h is the scale radius of the host halo and r is the radial coordinate inside the host halo. We normalize the subhalo distribution function $\rho_{sh}(M_h, M_{sub}, r)$ such that 10 % of the mass of the host halo before the tidal stripping is distributed in substructures with masses between $10^{-5} M_h$ and $10^{-2} M_h$, adopting two choices for the mass slope $\alpha = 2$ and $\alpha = 1.9$. We have checked that modeling the spatial substructure distribution function according to *Aquarius* does not significantly change our results.

As a second step, we remove all of the subhalos which lie beyond r_{tid}. This is indeed an upper value for the number of surviving sub-subhaloes, since we are not considering here the fifty percent of the subhalos that exit the virial radius of the parent halo during their first orbit (Tormen et al., 2004) and are therefore dispersed into the halo of the Milky Way.
The contribution of such a population of sub-substructures to the annihilation signal can be written as (Pieri et al., 2008):

$$LOS(M_h, \mathbf{r}, d, \theta) \propto \int_{M_{sub}} dM_{sub} \int_c dc \int \int_{\Delta\Omega} d\theta d\phi$$

$$\int_{los} d\lambda [\rho_{sh}(M_h, M_{sub}, \mathbf{r}) P(c(M_{sub}, r)) LOS_{sh}(M_{sh}, \mathbf{r}, d, \theta)] \tag{F.2.9}$$

where the contribution from each sub-subhalo (LOS_{sh}) is convolved with its distribution function (ρ_{sh}). $P(c)$ is the lognormal distribution of the concentration parameter with dispersion σ_c = 0.24 (Bullock et al., 2001) and mean value $\bar{c}$:

$$P(\bar{c}, c) = \frac{1}{\sqrt{2\pi}\sigma_c c} e^{-\left(\frac{\ln(c) - \ln(\bar{c})}{\sqrt{2}\sigma_c}\right)^2}. \tag{F.2.10}$$

Again, the integral along the line-of-sight will be different from zero only in the interval $[d - r_{tid}, d + r_{tid}]$.

For each sub-substructure, we use an NFW density profile whose concentration parameter $c(M_{sub}, r)$ relative to the radius R_{vir} that encloses an average density of 200 $\times$ the critical one, depends on its mass and on its position inside the host halo, according to the results of *Via Lactea II* and Bullock et al.

Draco fit	mass slope	$LOS^{D,sub}_{\psi_D=0}$	$LOS^{S,sub}_{\psi_S=0}$
NFW	-2	4.13×10^{-5}	5.40×10^{-5}
NFW	-1.9	1.03×10^{-5}	1.34×10^{-5}
NFW $+2\sigma$	-2	3.85×10^{-6}	4.25×10^{-6}
NFW $+2\sigma$	-1.9	9.5×10^{-7}	1.05×10^{-6}
NFW -2σ	-2	1.98×10^{-4}	3.10×10^{-4}
NFW -2σ	-1.9	4.94×10^{-5}	7.71×10^{-5}

Table F.4.: Line of sight integral for the clumpy component of the dwarf galaxies. First column: models reflecting the astronomical uncertainties from a fit to the Draco stellar velocity dispersion. Second column: subhalo mass slope. Third column: values for the LOS integral toward the center of Draco. Fourth column: values for the LOS integral toward the center of Sagittarius.

(2001) extrapolated to $10^{-6}\,\mathrm{M}_\odot$:

$$c(M_{sub}, r) = \left(\frac{r}{R_{vir}}\right)^{-0.286} \times \left(89.04\left(\frac{M_{sub}}{\mathrm{M}_\odot}\right)^{-0.0135} - 42.43\left(\frac{M_{sub}}{\mathrm{M}_\odot}\right)^{0.006}\right) \tag{F.2.11}$$

We numerically integrate Eq. F.2.9 to estimate the LOS contribution from the sub-substructures in a 10^{-5} sr solid angle along the direction ψ_D or ψ_S towards the center of the dwarfs. The result of this computation for the subhalo population of Draco is depicted in Fig.F.7 as a function of ψ_D, for the central value of the NFW fit to the stellar kinematics and for a mass slope of -2. As expected, this contribution becomes relevant only away from the center, where it anyway gives a flux which is one order of magnitude smaller.

We repeat the same analysis for Sagittarius, assuming its sub-subhalo population is modeled in the same way as the Draco's one, yet with a smaller todal radius. The result of the integration of Eq. F.2.9 along a direction pointing towards the center of the dwarfs is listed in Table F.4. Although the values in the case of Sagittarius are slightly larger than for Draco, due to its proximity to us, the relative strength of the smooth to clumpy component is larger in Draco, making the presence of sub-subhalos in Sagittarius almost irrelevant with respect to the smooth component.

In Table F.5 we compute the values of the LOS flux computed for the clumpy component of the MW in the direction of the dwarf galaxies. We observe that, both for Draco and for Sagittarius, the dwarf center is brighter in γ-rays than the MW clumpy foreground. We do not describe in this paper the details

subhalo mass slope	$LOS^{sub}_{\psi_{MW}=\psi_D}$	$LOS^{sub}_{\psi_{MW}=\psi_S}$
-2	2×10^{-5}	5.5×10^{-5}
-1.9	2.5×10^{-6}	6.5×10^{-6}

Table F.5.: Line of sight integral for the clumpy component of the Milky Way integrated along a direction pointing towards the center of the dwarf galaxies. First column: Subhalo mass slope. Second column: line of sight integral towards the center of Draco. Third column: line of sight integral towards the center of Sagittarius.

of these computations, which can be found in Pato et al. (2009) and Pieri, Bertone & Branchini (in preparation). The MW foreground contribution to Draco, computed including its smooth and clumpy component, is shown in Fig.F.7. The band of values accounts for the different simulations as well as for the different subhalo mass slope. The MW foreground begins hiding Draco at around 0.3 degrees from the Draco center. We have checked that the same happens in the case of Sagittarius.

The mass modeling of the dwarf galaxies at large distances from their centers is just an educated guess; as a check of consistency of our results, we repeated our calculations in the case when the DM halo extends only up to 600 pc, that is to say to the King radius (we remind that the mass within the King radius is directly measured through stellar kinematics). The differences between the computations extending to R_{vir} and the ones extending to the 600 pc amount to 5% at most.

In the following section we will compare our predictions with the available data and expected sensitivities from the atmospheric Cherenkov telescopes (ACTs). To compare with the data, we will consider the sum of the four contributions to the photon flux: 1) annihilations in the smooth halo of the dwarf galaxy, 2) annihilations in the subhalos of the dwarf galaxy, 3) annihilations in the smooth halo of the Milky Way and 4) in the subhalos of the Milky Way, computed along the direction which corresponds to the position of the dwarf galaxy in the sky. The relative importance of the four terms depends on the angle of view from the centre of the dwarf galaxy, as well as on the particle physics model. The contribution due to the annihilation in the smooth halo of the dwarf galaxy is always predominant when looking at the dwarf center.

F.2.3. Comparison with the experimental data

The MAGIC and HESS ACTs have put 95 % upper limits on the γ-ray fluxes from Draco and Sagittarius, respectively. The upper limit for Draco inte-

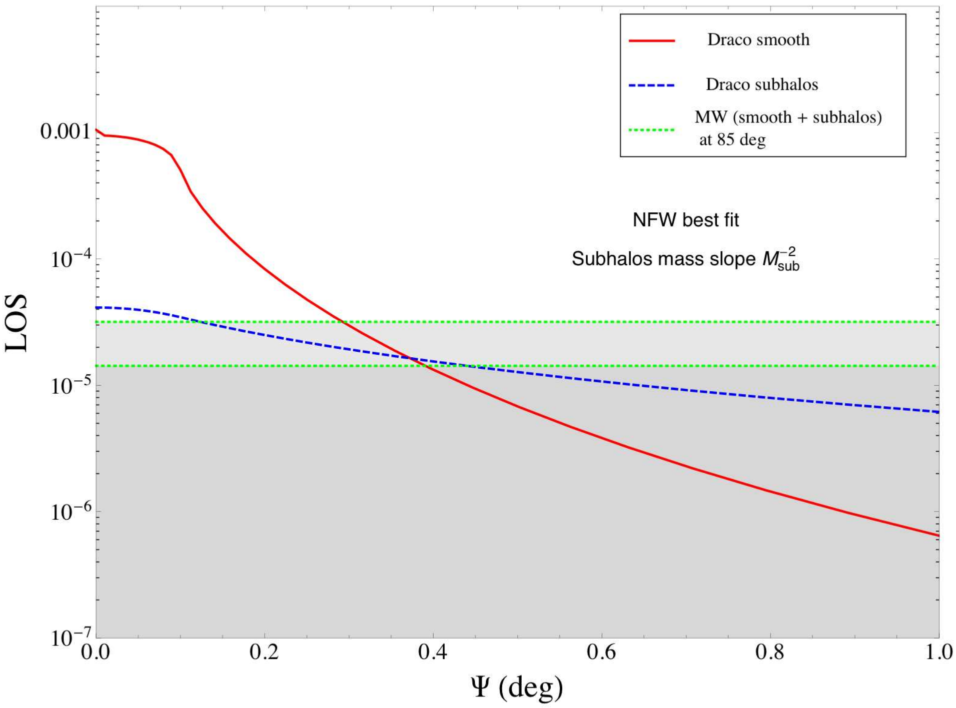

Figure F.7.: Φ_{cosmo} as a function of the angle of view ψ from the centre of halo, computed in the case of Draco and Sagittarius, for the smooth halo and from the subhalo population.

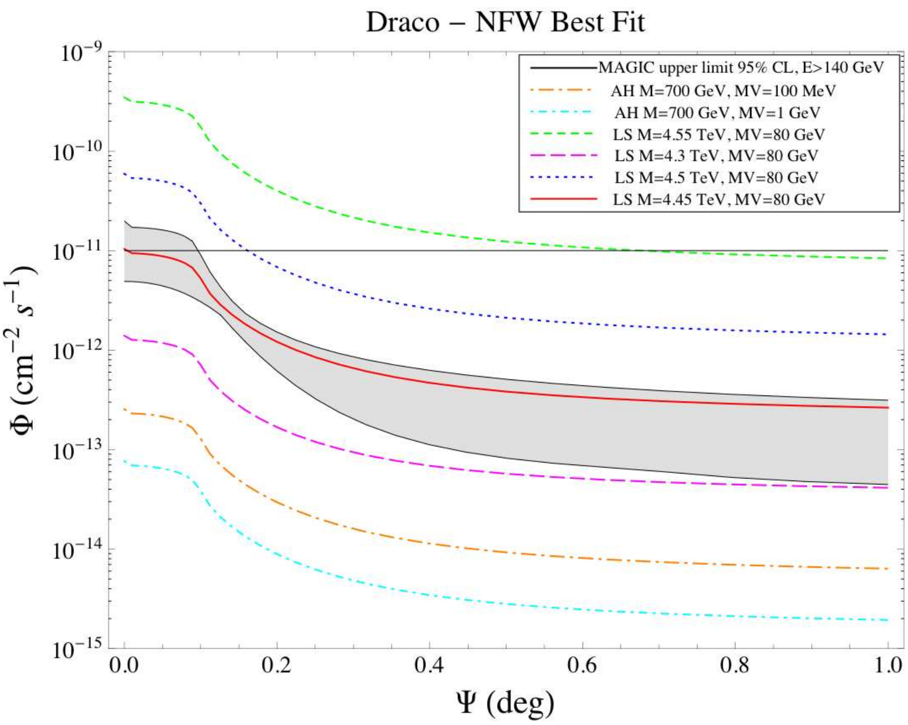

Figure F.8.: Expected γ-ray flux above 140 GeV as a function of the angle of view ψ from the centre of Draco.

grated over energies above 140 GeV is 10^{-11} ph cm^{-2} s^{-1}. In the case of Sagittarius, this limit is 3.6×10^{-12} ph cm^{-2} s^{-1}, integrated above 250 GeV.

In Fig. F.8 and F.9 we compare these values with the prediction of the γ-ray flux from DM annihilations. We compute the flux for the particle DM models described in Sec.F.2.2. We show the result in the case of the central value for the scale radius in the NFW best fit to the kinematic data, as derived in Walker et al. (2009). Indeed, in the case of M=4.45 TeV, we show the astrophysical uncertainty by plotting the curves relative to NFW and cored fits, for central and 95 % CL values of the scale radius.
We note that our dwarfs actually appear as point sources for an angular resolution of 0.1°.
The data from both MAGIC and HESS already exclude the highest Sommerfeld-enhanced cross-sections.

Since the main contribution to the γ-ray flux at the center of the dwarf comes from halos which are in saturation with respect to the velocity-dependent enhancement, we can present the previous results in terms of an exclusion plot on the effective Sommerfeld-enhanced cross-section. In Fig.F.10 we show the exclusion limit on the effective annihilation cross-section imposed by the MAGIC upper limit on Draco, in the case when the DM particle annihilates

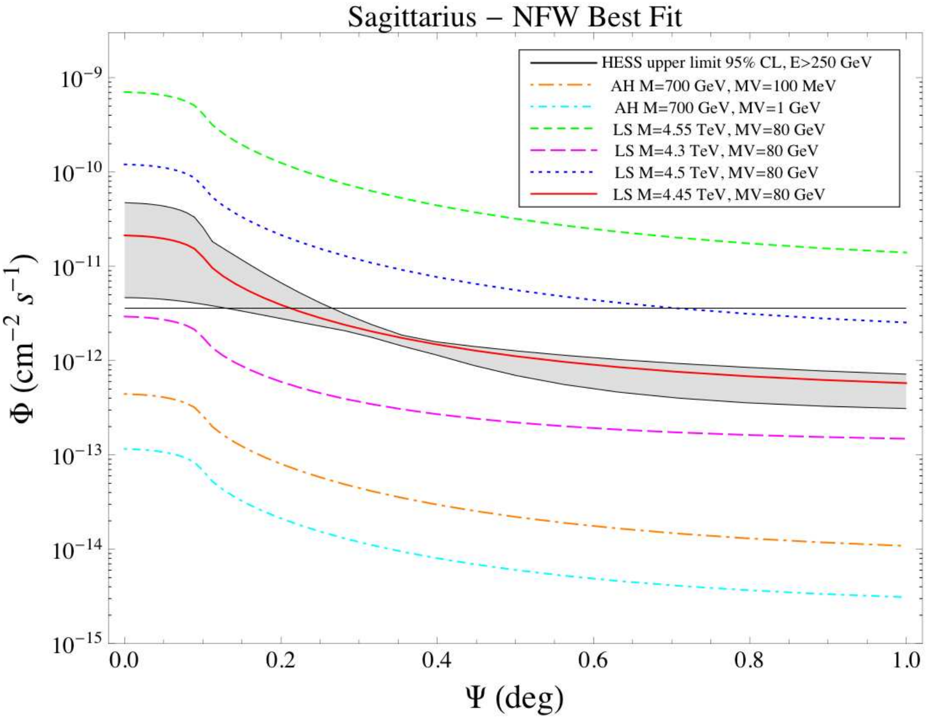

Figure F.9.: Expected γ-ray flux above 250 GeV as a function of the angle of view ψ from the centre of Sagittarius.

in gauge bosons. The band of values reflects the astrophysical uncertainties due to astronomical data and numerical simulations. For comparison, we also show the exclusion plot obtained by the observation of the GC with the HESS telescope. HESS has extensively observed the Galactic Center (GC) source, measuring an integrated flux above 160 GeV of $\Phi(> 160\text{TeV}) = 1.87 \times 10^{-11}\,\text{ph}\,\text{cm}^{-2}\,\text{s}^{-1}$ in 2003 and 2004 (Aharonian et al., 2006).
In order to compute the Sommerfeld enhancement of the MW halo towards the GC, it is necessary to convolve the information on the rotation curve of our Galaxy with the β-dependence of the effect, and including the presence of the black hole at the center of the Galaxy. This computation has been done in Pato et al. (2009) and brings enhancements of the order of 10^3 to 10^4 for the Lattanzi & Silk models, and of the order of 10^2 for the Arkani-Hamed model. In Fig.F.10 we report the exclusion limit with respect to a constant effective Sommerfeld-enhanced annihilation cross-section. The band of values for each experiment reflects the astrophysical uncertainty due to the inner profile. We have used the spiky NFW profiles obtained by *Via Lactea II* and a cored isothermal profile with scale radius $r_s = 5$kpc normalized to the same local value for the DM density as found in *Via Lactea II* (i.e. $\sim 0.4\text{GeV}\,\text{cm}^{-3}$). Since simulations do not include baryons which may play an important role at the GC, the large uncertainty on the inner pro-

file prevents this measurement to put strong limits. As an exercise, we computed the sensitivity to Draco to the space-based telescope Fermi and the future Cherenkov Telescope Array (CTA) [2]. The CTA is a proposed experiment which will make use of Cherenkov Telescope technology on a large scale, in order to lower the threshold energy down to $\sim$ 50GeV. The instrument is being designed. The tens of telescopes in the array could either look at different portions of the sky, thus reaching up to $\sim 1\,\mathrm{sr}$ of field of view, or focus on the same source, thus dramatically increasing the single telescope sensitivity. We take a sample sensitivity from the CTA home page, according to which the CTA will be able to detect $\Phi(> 50\mathrm{GeV}) = 7 \times 10^{-12}\,\mathrm{ph\,cm^{-2}\,s^{-1}}$ and $\Phi(> 1\mathrm{TeV}) = 2.9 \times 10^{-14}\,\mathrm{ph\,cm^{-2}\,s^{-1}}$. Such a sensitivity to a single source could improve if more telescopes could point at the same source. In the case of Fermi, we took the sensitivity to point sources from Baltz et al. (2008), that is to say, $\Phi(> 3\mathrm{GeV}) = 10^{-10}\,\mathrm{ph\,cm^{-2}\,s^{-1}}$. We show the sensitivity bands for Fermi and the CTA in Fig.F.10. The uncertainty always derives from astrophysics. Although a boost to the thermal annihilation cross-section is always required to observe Draco (see also Pieri et al., 2009a), the limits will improve significantly with the future data.
In Fig.F.11 we show the same kind of exclusion limits and expected sensitivities as in Fig.F.10, yet computed for a DM particle annihilating into e^+e^- and producing photons as a final state radiation. The limits and sensitivities at high DM masses are in this case poorly restrictive.

Finally, in Fig.F.12 we show the sensitivity to Sagittarius with Fermi and the CTA, under the assumption that we have used all throughout the paper, namely that the inner DM halo of Sagittarius is modeled as the one of Draco. We superimpose the effective cross-section as a function of the DM particle mass in the case of a Sommerfeld effect mediated by a 80 GeV boson, for different values of β. For TeV DM masses close to the resonance, with a boost of a factor $\sim 10^3$, the CTA would be the only instrument able to detect the signal.

In general, the constraints will depend, among other things, on the final states for annihilation. In the case of the WIMP scenario, the results discussed so far have been obtained considering a dark matter particle of mass $M \simeq 4.5$ TeV annihilating exclusively into gauge bosons. Considering instead annihilation into heavy quarks or leptons as possible final states changes the predicted fluxes by factors of order unity, thus leaving our conclusions basically unchanged. In particular, a particle that annihilates only to heavy quarks would produce a flux 1.6-1.7 times larger than that shown in the figures, for all experiments. The limits on the Sommerfeld boost would then be proportionally tighter. In the case of a particle annihilating to τ leptons, the change in the flux depends on the energy threshold: for MAGIC, HESS and CTA it is respectively 0.5, 0.8, and 3.8 times the flux from the gauge boson channel.

[2]CTA homepage: http://www.cta-observatory.org/

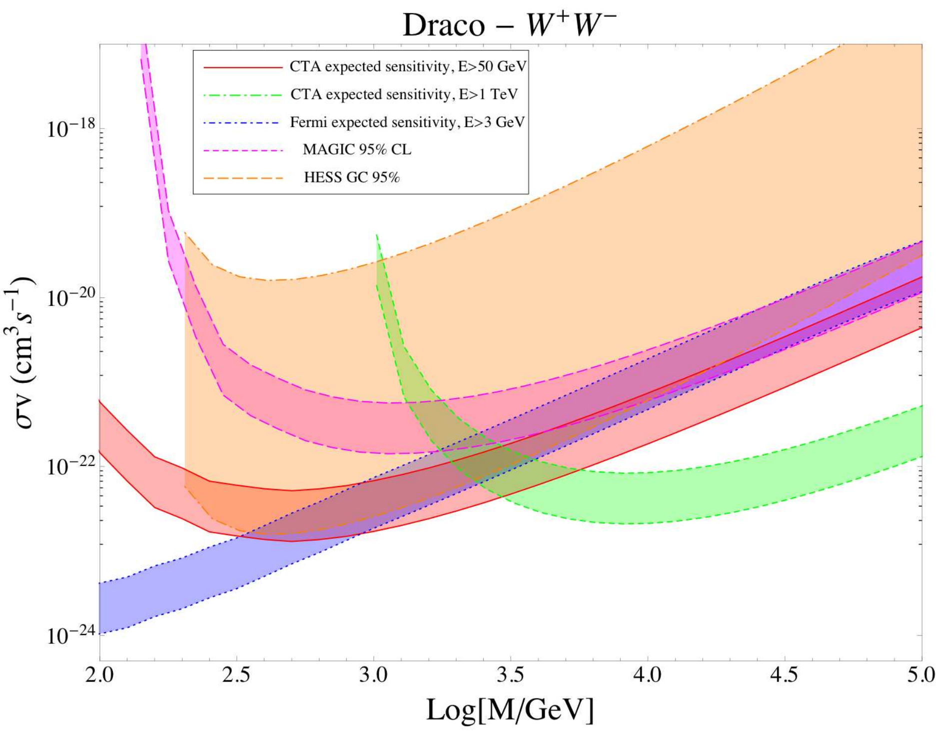

Figure F.10.: Exclusion plot (MAGIC and HESS GC) and expected sensitivity (CTA and Fermi) for the effective annihilation cross section, in the case of γ-ray observations of the Draco galaxy and for dark matter particles annihilating into WW.

Ligther leptonic and quark final states are strongly disfavoured due to the helicity suppression; however they could become important if the helicity suppression is lifted in some way. In the case of the AH scenario, the final spectrum is instead naturally driven to light leptons (electrons and muons) since heavier states are kinematically forbidden.

F.2.4. Conclusions

The excess in cosmic-ray positrons and electrons has motivated a wealth of theoretical efforts in order to be explained in terms of DM. In particular, the annihilation mechanism has been revised in the light of the Sommerfeld enhancement, a velocity-dependent effect. Such an effect is maximal in the dwarf galaxies and in their substructures. The enhancement actually saturates for DM halo masses smaller than the dwarf scale. Several studies (see. e.g. Bertone et al., 2009; Cirelli and Panci, 2009; Galli et al., 2009; Pato et al., 2009) have recently constrained the Sommerfeld enhancement and thus the interpretation of the Pamela excess in terms of dark matter. However, the DM halo of the dwarf galaxies can now be modeled making use of kinematic stel-

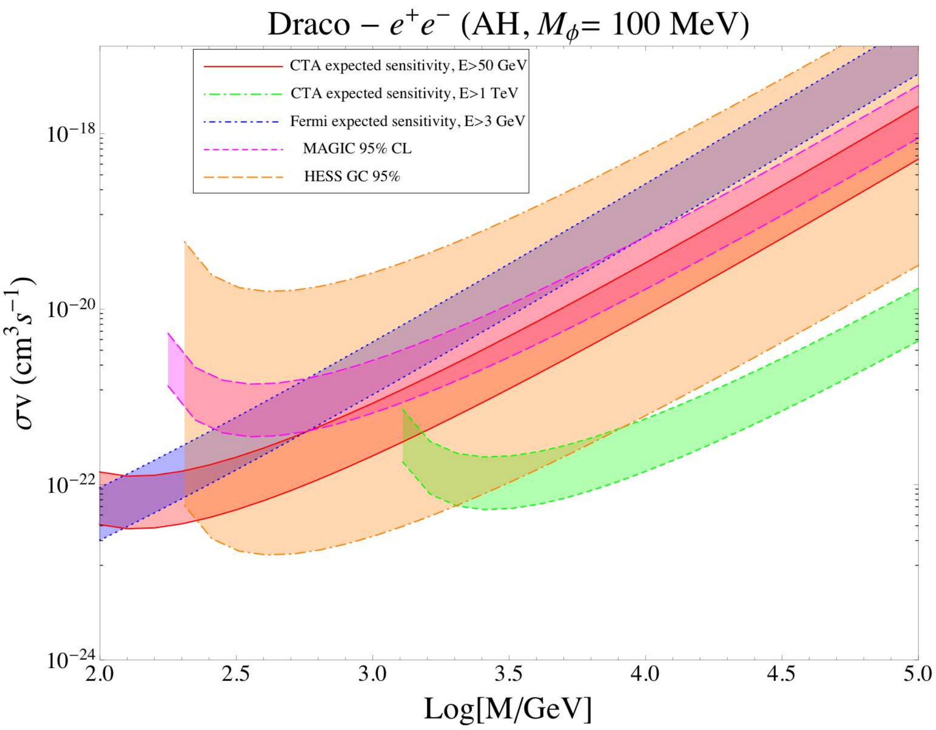

Figure F.11.: Exclusion plot (MAGIC and HESS GC) and expected sensitivity (CTA and Fermi) for the effective annihilation cross section, in the case of γ-ray observations of the Draco galaxy and for dark matter particles annihilating into e^+e^- in the AH case with $M_V = 100$ MeV.

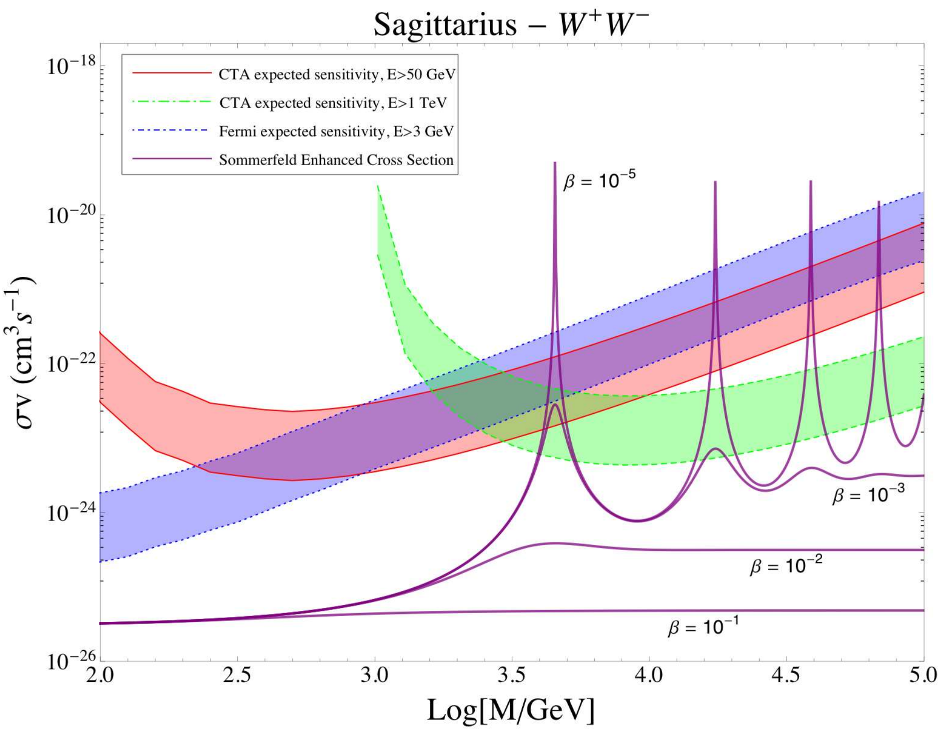

Figure F.12.: Expected sensitivity for the effective annihilation cross section, in the case of γ-ray observations of the Sagittarius galaxy and for dark matter particles annihilating into WW.

lar data with a precision which is far better than the uncertainties on the MW DM profile or on the subhalo population or on the propagation parameters which affect the limits set by antimatter, radio and γ-ray signals. We have computed the expected γ-ray flux from the Draco and the Sagittarius dwarf galaxies, for which upper limits are available from the ACTs. We have computed the flux within the astrophysical uncertainties and we find that the measurements of MAGIC and HESS are able to constrain the enhancement and set an upper limit of $\sim 10^4$. We have shown that the future CTA experiment should be able to test the boost relative to the thermal annihilation cross-sections up to values of a few hundred.

F.3. Signatures of clumpy dark matter in the global 21 cm background signal

F.3.1. Introduction

The standard cosmological model, motivated by measurements of temperature anisotropies in the Cosmic Microwave Background (CMB) (Spergel et al., 2003, 2007; Komatsu et al., 2009; Dunkley et al., 2009), the large scale distribution of galaxies (Cole et al., 2005; Tegmark et al., 2006b), and by evidence of the accelerated expansion of the Universe from supernova observations (Astier et al., 2006; Wood-Vasey et al., 2007), requires that the Universe possesses a flat spatial geometry with a corresponding critical density, approximately 27 percent of which consists of physical matter. However these observations also indicate that only 4 percent of this matter is baryonic in nature, implying that the remaining 23 percent consists of an elusive, non-baryonic component called dark matter (DM) owing to the severe constraints that current astronomical data sets on its radiative capabilities.

Despite this compelling evidence for the existence of DM, its precise nature is still a topic of debate. Particle physicists have independently supported DM by postulating the existence of a variety of exotic particles with wide-ranging properties that may potentially solve problems in particle physics whilst resulting in a thermal relic particle density that is consistent with current observational constraints.

The most intensely studied DM candidate is the lightest neutralino (Bertone, Hooper and Silk, 2005), a weakly-interacting massive particle (WIMP) motivated by supersymmetric extensions of the Standard Model of particle physics. In many of these extensions the neutralino is the lightest supersymmetric particle (LSP). In theories where the LSP is stable, for example theories where R-Parity is a conserved quantum number (Weinberg, 1982; Hall and Suzuki, 1984; Allanach, Dedes and Dreiner, 1999), the neutralino is thus a highly-motivated DM candidate. Furthermore, an attractive feature of neutralinos is that a large region of the relevant supersymmetric parameter space can be investigated using CERN's Large Hadron Collider (LHC)[3].

Whilst neutralino DM is "cold", owing to its negligible free-streaming length (i.e. the length scale below which fluctuations in DM density are suppressed), warm DM (WDM) is typically lighter and possesses a much longer free-streaming length. WDM is a viable alternative to cold dark matter (CDM) models which may potentially resolve several shortfalls of the standard CDM model, such as for example the over-prediction of low mass satellites and the existence of cuspy halos (Hogan and Dalcanton, 2000; Dalcanton and Hogan, 2001; Avila-Reese, Colin, Valenzuela, D'Onghia and Firmani, 2001; Colin, Valenzuela and Avila 2008). Among WDM candidates, there are sterile neutrinos (Dodelson and Widrow, 1994; Asaka, Blanchet and Shaposhnikov, 2005; Asaka and Shaposhnikov, 2005), majorons (Akhmedov, Berezhiani and Senjanovic, 1992; Berezinsky and Valle, 1993; Lattanzi and Valle, 2007) and light DM (LDM) particles (Boehm and Fayet, 2004). What makes LDM interesting for this study is the fact that it can self-annihilate, as opposed to other forms of WDM, and therefore its annihilation rate can be enhanced by overdensities.

In Cumberbatch et al. (2010) we have reexamined the influence of neutralino and LDM annihilations on the thermal history of the Universe at times between the epochs of recombination and reionisation, commonly referred to as the "Dark Ages", when gas existed in a nearly uniform, dark, neutral state. The investigation of the Dark Ages is one of the frontiers of modern cosmology, and will be carried on by a new generation of radio interferometers such as LOFAR[4], MWA[5], 21 CMA[6], and SKA[7], as well as single antenna experiments such as EDGES[8] and CORE.

These experiments will look for the redshifted 21 cm signal associated with the hyperfine triplet-singlet transition of neutral hydrogen. If DM annihilates or decays, the resulting products subsequently collide and heat the surrounding gas, increasing its kinetic temperature and ionisation fraction. This is in turn manifested as distinct features in the 21 cm background signal that can be used to constrain the properties of DM Furlanetto et al. (2006b); Shchekinov and Vasiliev (2007); Valdes et al. (2007).

With few exceptions (e.g. Chuzhoy (2007); Yuan et al. (2010)), past studies proclaim that the heating effects associated with the annihilation of SUSY WIMP DM are too small to be detected by current radio interferometers. However, these studies overlook the enhancements to the DM annihilation rate in galactic halos and in their substructures (Taylor and Silk, 2003), which could be large enough to make the DM signature detectable by the next gen-

[3] www.cern.ch/LHC
[4] http://www.lofar.org
[5] http://www.haystack.mit.edu/ast/arrays/mwa
[6] http://web.phys.cmu.edu/past/
[7] http://www.skatelescope.org
[8] http://www.haystack.mit.edu/ast/arrays/Edges/index.html

eration radio telescopes. In this paper, we calculate the effect of neutralino and LDM annihilations on the 21 cm signal when accounting for the effect of DM clustering.

The rest of this section is organized as follows. In § F.3.2 we elaborate on the basic properties of neutralinos and LDM. We also discuss the basic physics describing the way in which energy from annihilations is injected into the intergalactic medium (IGM). In § F.3.3 and § F.3.4 we calculate the enhancement in the DM annihilation rate caused by the presence of halos and their substructures. In § F.3.5 we estimate how much of the energy produced in a single DM annihilation is actually injected into the IGM. In § F.3.6 we discuss the modifications to the differential equations describing the evolution of the ionised fraction and kinetic temperature of the IGM and subsequently use these equations to calculate the modified 21 cm background. In § F.3.7 we calculate the predicted 21 cm background for our benchmark neutralino and LDM models and discuss the potential for a detection. Finally, in § F.3.9 we summarise our results and draw our conclusions.

F.3.2. Dark matter candidates

The lightest supersymmetric (SUSY) neutralino is a superposition of higgsinos, winos and binos. Consequently, neutralinos are electrically neutral and colourless, only interacting weakly and gravitationally, and hence very difficult to detect directly. In SUSY models that conserve R-parity, the LSP is stable (Weinberg, 1982; Hall and Suzuki, 1984; Allanach et al., 1999). Consequently, in a scenario where present-day CDM exists as a result of thermal freeze-out, the dominant species of CDM could quite possibly include the LSP. The relic density of the LSP will then heavily depend on its mass and annihilation cross section. Throughout this paper we assume that the LSP is the lightest SUSY neutralino. The neutralino is a popular candidate for CDM because the theoretically-motivated values of these parameters yield a corresponding value of the relic density that is in good agreement with observations (for a more detailed review of the various properties and motivations for neutralino DM see, e.g., Bertone et al. (2005)).

Neutralinos possess a wide-range of annihilation spectra owing to the vast extent of currently unexcluded SUSY parameter space. Owing to the Majorana nature of the neutralino, its annihilation to fermionic channels is suppressed by a factor proportional to the square of the mass of the final state. This means that, if the neutralino is lighter than the $W^{\pm}$ and Z bosons, annihilations will be dominated by the process $\chi\chi \rightarrow b\bar{b}$ with a minor contribution by $\chi\chi \rightarrow \tau^{+}\tau^{-}$. Assuming annihilations are dominated by the former process, the resulting spectrum will depend entirely on the LSP mass. For heavier LSPs, the annihilation products become more complex, often determined by several dominant annihilation modes, including $\chi\chi \rightarrow W^+W^-$, $\chi\chi \rightarrow ZZ$ or $\chi\chi \rightarrow t\bar{t}$ as well as $\chi\chi \rightarrow b\bar{b}$ and $\chi\chi \rightarrow \tau^+\tau^-$.

The other DM candidate we consider is LDM, consisting of MeV mass particles, which annihilate to electron-positron pairs [9] and consequently were considered to be a possible source of the positrons contributing to the 511 keV positronium decay signature from the bulge of the Galaxy observed by SPI/INTEGRAL (Knodlseder et al., 2005). While the current view favours the interpretation of the 511 keV feature as due to e^+e^- injection by a population of astrophysical sources, there is nevertheless continued interest in reviving a dark matter interpretation because of the possible connection with other anomalous spatially extended signals seen from the innermost Galaxy, specifically the WMAP and the FERMI hazes Dobler et al. (2010). More exotic dark matter models are required in this case, most specificaly some form of multicomponent dark matter (see e.g. Refs. Boehm et al. (2004); Feldman et al. (2010)).

Relevant analyses of the 511 keV emission impose the constraint on the LDM mass $m_{\rm DM} < 20\,\rm MeV$ in order not to overproduce detectable gamma-rays from inner bremsstrahlung processes (Beacom, Bell and Bertone, 2005) (although see Boehm and Uwer (2006)). A stronger, albeit less conservative constraint, $m_{\rm DM} < 3\,\rm MeV$ can be obtained if one considers the generation of gamma-rays from the in-flight annihilation between positrons produced from LDM annihilation and electrons residing in the interstellar medium of our Galaxy (Beacom and Yuksel, 2006).

Both in the case of neutralinos and LDM, the average rate of energy absorption per hydrogen atom in the IGM at a redshift z is given by

$$\dot{\epsilon}(z) = \frac{1}{2} f_{\rm abs.}(z) \frac{n^2_{\rm DM,0}}{n_{\rm H,0}} \langle \sigma_{\rm ann.} v \rangle m_{\rm DM} (1+z)^3 : C(z) \qquad (\rm F.3.1)$$

where $m_{\rm DM}$ is the mass of the DM particle, $\langle \sigma_{\rm ann.} v \rangle$ is the thermally-averaged DM annihilation cross section, $n_{\rm DM,0}$ and $n_{\rm H,0}$ are the current *average* number densities of DM and hydrogen respectively, and $f_{\rm abs.}$ is the fraction of energy which is absorbed by the IGM. The "clumping factor" $C(z)$ is the redshift-dependent enhancement of the annihilation rate owing to the presence of DM structures, relative to a completely homogeneous Universe[10].

[9] MeV LDM particles can also potentially annihilate directly into neutrinos and photons. However most theories suppress this emission in order to be consistent with observational constraints. Here we only consider scenarios where LDM annihilates entirely to electron-positron pairs, so that our results can be considered as an upper limit to the more general case.

[10] The factor of 1/2 in Eq.(F.3.1) assumes Dirac DM particles; for Majorana particles this should be further multiplied by a factor of 2.

F.3.3. Extragalactic dark matter Annihilation Rate

In the standard cosmological model, all structure in the Universe originated from small amplitude quantum fluctuations during an epoch of inflationary expansion shortly after the Big Bang. The linear growth of the resulting density fluctuations is then completely determined by their initial power spectrum, which for ΛCDM is usually assumed to be a power law with spectral index n. Current limits on n from observations of temperature fluctuations in the CMB conducted by the Wilkinson Microwave Anisotropy Probe, $n_{\mathrm{WMAP}} = 0.963 \pm 0.012$ (at 68% confidence level) (Dunkley et al., 2009; Komatsu et al., 2010), support the existence of a power spectrum consistent with inflation.

During the expansion of the Universe, the aforementioned small initial density fluctuations will eventually grow and produce the structures that we observe today. In the currently accepted cosmological model, smaller structures form first and then merge to form larger ones in a process of "bottom-up" hierarchical structure formation. The mass distribution at any given redshift can potentially be determined through the use of numerical simulations.

As a first approximation, the smaller progenitors forming larger isolated structures are completely disrupted after merging and the resulting "smooth" DM density distribution can be described by a continuous function, conventionally of the form

$$\rho(r) = \frac{\rho_s}{(r/r_s)^{\gamma}\left[1 + (r/r_s)^{\alpha}\right]^{(\beta-\gamma)/\alpha}}, \tag{F.3.2}$$

where r is the distance from the centre of the halo, r_s is a scale radius, ρ_s is a normalisation factor, and α, β and γ are free parameters.

However, N-body simulations of CDM halos reveal that a wealth of substructure halos (henceforth referred to as subhalos) exist within such halos. Moreover, utilising results from the Via Lactea II simulations, Diemand et al. (2008) claimed that a further generation of sub-subhalos exist with a near self-similar mass distribution relative to their parent subhalo. This suggests the possibility that if one were to conduct simulations with sufficiently high resolution, one would find a long nested near self-similar series of halos within halos within halos etc., all the way down to the smallest halos[11]. This has significant implications for the indirect detection of annihilating DM since the rate of DM annihilations is proportional to the square of the local density, and hence the presence of over-densities can significantly increase the annihilation rate relative to that obtained with a smooth DM distribution.

The above scenario applies to structures formed in a CDM-dominated Universe. In a WDM-dominated Universe, the significant damping of small-scale

[11]However, there are results from the more recent Aquarius simulations Springel et al. (2008a,b), conducted by the Virgo consortium, that are in contention with these results (see § F.3.9).

density fluctuations, due to the larger free-streaming length, should be taken into account. Following Bardeen et al. (1986), this can be accounted for by using the modified power spectrum $P(k) = T^2_{\rm WDM}(k)P_{\Lambda\rm CDM}(k)$, where the WDM transfer function is approximated by

$$T_{\rm WDM}(k) = \exp\left[-\frac{kR_f}{2} - \frac{(kR_f)^2}{2}\right], \tag{F.3.3}$$

where R_f is the free-streaming length.

For WDM particles with negligible interaction rates, the free-streaming length is related to the particle mass $m_{\rm DM}$ by (Bardeen et al., 1986).

$$R_{f,n} = 7.4 \times 10^{-6} \left(\frac{m_{\rm DM}}{1\,\rm MeV}\right)^{-4/3} \left(\frac{\Omega_{\rm DM}}{0.258}\right)^{1/3} \times \left(\frac{h}{0.719}\right)^{5/3} h^{-1}\,\rm Mpc. \tag{F.3.4}$$

However, as we will show below, the interaction rates for self-annihilating LDM in the models considered here are non-negligible. In this case, the free-streaming length is given by (Boehm and Schaeffer, 2004)

$$R_{f,i} = 0.3 \left(\frac{\Gamma_{\rm dec.,DM}}{6 \times 10^{-24}\,\rm s^{-1}(1+z_{\rm dec.})^3}\right)^{1/2} \tag{F.3.5}$$

$$\times \left(\frac{1\,\rm MeV}{m_{\rm DM}}\right)^{1/2} \rm Mpc, \tag{F.3.6}$$

where $\Gamma_{\rm dec.,DM}$ is the WDM self-annihilation rate at the decoupling redshift $z_{\rm dec.}$ given by

$$\Gamma_{\rm dec.,DM} = \frac{1}{2}\frac{\rho_{c,0}\Omega_{\rm DM,0}}{m_{\rm DM}} \langle\sigma_{\rm ann.}v\rangle_{\rm dec.}(1+z_{\rm dec.})^3, \tag{F.3.7}$$

and $\langle\sigma_{\rm ann}v\rangle_{\rm dec.}$ is the thermally-averaged product of the WDM annihilation cross section and relative speed of two annihilating WDM particles, evaluated at the same time. In order to obtain the thermal relic density observed today, one requires $\langle\sigma_{\rm ann.}v\rangle_{\rm dec.} \simeq 10^{-26}\,\rm cm^3\,s^{-1}$.

For $m_{\rm DM} = 3\,\rm MeV$ we obtain $R_{f,n} = 2.4\,\rm pc$ and $R_{f,i} = 98\,\rm pc$, while for $m_{\rm DM} = 20\,\rm MeV$, we obtain $R_{f,n} = 0.19\,\rm pc$ and $R_{f,i} = 15\,\rm pc$. Hence, in both cases the co-moving free-streaming length set by WDM interactions is at least an order of magnitude larger than that when interactions are completely negligible, and consequently we must use the former in our determination of the cut-off scale in the WDM power spectrum.

We follow the treatment by Avila-Reese et al. (2001) and define a characteristic free-streaming wavenumber k_f such that $T_{\mathrm{WDM}}(k_f) \simeq 0.5$, leading to $k_f \simeq 0.46/R_f$. This wavenumber is then related to a characteristic filtering mass M_f by

$$M_f = \frac{4\pi}{3}\bar{\rho}_{\mathrm{WDM}}\left(\frac{\lambda_f}{2}\right)^3, \tag{F.3.8}$$

where $\lambda_f = 2\pi/k_f = 13.6R_f$. In this paper we invoke the approximation $M_{\mathrm{min.}} \sim M_f$, where here $M_{\mathrm{min.}}$ is the minimum mass of a LDM halo, and equal to approximately $46\,M_\odot$ and $0.16\,M_\odot$ for $m_{\mathrm{DM}} = 3\,\mathrm{MeV}$ and $20\,\mathrm{MeV}$ respectively. Since the mass within a given co-moving volume is constant as the Universe expands, the result (F.3.8) is independent of redshift.

Below, we perform a series of detailed calculations illustrating the enhancement of the annihilation rate relative to that obtained with a completely smooth Universe, known as the *clumping factor*.

F.3.4. Calculation of the clumping factor

We assume a standard homogeneous, isotropic Universe with a flat spatial geometry. Let $R(M,z)$ be the average annihilation rate within a generic DM halo of mass M located at redshift z. Even for large M, this source can be regarded as an unresolved point-source and we assume this throughout, for all halos considered. The rate of annihilations per unit volume at a given redshift is then equal to

$$\Gamma(z) = (1+z)^3 \int_{M_{\mathrm{min.}}}^{M_{\mathrm{max.}}} \mathrm{d}M \frac{\mathrm{d}n}{\mathrm{d}M}(M,z)R(M,z), \tag{F.3.9}$$

where we have introduced the unconditional halo mass function, $\mathrm{d}n/\mathrm{d}M$, i.e. the co-moving number density of virialised halos with mass M located at redshift z, (the factor $(1+z)^3$ converts this from co-moving to proper density). The integral spans over the mass range $M > M_{\mathrm{min.}}$, where $M_{\mathrm{min.}}$ can be as small as $\sim 10^{-12}M_\odot$, due to kinetic decoupling in the case of CDM (Profumo et al., 2006), and approximated by the filtering mass (F.3.8) in the case of WDM.

Three ingredients are required in order to calculate the annihilation rate (F.3.9). Firstly, we need to specify the annihilation cross section of our DM candidates (in our case neutralinos or LDM). Secondly, we need to specify the DM density profile of a generic halo of mass M at redshift z. Finally, we need an estimate of the distribution of halos, i.e. an estimate of the halo mass function $\mathrm{d}n(M,z)/\mathrm{d}M$.

The halo mass function

Press-Schechter theory (Press and Schechter, 1974) postulates that the cosmological mass function of DM halos can be expressed in the universal form

$$\frac{\mathrm{d}n}{\mathrm{d}M} = \frac{\bar{\rho_0}}{M^2}\nu f(\nu)\frac{\mathrm{d}\log(\nu)}{\mathrm{d}\log(M)}, \tag{F.3.10}$$

where $\bar{\rho_0}$ is the average co-moving DM density, $\bar{\rho}_0 = \rho_c\Omega_M$, and ρ_c is the present critical density of the Universe. The parameter $\nu = \delta_{\rm sc}/\sigma(M)$ is defined as the ratio of the critical overdensity required for spherical collapse at redshift z extrapolated using linear theory to present time, and $\sigma(M)$ is the r.m.s. of primordial density fluctuations when smoothed on a scale which contains mass M, again extrapolated using linear theory to present time. The form of $\delta_{\rm sc}(z)$ can be found in Tegmark et al. (2005). $\sigma(M)$ is related to the power spectrum $P(k)$ of the linear density field extrapolated to the present time by

$$\sigma^2(M) = \int \mathrm{d}^3k W^2(kR)P(k), \tag{F.3.11}$$

where W is the top-hat window function at the length scale $R = (3M/4\pi\bar{\rho})^{1/3}$ and $\bar{\rho}$ is the mean matter density. We utilise the analytical approximation specified in Tegmark et al. (2006a), relevant in the linear regime long after the relevant fluctuation modes have entered the horizon, when all modes grow at the same rate, which means that $\sigma(M)$ can be factored as a product of two functions, one solely dependent on redshift z and the other solely dependent on the comoving spatial scale R. We normalise P and σ by computing σ at $R = 8h^{-1}$ Mpc and setting the result equal to the cosmological parameter σ_8 as measured by WMAP, $\sigma_8 = 0.796 \pm 0.036$ (Dunkley et al., 2009).

The first-crossing distribution $f(\nu)$ has the following analytical fit (Sheth and Tormen, 2002) to the N-body simulation results from the Virgo consortium (Jenkins et al., 1998)

$$\nu f(\nu) = A\left[1 + (a\nu)^{-p}\right]\left(\frac{a\nu}{2\pi}\right)^{1/2}\exp\left(-\frac{a\nu}{2}\right), \tag{F.3.12}$$

where $a \simeq 0.7$, $p = 0.3$, and A is determined by the requirement that all mass lies within a given halo, i.e. $\int \mathrm{d}\nu f(\nu) = 1$ or equivalently $\int \mathrm{d}MM\mathrm{d}n/\mathrm{d}M = \bar{\rho}_0$.

The density profile of dark matter halos

Since the rate of DM annihilation scales with density squared, it depends sensitively on the density profile of each halo. We consider three universal density profiles to model the smooth distribution of DM within each halo (substructure will be dealt with later in this section). Firstly, we consider the popular profile proposed by Navarro, Frenk and White (1996, 1997) (NFW), which corresponds to $\alpha = 1$, $\beta = 3$ and $\gamma = 1$ in Eq.(F.3.2). Secondly, we consider a profile with a significantly larger slope, specifically the one proposed by Moore et al. (1999), corresponding to $\alpha = 1.5$, $\beta = 3$ and $\gamma = 1.5$. Both of these profiles have the same functional form and are both singular towards the Galactic centre (in fact, the slope of the Moore profile must necessarily be truncated for $r < r_{\rm min.}$, where $r_{\rm min.} \sim 0$ - see below, otherwise the integral of density squared will diverge). However, there have been indications that cuspy profiles are inconsistent with observations, specifically regarding the rotation curves of small-scale galaxies (Flores and Primack, 1994; Moore, 1994; Weldrake et al., 2003; Donato and Salucci, 2004; Gentile et al., 2007), which are more likely to be consistent with density profiles possessing flattened cores similar to that which may be achieved with WDM (Hogan and Dalcanton, 2000; Colin et al., 2008). Therefore, we lastly consider the Burkert density profile (Burkert, 1996):

$$\rho(r) = \frac{\rho_s}{[1 + (r/r_s)]\,[1 + (r/r_s)^2]}, \tag{F.3.13}$$

which has been shown to be fairly consistent with the rotation curves of a large number of spiral galaxies (Salucci and Burkert, 2000).

Concentration-mass relation for dark matter halos

Here we introduce the virial concentration parameter $c_{\rm vir.}$, defined by $c_{\rm vir.} = r_{\rm vir.}/r_s$, where r_s is the scale radius defined above and $r_{\rm vir.}$ is the virial radius of the halo. The latter is defined as the radius encapsulating the virial mass M of the halo within which the average density is equal to the overdensity $\Delta_{\rm vir.}$ times the average cosmological density $\bar{\rho}(z)$ at that redshift

$$M = \frac{4\pi}{3}\Delta_{\rm vir.}\bar{\rho}(z) r^3_{\rm vir.}. \tag{F.3.14}$$

For $\Delta_{\rm vir.}$, we use the approximation provided in Tegmark et al. (2006a), namely $\Delta_{\rm vir.} \simeq 18\pi^2 + 52.8x^{0.7} + 16x$, where $x(z) = \Omega_\Lambda(z)/\Omega_{\rm M}(z)$, ($\Delta_{\rm vir.} \simeq 311$ at $z = 0$ for $\Omega_{\rm M} = 0.3$ and $\Omega_\Lambda = 0.7$). This is accurate to within 4% of the exact numerical calculation at relevant times.

There has been evidence from simulations revealing a strong correlation between the halo mass M and its corresponding concentration $c_{\rm vir.}$, with larger concentrations in smaller mass halos, which is consistent with the idea of bottom-up hierarchical structure formation with smaller halos collapsing at earlier times when the average density of the Universe was much greater (Navarro et al., 1996, 1997). This relationship was later re-affirmed by Bullock et al. (2001) (B2001 hereafter) using a sample of simulated halos in the mass range $10^{11} \lesssim M/h^{-1}M_\odot \lesssim 10^{14}$, who proposed a toy model to describe this behaviour, which is popular in the relevant literature: on average, a collapse redshift z_c is assigned to each halo of mass M through the relation $M_* = FM$, where at a redshift z the typical collapsing mass $M_*(z)$ is defined implicitly by the relation $\sigma(M_*(z)) = \delta_{sc}(z)$ and is postulated to be a fixed fraction F of M, which, following Wechsler et al. (2002), we set equal to 0.015. The density of the Universe at redshift z_c is then associated with a characteristic density of the halo at redshift z. Therefore, here we use the average concentration-mass relation obtained using the above method, which is given by

$$c_{\mathrm{vir.}}(M,z) = K\frac{1+z_c}{1+z} = \frac{c_{\mathrm{vir.}}(M,z=0)}{1+z} \tag{F.3.15}$$

where $K \simeq 5$, for $\Omega_\Lambda = 0.742$, $\Omega_{\mathrm{M}} = 0.258$, $h = 0.719$ and $\sigma_8 = 0.796$ (Dunkley et al., 2009).

Since this relation has been derived for halos with a minimum mass of $\sim 10^{11} M_\odot$, the extrapolation to very small values of the mass, down to the mass associated with the DM free streaming length (that we take to be as small as $\sim 10^{-12} M_\odot$), could be unreliable, since small mass halos become increasingly concentrated. For this reason, following Ullio et al. (2002), we introduce a cut-off mass M_{cut} such that $c_{\mathrm{vir.}}(M,z) = c_{\mathrm{vir.}}(M_{\mathrm{cut}},z)$ for $M < M_{\mathrm{cut}}$. In the following, we will either take M_{cut} equal to the mass of the smallest DM halos (i.e. no cut-off) or equal to $10^6 M_\odot$, which is the typical (mass) resolution of current numerical simulations of Galaxy-sized DM halos.

Clumping factor for smooth halos

We are now able to calculate the clumping factor $C(z)$ attributed to extra-galactic halos with smooth DM density profiles and concentrations. We start by calculating the annihilation rate $R(M,z)$ within a DM halo of mass M located at redshift z given by

$$R(M,z) = \frac{1}{2}\frac{\langle\sigma_{\mathrm{ann.}}v\rangle}{m_{\mathrm{DM}}^2}\int\limits_{r=0}^{r_{\mathrm{vir.}(M,z)}} \rho^2(r)4\pi r^2 \mathrm{d}r. \tag{F.3.16}$$

The integral in (F.3.16) can be expressed in analytical form for the NFW and Moore profiles; we present the relevant formulas in Appendix F.3.4. In the case of the Moore profile, however, in order for the integral over density squared to be finite, the density must be truncated below a radius $r_{\mathrm{min.}}$.

To obtain a value for $r_{\mathrm{min.}}$ we assume that, within some minimum distance from the center of the halo, most of the neutralino DM has self-annihilated, leaving a flattened density core. The size of the core is roughly determined by the condition that within it the time-scale for DM annihilation, $t_{\mathrm{ann.}} \sim (n_\varnothing\langle\sigma_{\mathrm{ann.}}v\rangle)^{-1}$, should be smaller than the average time-scale $t_{\mathrm{in.}}$ for the replenishment of the core owing to the infall of DM from larger radii. Then $r_{\mathrm{min.}}$ will be defined as the radius where $t_{\mathrm{ann.}} \simeq t_{\mathrm{in.}}$. We do not try to estimate

$t_{\rm in.}$; instead, since we must have $t_{\rm in.} \ll t_h$, where $t_h \sim 10^{17}\,{\rm s}$ is the Hubble time, we have that within the core $n_{\varnothing}\langle\sigma_{\rm ann.}v\rangle \gg {t_h}^{-1}$, and since the density decreases monotonically with increasing radius we can obtain a conservative upper limit for $r_{\rm min.}$ from the condition $n_{\varnothing}\langle\sigma_{\rm ann.}v\rangle \simeq t_h^{-1}$. Then, we adopt the conservative criterion $(\rho_{\varnothing}r_{\rm min.}/m_\chi)\langle\sigma_{\rm ann.}v\rangle \sim t_h^{-1}$, with canonical values of the neutralino mass and annihilation cross section of $m_\chi \sim 100\,{\rm GeV}$ and $\langle\sigma_{\rm ann.}v\rangle \sim 10^{-26}\,{\rm cm}^3\,{\rm s}^{-1}$. This sets an upper limit for $x_{\rm min.}$ which is $\sim 10^{-8}$ for the Galactic halo at present day, which is consistent with similar approximations by other authors (see, e.g., Taylor and Silk (2003)).

Then, it follows from Eq.(F.3.9) that the contribution to the DM annihilation rate per unit volume, $\Gamma_{\rm halos}(z)$, by halos located at redshift z is

$$\Gamma_{\rm halos}(z) = \frac{1}{2}\frac{\langle\sigma_{\rm ann.}v\rangle}{m_{\rm DM}^2}(1+z)^3 \times \int\limits_{M=M_{\rm min.}}^{M_{\rm max.}} {\rm d}M\frac{{\rm d}n}{{\rm d}M}(M,z) \int\limits_{r=0}^{r_{\rm vir.(M,z)}} \rho^2(r)4\pi r^2{\rm d}r. \tag{F.3.17}$$

The corresponding rate of DM annihilation per unit volume contributed by the smooth background density at redshift z is given by

$$\Gamma_{\rm smooth}(z) = \frac{1}{2}\frac{\langle\sigma_{\rm ann.}v\rangle}{m_{\rm DM}^2}\bar{\rho}_{\rm DM}^2(z), \tag{F.3.18}$$

where $\rho_{\rm DM}(z) = \rho_{c,0}\Omega_{\rm DM,0}(1+z)^3$. Therefore, we define the *clumping factor* for smooth halos, $C_{\rm halo}(z)$, as

$$\begin{aligned} C_{\rm halo}(z) &\equiv 1 + \frac{\Gamma_{\rm halo}(z)}{\Gamma_{\rm smooth}(z)} = \\ &= 1 + \frac{(1+z)^3}{\bar{\rho}_{\rm DM}^2(z)} \\ &\times \int\limits_{M=M_{\rm min.}}^{M_{\rm max.}} {\rm d}M\frac{{\rm d}n}{{\rm d}M}(M,z) \int\limits_{r=0}^{r_{\rm vir.(M,z)}} \rho^2(r)4\pi r^2{\rm d}r, \end{aligned} \tag{F.3.19}$$

so that $C_{\rm halo}(z) \to 1$ for a completely smooth universe.

In Fig. F.13 we display plots of $C_{\rm halo}(z)$ as a function of z for halos with NFW profiles (top panel), Moore profiles (central panel) and Burkert profiles (bottom panel). Halos with cuspy density profiles, such as the NFW and

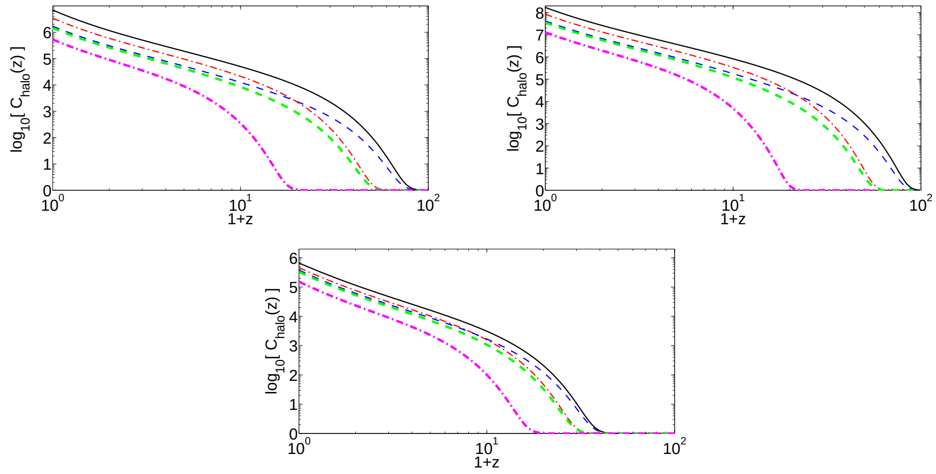

Figure F.13.: Clumping factor as a function of redshift for DM halos with mass $M > M_{\mathrm{min.}}$ with smooth NFW (upper panel), Moore (central panel) and Burkert (bottom panel) DM density profiles with a $c_{\mathrm{vir.}} - M$ relation, truncated at a halo mass M_{cut}. The displayed curves correspond to values of $(M_{\mathrm{min.}}/M_\odot, M_{\mathrm{cut}}/M_\odot)$ of $(10^{-12}, 10^{-12})$ (thin black solid), $(10^{-12}, 10^{6})$ (thin blue dashed), $(10^{-4}, 10^{-4})$ (thin red dot-dashed), $(10^{-4}, 10^{6})$ (thick green dashed) and $(10^{6}, 10^{6})$ (thick magenta dot-dashed) for the NFW and Moore profiles, and equal to $(0.16, 0.16)$ (thin black solid), $(0.16, 10^{6})$ (thin blue dashed), $(46, 46)$ (thin red dot-dashed), $(46, 10^{6})$ (thick green dashed) and $(10^{6}, 10^{6})$ (thick magenta dot-dashed) for the Burkert profile.

Moore profiles, are typical of CDM halos for which the minimum mass cut-off scale in the matter power spectrum is determined by collisional damping and free streaming in the early Universe. For WIMP DM the value of $M_{\mathrm{min.}}/M_\odot$ can range from 10^{-12} to 10^{-4} for typical kinetic decoupling temperatures. Hence in the upper panels of Fig. F.13 we illustrate the effect on the clumping factor for values of $M_{\mathrm{min.}}/M_\odot$ of $10^{-12}, 10^{-4}$ and 10^{6}, where, as mentioned above, the latter value is the typical minimum mass of resolved subhalos in numerical simulations of Galactic halos. We also demonstrate the influence of truncating the Bullock *et al.* concentration-mass relation (referred to as the "B2001 relation" hereafter) below a mass of $10^{6} M_\odot$, as well as using the relation when extrapolated to $M_{\mathrm{min.}}$.

In the bottom panel of Fig. F.13 we show the clumping factor for halos with flattened cores like the ones possibly formed by WDM. In particular, we plot C_{halo} for minimum halo masses $M_{\mathrm{min.}} \simeq 46\, M_\odot$ and $0.16 M_\odot$, corresponding to the values of the damping mass (F.3.8), obtained using $m_{\mathrm{WDM}} = 3\,\mathrm{MeV}$ and $m_{\mathrm{WDM}} = 20\,\mathrm{MeV}$ respectively. The selected values of m_{WDM} correspond to the respective upper limits on the LDM particle mass from constraints on inner bremsstrahlung gamma ray flux from the galactic centre (Beacom et al.,

2005) (although see Boehm and Uwer (2006)), and from in-flight annihilation (Beacom and Yuksel, 2006) between positrons from LDM annihilation and electrons in the interstellar medium.

An analysis of Fig. F.13 reveals some interesting trends. Firstly, Moore profiles tend to yield larger clumping factors than NFW profiles, which in turn yield larger clumping factors than Burkert profiles. This is clearly related to the relative cuspiness of the three profiles and the fact that DM annihilations are enhanced in higher-density regions. In general, we have that C_{halo} at $z = 10$ is between 10^4 and 10^6 for Moore profiles, 10^3 and 10^5 for NFW profiles, and 10^2 and 10^4 for Burkert profiles. Secondly, we observe that the smaller the value of $M_{\text{min.}}$ the sooner the clumping factor starts to deviate from unity and the larger the clumping factor is at present day. This is due to the contribution in the integral in Eq.(F.3.17) of the smaller halos, that form earlier, and are thus denser, than larger halos. It is however worth stressing that the mass function and the concentration parameters have not been well measured for these extremely small, high-z halos. Finally, when the Bullock et al. relation is truncated at a value $M_{\text{cut}} = 10^6\, M_\odot > M_{\text{min.}}$, the clumping factor is smaller. In particular, this roughly amounts to an order of magnitude difference at $z = 10$ for the NFW and Moore profiles with $M_{\text{min.}} = 10^{-12} M_\odot$, and, as can be expected, the difference is smaller for larger values of $M_{\text{min.}}$ and in the case of Burkert profiles.

Clumping factor for halos possessing sub-halos and sub-sub halos

Thus far we have considered the amplification of the DM annihilation rate for isolated halos with smooth density profiles. However, as already mentioned, N-body simulations indicate that a significant proportion of the smaller progenitors giving rise to larger mass halos survive the merging processes and the tidal forces exerted upon them during their orbital motion within halos. In particular, the Via Lactea II ΛCDM simulations of Galactic halos presented in Diemand et al. (2008) and in Kuhlen, Diemand and Madau (2008) (KDM hereafter), revealed a second generation of surviving substructures within halos (designated as "sub-subhalos"). Further, these simulations suggest that the mass distribution of sub-subhalos within their host subhalo is approximately the same as the mass distribution of subhalos within their host halo[12].

Since the DM annihilation rate scales with density squared, these subhalos and sub-subhalos could provide significant enhancement to the annihilation rate, even for modest substructure mass fractions, within halos/subhalos. For halos of mass M these have been suggested to be as much as 10% for subhalo masses M_s in the range $10^{-5} < M_s/M < 10^{-2}$ (Diemand et al., 2008) (which approximately corresponds to a constant mass fraction per subhalo

[12]Once again, we remind the reader that there are results from the more recent Aquarius simulations Springel et al. (2008a,b) that are in contention with these results (see § F.3.9).

mass decade of 3%, owing to the fact that the subhalo mass function has a slope of approximately 2 - see below). However, owing to the fact that substructures invariably form earlier than their host halos, and that tidal disruption is unlikely to effect the inner density profiles of structures (i.e. where the majority of the enhancement originates), the concentration of substructures may be significantly greater than that of their host halos. The simulation results recently presented in KDM are consistent with the ratio $N_c = c_{\mathrm{vir.}}^{\mathrm{halo}}/c_{\mathrm{vir.}}^{\mathrm{subhalo}} \simeq 3$ for subhalos located at solar radii within galactic halos[13], whilst the numerical simulations of Bullock *et al.* show that, on average, $N_c \simeq 1.5$ for halos of mass $M \sim 5 \times 10^{11} M_{\odot}$ (B2001).

Here we calculate the contribution to the clumping factor by halos possessing substructures with a self-similar mass distribution. Consider a DM halo of mass M with a subhalo mass distribution function given by

$$\frac{\mathrm{d}N(M)}{\mathrm{d}M_{\mathrm{s}}} \propto M_{\mathrm{s}}^{-\beta}, \tag{F.3.20}$$

where the index β is assumed to be time-independent and approximately equal to 2, i.e. equal mass per decade in subhalos (KDM). Whilst we adopt a minimum subhalo mass equal to the minimum halo mass, $M_{\mathrm{min.}}$, for which we utilise several values as discussed above, we utilise an upper limit on M_{s} of $10^{-2}M$, where M is the mass of the host halo, a choice motivated by recent numerical simulations (see, e.g., Diemand et al. (2008)).

There are indications that β may slightly deviate from this value, particularly for WDM substructures, for which Knebe et al. (2008) claim that β may be as small as 1.6. However, as shown in Fig. F.14, the effect on the clumping factor by varying β slightly from 2 is small at the times of interest. We therefore adopt the value $\beta = 2$ for both CDM and WDM. Consequently, each subhalo mass decade contributes a constant fraction $F_{\mathrm{sub.}}$ of the halo mass.

Adopting a course of reasoning analogous to that used to derive Eq. (F.3.16), the rate of DM annihilations within a similar halo, solely due to the subhalos

[13] Although N_c demonstrates a slight galactocentric radial dependence, the authors of KDM claim that the effect on the overall annihilation rate is negligible.

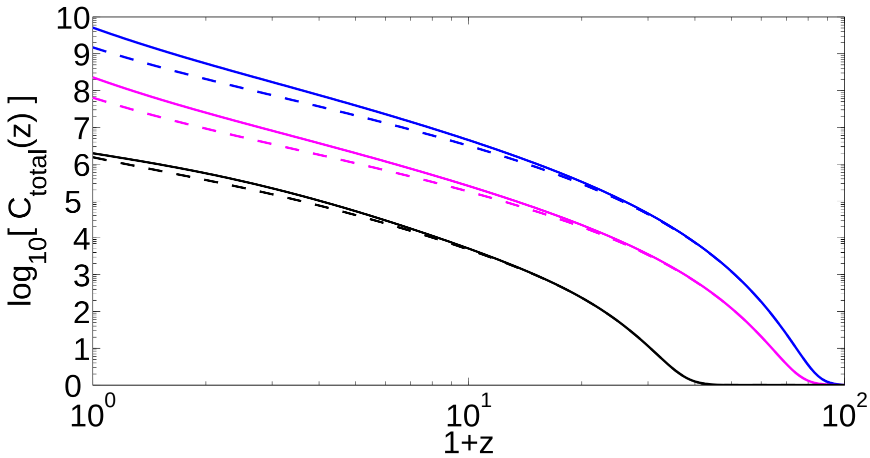

Figure F.14.: Total clumping factor from halos and subhalos $C_{\text{total.}}(z) = 1 + C_{\text{halos}}(z) + C_{\text{subhalos}}(z)$, for different values of the substructure mass function index β. We show the values of C_{total} for structures with NFW (purple) and Moore (blue) density profiles for $\beta = 2$ and 1.8 (solid and dashed curves respectively) and $\beta = 2$ and 1.6 for the Burkert profile (black solid and dashed curves respectively). We take $M_{\text{cut}} = M_{\text{min.}} = 10^{-12}\,M_\odot$ for NFW and Moore profiles and $0.16\,M_\odot$ for Burkert profiles. In all cases $F_{\text{sub.}} = 3\%$, $N_c = 3$.

within it, possessing smooth density profiles $\rho(r)$, is then given by

$$\begin{aligned} R_{\text{sub.}}(M,z) &= \frac{\langle \sigma_{\text{ann.}} v \rangle}{2m_{\text{DM}}^2} \int\limits_{M_{\text{s}}=M_{\text{min.}}}^{10^{-2}M} \mathrm{d}M_{\text{s}} \frac{\mathrm{d}N(M, F_{\text{sub.}})}{\mathrm{d}M_{\text{s}}} \\ &\times \int\limits_{r=0}^{r_{\text{vir.}}(z,M_{\text{s}})} \rho^2(r, c_{\text{vir.}}^{\text{sub.}}[M_{\text{s}}, z]) 4\pi r^2 \mathrm{d}r \\ &= \frac{\langle \sigma_{\text{ann.}} v \rangle}{2m_{\text{DM}}^2} A(M, F_{\text{sub.}}) \int\limits_{M_{\text{s}}=M_{\text{min.}}}^{10^{-2}M} \mathrm{d}M_{\text{s}} M_{\text{s}}^{-\beta} \\ &\times \int\limits_{r=0}^{r_{\text{vir.}}(z,M_s)} \rho^2(r, c_{\text{vir.}}^{\text{sub.}}[M_s, z]) 4\pi r^2 \mathrm{d}r, \end{aligned} \tag{F.3.21}$$

where A is the appropriate normalisation of $\mathrm{d}N/\mathrm{d}M_{\text{s}}$. The subhalo scale density can be obtained from the expressions (F.3.29) or (F.3.32) for NFW and Moore profiles respectively, with the substitutions $c_{\text{vir.}} \to c_{\text{vir.}}^{\text{sub.}}$ and $M \to M_{\text{s}}$. Then integrating this contribution over all halos at redshift z we obtain the annihilation rate for all subhalos residing within such halos

$$\begin{aligned}\Gamma_{\text{subhalos}}(z) = (1+z)^3 & \\ \times \int\limits_{M=M_{\text{min.}}}^{M_{\text{max.}}} & \mathrm{d}M \frac{\mathrm{d}n(M,z)}{\mathrm{d}M} R_{\text{sub.}}(M,z,F_{\text{sub.}}) \\ = & \frac{\langle \sigma_{\text{ann.}} v \rangle}{2m_{\text{DM}}^2}(1+z)^3 \\ \times \int\limits_{M=M_{\text{min.}}}^{M_{\text{max.}}} & \mathrm{d}M \frac{\mathrm{d}n(M,z)}{\mathrm{d}M} A(M,F_{\text{sub.}}) \\ \times \int\limits_{M_{\text{s}}=M_{\text{min.}}}^{10^{-2}M} & \mathrm{d}M_{\text{s}} M_{\text{s}}^{-\beta} \\ \times \int\limits_{r=0}^{r_{\text{vir}}(z,M_{\text{s}})} & \rho^2(r, c_{\text{vir}}^{\text{sub}}[M_{\text{s}}, z]) 4\pi r^2 \mathrm{d}r,\end{aligned} \tag{F.3.22}$$

and we obtain the associated subhalo clumping factor

$$\begin{aligned}C_{\text{subhalos}} &= 1 + \frac{\Gamma_{\text{subhalos}}(z)}{\Gamma_{\text{smooth}}(z)} \\ &= 1 + \frac{(1+z)^3}{\bar{\rho}_{\text{DM}}^2(z)} \int\limits_{M=M_{\text{min.}}}^{M_{\text{max.}}} \mathrm{d}M \frac{\mathrm{d}n(M,z)}{\mathrm{d}M} A(M,F_{\text{sub.}}) \\ &\times \int\limits_{M_{\text{s}}=M_{\text{min.}}}^{10^{-2}M} \mathrm{d}M_{\text{s}} M_{\text{s}}^{-\beta} \\ &\times \int\limits_{r=0}^{r_{\text{vir.}}(z,M_{\text{s}})} \rho^2(r, c_{\text{vir.}}^{\text{sub.}}[M_{\text{s}}, z]) 4\pi r^2 \mathrm{d}r.\end{aligned} \tag{F.3.23}$$

However as mentioned above, each subhalo is likely to itself host substructures with mass function approximately equal to

$$\frac{\mathrm{d}N}{\mathrm{d}M_{\text{ss}}} = A(M_{\text{s}}, F_{\text{ss}}, \beta) M_{\text{s}}^{-\beta_{\text{ss}}}. \tag{F.3.24}$$

Owing to the near self-similar nature of the mass distribution of substructures within halos, we take the values of the index $\beta_{\rm ss}$ and the sub-subhalo mass fraction per mass decade $F_{\rm ss}$ to be equal to β and $F_{\rm sub.}$ respectively. Hence, following the above treatment for halos and their constituent subhalos, the clumping factor for all sub-subhalos with virial concentration $c^{\rm ss}_{\rm vir.}$residing within subhalos, themselves residing within halos located at redshift z, is given by

$$\begin{aligned} C_{\rm sub-subhalos} = 1 + \frac{(1+z)^3}{\bar{\rho}^2_{\rm DM}(z)} & \int\limits_{M=M_{\rm min.}}^{M_{\rm max.}} {\rm d}M \frac{{\rm d}n(M,z)}{{\rm d}M} \\ \times A(M_{\rm s}, F_{\rm s}) & \int\limits_{M_{\rm s}=M_{\rm min.}}^{10^{-2}M} {\rm d}M_{\rm s} M_{\rm s}^{-\beta} \\ \times A(M_{\rm ss}, F_{\rm ss}) & \int\limits_{M_{\rm ss}=M_{\rm min.}}^{10^{-2}M_{\rm s}} {\rm d}M_{\rm ss} M_{\rm ss}^{-\beta_{\rm ss}} \\ \times & \int\limits_{r=0}^{r_{\rm vir.}(z,M_{\rm s})} \rho^2(r, c^{\rm ss}_{\rm vir.}[M_{\rm ss}, z]) 4\pi r^2 {\rm d}r. \end{aligned} \tag{F.3.25}$$

where, analogous for subhalos, for a given host subhalo of mass $M_{\rm s}$ and minimum permitted mass $M_{\rm min.}$, we allow for sub-subhalo masses in the range $M_{\rm min.} \leq M_{\rm ss} \leq 10^{-2} M_{\rm s}$.

Finally, using Eqs. (F.3.23) and (F.3.25), we obtain the total clumping factor for all structures at redshift z

$$\begin{aligned} C_{\rm total} = 1 &+ (C_{\rm halo}(z) - 1) \\ &+ (C_{\rm subhalos}(z) - 1) \\ &+ (C_{\rm sub-subhalos}(z) - 1), \end{aligned} \tag{F.3.26}$$

where it should be understood that the normalisation of expressions $C_{\rm halo}$ and $C_{\rm subhalos}$ is modified to take into account the fact that a specified percentage of the mass of each halo and subhalo is provided by smaller substructures.

In Fig. F.15 we show the total clumping factor as a function of z for halos with NFW profiles (left panel), Moore profiles (central panel) and Burkert profiles (right panel). We find the same trends as in the case of smooth halos. However, the presence of substructures boosts the clumping factor, more effectively so for cuspier (i.e. Moore and NFW) profiles and for smaller values of $(M_{\rm min.}, M_{\rm cut})$. In particular, we find that $C_{\rm halo}$ at $z = 10$ is in the range between 10^4 and 10^8 for Moore profiles, between 10^3 and 10^6 for NFW profiles,

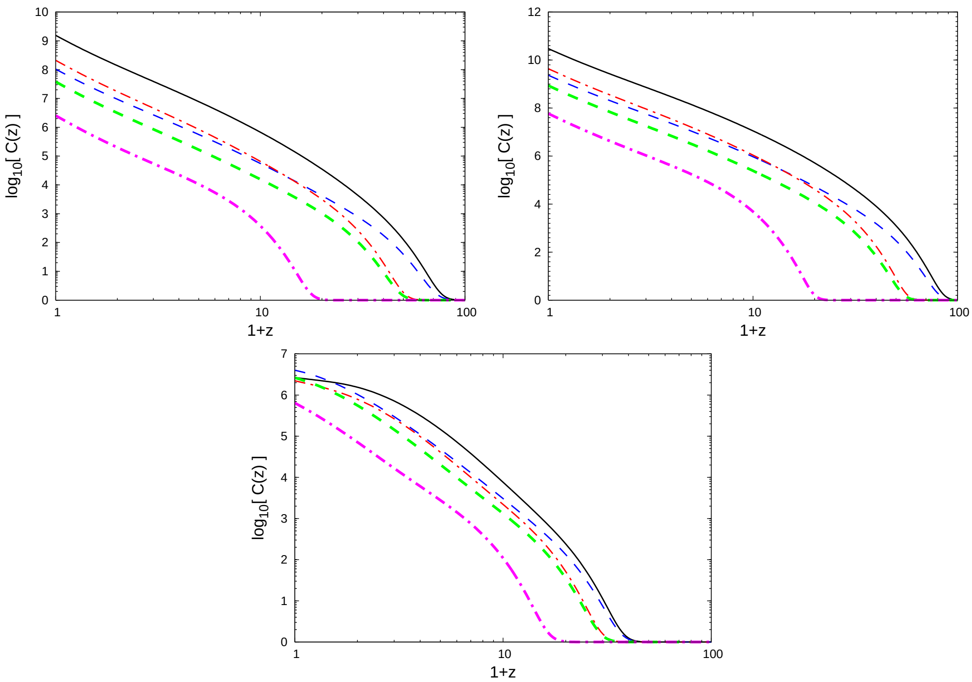

Figure F.15.: Plots of $C_{\text{total}}(z)$ for structures with NFW (top panel), Moore (central panel) and Burkert (bottom panel) density profiles with subhalo and sub-subhalo mass fractions per decade $F_{\text{sub.}}$ and F_{ss} of 0.03, and a relative concentration ratio N_c of 3.0. The different curves correspond to different values of $(M_{\text{min.}}/M_{\odot}, M_{\text{cut}}/M_{\odot})$, as in Fig. F.13.

and between 10^2 and $\sim 10^4$ for Burkert profiles.

From the recursive structure of Eq.(F.3.25), one can easily observe how to extend the present scenario to include higher generations of substructures, but since there is no evidence for such structures we omit them in this study. Moreover, we have found that the relative contribution of halos, subhalos and sub-subhalos to $C_{\text{total}}(z)$ is increasingly smaller at the redshifts of interest for realistic values of the concentration ratio N_c and substructure fraction F_{sub} such that further generations of substructures, if they exist, are unlikely to increase $C_{\text{total}}(z)$ by more than a few percent.

Analytical expressions for the halo annihilation rate

In this appendix we report the analytical formulas for the annihilation rate within halos with NFW and Moore DM density profiles. For the Burkert profile, it is not possible to express the relevant integrals in analytical form.

Applying Eq. (F.3.16) to the case of a halo of mass M with an NFW profile with concentration $c_{\text{vir.}}(M,z)$, the annihlation rate $R(M,z)$ is easily calculated to be

$$R(M,z) = \frac{1}{2}\langle\sigma_{\text{ann.}}v\rangle\left(\frac{\rho_s}{m_{\text{DM}}}\right)^2\frac{4\pi}{3}\left(\frac{r_{\text{vi.r}}(z,M)}{c_{\text{vir.}}(z,M)}\right)^3 \times\left\{1-\frac{1}{[1+c_{\text{vir.}}(M,z)]^3}\right\}. \tag{F.3.27}$$

By equating (F.3.14), for the virial mass, M, to the integral

$$\begin{aligned} M &= \int_{r=0}^{r_{\text{vir.}}}\rho(r,c_{\text{vir.}}(M,z))4\pi r^2\mathrm{d}r \\ &= 4\pi\left(\frac{r_{\text{vir.}}}{c_{\text{vir.}}(M,z)}\right)^3\rho_s(M,z) \\ &\times\left[\log\left[1+c_{\text{vir.}}(z,M)\right]-\left(\frac{c_{\text{vir.}}(z,M)}{[1+c_{\text{vir.}}(z,M)]}\right)\right], \end{aligned} \tag{F.3.28}$$

we obtain the relation for the scale density

$$\rho_s(M,z) = \frac{M}{4\pi\left(\frac{r_{\text{vir.}}}{c_{\text{vir.}}(M,z)}\right)^3} \times\frac{1}{\left[\log\left[1+c_{\text{vir.}}(z,M)\right]-\left(\frac{c_{\text{vir.}}(z,M)}{[1+c_{\text{vir}}(z,M)]}\right)\right]}. \tag{F.3.29}$$

For the Moore profile, in order for the integral over density squared to be finite we must truncate the density below a radius $r_{\text{min.}}$ (see discussion in § F.3.4). Defining the variable $x = rc_{\text{vir.}}/r_{\text{vir.}}$ with $x_{\text{min.}} = r_{\text{min.}}c_{\text{vir.}}/r_{\text{vir.}}$ we find that for a Moore profile

$$R(M,z) = \frac{1}{2}\frac{\langle\sigma_{\text{ann.}}v\rangle}{\bar{n}_b(z)}\left(\frac{\rho_s}{m_{\text{DM}}}\right)^2\frac{4\pi}{3}\left(\frac{r_{\text{vir.}}(z,M)}{c_{\text{vir.}}(z,M)}\right)^3 \times F_1(c_{\text{vir.}},x_{\text{min.}}), \tag{F.3.30}$$

where

$$F_1(c_{\text{vir.}}, x_{\text{min.}}) = \frac{1}{3}\frac{1}{(1+x_{\text{min.}})^2} + \frac{1}{1.5}\left[\log\left(\frac{c_{\text{vir.}}^{1.5}(1+x_{\text{min.}}^{1.5})}{x_{\text{min.}}^{1.5}(1+c_{\text{vir.}}^{1.5})}\right)\right] + \frac{1}{1.5}\left[\frac{1}{1+c_{\text{vir.}}^{1.5}} - \frac{1}{1+x_{\text{min.}}^{1.5}}\right], \tag{F.3.31}$$

and

$$\rho_s(M,z) = \frac{M}{4\pi\left(\frac{r_{\text{vir.}}}{c_{\text{vir.}}(M,z)}\right)^3} \times \left[\frac{1}{1.5}\log\left(\frac{1+c_{\text{vir.}}^{1.5}}{1+x_{\text{min.}}^{1.5}}\right) + \frac{1}{3}\frac{x_{\text{min.}}^{1.5}}{(1+x_{\text{min.}}^{1.5})}\right]^{-1} \equiv \frac{M}{4\pi\left(\frac{r_{\text{vir.}}}{c_{\text{vir.}}(M,z)}\right)^3 F_2(c_{\text{vir.}}, x_{\text{min.}})} \tag{F.3.32}$$

respectively.

Clumping factor parameters

In this section we conveniently list the relevant parameters associated with each of the clumping factors utilised throughout this study, for clumping factors calculated using structures possessing NFW (Table F.6) and Moore (Table F.7) DM density profiles for our four neutralino DM models, and for Burkert profiles using our two LDM candidates (Table F.8).

F.3.5. Energy absorbed fraction

A key quantity entering our computations is the fraction $f_{\text{abs.}}$ of energy produced in each DM annihilation that is effectively absorbed by the IGM. In fact, taking $f_{\text{abs.}} = 1$ would be quite a poor approximation as sometimes just a very small fraction of the total energy actually goes into the heating/ionisation of the IGM. We describe in detail the method used to compute $f_{\text{abs.}}$ in Appendix F.3.5; here we describe the annihilation spectra used for the different particle physics models that we adopt, provide some qualitative arguments to gain a physical insight on the mechanisms that lead to the absorption of

	$n_{\text{min.}}$	n_{cut}	$F_{\text{sub.}}, F_{\text{ss}}$ (%)	N_c	Model 1	Model 2	Model 3	Model 4
N0[14]	–	–	–	–	−0.022	−0.007	−0.007	−0.001
N1	−12	−12	3	3	–	–	–	–
N2	−12	−12	3	1.5	–	2.35	3.72	−1.12
N3	−12	−12	0.3	3	–	1.89	3.16	−1.07
N4	−12	−12	0.3	1.5	18.0	1.28	2.41	−0.987
N5	−12	6	3	3	–	–	−0.905	−0.671
N6	−12	6	3	1.5	3.95	−1.26	−1.23	−0.366
N7	−12	6	0.3	3	4.25	−1.28	−1.23	−0.379
N8	−12	6	0.3	1.5	3.87	−1.25	−1.22	−0.360
N9	−4	−4	3	3	–	–	–	−0.587
N10	−4	−4	3	1.5	4.15	−1.59	−1.59	−0.417
N11	−4	−4	0.3	3	3.83	−1.57	−1.58	−0.401
N12	−4	−4	0.3	1.5	3.59	−1.55	−1.56	−0.387
N13	−4	6	3	3	–	−1.10	−1.22	−0.199
N14	−4	6	3	1.5	−0.993	−0.925	−1.04	−0.162
N15	−4	6	0.3	3	−1.02	−0.927	−1.04	−0.162
N16	−4	6	0.3	1.5	−1.04	−0.912	−1.03	−0.159
N17	6	6	3	3	−0.034	−0.009	−0.009	−0.002
N18	6	6	3	1.5	−0.034	−0.009	−0.009	−0.002
N19	6	6	0.3	3	−0.033	−0.009	−0.009	−0.002
N20	6	6	0.3	1.5	−0.033	−0.009	−0.009	−0.002

Table F.6.: Parameters used for the calculation of the clumping factors for structures with NFW DM density profiles.
Column (1) - clumping factor label;
Column (2) - $n_{\text{min.}} = \log(M_{\text{min.}}/M_\odot)$, where $M_{\text{min.}}$ is the minimum halo mass considered [see Eq. (F.3.9)];
Column (3) - $n_{\text{cut}} = \log(M_{\text{cut}}/M_\odot)$, where M_{cut} is the mass below which the concentration-mass relation for halos is truncated;
Column (4) - percentage of the host halo (subhalo) mass contributed by each subhalo (sub-subhalo) mass decade
Column (5) - ratio of concentrations for a subhalo and halo of the same mass located at the same redshift;
Column (6 - 9) - value of the difference in the differential brightness temperature relative to the standard “no DM” scenario, $\delta T_b - \delta T_{b,0}$ (mK), evaluated at redshift $z = 30$ in the four SUSY models described in the text. A dash – indicates that the model does not satisfy the constraints on the reionization redshift and/or on the diffuse gamma background (see Sec. F.3.7 for details).

	$n_{\text{min.}}$	n_{cut}	$F_{\text{sub.}}, F_{\text{ss}}$ (%)	N_c	Model 1	Model 2	Model 3	Model 4
M0[15]	–	–	–	–	−0.022	−0.007	−0.007	−0.001
M1	−12	−12	3	3	–	–	–	–
M2	−12	−12	3	1.5	–	–	–	–
M3	−12	−12	0.3	3	–	–	–	–
M4	−12	−12	0.3	1.5	–	–	–	6.69
M5	−12	6	3	3	–	–	–	–
M6	−12	6	3	1.5	–	–	–	−0.912
M7	−12	6	0.3	3	–	–	11.3	−0.860
M8	−12	6	0.3	1.5	–	8.61	10.6	−0.910
M9	−4	−4	3	3	–	–	–	–
M10	−4	−4	3	1.5	–	–	–	–
M11	−4	−4	0.3	3	–	–	–	−1.20
M12	−4	−4	0.3	1.5	–	–	–	−1.23
M13	−4	6	3	3	–	–	3.62	–
M14	−4	6	3	1.5	–	–	2.09	−1.21
M15	−4	6	0.3	3	–	–	2.19	−1.22
M16	−4	6	0.3	1.5	–	0.893	2.06	−1.20
M17	6	6	3	3	–	−0.025	−0.029	−0.004
M18	6	6	3	1.5	−0.147	−0.025	−0.029	−0.004
M19	6	6	0.3	3	−0.147	−0.025	−0.029	−0.004
M20	6	6	0.3	1.5	−0.147	−0.025	−0.029	−0.004

Table F.7.: Same as for Table F.6 but for clumping factors associated with structures possessing Moore density profiles.

	n_{min}	n_{cut}	$F_{\mathrm{sub,ss}}(\%)$	N_c	20 MeV $\langle\sigma v\rangle_{28}$[16] $= 4.4$	20 MeV $\langle\sigma v\rangle_{2}8 = 0.44$	3 MeV $\langle\sigma v\rangle_{2}8 = 1.2$	3 MeV $\langle\sigma v\rangle_{2}8 = 0.12$
B0[17]	–	–	–	–	−0.022	−0.007	−0.007	−0.001
B1	−0.80	−0.80	3	3	–	–	–	–
B2	−0.80	−0.80	3	1.5	–	–	–	–
B3	−0.80	−0.80	0.3	3	–	20.2	–	–
B4	−0.80	−0.80	0.3	1.5	–	20.0	–	–
B5	−0.80	6	3	3	–	–	–	–
B6	−0.80	6	3	1.5	–	13.1	–	–
B7	−0.80	6	0.3	3	–	12.8	–	–
B8	−0.80	6	0.3	1.5	–	12.8	–	–
B9	1.66	1.66	3	3	–	–	–	–
B10	1.66	1.66	3	1.5	–	–	–	–
B11	1.66	1.66	0.3	3	–	–	–	−1.81
B12	1.66	1.66	0.3	1.5	–	–	–	−1.81
B13	1.66	6	3	3	–	–	–	–
B14	1.66	6	3	1.5	–	–	–	−2.32
B15	1.66	6	0.3	3	–	–	–	−2.37
B16	1.66	6	0.3	1.5	–	–	–	−2.37
B17	6	6	3	3	–	−0.552	–	−0.230
B18	6	6	3	1.5	–	−0.552	–	−0.230
B19	6	6	0.3	3	0.284	−0.542	−1.01	−0.225
B20	6	6	0.3	1.5	0.284	−0.542	−1.01	−0.225

Table F.8.: Same as for Table F.6 but for clumping factors associated with structures possessing Burkert density profiles, using LDM of mass 20 MeV [columns (6) and (7)] and 3 MeV [columns (8) and (9)]).

particles, and finally, show the results obtained when the full method is invoked.

Dark matter annihilation spectra

Neutralino DM can annihilate directly into either a fermion pair or weak gauge bosons. Since the cross section for annihilation to fermion pairs is proportional to the square of the final state fermion mass, this process will be dominated by heavy final states, namely $b\bar{b}$, $\tau^-\tau^+$ and $t\bar{t}$ (if kinematically allowed), while direct annihilation into electron-positron pairs will be strongly suppressed. Hence we need only consider the following annihilation modes: $\chi\chi \to W^+W^-$, $\chi\chi \to ZZ$, $\chi\chi \to b\bar{b}$, $\chi\chi \to \tau^+\tau^-$ and $\chi\chi \to t\bar{t}$. Both the gauge bosons and the fermion pairs produced in neutralino annihilations will initiate a cascade that will eventually lead to a continuum of photons, neutrinos, electron/positrons pairs and protons in the final states, extending to energies much smaller than the rest mass of the DM particle. Here we utilise PYTHIA[18] (Sjostrand et al., 2001) to calculate these spectra.

The actual spectrum produced by the annihilations will depend on the branching ratios of the various channels; this in turn will be determined by the gaugino and higgsino fractions of the neutralino. In the following, we will consider four representative supersymmetric scenarios, in a similar way to what was done by Hooper et al. (2004). First, we consider a 50 GeV neutralino with an annihilation branching ratio of 0.96 to $b\bar{b}$ and of 0.04 to $\tau^+\tau^-$ (designated as model 1). Such a particle could be gaugino-like or higgsino-like, since for masses below the gauge boson masses, these modes dominate for either case. Second, we consider two cases for a 150 GeV neutralino: One (designated as model 2) which annihilates as described in model 1, and another (designated as model 3) which annihillates entirely to gauge bosons (W^+W^- or ZZ). Such neutralinos are typically gaugino-like and higgsino-like respectively. Finally, we consider heavy, 600 GeV neutralinos, which annihilate to $b\bar{b}$ with a ratio of 0.87 and to $\tau^+\tau^-$ or t^+t^- the remaining time (designated as model 4). Although these models do not fully encompass the extensive parameter space available to neutralinos at present, they do describe effective MSSM benchmarks. Furthermore, the relevant results for neutralinos with a mixture of the properties of those above can be inferred by interpolating between those presented.

In Fig. F.16 we show the spectrum of photons and electrons produced in a single annihilation for our four neutralino models. As we shall describe in more detail in Appendix F.3.5, in the numerical computation of $f_{\mathrm{abs.}}$ we will be make the approximation that the annihilation spectra are monochromatic and peaked at the average energy. In Table F.9 we show the average photon and electron energy for the four models described above, together with the

[18] http://home.thep.lu.se/ torbjorn/Pythia.html

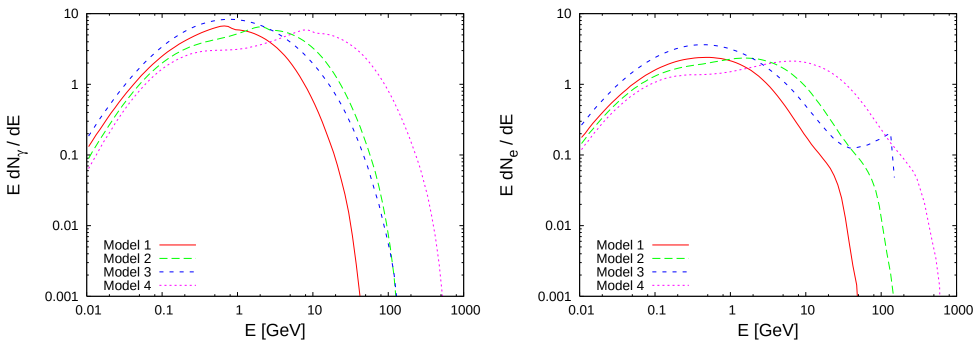

Figure F.16.: Photon (left) and electron (right) energy spectra $E\,\mathrm{d}N/\mathrm{d}E$ resulting from a single neutralino annihilation, for our four benchmark models.

Model	$\bar{N}_\gamma$	$\bar{E}_\gamma$	$\bar{N}_{e^\pm}$	$\bar{E}_{e^\pm}$
SUSY-1	21.6	1.3 GeV	9.2	1.1 GeV
SUSY-2	24.7	3.5 GeV	10.6	2.8 GeV
SUSY-3	31.5	2.1 GeV	14.6	2.6 GeV
SUSY-4	25.8	12 GeV	11.3	9.8 GeV
LDM 3 MeV	-	-	1	3 MeV
LDM 20 MeV	-	-	1	20 MeV

Table F.9.: Average number and energy of the photons and electrons (positrons) produced in a single DM annihilation, for the different models considered.

average number of particles produced in each annihilation.

In addition to neutralinos, we also consider light (MeV) DM candidates, which annihilate directly into electron-positron pairs. This will result in a monochromatic spectrum with $E_{e^\pm} = m_{\mathrm{DM}}c^2$. We consider two different LDM candidates with masses $m_{\mathrm{DM}} = 3$ and 20 MeV respectively. For completeness, we present the "average" energy and number of electrons (which is equal to the number of positrons) produced in each annihilation in Table F.9.

Interaction of the annihilation products with the IGM

In this section we discuss the different processes by which the annihilation products of our DM candidates inject energy into the IGM. We will be only concerned with the interaction of photons and electron-positron pairs with the IGM. Protons are very penetrating and thus do not transfer energy to the IGM; neutrino interactions are so weak that they are also unable to transfer energy to the IGM, so that the annihilation energy that ends up into protons and neutrinos is effectively lost for the purpose of heating/ionising the IGM.

We will compute the transparency and opacity windows for photons and e^+e^- pairs in order to gain a qualitative insight to the regions in the (E, z) plane where energy injection is expected to be efficient or not. However, for the actual calculations of the absorbed energy fraction, the energy transfer between the annihilation products and the IGM is treated in more detail as explained in Appendix F.3.5.

Photons As far as photons are concerned, we are mostly interested in the absorption of γ-ray photons. The absorption processes of x-ray and γ-ray photons at cosmological distances were discussed by Zdziarski (1984). In principle, the possible energy loss mechanisms for photons are: photoionisation of atoms; Compton scattering on electrons; pair production on atoms; pair production of free electrons or nuclei; scattering on CMB photons; pair production on CMB photons. The total rate for fractional energy loss, $\phi_\gamma(z,\, E)$, i.e., the fraction of the photon energy that is lost in a unit time, is given by a sum over the contributions of the individual processes:

$$\phi_\gamma(z,\, E) = -\frac{1}{E}\frac{dE}{dt} = \sum_i \phi_{\gamma,i} \tag{F.3.33}$$

where the index i runs over the different processes listed above. However, for $z \lesssim 1500$, and in the range of energies we are interested (namely $E \lesssim 10\,\text{GeV}$), the relevant processes are photoionization, Compton scattering and pair production on atoms or free electrons and nuclei. The effectiveness of these processes depends upon, other than on the photon energy, the density of the Universe at the redshift of interest. Roughly speaking, we can say that photoionization is effective for energies below $\sim 10\,\text{keV}$, while pair production is the dominant absorption mechanism at $z \gtrsim 1000$ for $100\ \text{MeV} \lesssim E \lesssim 10\,\text{GeV}$. Compton scattering is effective only for $z \gtrsim 100$, in a range of photon energies roughly centered around ~ 1 MeV; at $z = 500$, the region where absorption is dominated by Compton scattering extends roughly from 10 keV to 30 MeV. The other processes, namely scattering on CMB photons and photon-photon pair production, can be safely neglected for our purposes since they are only relevant either at large redshifts or for very large ($E \gtrsim 100\,\text{GeV}$) energies.

The rate for fractional energy loss by photoionisation $\phi_{\gamma,\text{ion.}}$ is given by

$$\phi_{\gamma,\text{ion.}}(z, E) = \frac{\sigma_{\text{He+H}}(E)}{16} n_b(z) c, \tag{F.3.34}$$

where $n_b(z)$ is the number density of baryons at redshift z, and $\sigma_{\text{He+H}}$ is the absorption cross section per helium atom (hence the factor of 16 in Eq.(F.3.34), since $n_{\mathrm{He}} = n_b/16$), given by

$$\sigma_{\mathrm{He+H}}(E) = 5.1 \times 10^{-20} \left(\frac{E}{250\,\mathrm{eV}} \right)^{-p} \mathrm{cm}^2, \tag{F.3.35}$$

where $p = 3.3$ for $E > 250\,\mathrm{eV}$, $p = 2.65$ for $25\,\mathrm{eV} \leq E \leq 250\,\mathrm{eV}$.

The fractional energy loss rate by Compton scattering is

$$\phi_{\gamma,\mathrm{Com.}}(z, E) = \sigma_T \, \epsilon \, g(\epsilon) n_e(z) c, \tag{F.3.36}$$

where σ_T is the Thomson cross section, $\epsilon = E/m_e c^2$ is the photon energy in units of the electron mass, $n_e \simeq 0.88\, n_b$ is the total electron density at redshift z (including both free and bound electrons), and $g(\epsilon)$ is

$$g(\epsilon) = \frac{3}{8} \left[\frac{(\epsilon - 3)(\epsilon + 1)}{\epsilon^4} \ln(1 + 2\epsilon) + \frac{2\left(3 + 17\epsilon + 31\epsilon^2 + 17\epsilon^3 - 10\epsilon^4/3\right)}{\epsilon^3 (1 + 2\epsilon)^3} \right]. \tag{F.3.37}$$

The corresponding term for pair production over atoms is given by

$$\phi_{\gamma,\mathrm{pair}}(z, E) = 0.63 \times \alpha \sigma_T n_e(z) c \ln \left(\frac{513\epsilon}{\epsilon + 825} \right), \tag{F.3.38}$$

while the one for pair production over ionized matter is

$$\phi_{\gamma,\mathrm{pair}}(z, E) = 0.8 \times \alpha \sigma_T n_e(z) c \left(\ln 2\epsilon - \frac{109}{42} \right), \tag{F.3.39}$$

where α is the fine structure constant.

A simple rule of thumb to assess the efficiency of the above energy loss mechanisms is to compare the rate ϕ_γ with the expansion rate, as given by the value of the Hubble constant $H(z)$. When $\phi_\gamma \gg H(z)$, the photon loses all of its energy on a time scale small compared to the cosmological time, so that the energy loss mechanisms are very effective and the universe is opaque to its propagation. It can then be assumed that all the photon energy is instantly lost, and, in the case of photoionisation and Compton scattering, instantly deposited into the IGM (in the case of pair production, one should take into account the subsequent interaction of the pair with the IGM - see Appendix F.3.5 for details). In the opposite regime, $\phi_\gamma \ll H(z)$, the photon loses a significant fraction of its energy on a time scale larger than the cosmological time, and the Universe is effectively transparent to the photon propagation.

Following Chen and Kamionkowski (2004), in Fig. F.17 we show the pho-

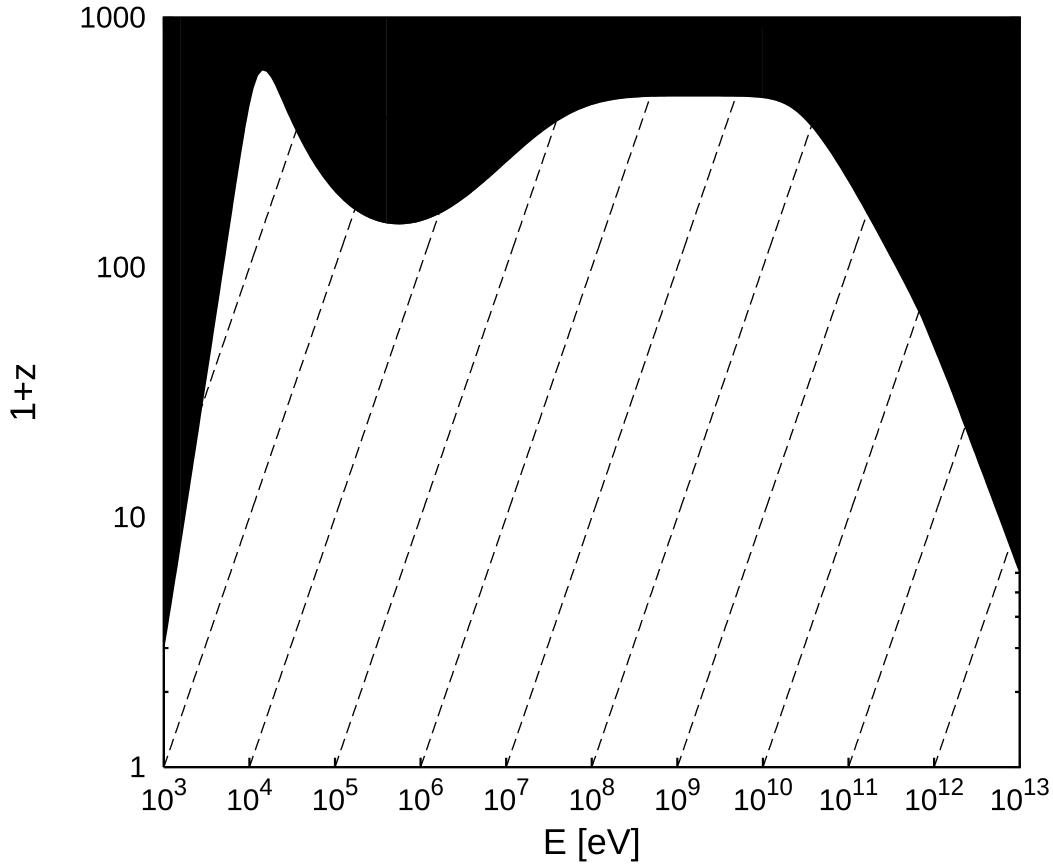

Figure F.17.: Photon transparency window. In the black region, the photon loses all of its energy through interaction with particles in the IGM and CMB photons. In the white region, the photon can propagate freely. The dashed lines represent photon trajectories.

ton transparency window in the (E, z) plane. For illustrative purposes, we consider redshifts as large as $z = 1000$ and energies up to 10 TeV in the figure, so that, in addition to the three processes for which we have listed explicitly the energy loss rates, we have also included the scattering and pair production over CMB photons in the total rate ϕ_γ. In the filled region, $\phi_\gamma > H(z)$, corresponding to the optically thick regime. In the white region, $\phi_\gamma < H(z)$, corresponding to the optically thin regime.

Although the transparency window can be useful as a preliminary tool, in order, for example, to assess which processes are important at a given redshift and energy range, it has some limitations nevertheless. First of all, it does not allow us to treat properly the regime $\phi_\gamma \simeq H(z)$, i.e. the regime where the energy loss happens on cosmological time scales. In this case, the approximation of an instantaneous energy deposition is not appropriate, since part of the energy can be deposited at a redshift lower than the redshift of emission. Secondly, even if in the regime $\phi_\gamma \gg H(z)$ one can safely conclude that all the energy of the annihilation products is instantaneously lost, this does not mean that it is instantaneously transferred (or even transferred at all) into the IGM: in some cases the interactions of the annihilation products generate secondary particles, like the e^+e^- generated by the pair production of photons on atoms or nuclei, whose propagation has to be followed as well. For these reasons we follow (with some small modifications) the approach of (Ripamonti et al., 2007) to calculate $f_{\rm abs.}$; the detailed calculations and the results for $f_{\rm abs.}$ are described in Appendix F.3.5.

In any case we can gain some qualitative insight by looking at the Figs. F.16 and F.17. For the supersymmetric models considered, the average energy of the photons produced in each annihilation is of order of a few GeV, and their energy is at most a few hundred GeV (in the case of our heaviest candidate, the 600 GeV neutralino of model 4, only $\sim$ 1% of the total energy produced in the annihilation is released in the form of photons with energy $E_\gamma > 200\,\mathrm{GeV}$). As it can be seen from Fig. F.17 above, these photons lie in the middle of the transparency window: their energy is too low for pair production, as already noticed, but on the other hand it is too high for photoionisation (or Compton scattering at $z > 100$) to be effective. These photons will propagate freely and their energy will decrease due to cosmological expansion. Although it is in principle possible that, due to cosmological redshifting, a photon produced in the transparency window at a given time will be absorbed later, we see from Fig. F.17 that this is practically never the case. In conclusion, we expect that the absorbed fraction for photons at $z < 1000$ will be very small, and that the photons produced in neutralino annihilations will instead show up in the diffuse gamma-ray background.

Electron-positron pairs Electrons and positrons can lose energy through collisional ionisation of atoms or through inverse Compton scattering off of CMB photons. In addition, positrons can annihilate with thermal electrons. Other energy loss mechanisms, like synchrotron radiation loss, can be safely neglected.

The rate of energy loss through collisional ionisation is given by

$$\phi_{e,\text{ion.}}(E,z) = \frac{v}{E}\frac{2\pi e^4}{m_e v^2} \times \left\{ Z_{\text{H}} n_{\text{H}} \left[\ln\left(\frac{m_e v^2 \gamma^2 T_{\text{max,H}}}{2 I_{\text{H}}^2} \right) + \mathcal{D}(\gamma) \right] + Z_{\text{He}} n_{\text{He}} \left[\ln\left(\frac{m_e v^2 \gamma^2 T_{\text{max,He}}}{2 I_{\text{He}}^2} \right) + \mathcal{D}(\gamma) \right] \right\}, \quad \text{(F.3.40)}$$

where v is the electron velocity, $\gamma = E/m_e c^2$ is the electron Lorentz factor, $I_{\text{H}} = 13.59\,\text{eV}$ and $I_{\text{He}} = 24.6\,\text{eV}$ are the hydrogen and helium ionisation thresholds respectively, Z_{H} and Z_{He} are the hydrogen and helium atomic numbers respectively, the function $\mathcal{D}(\gamma)$ is given by

$$\mathcal{D}(\gamma) = \frac{1}{\gamma^2} - \left(\frac{2}{\gamma} - \frac{1}{\gamma^2} \right) \ln 2 + \frac{1}{8}\left(1 - \frac{1}{\gamma} \right)^2, \quad \text{(F.3.41)}$$

and $T_{\text{max.,H}}$ and $T_{\text{max.,He}}$ are the maximum energy transfers in a single collision

$$T_{\text{max.,H}} = \frac{2\gamma^2 m_{\text{H}}^2 m_e v^2}{m_e^2 + m_{\text{H}}^2 + 2\gamma m_e m_{\text{H}}}, \quad \text{(F.3.42)}$$

$$T_{\text{max.,He}} = \frac{2\gamma^2 m_{\text{He}}^2 m_e v^2}{m_e^2 + m_{\text{He}}^2 + 2\gamma m_e m_{\text{He}}}. \quad \text{(F.3.43)}$$

The fractional energy loss rate through inverse Compton scattering is given by

$$\phi_{e,\text{Com.}}(z,E) = \frac{4}{3}\frac{\sigma_T U_{\text{CMB}}(z)}{m_e}\frac{\gamma^2 - 1}{\gamma}, \quad \text{(F.3.44)}$$

where $U_{\text{CMB}}(z)$ is the CMB energy density at redshift z.

In the case of inverse Compton losses, we must take into account that the electrons and positrons do not transfer their energy directly into the IGM; instead, they accelerate the CMB photons they interact with, boosting their energy by a factor $\sim \gamma^2$. These up-scattered photons can either be absorbed by the IGM or escape, depending on their energy. As explained above, at redshifts below a few hundred, the only relevant photon absorption processes are photoionisation, Compton scattering and pair production; however, a simple calculation shows that the electrons and positrons produced in the annihilation of the DM candidates considered here are not energetic enough to boost the CMB photons above the threshold for pair production. We can also safely neglect Compton scattering, since it is only efficient for $z > 100$

and in a small energy region around 1 MeV. Therefore we need only consider photoionisation as the secondary process leading to the absorption of the photons produced by inverse Compton scattering of electrons and positrons. The method that we use to estimate the energy injected in the IGM by the up-scattered photons is described in detail in Appendix F.3.5. Here we just show the results concerning the opacity window of electrons and positrons.

The behaviour of electron-positron pairs with respect to the energy transfer to the IGM is summarised in Fig. F.18. In the white region, the total energy loss rate is smaller than the expansion rate: $\phi_{e,\text{ion.}} + \phi_{e,\text{Com.}} < H$, so that the Universe is transparent to the propagation of electrons. In the grey regions, the electrons and positrons interact by inverse Compton scattering, but the resulting photons fall in the photon transparency window. This means that the Universe is opaque to the propagation of electrons, but nevertheless their energy is not transferred to the IGM. Finally, in the black regions the electron energy is efficiently transferred to the IGM. In particular, the region on the left correspond to the case in which collisional ionisation is the dominant process; the region on the right is where inverse Compton is the dominant interaction, and the up-scattered CMB photons fall into the photon absorption window.

Computation of the absorbed fraction

Here we describe the method that we have used to compute the energy absorbed fraction $f_{\text{abs.}}$. It is mainly based on the method first described in Ripamonti et al. (2007) (henceforth referred to as RMF07).

We denote with $N(z, z')$ the number of particles (per hydrogen nucleus) produced in the annihilations at redshift z', that are still present (and able to transfer energy to the IGM) at redshift $z \leq z'$, and their energy spectrum with $\mathrm{d}N(z, E, z')/\mathrm{d}E$. The rate $\dot{\epsilon}$ of energy absorption per H nucleus at redshift z is obtained by integrating over all energies and production redshifts:

$$\dot{\epsilon} = \int_z^\infty \mathrm{d}z' \int \mathrm{d}E \frac{\mathrm{d}N}{\mathrm{d}E}(z, E, z') E \Phi(z, E), \tag{F.3.45}$$

where $\Phi(z, E)$ is the fractional energy transfer rate to the IGM by a particle with energy E at redshift z. A summation over the different particle species produced in the annihilations is also implicit in Φ. The upper integration limit over redshift is formally infinite, but from the numerical point of view it is enough to take a redshift large enough so that all the absorption happens locally and does not give contributions at later times. In our calculations, we have taken, as an upper integration limit, $z_{\text{max.}} = 1500$, and checked explictly that increases in $z_{\text{max.}}$ do not significantly alter our results.

This expression can be simplified assuming that the energy spectrum of the particles is very peaked around the mean energy (as it is often the case)

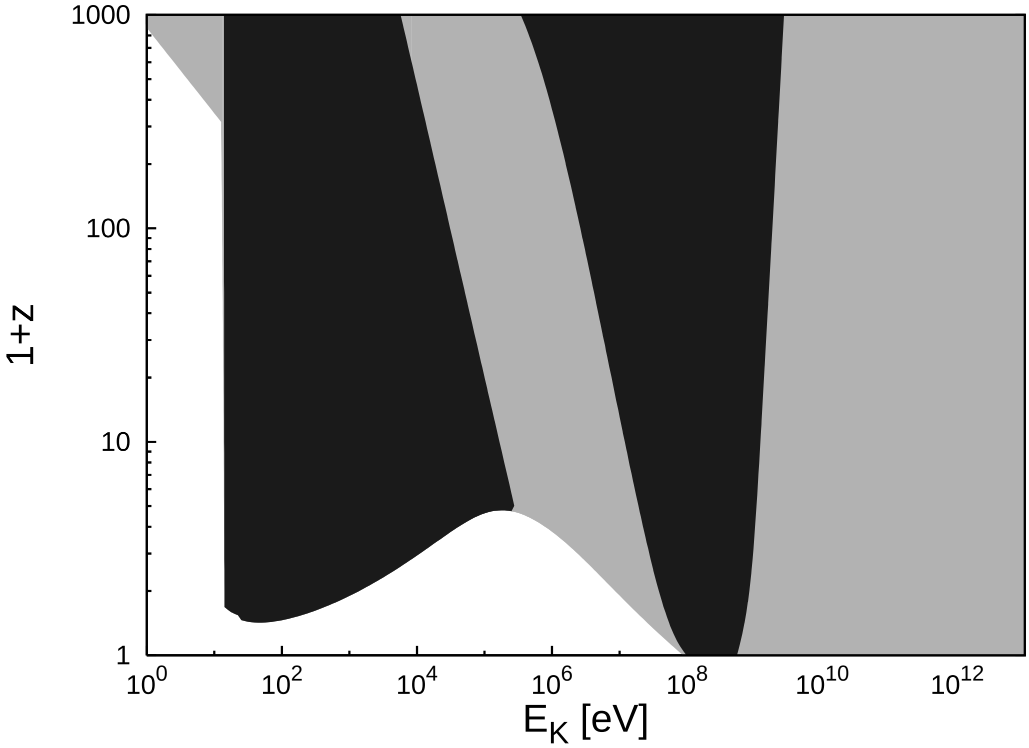

Figure F.18.: Transparency window for electrons. In the white region, electrons propagate freely. In the grey regions, electrons transfer all of their energy to the CMB photons, but these are subsequently lost, so that no energy is injected in the IGM. In the black regions, all the electron energy is efficiently injected in the IGM. See text for discussion.

and thus approximating the energy spectrum with a Dirac delta function: $\mathrm{d}N/\mathrm{d}E(z,z',E) \propto \delta(E-\bar{E}(z,z'))$, where of course the peak energy $\bar{E}$ depends on both z and z'. The normalization is given by the condition that $\int \mathrm{d}N/\mathrm{d}E(z,z',E)\mathrm{d}E = N(z,z')$. Then:

$$\dot{\epsilon} = \int_z^\infty \mathrm{d}z' N(z,z')\bar{E}(z,z')\Phi(z,\bar{E}(z,z')). \tag{F.3.46}$$

Finally, the energy absorbed fraction is simply given by the ratio between the energy absorbed and the energy produced by the annihilations:

$$f_{\mathrm{abs.}} = \frac{\dot{\epsilon}}{\frac{1}{2}\frac{n^2_{\mathrm{DM},0}}{n_{\mathrm{H},0}}\langle\sigma_{\mathrm{ann}}v\rangle m_{\mathrm{dm}}(1+z)^3} \tag{F.3.47}$$

The problem then reduces to the computation of the two functions $N(z,z')$ and $\bar{E}(z,z')$ and to the subsequent computation of the integral in Eq. (F.3.46). In the following, we will describe how we computed the evolution of N and $\bar{E}$ for different DM particles (in our case, SUSY neutralinos and LDM) and annihilation products (in our case, namely photons, electrons and positrons).

In order to compute the evolution of the two quantities $N(z,z')$ and $\bar{E}(z,z')$ with redshift, it is useful to divide the possible interactions of the annihilation products between those that result in the loss of a particle, without changing their average energy, and those that, conversely, reduce the average energy without changing the number of particles. An example of the first class is the photoionisation of hydrogen atoms by photons produced in the annihilation, as the photon responsible for the ionisation is effectively removed; an example of the second class is the Compton scattering of photons over electrons. We shall denote with $\phi_N(z,E)$ and $\phi_E(z,E)$ the interaction rates for the two kind of processes, respectively. Another thing that should be considered is that the total energy loss rate, $\phi = \phi_N + \phi_E$, is not necessarily equal to the total rate of energy transfer, Φ, that appears in Eq. (F.3.46). The reason is that not all the energy that is lost by the particles is actually transferred to the IGM; for example, as we shall see later, high energy electrons produced in DM annihilations can lose all of their energy very rapidly by inverse Compton scattering on CMB photons, but it can be the case that the up-scattered photons do not subsequently interact with the IGM. The net result is that, although the electrons lose all of their energy, this does not end up heating or ionising the IGM. We shall take this into account using, for a given process, an efficiency factor, $\eta(z,E) \leq 1$, such that $\Phi = \eta\phi$.

We first consider the absorption of photons. We can write the equations describing the evolution of $N_\gamma(z,z')$ and $\bar{E}_\gamma(z,z')$ (for $z < z'$) as:

$$\frac{\mathrm{d}N_\gamma}{\mathrm{d}z}(z,z') = N_\gamma(z,z')\frac{\phi_{N,\gamma}[z,\bar{E}_\gamma(z,z')]}{H(z)(1+z)}$$

and

$$\frac{\mathrm{d}\bar{E}_\gamma}{\mathrm{d}z}(z,z') = \bar{E}_\gamma(z,z')\left(\frac{\phi_{E,\gamma}[z,\bar{E}_\gamma(z,z')]}{H(z)(1+z)} + \frac{1}{1+z}\right),$$

where the second term takes into account the cosmological redshifts of photons, and the factor $H(z)(1+z)$ originates from the transformation from cosmological time to redshift. The initial conditions at $z = z'$ for the above system are:

$$N_\gamma(z',z') = \zeta_{\gamma,1}\frac{\dot{N}_{\mathrm{DM}}(z')}{H(z')(1+z')} \tag{F.3.48}$$

$$\bar{E}_\gamma(z',z') = \zeta_{\gamma,2} m_{\mathrm{dm}} c^2 \tag{F.3.49}$$

where $\dot{N}_{\mathrm{DM}}$ is the rate of decrease of DM particles per H nucleus, $\zeta_{\gamma,1}$ is the average number of photons produced per every annihilating DM particle (i.e., it is equal to the number of photons produced in the annihilation, divided by 2), and $\zeta_{\gamma,2}$ is the average fraction of the DM rest mass energy that goes to each photon. The values of $\zeta_{\gamma,1}$ and $\zeta_{\gamma,2}$ can be easily inferred from the values presented in Table F.9, while the rate of decrease of DM particles is given by

$$\dot{N}_{\mathrm{DM}} = \frac{1}{2}\frac{n_{\mathrm{dm}}(z)}{n_H(z)}^2\langle\sigma v\rangle \tag{F.3.50}$$

The next step is to model the rates ϕ_N and ϕ_E in order to include the relevant processes in the energy and redshift ranges of interests. For the supersymmetric models we consider here, the average photon energy ranges from $\sim 1\,\mathrm{GeV}$ in model 1 to $\sim 10\,\mathrm{GeV}$ in model 2. From Zdziarski (1984) and from the discussion in § F.3.5 we know that at these energies the only relevant absorption process is pair production over atoms (if $z < z_{\mathrm{dec.}}$) or over ions and free electrons (if $z > z_{\mathrm{dec.}}$); even this process is only effective for redshifts larger than a few hundred. At more recent times, the Universe is basically transparent to GeV photons. Compton scattering over electrons should also be taken into account as it can contribute to the absorbed fraction, and is in fact the main mechanism of energy transfer at redshifts $z \lesssim 100$, as we have checked explicitly by computing the absorbed fraction with and without the Compton term. Since pair production results in the loss of a photon, while Compton scattering just changes its energy, we take $\phi_N = \phi_{\gamma,\mathrm{pair}}$ and $\phi_E = \phi_{\gamma,\mathrm{Com.}}$.

Once the time evolution of $N(z,z')$ and $\bar{E}(z,z')$ is known, the only ingredient required before we can proceed with the computation of the integral in Eq .(F.3.46) is the estimation of the photon absorption rate, Φ_γ, i.e. of the total photon energy loss rate weighted with the absorption efficiency. We can in general write

$$\Phi_\gamma = \sum_i \eta_i\phi_i, \tag{F.3.51}$$

the sum running over all relevant processes. In the present case, all the energy lost through Compton scattering over electrons directly goes into the IGM, so we can take $\eta_{\mathrm{Com.}} = 1$. On the other hand, not all electron-positron pairs produced by the interaction of photons actually inject energy into the IGM. We model the subsequent absorption as follows. Every photon will produce an electron and a positron, each with energy $E_{e^\pm} \simeq E_\gamma/2$. These electrons and positrons very quickly lose all of their energy through inverse Compton scattering off of CMB photons. The up-scattered photons have an average energy $E'^{2}_{\gamma} k_{\mathrm{B}} T^0_{\mathrm{CMB}}(1+z)$, where $\gamma = E_{e^\pm}/(m_e c^2)$ is the Lorentz factor of the electron or positron. Finally, following RMF07, we assume that these secondary photons are absorbed through Compton scattering with an efficiency η given by

$$\eta(z, E_\gamma) = f_1 \left[1 - e^{-\tau_\gamma(z, E'_\gamma)}\right], \tag{F.3.52}$$

where τ is the optical depth for Compton scattering, given by

$$\tau_\gamma(z, E'_\gamma) = \frac{f_2}{H(z)} \phi_{\gamma,\mathrm{Com.}}(z, E'_\gamma), \tag{F.3.53}$$

where $f_1 = 0.91$ and $f_2 = 0.6$.

We can now proceed with the evaluation of the photon channel contribution to $\dot{\epsilon}$, as given by expression (F.3.46), and consequently to $f_{\mathrm{abs.}}$. The results are shown in Fig. F.19. (long dashed green lines).

We now turn our attention to the absorption of electrons and positrons produced in neutralino annihilations. Relativistic electrons and positrons lose their energy through inverse Compton scattering off of CMB photons, while slow electrons and positrons lose their energy through collisional ionisation of neutral atoms. In addition, positrons can annihilate over thermal electrons; this process also is very effective for particles with very low kinetic energy, i.e. $E_{e^+} \simeq m_e c^2$. Since the relevant energy range is the same as for photons, i.e. $1 - 10\,\mathrm{GeV}$, we expect inverse Compton scattering to be the only relevant process. In any case, we included collisional ionisation and annihilation over thermal electrons (just for positrons) in our equations and explicitly checked that such terms have a negligible impact on our results. The evolution equations for ultra-relativistic electrons and positrons then have the same form as the ones for photons:

$$\frac{\mathrm{d}N_{e^\pm}}{\mathrm{d}z}(z, z') = N_{e^\pm}(z, z') \frac{\phi_{N,e^\pm}(z, \bar{E}_{e^\pm}(z, z'))}{H(z)(1+z)} \tag{F.3.54}$$

$$\frac{\mathrm{d}\bar{E}_{e^\pm}}{\mathrm{d}z}(z, z') = \bar{E}_{e^\pm}(z, z') \left[\frac{\phi_{E,e^\pm}(z, \bar{E}_{e^\pm}(z, z'))}{H(z)(1+z)} + \frac{1}{1+z}\right] \tag{F.3.55}$$

where we take $\phi_{N,e^\pm} = \phi_{e,\mathrm{ion.}}$ and $\phi_{E,e^\pm} = \phi_{e,\mathrm{Com.}}$ for electrons, while for positrons we also include the annihilation term in ϕ_N. As we have just mentioned, one can in practice take $\phi_N = 0$ in both cases and still obtain the same results.

The efficiency of inverse Compton scattering in transferring energy to the IGM can be estimated as follows. The average energy of the upscattered photons is given by $E_\gamma'^2 k_\mathrm{B} T^0_\mathrm{CMB}(1+z)$; for an electron in the 1 to 10 GeV energy range, this gives a corresponding photon energy of $(1-100)(1+z)$ keV. This means that, especially at low redshifts, the up-scattered photons can have the right energy to transfer energy to the IGM by ionising neutral atoms. We quantify this effect as follows. The energy $E_\mathrm{ion.}$ corresponding to unitary optical depth for photoionisation (i.e. $\phi_{\gamma,\mathrm{ion.}} = H$) at a given redshift z is given by

$$E_\mathrm{ion.}(z) = 0.64\,\mathrm{keV} \times (1+z)^{0.45}. \tag{F.3.56}$$

We consider that upscattered photons with $E'_\gamma < E_\mathrm{ion.}$ transfer their energy to the IGM, while the others are lost. We then take the efficiency of inverse Compton scattering as being equal to a fraction F of the total CMB energy density carried by photons that after scattering have an energy below the ionisation threshold. The efficiency $\eta_\mathrm{Com.}$ is then given by

$$\eta_\mathrm{Com.} = F(E < E_\mathrm{max.}) = \left[\int_0^{E_\mathrm{max.}/c} pf(p,z)\mathrm{d}^3p\right] \times \left[\int_0^\infty pf(p',z)\mathrm{d}^3p\right]^{-1}, \tag{F.3.57}$$

where $f(p,z) = \left[e^{pc/k_\mathrm{B}T(z)} - 1\right]^{-1}$ is the Bose-Einstein distribution, and $E_\mathrm{max.} = E_\mathrm{ion.}(z)/\gamma^2$. Using the dimensionless variable $y = pc/k_\mathrm{B}T$ this can be rewritten as

$$\eta_\mathrm{Com.}(z) = \frac{\pi^4}{15}\left[\int_0^{y_\mathrm{max.}} \frac{y^3}{e^y - 1}\mathrm{d}y\right], \tag{F.3.58}$$

where $y_\mathrm{max.} = E_\mathrm{max.}c/k_\mathrm{B}T$. Then we finally take the absorption rate in Eq.(F.3.46) to be

$$\Phi_{e^\pm} = \eta_\mathrm{Com.}\phi_\mathrm{Com.}. \tag{F.3.59}$$

The results for $f_\mathrm{abs.}$ are displayed in Fig. F.19.

In addition to supersymmetric neutralinos, we have also considered the case of MeV light dark matter annihilating directly to e^+e^- pairs. In this case the spectrum is monochromatic at $E_{e^\pm} = m_\mathrm{DM}c^2$. We consider two particular cases of LDM with particle masses $m_\mathrm{DM} = 3$ MeV and 20 MeV. The treatment is basically the same as that in the previous section for electrons and positrons produced in neutralino annihilation, apart from the fact that, especially for the 3 MeV case, the annihilation of positrons over thermal IGM elec-

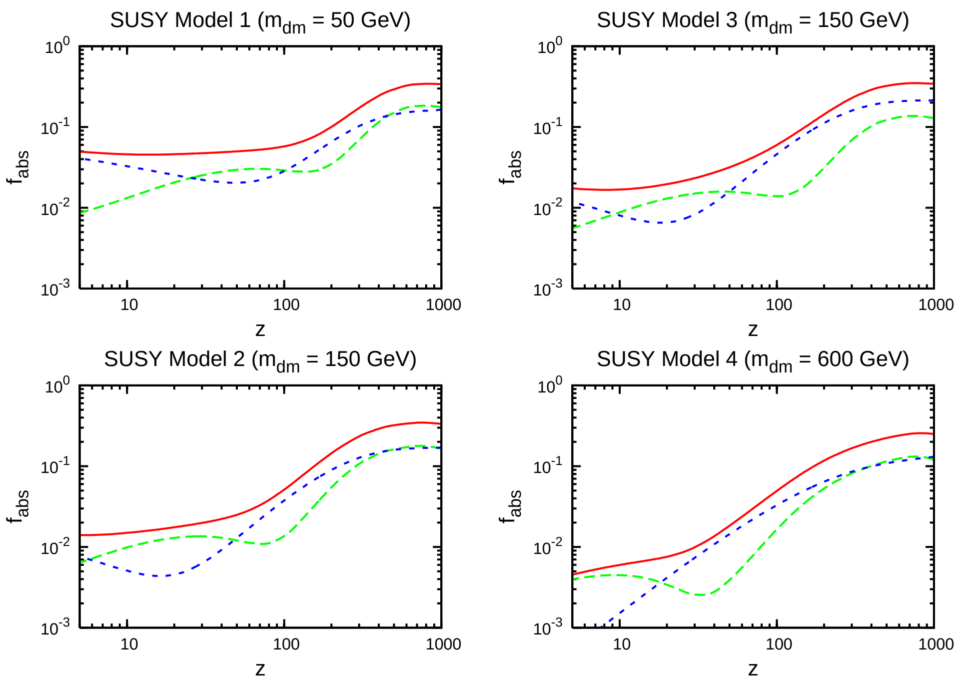

Figure F.19.: Absorbed energy fraction for neutralino models 1, 2, 3 and 4. We show the total absorbed fraction (solid red line) together with the contribution from the photon (long dashed green curves) and electron/positron (short dashed blue curves) channels.

trons gives an appreciable contribution to the total absorbed energy fraction. Annihilations are only important when the positron has lost all of its kinetic energy through inverse Compton scattering; it can be seen in fact that the energy loss rate for ionisation is always larger than the loss rate for annihilations. Then the only regime where annihilations can be effective is when the kinetic energy of the positron is below the H ionisation threshold at 13.6 eV, i.e. where $E_{e^+} \simeq m_e c^2$.

We then use the following scheme to follow the evolution of the N and $\bar{E}$ for positrons. Based on the argument above, we split the integral in the Eq. (F.3.46) in two parts. The first integral, evaluated from $z' = z$ to $z' = z_1$, takes into account the contribution from positrons that still retain an appreciable fraction of their kinetic energy at redshift z, and are thus losing energy mainly through inverse Compton scattering and collisional ionisation. The second integral, evaluated from $z' = z_1$ to $z' = z_{\mathrm{max.}}$, takes into account the contribution of positrons that have already lost all their kinetic energy (i.e. slow positrons) and can only lose more energy by annihilating with thermal electrons. The redshift z_1 is simply obtained by solving the differential equation for $\bar{E}$ and finding the redshift where $\bar{E} = 13.6\,\mathrm{eV}$.

Finally, it should be taken into account that the photons produced in the annihilation will not necessarily transfer all of their energy to the IGM. We follow a method similar to the one described in the previous section, and assume that energy is transferred via Compton scattering, with an efficiency given by

$$\eta_{\mathrm{ann.}}(z, E_\gamma) = f_1 \left[1 - e^{-\tau_\gamma(z, E'_\gamma)}\right], \tag{F.3.60}$$

where τ is the optical depth for Compton scattering defined above, the parameters f_1 and f_2 have also been defined above, and $E_\gamma = m_e c^2$ since the positron and electron annihilate basically whilst at rest.

The absorbed energy fraction for annihilating MeV DM has been computed explicitly in RMF07 for $m_{\mathrm{DM}} = 1$, 3 and 10 MeV. We have compared our results to theirs in the case of 3 MeV and although the results are qualitatively similar (the absorbed fraction is appreciable at large redshifts, has a large decrease at intermediate redshifts, and then starts increasing again to $f_{\mathrm{abs.}} \sim O(0.1)$ at $z = 5$) there are also some quantitative differences. As we could not track down the origin of such discrepancies, we have decided to compute the expected brightness temperature for 3 MeV annihilating DM particles using both, the version of the function $f_{\mathrm{abs.}}$ that we have obtained in this paper ($f^{\mathrm{CLS}}_{\mathrm{abs.}}$) and the one from RMF07 ($f^{\mathrm{RMF}}_{\mathrm{abs.}}$), for which they provide an analytic approximation. However, for comparison we have also computed the absorbed fraction for the 10 MeV case (not considered elsewhere in this paper) and we have found an excellent agreement between our results and those of RMF07, so the discrepancies are likely due to the different handling of positron annihilations, which only contribute to the lower masses.

We present our results for the absorbed fraction for MeV DM in Fig. F.20,

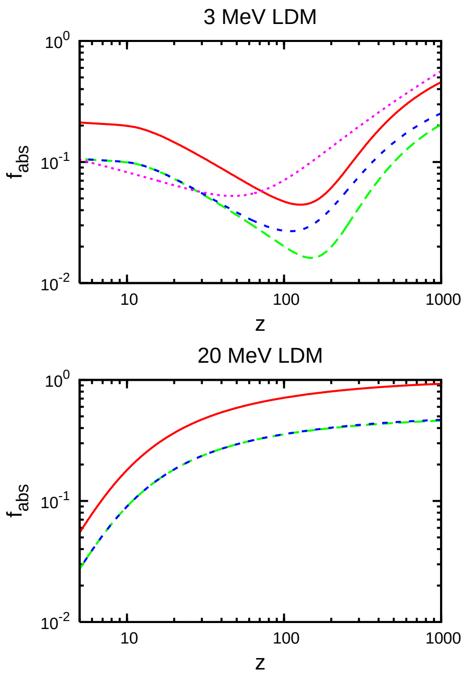

Figure F.20.: Absorbed energy fraction for the 3 MeV (upper panel) and 10 MeV (lower panel) LDM. We show the total $f_{\text{abs.}}$ (solid red line) together with the contribution from electrons and positrons (long dashed green and short dashed blue lines, respectively). For the 3 MeV case, we also show the absorbed fraction compute in RMF07 (dotted magenta line).

together with the result for $f_{\text{abs.}}$ for 3 MeV LDM from RMF07.

F.3.6. The 21 cm Background

CMB-kinetic temperature coupling

In this section we briefly review the basic physics behind the 21 cm signal. For a more in-depth discussion, we refer the reader to Refs. Madau et al. (1997); Furlanetto et al. (2006a); Barkana and Loeb (2007) and references therein.

The emission or absorption of the 21 cm line signal emanating from neutral gas is associated with the transition between the $n = 1$ triplet and singlet hyperfine levels of hydrogen. The transition rate is governed by the spin temperature, T_s, defined as

$$\frac{n_1}{n_0} = 3 \exp\left(-\frac{T_*}{T_S}\right), \tag{F.3.61}$$

where n_0 and n_1 are the respective number densities of hydrogen atoms in the singlet and triplet states, and $T_* = 0.068$K is the equivalent temperature corresponding to the transition energy.

In the presence of the CMB radiation field, the spin temperature of the neutral hydrogen gas rapidly tends towards the CMB temperature $T_{\rm CMB} \simeq 2.725(1+z)$K. In order for neutral hydrogen gas to produce a detectable signal in the 21 cm background, be it in absorption or emission, that is distinguishable from that generated from the CMB, the kinetic temperature T_K of the gas must decouple from $T_{\rm CMB}$.

In a Universe containing stable, non-annihilating DM, the spin temperature and the kinetic temperature of HI gas are coupled to $T_{\rm CMB}$ until $z \simeq 200$ Peebles (1993). At $30 \lesssim z \lesssim 200$, prior to the formation of non-linear baryonic structures, the IGM cools adiabatically, i.e. $T_K \propto (1+z)^2$, compared to $T_{\rm CMB} \propto (1+z)$. During this epoch, spin-exchange collisions between hydrogen atoms, protons and electrons are efficient at coupling T_K and T_S of the gas, and consequently an absorption at wavelength $\lambda = 21(1+z)$ cm can be observed until approximately $z \simeq 70$. At later times cosmological expansion reduces the frequency of these collisions significantly, to the extent where T_S re-couples with $T_{\rm CMB}$, diminishing the 21 cm absorption signal.

However, in a Universe containing annihilating/decaying DM which injects appreciable energy into the IGM, the thermal history of the gas may be significantly altered to the extent where the corresponding changes in the evolution of the 21 cm signal are detectable by current and future radio experiments. Of particular importance is the high sensitivity of these changes with respect to the nature of the DM, making them a powerful tool for constraining the properties of potential DM candidates.

There are two mechanisms which can decouple T_S from $T_{\rm CMB}$: firstly, the aforementioned spin-exchange collisions between neutral atoms, electrons and protons (Purcell and Field, 1956), which are effective at $z \geq 70$ before the Hubble expansion has rarefied the gas in the IGM, and secondly, scattering by Lyman-α radiation (known as the "Wouthuysen-Field" effect, also known as "Lyman-α pumping" (Wouthuysen, 1952; Field, 1959; Hirata, 2006)), which couples T_S to T_K via the mixing of the $n = 1$ hyperfine states through intermediate transitions to the $2p$ state.

In the quasi-static approximation for the population of the hyperfine levels in question, and in the absence of radio sources, the HI spin temperature is a weighted mean involving T_K and $T_{\rm CMB}$,

$$T_S = \frac{T_{\rm CMB} + yT_K}{1+y}, \tag{F.3.62}$$

The coupling coefficient y can be written as

$$y = y_\alpha + y_C, \tag{F.3.63}$$

where y_α is the term associated with Lyman-α pumping, given by

$$y_\alpha = \frac{P_{10} T_*}{A_{10} T_K}, \tag{F.3.64}$$

whilst y_C is associated with the de-excitation of the HI hyperfine triplet state due to collisions with neutral atoms, electrons and protons, collectively written as

$$y_C = \frac{T_*}{A_{10} T_K}(C_{\rm H} + C_e + C_p). \tag{F.3.65}$$

In the above equations $A_{10} = 2.85 \times 10^{-15}\,{\rm s}$ is the rate of spontaneous photon emission, P_{10} is the de-excitation rate of the hyperfine triplet state due to Lyman-α scattering, and $C_{\rm H}, C_e$ and C_p are the de-excitation rates associated with collisions of hydrogen atoms with other hydrogen atoms, electrons and protons respectively. We write $P_{10} = (16\pi J_\alpha \sigma_\alpha)/(27 h_p \nu_\alpha)$, where J_α is the background intensity of Lyman-α photons, σ_α is the Lyman-α photon absorption cross section for neutral hydrogen and h_p is Planck's constant. We neglect the small corrections to the above expressions proposed by Hirata (2006). The H-H collision term can be written as $C_{\rm H} = k_{10} n_{\rm HI}$, where k_{10} is the effective single-atom collision rate coefficient for which we adopt the fit: $k_{10} = 3.1 \times 10^{-11} T_K^{0.357} \exp(-32\,{\rm K}/T_K)\,{\rm cm}^3\,{\rm s}^{-1}$ proposed by Kuhlen et al. (2006), which is accurate to within 0.5% in the range $10 < T_K < 10^3\,{\rm K}$. For the e-H collision term, $C_e = n_e \gamma_e$, we have used the following fit[19] proposed by Liszt (2001): $\log(\gamma_e/{\rm cm}^3\,{\rm s}^{-1}) = -9.607 + 0.5\,\log(T_K/1\,{\rm K})\exp\left\{-\left[\log(T_K/1\,{\rm K})\right]^{4.5}/1800\right\}$ for $1 < T_K < 10^4\,{\rm K}$, $\log(\gamma_e/{\rm cm}^3\,{\rm s}^{-1}) = -9.607 + 0.5\,\log(T_K/1\,{\rm K})$ for $T_K < 1\,{\rm K}$ (Smith, 1966), and $\gamma_e(T_K > 10^4\,{\rm K}) = \gamma_e(10^4\,{\rm K})$. We ignore de-excitations involving collisions with protons since they are typically much weaker than those involving electrons at the same temperature, although it has been shown that they can be relevant at low temperatures Furlanetto and Furlanetto (2007b).

Modifications to IGM thermal evolution in the presence of DM

In this section we describe the modifications to the standard equations describing the thermal and ionisation history of the IGM when we incorporate the potentially significant energy deposition of the products of annihilating DM.

We parameterize the effect of DM annihilation by the rate of energy injection given by Eq.(F.3.1). This energy is then used to excite and ionise the hydrogen and helium atoms in the IGM. We will not enter here into the detail of the partition of energy between hydrogen and helium, but instead assume that it is divided proportionally to the respective number densities. This means that a fraction $1/(1 + f_{\rm He})$ of the absorbed energy will

[19] Updated rates can be found in Furlanetto and Furlanetto (2007a).

go to hydrogen, while a fraction $f_{\rm He}/(1+f_{\rm He})$ will go to helium, $f_{\rm He}$ being the helium to hydrogen number ratio. Then we need to know how the energy is partitioned between the different processes. The relative fractions χ_i, χ_h and χ_e of the energy absorbed which is diverted towards respectively ionising, heating and exciting hydrogen and helium atoms were calculated by Shull and van Steenberg (1985). Their results can be approximated by (Chen and Kamionkowski, 2004)

$$\chi_{i,j}(z) \sim \frac{[1-x_j(z)]}{3}, \tag{F.3.66}$$

$$\chi_{h,j}(z) \sim \frac{[1+2x_j(z)]}{3}, \tag{F.3.67}$$

$$\chi_{e,j}(z) \sim \frac{[1-x_j(z)]}{3}, \tag{F.3.68}$$

where $x_j(z)$ is the ionisation fraction of the relevant nuclear species j (i.e. j=H or He for hydrogen or helium nuclei respectively), defined as

$$x_j = \frac{n_{j^+}}{n_j}, \tag{F.3.69}$$

where n_{j^+} is the number density of ionised nuclei of the species j. We can also define a total ionisation efficiency $\chi_i \equiv (\chi_{i,\rm H} + f_{\rm He}\chi_{i,\rm He})/(1+f_{\rm He})$, and similar quantities for heating and excitation.

Following (Padmanabhan and Finkbeiner, 2005), we compute the ionisation and thermal history of the IGM, when incorporating our chosen species of DM, using the publicly available code RECFAST (Seager, Sasselov and Scott, 1999, 2000), modifying the standard evolution equations for the ionisation fractions of hydrogen and helium nuclei, as well as the evolution equation for the kinetic temperature as follows:

$$-\delta\left(\frac{\mathrm{d}x[\mathrm{H}]}{\mathrm{d}z}\right) = \frac{\dot{\epsilon}}{I_H}\frac{\chi_{i,\rm H}}{(1+f_{\rm He})}\frac{1}{H(z)(1+z)}, \tag{F.3.70}$$

$$-\delta\left(\frac{\mathrm{d}x[\mathrm{He}]}{\mathrm{d}z}\right) = \frac{\dot{\epsilon}}{I_{\rm He}}\frac{\chi_{i,\rm He}}{(1+f_{\rm He})}\frac{1}{H(z)(1+z)}, \tag{F.3.71}$$

$$-\delta\left(\frac{\mathrm{d}T_k}{\mathrm{d}z}\right) = \frac{2\dot{\epsilon}}{3k_{\rm B}}\frac{(\chi_{h,\rm H} + f_{\rm He}\chi_{h,\rm He})}{(1+f_{\rm He})H(z)(1+z)}. \tag{F.3.72}$$

A further equation needed to calculate the 21 cm signal is that describing the evolution of the Lyman-α background intensity J_α, which can couple the spin and kinetic temperatures of the H-atoms in the IGM via the Wouthuysen-Field effect. H-atoms, excited by collisions with fast photoelectrons subsequently produce a cascade of line photons, including Lyman-α photons which are then likely to be re-absorbed by the optically-thick IGM. We utilise the approximation adopted by Furlanetto et al. (2006b) that approximately half of the total energy which is diverted to excite hydrogen is used to produce Lyman-α photons[20], i.e. $\chi_\alpha \sim \chi_{e,\mathrm{H}}/2$.

Following the treatment by Valdes et al. (2007) we obtain (however, note the additional correction factor of ν_α in front of the expression)

$$J_\alpha = \frac{n_{\mathrm{H}}^2 hc\nu_\alpha}{4\pi H(z)} \left[x_e x_{e,\mathrm{H}} \alpha_{2^2P}^{\mathrm{eff.}} + x_{e,\mathrm{H}} x_{\mathrm{HI}} \gamma_{\mathrm{eH}} + \frac{\chi_\alpha \dot{\epsilon}}{n_{\mathrm{H}} h\nu_\alpha} \right], \tag{F.3.73}$$

where the first two terms are the contributions associated with the collisional excitation involving electrons discussed above, and the last term is the contribution from DM. Also, $\alpha_{2^2P}^{\mathrm{eff.}}$ is the effective recombination coefficient to the 2^2P level (Pengelly, 1964), and $\gamma_{e\mathrm{H}} \simeq 2.2 \times 10^{-8} \exp\left[-11.84/(T/10^4\,\mathrm{K})\right] \mathrm{cm}^3\,\mathrm{s}^{-1}$ is the collisional excitation rate of HI atoms involving electrons (Shull and van Steenberg, 1985).

The quantity most intimately associated with observations of the cosmological 21 cm signal is the differential brightness temperature deviation, δT_b, between the 21 cm signal and the CMB, approximately given by (Field, 1959; Ciardi and Madau, 2003)

$$\begin{aligned} \delta T_b \simeq 26\ \mathrm{mK}\ x_{\mathrm{HI}} \left(1 - \frac{T_{\mathrm{CMB}}}{T_S}\right) \left(\frac{\Omega_b h^2}{0.02}\right) \\ \times \left[\left(\frac{1+z}{10}\right)\left(\frac{0.3}{\Omega_{\mathrm{M}}}\right)\right]^{1/2}, \end{aligned} \tag{F.3.74}$$

where $x_{\mathrm{HI}} = 1 - x_{\mathrm{H}}$ is the average fraction of neutral hydrogen in the patch of sky being observed.

F.3.7. Results

In the following section, we illustrate our predictions for the effects on the thermal history of the IGM caused by the additional energy injected into it by annihilating neutralino CDM and LDM, when including the enhancement effects from DM structures.

Since, as we have seen, this enhancement can be very large, boosting the DM annihilation rate by several orders of magnitude, we want to be sure that this does not contradict other observations. Consequently, we perform two tests on each of the clumping factors investigated, before taking into consideration its effect on the 21 cm brightness temperature. First of all, we

[20] The authors of Pritchard and Furlanetto (2007) actually find that χ_α is somewhat larger than the value used here, $\chi_\alpha \simeq 0.79\chi_{e,\mathrm{H}}/2$. However we do not think this would alter our results significantly; in any case it would result in a larger deviation of the brightness temperature, so our results can be considered as more conservative.

check that the huge injection of energy into the IGM does not lead to premature re-ionisation. We use for this purpose our modified version of the RECFAST code described above, and discard all clumping factors for which the ionised fraction $x_e > 0.01$ at $z = 14$. We choose this value of the redshift because it is close to the 3σ upper limit to $z_{\rm reion.}$ coming from WMAP7 observations Komatsu et al. (2010). Secondly, we check that the diffuse photon flux produced does not exceed the observed diffuse gamma-ray and x-ray background (adopting the conservative approximation that $f_{\rm abs.} \sim 0$, that for all the models we consider is quite a good approximation at the present time $z = 0$, where the clumping factor reaches its maximum value). We use to this purpose the measurements of the diffuse gamma-ray background in the 1 MeV - 100 GeV range conducted by EGRET (Sreekumar et al., 1998; Strong et al., 2004) and COMPTEL (Weidenspointner et al., 2000), and those of the diffuse x-ray background in the sub-MeV range conducted by the SPI spectrometer aboard INTEGRAL (Churazov et al., 2007).

In the following, owing to the fact that the effects on the spin and brightness temperature can be very subtle, we display results only for the the most optimistic clumping factors, which we define, for a given DM model, as those which yield the largest difference in the differential brightness temperature, $\delta T_b - \delta T_{b,0}$ (see § F.3.9), at $z = 30$ (i.e., the smaller z were plausibly astrophysical effects are not important, see discussion at the end), while at the same time conforming to the above criteria. For reference, in Appendix F.3.4 we have tabulated the relevant astrophysical parameters associated with all clumping factors investigated, indicating which have been excluded on the basis of the criteria described above.

Neutralino dark matter

We show the results for the supersymmetric models described in § F.3.5 in Figs. F.21 and F.22 for halos with NFW and Moore density profiles respectively. In particular, in each panel we show the evolution of T_K and T_S for the most optimistic clumping factors consistent with our selection criteria, as described above. For comparison, we also display the corresponding results for the "no DM" scenario, i.e., in the absence of annihilating DM.

We start by considering model 1, i.e., 50 GeV neutralinos that annihilate to $b\bar{b}$ pairs 96% of the time and to $\tau^+\tau^-$ otherwise, with a canonical annihilation cross section of $\langle\sigma_{\rm ann.}v\rangle = 3\times10^{-27}{\rm cm}^3\,{\rm s}^{-1}/\Omega_{\rm DM,0}h^2 \simeq 2.7\times10^{-26}{\rm cm}^3\,{\rm s}^{-1}$. Owing to the relatively small mass of this neutralino, the associated energy injection rate into the IGM per annihilation is large (since overall, $\dot{\epsilon}_{\rm DM}$ scales as $m_{\rm DM}^{-1}$). Consequently, the majority of the clumping factors calculated using the Moore profile are excluded based on our criterion involving the diffuse radiation background. The most optimistic clumping factors consistent with our selection criteria are N4 and M18, for the NFW and Moore profiles resepectively. It is known that when the enhancement inside structures is ne-

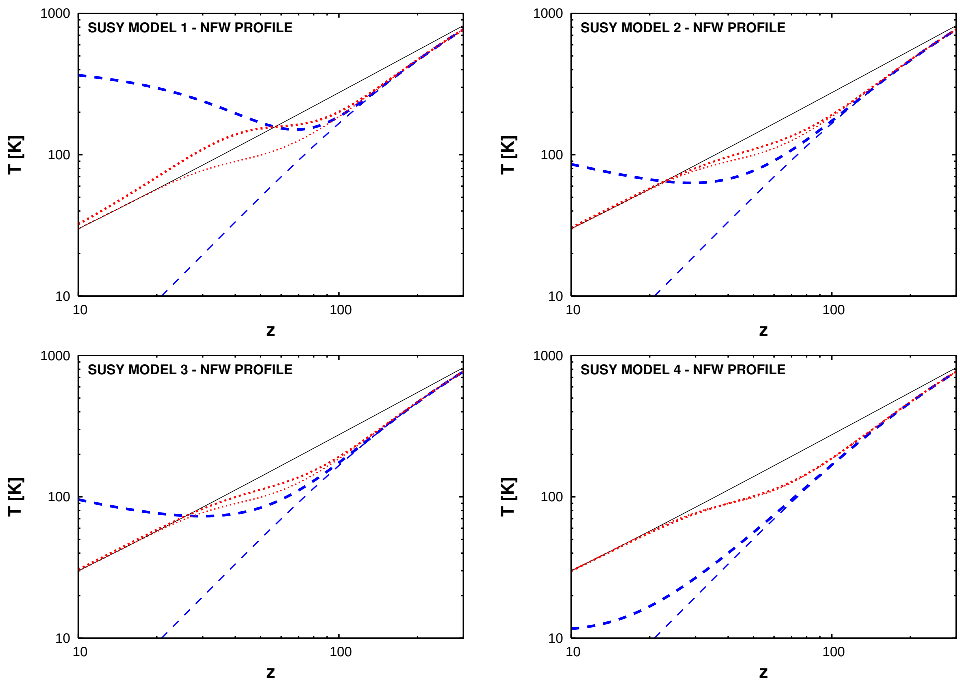

Figure F.21.: Evolution of the IGM kinetic (thick dashed blue curves) and spin (dotted red curves) temperatures for our four supersymmetric models. In each plot we show the results for the most optimistic clumping factors using the NFW density profile (thick curves) and, for comparison, the kinetic and spin temperatures in the absence of DM annihilations (thin curves). The CMB temperature is also shown (black solid curve). The annihilation cross section $\langle\sigma_{\mathrm{ann.}}v\rangle = 2.7\times10^{-26}\,\mathrm{cm}^3\,\mathrm{s}^{-1}$ in all plots. The clumping factors used are N4 for model 1, and N2 for models 2, 3, and 4.

glected (i.e. when $C = 1$), the energy injection from neutralino annihilation is insufficient to significantly alter the evolution of the IGM kinetic temperature. It can then be expected that significant heating of the IGM by annihilations can only start once the clumping factor is deviates significantly from unity. This corresponds to $z \simeq 25$ for M18 and $z \simeq 85$ for N4, corresponding to the time when the least massive DM structures start to form in these scenarios. The function $f_{\mathrm{abs.}}$ for model 1 neutralinos is almost constant during the period $10 < z < 90$, therefore we expect the evolution of the clumping factor to almost completely determine the evolution of the deviations from the "no DM" scenario. This is illustrated somewhat by the rapid elevation in T_K corresponding to the rapid increase in the M18 clumping factor at $z \simeq 20$, compared to that associated with N4, which maintains a more uniform increase in $\log(T_K)$, reflecting the almost constant value of $d\log(C)/d\log(1+z)$ at this time.

Next, we consider DM composed of neutralinos described by model 2, that

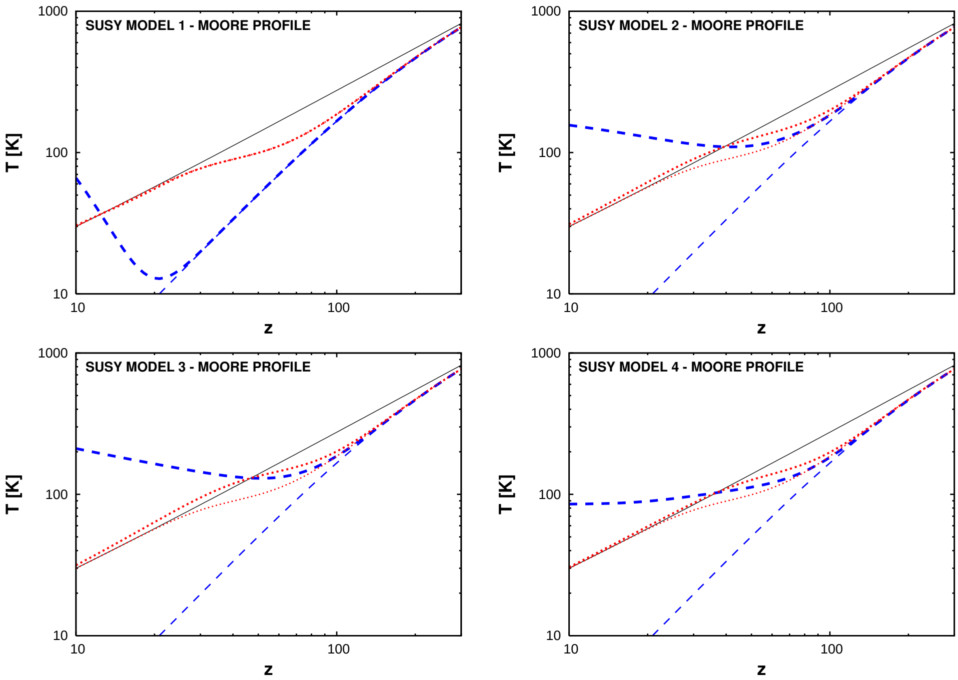

Figure F.22.: Evolution of the IGM kinetic (dashed blue curves) and spin (dotted red curves) temperatures for our four supersymmetric models. In each plot we show the results for the most optmistic clumping factors using the Moore density profile (thick curves) and, for comparison, the kinetic and spin temperatures in the absence of DM annihilations (thin curves). The CMB temperature is also shown (black solid curve). The annihilation cross section $\langle \sigma_{\rm ann.} v \rangle = 2.7 \times 10^{-26}\,{\rm cm}^3\,{\rm s}^{-1}$ in all plots. The clumping factors used are M18, M8, M7 and M4 for models 1, 2, 3, and 4 respectively.

is, 150 GeV gaugino-dominated neutralinos that annihilate 96% to $b\bar{b}$ and 4% to $\tau^+\tau^-$. As for model 1 neutralinos, the majority of the clumping factors calculated using the Moore profile are excluded owing to the overproduction of the diffuse radiation background with M8 being the most optimistic clumping factor to survive this constraint. For structures with NFW profiles, nearly all clumping factors are permitted, with N2 being the most optimistic. The clumping factors M8 and N2 are very similar in their evolution, both significantly exceeding unity at approximately $z = 85$, although M8 always exceeds N2 for the times $100 \gtrsim z \gtrsim 2$. Hence, we expect the evolution of T_K and T_S in both cases to be similar, with larger deviations from the "no DM" scenario expected for the M8 scenario. Unlike model 1, $f_{\text{abs.}}$ for model 2 neutralinos decreases by nearly a factor of 3 during this period. The decrease in $f_{\text{abs.}}$ largely mitigates the increasing heating rate resulting from the formation of DM structures, leading to the rather flatter evolution of T_K that is observed. This can be compared with the earlier results for model 1 neutralinos, which display constantly increasing T_K's (for $C \gg 1$), owing to the constant value of $f_{\text{abs.}}$ during such times.

Next we consider DM composed of neutralinos described by model 3, that is, 150 GeV higgsino-dominated neutralinos that annihilate 58% to W^+W^- and 42% to ZZ. Despite the fact that the gaugino fractions of the neutralinos described by models 2 and 3 are significantly different, their spectra of injected electrons and photons, and thus the absorbed fraction f_abs are quite similar. Hence we expect that the permitted clumping factors will also be quite similar, and in fact, this is the case: the most optmistic clumping factors are N2 and M7 for the NFW and Moore profiles, respectively. This results in the evolution of T_K to be very similar to that predicted for model 2, and all the considerations made above apply.

Finally, we consider DM composed of neutralinos described by model 4, that is, 600 GeV gaugino-dominated neutralinos that annihilate 87% to $b\bar{b}$ and 13% to $\tau^+\tau^-$. The relatively low energy injection rate per annihilation (arising from the large neutralino mass) allows for correspondingly larger clumping factors that satisfy our diffuse background constraints. In fact, the most optimistic clumping factors that are allowed are N2 and M4. Both M4 and N2 have similar patterns of evolution owing to the similar values of the parameters associated with each model (see Table F.7). However, despite this, M4 is always much larger than N2 (as can be expected when comparing clumping factors for structures possessing Moore and NFW profiles with similar structural parameters), with a maximum difference of approximately one order of magnitude at $z \simeq 30$. Also, M4 increases slightly more quickly than N2 for times $20 < z < 90$, explaining the correspondingly larger increase in T_K associated with the M4 model despite the larger substructure mass fraction associated with N2. This explains why the displayed M4 result for T_K increases so rapidly compared to that for N2 during these times. The associated $f_{\text{abs.}}$ function for model 4 decreases significantly over the period

$100 > z > 10$ (approximately 0.05 to 0.006), owing to the significantly larger energies of annihilation products produced compared to the lighter neutralinos of models 1, 2 and 3. Further, unlike the other three models, $f_{\mathrm{abs.}}$ here has no minimum within the times of interest. This, in addition to the steeply decreasing nature of $f_{\mathrm{abs.}}$ explains the distinct lack of a rise in T_K at later times, unlike that observed in models 1, 2 and 3. However, the similar values in $d\log(C)/d\log(1+z)$ for $z < 20$ for both M4 and N2 result in similar rates of decrease in $\log(T_K)$ at such times.

Light dark matter

In this section we consider the effects on the kinetic and spin temperature of the IGM caused by LDM particles that annihilate entirely to monochromatic e^+e^- pairs.

In the following, we calculate results utilising values of the LDM annihilation cross section $\langle\sigma_{\mathrm{ann.}}v\rangle$ based on constraints derived from the predicted effects of LDM annihilations on the CMB presented in Zhang et al. (2006); Ripamonti et al. (2007) as

$$\langle\sigma_{\mathrm{ann.}}v\rangle \leq 2.2\times10^{-29}\,\mathrm{cm^3\,s^{-1}}\,f_{\mathrm{abs.}}^{-1}\left(\frac{m_{\mathrm{LDM}}}{1\,\mathrm{MeV}}\right). \tag{F.3.75}$$

We follow the conservative treatment in Ripamonti et al. (2007) and substitute a value of $f_{\mathrm{abs.}}$ approximately equal to its maximum value, $f_{\mathrm{abs.}}^{\mathrm{max.}}$, into Eq.(F.3.75), in order to determine our conservative estimate for $\langle\sigma_{\mathrm{ann.}}v\rangle$. For comparison, we also calculate results for a value of $\langle\sigma_{\mathrm{ann.}}v\rangle$ one order of magnitude smaller than this limiting value. We show our results for T_K and T_S in Fig. F.23.

Firstly we consider 3 MeV LDM particles. In the left panels of Fig. F.23 we display the effects of DM composed of these particles on the evolution of T_K and T_S, when using annihilation cross sections $\langle\sigma_{\mathrm{ann.}}v\rangle$ equal to $1.2\times10^{-28}\,\mathrm{cm^3\,s^{-1}}$ (upper left panel) and $1.2\times10^{-29}\,\mathrm{cm^3\,s^{-1}}$ (lower left panel). We display results calculated using the B19 (upper left panel) and B15 (lower left panel) clumping factors, calculated for structures possessing Burkert density profiles, deduced to be the most optimistic models consistent with our constraints involving the diffuse radiation background when using values of $\langle\sigma v\rangle$ equal to $1.2\times10^{-28}\,\mathrm{cm^3s^{-1}}$ and $1.2\times10^{-29}\,\mathrm{cm^3s^{-1}}$ respectively. As usual, we compare these results for T_K and T_S to the "no DM" scenario. In the 3 MeV case, we also compare our results to those obtained using the formula for $f_{\mathrm{abs.}}$ provided by Ripamonti et al. (2007) (see Appendix F.3.5 for details).

The clumping factors B19 and B15 possess significant differences in their evolution owing to the different values of the minimum halo mass associated with them ($10^6\,M_\odot$ for B19 and $46\,M_\odot$ for B15). This results in the time at which B19 starts to significantly exceed unity occurring much more recently ($z\simeq20$) than for B15 ($z\simeq35$). As can be observed from Fig. F.23, these times closely correspond with the respective minima in T_K immediately before its rapid increase. However, unlike neutralinos, LDM can still significantly heat the IGM at times when $C \sim 1$, provided that $\langle \sigma_{\mathrm{ann.}} v \rangle$ is large enough. This can again be observed in Fig. F.23, where in the upper left panel significant deviations in T_K relative to the "no DM" scenario occur for $z > 20$, whereas such deviations are negligible for $\langle \sigma_{\mathrm{ann.}} v \rangle = 1.2 \times 10^{-29}\,\mathrm{cm}^3\,\mathrm{s}^{-1}$ at times $z > 35$, as can be seen from the lower left panel. Further, at recent times, B19 increases much more rapidly than B15, resulting in the correspondingly larger value of $d\log(T_K)/d\log(z)$ that is observed.

We also show the effect of using the function $f_{\mathrm{abs.}}$ as calculated in Ref. Ripamonti et al. (2007). At the respective times when the clumping factors B19 and B15 are much greater than unity, both the absorbed fraction calculated in this paper and that of Ref. Ripamonti et al. (2007) are monotonically increasing, with the former roughly twice larger than the latter (see upper panel of Fig. F.20). This is illustrated in the left panels of Fig. F.23 by the larger values T_K associated with our $f_{\mathrm{abs.}}$ relative to those associated with the $f_{\mathrm{abs.}}$ of Ref. Ripamonti et al. (2007).

Next, we consider 20 MeV LDM particles. In the right panels of Fig. F.23 we display the effects of DM composed of these particles on the evolution of T_K and T_S when using annihilation cross sections $\langle \sigma_{\mathrm{ann.}} v \rangle$ equal to $4.4 \times 10^{-28}\,\mathrm{cm}^3\,\mathrm{s}^{-1}$ (upper right panel) and $4.4 \times 10^{-29}\,\mathrm{cm}^3\,\mathrm{s}^{-1}$ (lower right panel). We display results calculated using the B19 and B3 clumping factors, calculated for structures possessing Burkert density profiles, deduced to be the most optimistic models consistent with our constraints involving the diffuse radiation background when using values of $\langle \sigma_{\mathrm{ann.}} v \rangle$ equal to $4.4 \times 10^{-28}\,\mathrm{cm}^3\,\mathrm{s}^{-1}$ and $4.4 \times 10^{-29}\,\mathrm{cm}^3\,\mathrm{s}^{-1}$ respectively. In all cases, we utilise the function $f_{\mathrm{abs.}}$ calculated according to the procedure described in Appendix F.3.5. Once again, we compare these results for T_K and T_S to those when DM is absent. The function $f_{\mathrm{abs.}}$ starts to deviate from unity at $z \sim 1000$, but the decrease is quite slow until $z \sim 30 - 50$; then it becomes more rapid until it reaches 0.2 at $z \simeq 10$ (see lower panel of Fig. F.20). This accounts for the slight decrease in $\mathrm{d}T_K/\mathrm{d}z$ observed during the period $z < 30$. Hence, at times $z > 30$, the evolution of the LDM heating rate is dominated by that of the clumping factor B19 (upper right panel) or B3 (lower right panel). There are significant differences in the evolution of these two clumping factors. In particular, the respective minima in T_K closely correspond to the times at which the clumping factor C starts to become much greater than unity. However, there appears to be significant heating by LDM at times when $C \sim 1$, indicated in the right panels of Fig. F.23 by the non-negligible deviations from the "no DM" model, especially when using $\langle \sigma_{\mathrm{ann.}} v \rangle = 4.4 \times 10^{-28}\,\mathrm{cm}^3\,\mathrm{s}^{-1}$ (upper right panel) at least up to $z = 300$, and up to $z \simeq 150$ when using $\langle \sigma v \rangle = 4.4 \times 10^{-29}\,\mathrm{cm}^3\mathrm{s}^{-1}$ (lower right panel).

F.3.8. The 21 cm global signature

Using the above results for the evolution of the spin temperature, T_S, in this section we present corresponding results for the differential brightness temperature δT_b, calculated using Eq.(F.3.74), that is most readily associated with measurements of the 21 cm background.

Neutralino dark matter

As in § F.3.7, we firstly consider neutralino DM. In Fig. F.24 we display our predictions for the evolution of δT_b in the presence of neutralino DM, relative to that calculated for the "no DM" scenario, $\delta T_{b,0}$, for our four benchmark SUSY models. In each case, we utilise an annihilation cross section $\langle \sigma v \rangle = 2.7 \times 10^{-26}\,\mathrm{cm}^3\,\mathrm{s}^{-1}$. For each DM model we display results when using the most optimistic clumping factors associated with Moore (lower panel) and NFW (upper panel) density profiles. For the Moore profiles, these are the clumping factors M18, M8, M7, M4 for models 1, 2, 3 and 4 respectively; for the NFW profile, they are the N4 clumping factors for model 1, and N2 for models 2, 3 and 4. For comparison, we have also calculated the differential brightness temperature for the least optimistic clumping factors, and also in the absence of structures (i.e. $C(z) = 1$). We do not show the results, but we have found that in both cases the deviations from the "no DM" behaviour are smaller than 1 mK at all redshifts greater than 10.

We observe that generally the evolution of δT_b using the most optimistic clumping factors presents some common features among the four models. In most cases we find a peak in the 21 cm emission at $z \simeq 60$ of up to ~ 40 mK. These features emphasise the additional heating by DM at times prior to the formation of baryonic structures, when the Universe cools adiabatically, when there is a characteristic absorption feature in the "no DM" scenario arising from the efficient coupling (via collisions) between T_K and T_S at these times (see, e.g., Ref. Valdes et al. (2007)). In the case of the NFW profile, we have that the clumping factors used for the four models are very similar (in fact, models 2, 3 and 4 use the same clumping factor N4, while model 1 uses N2), so that we expect the differences among the models to be mainly driven by the difference in the injected energy. In particular, lower-mass neutralino yield a larger signal, since overall the energy produced by annihilations scales as m_{DM}^{-1}. Also, in the case of lighter neutralinos, a larger part of the energy produced is effectively absorbed by the IGM (see Fig. F.19). For these reasons, model 1 gives a peak of $\simeq 35$ mK at $z = 60$ ($\simeq 18$ mK at $z = 30$), while model 4 presents only ~ 1 mK deviations from the "no dark matter" case.

In the case of the Moore profile, the clumping factors used differ more, so that we should factor this in when interpreting the results for δT_b. In the case of model 1, the large energy injection leads to the violation of the constraints on the diffuse background for nearly all clumping factors, so that has to be compensated by relatively small values of $C(z)$. The result is that there is actually an overcompensation, so that for the clumping factor considered there is no significant heating of the IGM and the brightness temperature basically has the same evolution as in the "no dark matter" case. Of course, our exploration of the parameter space for the clumping factor is far from complete, so that it could well be possible that there is a "soft spot" in parameter space (in particular a value of the minimum mass $M_{\rm min}$ somewhere between 10^{-6} and $10^4 M_\odot$) where the clumping factor is large enough to produce sizeable differences in δT_b, without at the same time violating the constraints on the reionization redshift and on the diffuse gamma backgrund. On the other hand, the clumping factors used for models 2 and 3 are very similar, and in fact, considering also that the neutralino mass is the same in the two models, the results for the brightness temperature are very similar. The differences can be traced in the larger value of the absorbed energy fraction for model 3. Finally, in the case of model 4, the smaller energy injection with respect to models 2 and 3 is nearly completely offset by the use of a larger clumping factor. In general, in models 2, 3 and 4, we find a peak of $\simeq$ 25 mK at $z = 60$ ($\simeq 5 - -10$ mK at $z = 30$) in the deviation of the differential brightness temperature with respect to the "no dark matter" case.

Light dark matter

We now consider light dark matter. In the top panel of Fig. F.25 we display predictions for the evolution of $\delta T_b - \delta T_{b,0}$ in the presence of DM solely composed of 3 MeV LDM particles. We use values of the annihilation cross section $\langle \sigma_{\rm ann.} v \rangle$ equal to $1.2 \times 10^{-28}\,{\rm cm^3\,s^{-1}}$ (red solid curves) and $1.2 \times 10^{-29}\,{\rm cm^3\,s^{-1}}$ (blue dashed curves). For comparison, we also show the corresponding results calculated using the function $f_{\rm abs.}$ derived in Ripamonti et al. (2007) (thin curves). For each value of $\langle \sigma_{\rm ann.} v \rangle$ we utilise the clumping factors associated with Burkert density profile which were determined to be the most optimistic, namely, B19 for the larger cross section and B15 for the smaller.

For both values of $\langle \sigma_{\rm ann.} v \rangle$, like neutralinos, there is a characteristic peak in $\delta T_b - \delta T_{b,0}$ which, as expected, is more distinct for the larger value of $\langle \sigma_{\rm ann.} v \rangle$ because of the larger deviations in the heating rate of the IGM relative to the "no DM" scenario. However, for LDM this peak occurs, in most cases, quite earlier ($z \simeq 100$) than for neutralino DM (with maxima at $z \simeq 60$).

Finally, in the bottom panel of Fig. F.25 we display predictions for the evolution of $\delta T_b - \delta T_{b,0}$ in the presence of DM solely composed of 20 MeV LDM particles. Our results are calculated using values of the annihilation cross section $\langle \sigma_{\rm ann.} v \rangle$ equal to $4.4 \times 10^{-28}\,{\rm cm^3\,s^{-1}}$ (red solid curve) and $4.4 \times 10^{-29}\,{\rm cm^3\,s^{-1}}$ (blue dashed curve). As for 3 MeV LDM particles, for each of these values of $\langle \sigma_{\rm ann.} v \rangle$ we utilise two most optimistic clumping factors associated with the Burkert density profile, which in this case were B19 for the larger cross section and B3 for the smaller.

For $\langle\sigma_{\text{ann.}}v\rangle = 4.4\times10^{-29}\,\text{cm}^3\,\text{s}^{-1}$, the most optimistic clumping factor, B3, results in a rate of IGM heating that yields a peak in $\delta T_b - \delta T_{b,0}$ of $\simeq 25$ mK at $z \simeq 40$. This results in a deviation at $z \simeq 30$ of roughly 20 mK. For $\langle\sigma_{\text{ann.}}v\rangle = 4.4\times10^{-28}\,\text{cm}^3\,\text{s}^{-1}$, the heating rate is sufficient to produce a significantly larger deviation of $\simeq 40$ mK at $z \simeq 100$; however, the deviation is < 1 mK at $z \simeq 30$.

F.3.9. Discussion

We have calculated predictions for the effects on the evolution of the cosmological HI 21 cm signal during the Dark Ages for various forms of annihilating neutralino and light dark matter. In doing so, we fully accounted for the significant enhancements made to the annihilation rate of these DM particles arising from DM structures. We utilised results from the state-the-art N-body simulations to calculate the evolution of the aforementioned enhancement in the annihilation rate, referred to here as the "clumping factor", owing to the distribution of halos and the near self-similar distribution of increasingly smaller substructures predicted to exist within them. We did this for a diverse range of values of astrophysical parameters consistent with the uncertainties in the dynamics of the simulated halos. We performed detailed calculations of the absorbed fraction of the energy injected into the IGM by the annihilation products of our DM candidates. We used the standard equations for the evolution of the kinetic and spin temperatures of the IGM with modifications to account for the additional energy injected into by the IGM from DM annihilations. Finally, we calculated the resulting deviations in the evolution of the differential brightness temperature δT_b relative to a scenario where DM is absent.

In our calculations of δT_b we have neglected the influence of astrophysical processes affecting the 21 cm background. In fact, these effects dominate the 21 cm signal, thus obscuring the cosmological information, once star formation becomes important at redshifts $z \simeq 25$ Pritchard and Loeb (2008). This means that the effect of the presence of annihilating DM at $z \lesssim 25$ (corresponding to frequencies $\nu \gtrsim 55$ Hz) will likely be undetectable due to the uncertainity in the astrophysical modelization.

The global 21 cm signal is the target of several experiments, like the "Cosmological Reionization Experiment" (CORE) and the "Experiment for Detecting the Global EOR Signature" (EDGES) Bowman et al. (2008); Rogers and Bowman (2008). Both experiments roughly operate in the frequency range from ~ 100 to ~ 200 MHz, corresponding to the redshift range $7 \lesssim z \lesssim 14$. In fact, the single antenna experiment EDGES has already released preliminary results Bowman et al. (2008); Rogers and Bowman (2008). This experiment attempts to separate the redshifted HI 21 cm signal from the contribution of the Galactic and Extragalactic foregrounds at the same frequencies by taking advantage of the fact that these foregrounds are anticipated to be smooth power-law spectra. Conversely, the cosmological signal, is expected to have up to three rapid transitions in brightness temperature corresponding to the cooling and heating of the IGM, and most recently from reionisation. However, the rapidly varying (with respect to frequency) systematic and instrumental contributions to the measured power spectrum can easily be mistaken for a cosmological signal. Currently, the r.m.s. level of systematic contributions is approximately $T \sim 75\,\mathrm{mK}$, but further reductions in these systematics are anticipated in the near future[21]. Unfortunately, both CORE and EDGES operate in a frequency range where, as explained above, the evolution of the ionized fraction and of the kinetic temperature is dominated by astrophysics, so that presently they cannot be useful in constraining the models considered here. However, the EDGES team plans to expand the frequency coverage of the instrument down to 50 MHz or lower Bowman et al. (2008), thus opening the possibility of exploring the regime where the 21 cm signal is dominated by the cosmological contribution. In order to exclude at least the most optimistic models considered here, the EDGES experiment should be able to reduce the systematics at 50 MHz to below $\sim 20\,\mathrm{mK}$, although the contribution of the Galactic synchrotron foreground increases significantly at the lower frequencies.

Another interesting way to potentially put observational constraints on the energy injection from DM annihilation would be to consider the effects on the spatial fluctuations of the brightness temperature, as encoded by their power spectrum, $\mathcal{P}_{T_b}$, rather than the average signal as we have done in this paper. This was done, for example, in Furlanetto et al. (2006b) (although the authors neglect the clumpiness of DM). Such fluctuations are somewhat easier to measure than the average signal since they are less contaminated by foregrounds.

Even more interestingly, peculiar velocities give rise to an anisotropy of the 21 cm power spectrum that can be used to separate the cosmological signal from the (uncertain) astrophysical contribution, thus allowing, at least in principle, one to detect the effects of DM annihilation in the astrophysics-dominated regime Barkana and Loeb (2005); McQuinn et al. (2006); Pritchard and Loeb (2008).

The 21 cm fluctuations are themselves the target of several experimens, such as LOFAR [22], MWA [23], PAPER [24], 21CMA [25] and SKA [26]. In particular, the impending LOFAR epoch of reionization experiment is designed

[21] J.D. Bowman (private communication).

[22] http://www.lofar.org/.

[23] http://www.haystack.mit.edu/ast/arrays/mwa/; http://www.MWAtelescope.org/.

[24] http://astro.berkeley.edu/~dbacker/eor/.

[25] http://web.phys.cmu.edu/~past/; http://21cma.bao.ac.cn/.

[26] http://www.skatelescope.org/.

to observe radio fluctuations at frequencies 115-215 MHz, corresponding to the redshifted 21 cm signal in the range $6 < z < 11.5$ (Best and Consortium, 2008). Unfortunately, the cosmological signal is contaminated by a plethora of astrophysical and non-astrophysical components - including, Galactic synchrotron emission from diffuse and localized sources (Shaver et al., 1999), Galactic free-free emission (Shaver et al., 1999), integrated emission from extragalactic sources, such as radio galaxies and clusters (Shaver et al., 1999; Di Matteo et al., 2002; Oh and Mack, 2003; Cooray and Furlanetto, 2004), ionospheric scintillation and instrumental response - the fluctuations in which can significantly exceed the cosmological signal (see e.g. (Harker et al., 2009; Liu et al., 2009a)).

We did not consider the possibility that the DM annihilation cross section is enhanced inside cold substructures due to non-perturbative quantum corrections Lattanzi and Silk (2009). This so-called Sommerfeld enhancement could increase the annihilation cross section by orders of magnitude with respect to its early-Universe value. The effect of such an enhancement on the heating/ionisation history of the IGM has been studied in Cirelli et al. (2009a), where it has been shown that it could similarly increase the IGM temperature by orders of magnitude.

An interesting extension of our analysis would be to consider other DM particles, such as "Exciting DM" (XDM) (see, e.g., (Finkbeiner and Weiner, 2007)). XDM can annihilate to produce two intermediate scalars ϕ that can subsequently decay to standard model particles. If $2m_e < m_\phi < 2m_\mu$, the ϕ will mainly decay to an e^+e^- pair, with an energy spectrum extending up to the mass of the XDM particle (Cholis et al., 2009). Such particles are well motivated DM candidates and have been proposed to explain several other astronomical observations Finkbeiner and Weiner (2007); Chen et al. (2009); Cholis et al. (2009). Like LDM, the direct production of boosted e^+e^- pairs following self-annihilation gives XDM the potential to produce observable features in the global 21 cm signal. In fact, recently it has been determined that particles with collisional long-lived excited states, and inspired by XDM models, may have observable effects on the CMB and the 21 cm background signal Finkbeiner et al. (2008).

We would also like to acknowledge the recent simulations by the Virgo Consortium as part of its Aquarius project Springel et al. (2008a,b), conducted during the writing of the most recent version of this paper. These simulations investigate the properties of a Galaxy-sized DM halo and its substructure with unprecedented resolution. Whilst the results are largely consistent with those deduced from the Via Lactea simulations, there are significant differences. These include (i) four generations of resolved substructure (rather than the two in Via Lactea II), (ii) a distribution of substructures that is not self-similar to its host halo (rather than a fractal-like distribution observed in Via Lactea), (iii) a subhalo mass function with an index of -1.9 (rather than the -2.0 used in this study, although a brief discussion of the significance of such deviations on the clumping factor are made in § F.3.4). Whilst we acknowledge that these differences may change some of our conclusions regarding the detectability of the 21 cm global signature, we do not pursue an investigation of these results here, but intend to incorporate them into a subsequent study.

Finally, we note that the effect of DM annihilations on the 21 cm signal has been further studied in Natarajan and Schwarz (2009), including the effects on the brightness temperature fluctuations, that we have not considered here. On the other hand, the authors do not include the effect of substructures in their calculations.

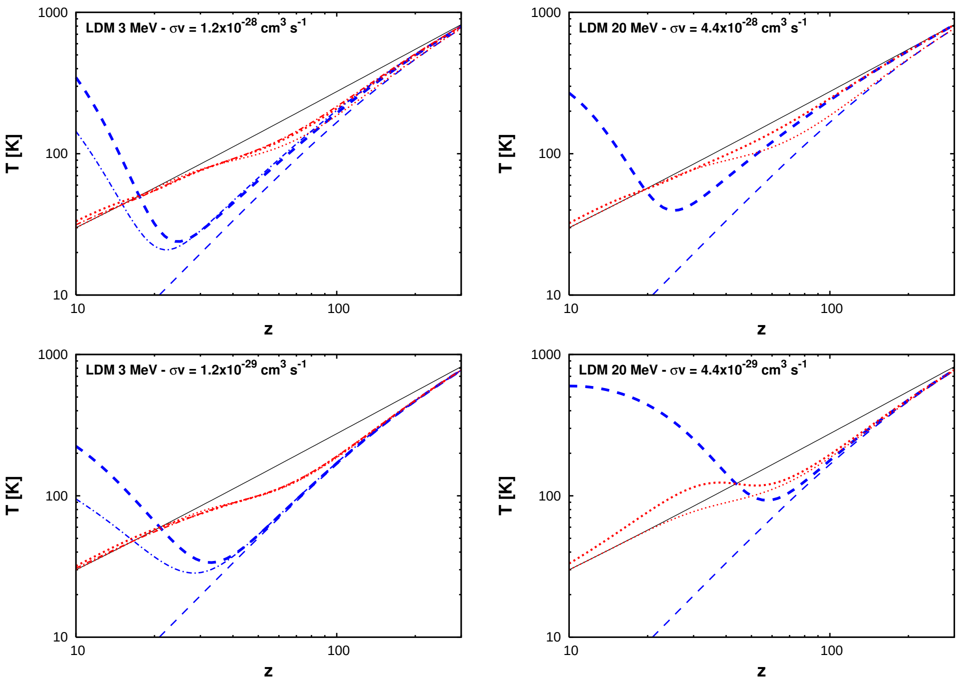

Figure F.23.: Evolution of the IGM kinetic (dashed blue curves) and spin (dotted red curves) temperatures for annihilating LDM particles with a mass of 3 MeV (left panels) and 20 MeV (right panels). In each plot we show the results for the most optmistic clumping factors using the Burkert density profile (thick curves) and, for comparison, the kinetic and spin temperatures in the absence of DM annihilations (thin curves). The CMB temperature is also shown (black solid curve). In the case of 3 MeV LDM, we also show the results for T_K and T_S, obtained using the fitting formula for $f_{\text{abs.}}$ of Ripamonti et al. (2007) (dot-dashed thin red curves). The annihilation cross section used is given by $\langle \sigma_{\text{ann.}} v \rangle = 1.2 \times 10^{-28}\,\text{cm}^3\,\text{s}^{-1}$ and $\langle \sigma_{\text{ann.}} v \rangle = 4.4 \times 10^{-28}\,\text{cm}^3\,\text{s}^{-1}$ in the upper left and right plots respectively, and a factor of 10 smaller in the corresponding lower plots. The clumping factors used are B19 in the two upper panels, B15 in the lower left panel, and B3 in the lower right panel.

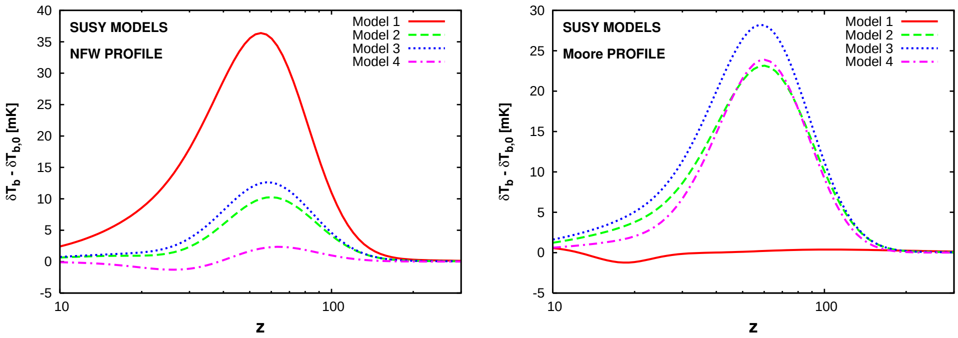

Figure F.24.: Evolution of the 21 cm differential brightness temperature δT_b, relative to $\delta T_{b,0}$ calculated for the "no DM" model, for the four supersymmetric models considered in the text, in the case of NFW (upper panel) and Moore (lower panel) profiles. For each model and density profile we display results using the most optmistic clumping factors compatible with our selection criteria based on the reionization redshift and on the gamma-ray background (top panel: N4 for model 1, N2 for models 2, 3, 4; bottom panel: M18, M8, M7, M4 for models 1, 2, 3 and 4 respectively). The annihilation cross section $\langle \sigma v \rangle = 2.7 \times 10^{-26}\,\mathrm{cm^3 s^{-1}}$ for all models.

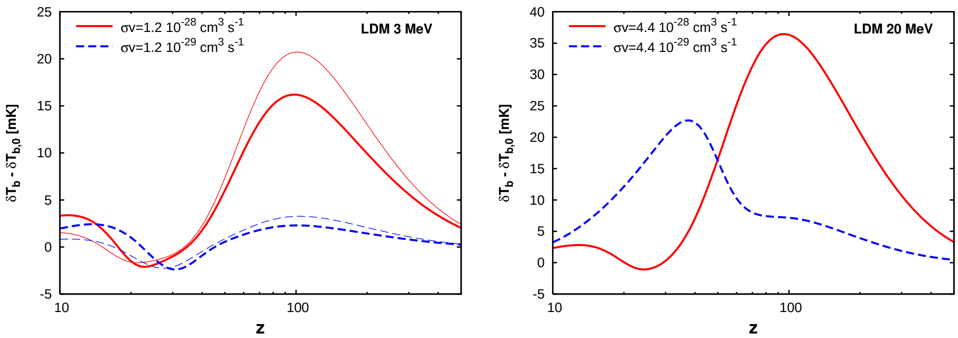

Figure F.25.: Evolution of the 21 cm differential brightness temperature δT_b, relative to $\delta T_{b,0}$ calculated for the "no DM" model, for LDM particles with a mass of 3 MeV (upper panel) and 20 MeV (lower panel), for structures with Burkert profiles. For each value of the mass, we consider two values of the annihilation cross section. In the case of 3 MeV LDM, we also show the results obtained using the fitting formula for $f_{\mathrm{abs.}}$ of Ripamonti et al. (2007) (thin curves). For each model we display results using the most optmistic clumping factors compatible with our selection criteria based on the reionization redshift and on the gamma-ray background [top panel: B19 for $\langle \sigma v \rangle = 1.2 \times 10^{-28}\,\mathrm{cm^3 s^{-1}}$, B15 for $\langle \sigma v \rangle = 1.2 \times 10^{-29}\,\mathrm{cm^3 s^{-1}}$; bottom panel: B19 for $\langle \sigma v \rangle = 4.4 \times 10^{-28}\,\mathrm{cm^3 s^{-1}}$, B3 for $\langle \sigma v \rangle = 1.2 \times 10^{-28}\,\mathrm{cm^3 s^{-1}}$].

G. Estimation of cosmological parameters

G.1. Inflation with primordial broken power law

In the past few years, a cosmological "concordance model" has emerged from precision measurements of the cosmological observables. According to this Λ cold dark matter (ΛCDM) model, the Universe has flat spatially geometry and its overall energy density is contributed by baryons, dark matter, and by an unclustered "dark energy" component. The structures we observe today have been formed through gravitational instability, from initial, nearly scale-invariant adiabatic Gaussian fluctuations. The observational basis for this concordance model mainly lies in the measurements of the anisotropies of the Cosmic Microwave Background (CMB) radiation Dunkley et al. (2009); Komatsu et al. (2009), of the large-scale structure (LSS) of the Universe Tegmark et al. (2004); Cole et al. (2005); Tegmark et al. (2006b), and of the Hubble diagram of distant type Ia supernovae Riess et al. (1998); Perlmutter et al. (1999); Frieman et al. (2008).

However, even if the model can satisfactorily explain the majority of cosmological observations, it still remains puzzling from a theoretical point of view. In particular, while there are many theoretically motivated (from the point of view of particle physics) candidates for the role of dark matter, on the contrary a satisfactory explanation concerning the nature of dark energy still does not exists, although many candidates have been proposed Frieman et al. (2008); Peebles and Ratra (2003); Caldwell and Kamionkowski (2009). In fact, a strong amount of fine tuning is required in order to explain the smallness of the dark energy density with respect to any significant high-energy scale, and the fact that dark energy and matter presently give the same contribution, within a factor of 3, to the total density of the Universe.

The above difficulties have led some authors to assess the robustness of the evidence for the existence of dark energy (in the simplest form of a cosmological constant), and in particular its dependence on the underlying assumptions related to the choice of a particular cosmological model. Recently, it has been shown that the CMB data can be well fitted by an Einstein-de Sitter model with zero cosmological constant, by relaxing the assumption that the primordial power spectrum is a simple power law Blanchard et al. (2003). Interestingly enough, the authors of Ref. Blanchard et al. (2003) find that the best-fit model with broken spectrum and no cosmological constant has a *better* χ^2 relative to the CMB power spectrum than the best concordance model. Models with zero Λ can also fit the spectrum of matter fluctuations provided that part of the matter content is given by a non-clustering component, for example neutrinos with eV mass. The price to pay is that these models do require a very low value of the Hubble constant, $H_0 \simeq 46$ km s^{-1} Mpc^{-1}, that is inconsistent with the HST Key Project measurements of the Hubble constant: $H_0 = 72 \pm 9$ km s^{-1} Mpc^{-1} Freedman et al. (2001). A possible explanation could be that we live in an underdense region, that is thus expanding faster than the average: this would imply that the locally measured "Hubble constant" probed by the HST would be larger than the actual, cosmological Hubble constant, probed by CMB observations. In any case, the analysis in Ref. Blanchard et al. (2003) would seemingly indicate that, once the usual assumptions on the form of the primordial power spectrum are dropped, the Hubble diagram of distant supernovae Ia is the only direct evidence for the presence of a cosmological constant.

Many generalization of the simple power-law shape of the primordial power spectrum have been proposed, both on physical and observational grounds. Here we will only consider models with a broken primordial power spectrum, since these were shown in Ref. Blanchard et al. (2003) to provide a very good fit to the CMB data also with a zero cosmological constant. For a bayesian analysis of other alternatives to the single power-law spectrum, see for example Refs. Bridges et al. (2007); Bridges et al. (2006); Bridges et al. (2009). Pandolfi et al. (2010b) have constrained the parameters of models with a broken power law primordial spectrum, and assessed whether these models (and in particular models with a broken power spectrum *and* $\Omega_\Lambda = 0$) really represent a viable alternative to the concordance model. In fact, the χ^2 goodness of fit is not the proper criterium to select which model, within a set, does a better job in explaining the experimental data. A very reliable way to assess the performance of a model is given by bayesian model selection. This method automatically encodes Occam's razor principle, since models with a larger number of parameters are naturally penalised.

This section is thus organized as follows. In section II we describe our data analysis method used, and we recall the basics of bayesian model comparison. In Sec. III we show our results, and finally in Sec. IV we draw our conclusions.

G.1.1. Likelihood Analysis

We consider three different cosmological models: the standard ΛCDM model, a CDM model (i.e. a model with $\Omega_m = 1$) with a modified spectrum of primordial fluctuations, and a ΛCDM model also with a modified spectrum. In particular, we consider the case of a broken power law spectrum $P(k)$, i.e.:

$$P(k) = \begin{cases} A_1 \left(\frac{k}{k_p}\right)^{n_1} & \text{for } k < k_*, \\ A_2 \left(\frac{k}{k_p}\right)^{n_2} & \text{for } k \geq k_*, \end{cases} \tag{G.1.1}$$

with the continuity condition $A_1 k_*^{n_1} = A_2 k_*^{n_2}$. Then, if the usual, single power law spectrum is defined in terms of two parameters, namely its amplitude A_s (as measured at the pivot wavenumber $k_p = 0.002\,\mathrm{Mpc}^{-1}$) and spectral index n_s, the broken power law spectrum will be defined in terms of four out of the five parameters $\{A_1, A_2, n_1, n_2, k_*\}$. We choose the four independent parameters to be n_1, n_2, k_*, and the amplitude A_s at k_p. This coincides with A_1 or A_2 depending if $k_* > k_p$ or $k_* < k_p$.

The parameters of the ΛCDM model are, as usual, the physical baryon density ω_b, the cold dark matter density ω_c, the ratio θ between the sound horizon and the angular diameter distance to the last scattering surface, the neutrino fraction f_ν, the reionization optical depth τ, the amplitude A_s of the primordial spectrum at k_p, and the scalar spetral index n_s. The CDM model with a broken spectrum, that we will call for simplicity "modified CDM" (MCDM), is described by the following eigth parameters: ω_b, θ, f_ν, τ, A_s, n_1, n_2, k_*. The value of ω_c is derived by the request that $\Omega_m = 1$. Finally, the ΛCDM model with a broken spectrum ("modified ΛCDM", or MΛCDM) is described by nine parameters, namely ω_b, ω_c, θ, f_ν, τ, A_s, n_1, n_2,k_*. In all three models we impose spatial flatness and purely adiabatic initial conditions, and we consider three neutrino families with equal mass. We take implicit flat priors on all the parameters. In particular, we take $0.8 \leq n_1 \leq 2$, $0.2 \leq n_2 \leq 1$ and $0.001\,\mathrm{Mpc}^{-1} \leq k_* \leq 0.02\,\mathrm{Mpc}^{-1}$. It is clear that the M$\Lambda$CDM model encompasses the other two for particular values of the parameters: it reduces to the ΛCDM when the two spectral indices are equal, $n_1 = n_2$, and thus the spectrum becomes a single power law; and it reduces to the MCDM when $\Omega_m = 1$.

We have modified the CAMB code in order to compute the spectrum of CMB anisotropies for models with a broken power law spectrum like the one in Eq. G.1.1. First, we constrain the variation of the parameters in the more general MΛCDM model by means of a Markov Chain MonteCarlo (MCMC) analysis of recent CMB data. The analysis method we adopt is based on the publicly available Markov Chain Monte Carlo package CosmoMC with a convergence diagnostics done through the Gelman and Rubin statistics. Since we are interested, among other things, in assessing whether modifying the assumptions on the shape of the primordial power spectrum reopens the possibility for a purely matter-dominated Universe, we want to make sure that our chains sufficiently explore the low-probability tails of the posterior distribution. For this reason, we have performed additional MCMC runs at different temperatures.

Our basic data set is the five-year WMAP data (temperature and polarization) with the routine for computing the likelihood supplied by the WMAP team. We marginalize over a possible contamination from Sunyaev-Zeldovich component, rescaling the WMAP template at the corresponding experimental frequencies. Then we also consider data on the matter power spectrum from the 2dF galaxy survey Cole et al. (2005).

Finally, we perform a model comparison between the three models (for an introduction to bayesian model comparison, see for example Ref. Trotta (2008)). The relevant quantity assessing a model's performance in explaining the data is the bayesian evidence, namely the probability of the data given the model: $p(d|\mathcal{M})$. This can be related to the quantity we are really interested in, the posterior probability of the model (i.e., the probability of the data given the model), by applying Bayes' Theorem, so that:

$$p(\mathcal{M}|d) \propto p(d|\mathcal{M})p(\mathcal{M}), \tag{G.1.2}$$

where we have dropped an irrelevant normalization constant $p(d)$ that depends only on the data. The quantity $p(\mathcal{M})$ is the prior probability assigned to the model.

When comparing two models $\mathcal{M}_0$ and $\mathcal{M}_1$, one is interested in the ratio between the posterior probabilities:

$$\frac{p(\mathcal{M}_0|d)}{p(\mathcal{M}_1|d)} = \frac{p(d|\mathcal{M}_0)p(\mathcal{M}_0)}{p(d|\mathcal{M}_1)p(\mathcal{M}_1)}. \tag{G.1.3}$$

In absence of significant preference for any of the models, one can take the prior to be equal, $p(\mathcal{M}_0) = p(\mathcal{M}_1)$, and the ratio of the posteriors is thus given by the ratio of the evidences, the so-called Bayes factor B_{01}:

$$\frac{p(\mathcal{M}_0|d)}{p(\mathcal{M}_1|d)} = \frac{p(d|\mathcal{M}_0)}{p(d|\mathcal{M}_1)} \equiv B_{01}. \tag{G.1.4}$$

A value of B_{01} larger than unity means that the current data favour model 0 with respect to model 1, and viceversa.

The bayesian evidence for each model can be in principle evaluated by writing

$$p(d|\mathcal{M}) = \int p(d|\theta, \mathcal{M})p(\theta|\mathcal{M})d\theta \tag{G.1.5}$$

i.e. as the integral of the product of the likelihood times the prior over the whole parameter space of the model. Unfortunately, evaluation of this integral is in general not easy, since it involves integration over a highly-dimensional parameter space. Also, it requires that the tail of the posterior distribution for the parameter have been adequately explored. However, this calculation can be simplified when the two models that are compared are nested one into the

Parameter	Mean WMAP	Max Like WMAP	Mean WMAP+2dF	Max Like WMAP+2df
$100\Omega_b h^2$	$2.14^{+0.10}_{-0.11}$	2.07	$2.206^{+0.080}_{-0.078}$	2.211
$\Omega_c h^2$	0.1221 ± 0.011	0.1214	$0.1118^{+0.0054}_{-0.0058}$	0.1097
Ω_Λ	$0.621^{+0.095}_{-0.094}$	0.648	$0.708^{+0.039}_{-0.034}$	0.728
Ω_m	$0.379^{+0.094}_{-0.095}$	0.352	$0.292^{+0.034}_{-0.039}$	0.271
H_0 [km sec^{-1} Mpc^{-1}]	62.8 ± 5.9	63.5	$68.2^{+3.3}_{-3.1}$	69.6
f_ν	≤ 0.064	0.014	≤ 0.042	0.0057
τ	$0.0882^{+0.0075}_{-0.0090}$	0.0810	$0.0914^{+0.0078}_{-0.0092}$	0.0838
z_r	11.1 ± 1.6	10.7	10.9 ± 1.5	10.2
t_0[Gyrs]	$14.23^{+0.33}_{-0.32}$	14.18	13.98 ± 0.21	13.92
n_1	$1.017^{+0.061}_{-0.063}$	1.02	$1.006^{+0.068}_{-0.067}$	0.979
n_2	$0.921^{+0.037}_{-0.039}$	0.897	$0.948^{+0.025}_{-0.023}$	0.944
k_* [Mpc^{-1}]	≤ 0.012	0.012	≤ 0.011	0.009
$\log[10^{10} A_s]$	$3.204^{+0.055}_{-0.056}$	3.165	$3.182^{+0.051}_{-0.054}$	3.160
$n_1 - n_2$	$0.095^{+0.087}_{-0.089}$	0.12	$0.057^{+0.085}_{-0.088}$	0.035

Table G.1.: MΛCDM model parameters and 68% credible intervals (first and third column) and best fit values (second and fourth column), obtained using the WMAP and WMAP+2dF datasets.

other, i.e., when one of the models reduces to the other for particular values of the parameters, as it is the case for the models considered here.

G.1.2. Results

Parameter estimation

We show the constraints for the parameters of the MΛCDM model, obtained using the WMAP and WMAP+2dF datasets, in Table G.1. For the sake of comparison, we also show in Table G.2 the constraints on some of the parameters of the MΛCDM together with the constraints obtained in the ΛCDM model, using in both cases the WMAP-only dataset. First of all, we notice that the value of $\Omega_\Lambda = 0.62 \pm 0.10$ for the WMAP dataset is lower than the ΛCDM value $\Omega_\Lambda = 0.67 \pm 0.07$. The uncertainity in the determination of Ω_Λ is also larger, probably as an effect of the introduction of the additional parameters describing the modified power spectrum. Adding the 2dF data shifts the dark energy to larger values and reduces the error, $\Omega_\Lambda = 0.71^{+0.04}_{-0.03}$. The value of the Hubble constant is also lower in the MΛCDM model when using only the WMAP data, and is shifted to larger values when the 2dF data are included. In the top panels of Fig. G.1 we show the posterior distribution for Ω_Λ and H_0 for the MΛCDM model, using the WMAP data only and the WMAP+2dF dataset.

For what concerns the parameters describing the shape of the primordial power spectrum, using the WMAP-only dataset, we find that the low-wavenumber

Parameter	MΛCDM (WMAP)	ΛCDM (WMAP)
Ω_Λ	$0.621^{+0.095}_{-0.094}$	0.669 ± 0.066
Ω_m	$0.379^{+0.094}_{-0.095}$	0.331 ± 0.066
H_0 [km sec^{-1} Mpc^{-1}]	62.8 ± 5.9	65.7 ± 4.9
n_1	$1.017^{+0.061}_{-0.063}$	0.950 ± 0.017
n_2	$0.921^{+0.037}_{-0.039}$	0.950 ± 0.017
k_* [Mpc^{-1}]	≤ 0.012	–
$\log[10^{10} A_s]$	$3.204^{+0.055}_{-0.056}$	$3.211^{+0.051}_{-0.058}$
$n_1 - n_2$	$0.095^{+0.087}_{-0.089}$	0

Table G.2.: Comparison between the MΛCDM and ΛCDM 68% credible intervals for selected parameters, obtained using the WMAP dataset.

spectral index $n_1 = 1.02 \pm 0.06$, so that the tilt of the spectrum could be either blue or red, while the high-wavenumber spectral index is constrained to be red, $n_2 = 0.92 \pm 0.04$. For comparison, the overall spectral index n_s in the ΛCDM model lies somewhere in the middle, $n_s = 0.95 \pm 0.02$. It is interesting to note that the 68% credible intervals for n_1 and n_2 do not overlap. This is made more clear if one looks a the marginalized posterior for $\Delta n \equiv n_1 - n_2$. We have that $\Delta n = 0.095^{+0.087}_{-0.089}$ and thus $\Delta n = 0$ lies sligthly outside the 68% credible interval, indicating a weak preference for models with $n_1 \neq n_2$. The wavenumber at the break of the spectrum, k_* is poorly constrained by the data and could lie nearly anywhere in its prior range, although values smaller than $\simeq 0.012$ Mpc^{-1} are preferred. The main effect of adding the 2dF data is that the mean value of n_2 is shifted to larger values, $n_2 = 0.95 \pm 0.01$, and then there is a small overlap of the 68% credible intervals for n_1 and n_2. We show the posterior distributions for n_1, n_2, k_* and Δn in the three lower panels of Fig. G.1.

The reason for the fact that Ω_Λ tends to be smaller in the enlarged MΛCDM model with respect to the concordance ΛCDM model is that it exists a partial degeracy between n_2 and Ω_Λ (or, equivalently, between n_2 and Ω_m). A mildly red spectrum at the large wavenumbers can partially compensate for the increased matter content and thus mimic of the effect a cosmological constant. This is clear in the first panel of Fig. G.2, where we show the two-dimensional 68% and 95% credible intervals in the $n_2 - \Omega_\Lambda$ plane. In the same figure, we also show the credible intervals in the $n_2 - H_0$ and $n_2 - n_1$ planes. On the other hand we do not find any appreciable correlation between the value of n_1 and that of Ω_Λ. One could naively expect that the late integrated Sachs-Wolfe effect would make the effect of Ω_Λ at the low multipoles partially degenerate with a change of the slope of the primordial spectrum in the same region. However this effect is probably masked by the large cosmic variance.

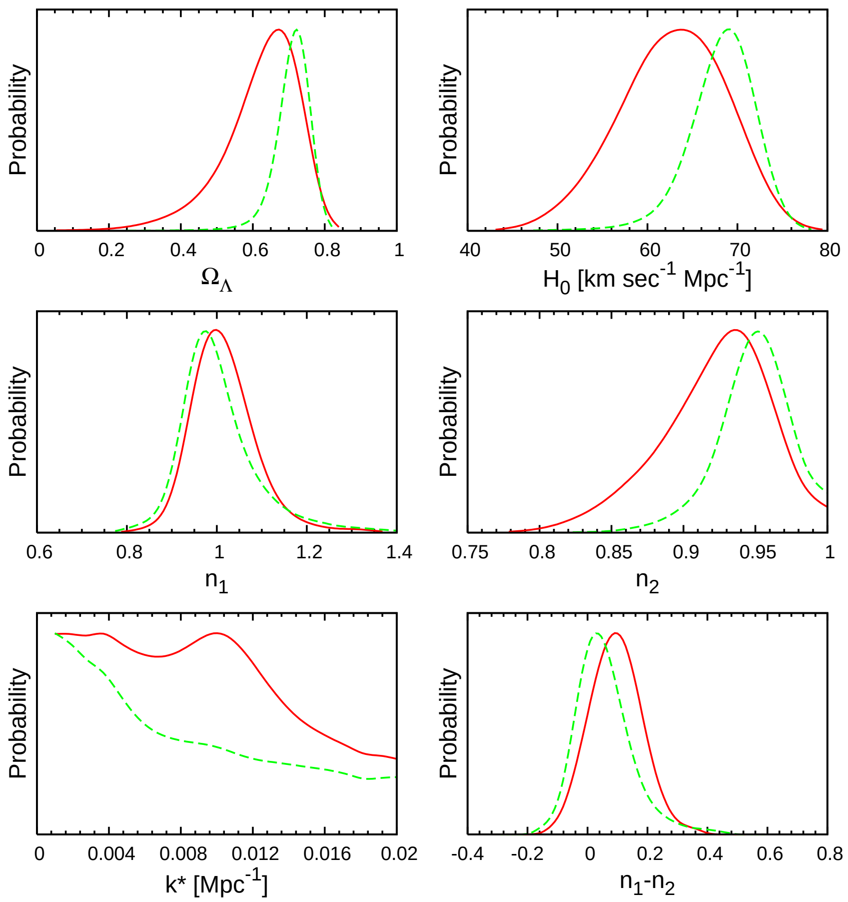

Figure G.1.: Marginalized one-dimensional posteriors for Ω_Λ, H_0, n_1, n_2, k_* and Δ_n using the WMAP data (solid [red] curves) and the WMAP+2dF dataset (green [dashed] curves).

The sligthly blue best-fit value that we find for n_1 is probably due to the effect of the low quadrupole in the WMAP data.

Model comparison

In order to assess the performance of the models we consider here in explaining the WMAP and 2dF data, we compute the Bayes factor between pairs of models. We assume equal priors for all the models. We start by considering the MΛCDM model and the MCDM model, namely the model studied in Ref. Blanchard et al. (2003). The MCDM model is equivalent to the more general MΛCDM when $\Omega_\Lambda = 0$. Assuming that the prior is separable, the Bayes factor can be shown to be equal to the Savage-Dickey density ratio, i.e. the ratio between the one-dimensional posterior and the prior, evaluated at the point where the more complex model reduces to the simpler one. Then

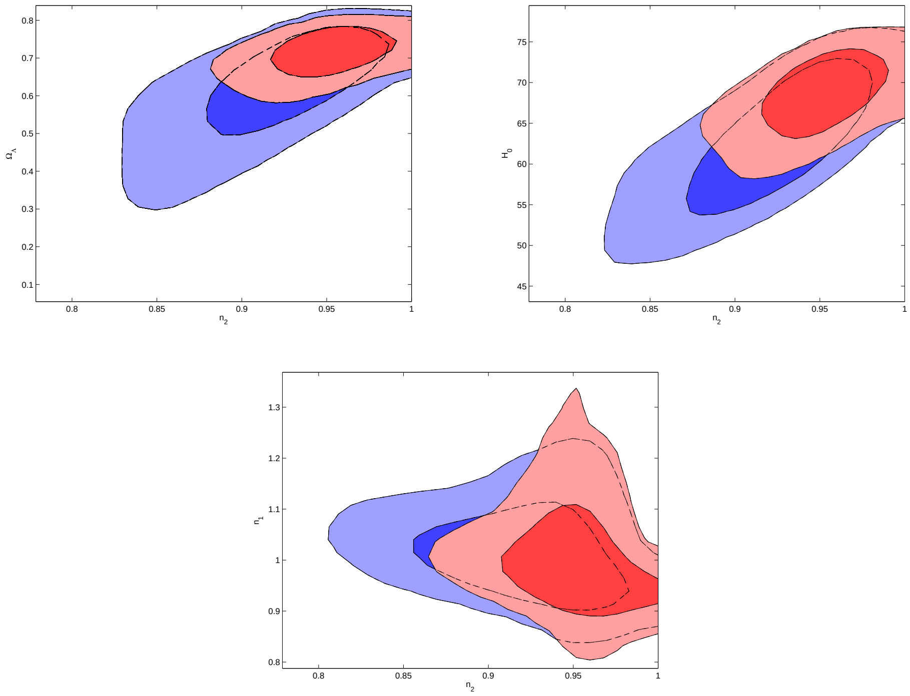

Figure G.2.: Two dimensional 68% (darker regions) and 95% (lighter regions) credible regions for (n_2, Ω_Λ) [upper left panel], (n_2, H_0) [upper right panel], $(n1, n_2)$ [lower panel], using the WMAP-only [blue] and WMAP+2dF [red] datasets.

we can write for the Bayes factor $B_{\rm MCDM}$:

$$B_{\rm MCDM} \equiv \frac{p(d|{\rm MCDM})}{p(d|{\rm M\Lambda CDM})} = \frac{p(\Omega_\Lambda = 0\,|\,d, {\rm M\Lambda CDM})}{p(\Omega_\Lambda = 0\,|\,{\rm M\Lambda CDM})}. \quad \text{(G.1.6)}$$

Since Ω_Λ is a derived parameter, we do not know the exact form of the prior $p(\Omega_\Lambda = 0\,|\,{\rm M\Lambda CDM})$. However, it is reasonable to assume that it is nearly flat between 0 and 1, so that we can take $p(\Omega_\Lambda = 0\,|\,{\rm M\Lambda CDM}) = \text{const.} = 1$. Another possible issue is due to the fact that the calculation of $B_{\rm MCDM}$ involves the value of the one-dimensional posterior for Ω_Λ in $\Omega_\Lambda = 0$, i.e. at the very extreme of the parameter space and very far from the region of maximum probablity. Usually the tails of the posterior are poorly sampled by the MonteCarlo methods used for parameter estimation, like the Metropolis-Hastings algorithm. To ensure that the value of $p(\Omega_\Lambda = 0)$ that we get is reliable, we have perfomed different MC runs at different temperatures, meaning that samples are drawn from $p(d\,|\theta, \mathcal{M})^{1/T} p(\theta|\mathcal{M})$ instead than from $p(d\,|\theta, \mathcal{M}) p(\theta|\mathcal{M})$ (i.e., the χ^2 for each model is divided by T). This lowers the height of the peak of the likelihood relatively to the tails and allows for better exploration of the latters. Under these assumptions, we find, using the WMAP data, that $\log(B_{\rm MCDM}) \simeq -4.3$, indicating a quite strong preference for the more complex MΛCDM model. In particular, the odds are $\sim 77:1$ in favour of this model. Adding the 2dF data makes the evidence in favour to the MΛCDM model even stronger: $\log(B_{\rm MCDM}) \simeq -4.9$, corresponding to odds of $\sim 133:1$.

Then we turn to the comparison of the MΛCDM with the concordance ΛCDM model. In this case the former model reduces to the latter for $n_1 = n_2$, whatever the value of k_*. In this case, always assuming the separability of the prior, the following generalization of the Savage-Dickey density ratio holds:

$$B_{\Lambda{\rm CDM}} \equiv \frac{p(d|\Lambda{\rm CDM})}{p(d|{\rm M\Lambda CDM})} = \\ = \int \left. \frac{p(n_1, n_2|d, {\rm M\Lambda CDM})}{p(n_2|{\rm M\Lambda CDM})} \right|_{n_2=n_1} dn_1. \quad \text{(G.1.7)}$$

We find that $\log(B_{\Lambda{\rm CDM}}) \simeq 0.77$ when using only the WMAP data, meaning that the evidence in favour of one or the other model is inconclusive. Adding the 2dF data yields $\log(B_{\Lambda{\rm CDM}}) \simeq 1.3$, corresponding to odds $7:2$, thus indicating a weak preference for the simpler ΛCDM model.

Finally we can combine the two results for $B_{\rm MCDM}$ and $B_{\Lambda{\rm CDM}}$ to compute the evidence of the ΛCDM model relative to the MCDM model, simply given by $B_{\Lambda{\rm CDM}}/B_{\rm MCDM}$. We get that $\log(B_{\Lambda{\rm CDM}}/B_{\rm MCDM}) \simeq 5.1$ or 6.2 using the WMAP-only or WMAP+2dF datasets respectively, indicating a strong preference for the concordance model with respect to broken power law spectrum, no-Λ models.

G.1.3. Conclusions

In this paper we have investigated the constraints on cosmological models with a broken power-law spectrum of primordial fluctuations. We have found that, using the WMAP data, it exists a weak preference for models with a redder spectrum after the break. In fact we find the constraint $\Delta n \equiv n_1 - n_2 = 0.095^{+0.087}_{-0.089}$ at 68% C.L. This preference tends to disappear when the 2dF data are taken into account. We also find that the limits on Ω_Λ are slightly relaxed with respect to the concordance ΛCDM model, allowing for smaller values of Ω_Λ. However, models with $\Omega_\Lambda = 0$ are still incompatible with the observations. The constraints obtained in this paper could be improved by using the small-scale data in the galaxy power spectrum on one side, and the Supernovae Ia and Hubble Space Telescope data on the other. The information from the smallest scales in the galaxy power spectrum would allow a more precise detemination of n_2, although it would crucially rely on a proper treatment of the non-linear effects. Using a prior on H would indirectly allow to reduce the constraints on n_2 by virtue of the correlation between the two parameters, as it is clear from the second panel of Fig .G.2. We do not expect instead that any of these additional data will improve the constrants on n_1, since it mainly affects the largest scales and is poorly degenerate with other parameters. Overall, using the non-linear scales and the Supernovae Ia or Hubble data will lead to a better determination of Δn.

We have also performed a bayesian model comparison analysis in order to assess whether models with a modified primordial spectrum provide a better interpretation of the WMAP and 2dF data. We find that the WMAP data alone are not yet able to discriminate between the models with a modified primordial spectrum considered here, and the concordance model. Considering also the 2dF data, we find that the concordance model is sligthly favoured. On the other hand, models with $\Omega_\Lambda = 0$ and a broken power-law primordial spectrum like those considered in Ref. Blanchard et al. (2003) are strongly disfavoured with respect to the concordance ΛCDM model.

Bibliography

ABDO, A.A., ACKERMANN, M., ARIMOTO, M., ASANO, K., ATWOOD, W.B., AXELSSON, M., BALDINI, L., BALLET, J., BAND, D.L., BARBIELLINI, G. ET AL.
Fermi Observations of High-Energy Gamma-Ray Emission from GRB 080916C.
Science, **323**, pp. 1688– (2009).
doi:10.1126/science.1169101.

ABDO, A.A. ET AL.
Measurement of the Cosmic Ray e+ plus e- spectrum from 20 GeV to 1 TeV with the Fermi Large Area Telescope.
Phys. Rev. Lett., **102**, p. 181101 (2009).
doi:10.1103/PhysRevLett.102.181101.

ABE, S. ET AL.
Precision Measurement of Neutrino Oscillation Parameters with KamLAND.
Phys. Rev. Lett., **100**, p. 221803 (2008).
doi:10.1103/PhysRevLett.100.221803.

ADRIANI, O. ET AL.
An anomalous positron abundance in cosmic rays with energies 1.5.100 GeV.
Nature, **458**, pp. 607–609 (2009).
doi:10.1038/nature07942.

AHARONIAN, .F.
Observations of the Sagittarius Dwarf galaxy by the H.E.S.S. experiment and search for a Dark Matter signal.
Astropart. Phys., **29**, pp. 55–62 (2008).
doi:10.1016/j.astropartphys.2007.11.007.

AHARONIAN, F. ET AL.
HESS observations of the galactic center region and their possible dark matter interpretation.
Phys. Rev. Lett., **97**, p. 221102 (2006).
doi:10.1103/PhysRevLett.97.221102.

AHARONIAN, F.A., ATOYAN, A.M. AND VOELK, H.J.
High energy electrons and positrons in cosmic rays as an indicator of the existence of a nearby cosmic tevatron.
A&A , **294**, pp. L41–L44 (1995).

AHARONIAN, H.E.S.S.C.F.
Probing the ATIC peak in the cosmic-ray electron spectrum with H.E.S.S (2009).

AHMAD, Q.R. ET AL.
Direct evidence for neutrino flavor transformation from neutral-current interactions in the Sudbury Neutrino Observatory.
Phys. Rev. Lett., **89**, p. 011301 (2002).
doi:10.1103/PhysRevLett.89.011301.

AKHMEDOV, E.K., BEREZHIANI, Z.G., MOHAPATRA, R.N. AND SENJANOVIC, G.
Planck scale effects on the majoron.
Phys. Lett., **B299**, pp. 90–93 (1993).
doi:10.1016/0370-2693(93)90887-N.

AKHMEDOV, E.K., BEREZHIANI, Z.G. AND SENJANOVIC, G.
Planck scale physics and neutrino masses.
Phys. Rev. Lett., **69**, pp. 3013–3016 (1992).
doi:10.1103/PhysRevLett.69.3013.

AKSENOV, A.G., BIANCO, C.L., RUFFINI, R. AND VERESHCHAGIN, G.V.
GRBs and the thermalization process of electron-positron plasmas.
In M. Galassi, D. Palmer, & E. Fenimore (ed.), *American Institute of Physics Conference Series*, volume 1000 of *American Institute of Physics Conference Series*, pp. 309–312 (2008).
doi:10.1063/1.2943471.

AKSENOV, A.G., MILGROM, M. AND USOV, V.V.
Structure of Pair Winds from Compact Objects with Application to Emission from Hot Bare Strange Stars.
ApJ , **609**, pp. 363–377 (2004).
doi:10.1086/421006.

AKSENOV, A.G., RUFFINI, R. AND VERESHCHAGIN, G.V.
Thermalization of Nonequilibrium Electron-Positron-Photon Plasmas.
Phys. Rev. Lett. , **99(12)**, pp. 125003–+ (2007).
doi:10.1103/PhysRevLett.99.125003.

AKSENOV, A.G., RUFFINI, R. AND VERESHCHAGIN, G.V.
Kinetics of the mildly relativistic plasma and GRBs.
to appear in the proceeding of the conference "The Sun, the Stars, the Universe, and General Relativity" held in Minsk, Belarus on April 20-23, 2009. (2009a).

AKSENOV, A.G., RUFFINI, R. AND VERESHCHAGIN, G.V.
Thermalization of the mildly relativistic plasma.
Phys. Rev. D, **79(4)**, p. 043008 (2009b).
doi:10.1103/PhysRevD.79.043008.

AKSENOV, A.G., RUFFINI, R. AND VERESHCHAGIN, G.V.
Pair plasma relaxation time scales.
Phys. Rev. E, **81**, p. 046401 (2010).

ALBERT, J. ET AL.
Upper limit for gamma-ray emission above 140 GeV from the dwarf spheroidal galaxy Draco.
Astrophys. J., **679**, pp. 428–431 (2008).
doi:10.1086/529135.

ALEXANDER, S. AND YUNES, N.
Chern-Simons Modified General Relativity.
Phys. Rept., **480**, pp. 1–55 (2009).
doi:10.1016/j.physrep.2009.07.002.

ALLANACH, B.C., DEDES, A. AND DREINER, H.K.
Bounds on R-parity violating couplings at the weak scale and at the GUT scale.
Phys. Rev., **D60**, p. 075014 (1999).
doi:10.1103/PhysRevD.60.075014.

ALOY, M.A., JANKA, H. AND MÜLLER, E.
Relativistic outflows from remnants of compact object mergers and their viability for short gamma-ray bursts.
A&A , **436**, pp. 273–311 (2005).
doi:10.1051/0004-6361:20041865.

ALOY, M.A., MÜLLER, E., IBÁÑEZ, J.M., MARTÍ, J.M. AND MACFADYEN, A.
Relativistic Jets from Collapsars.
ApJ , **531**, pp. L119–L122 (2000).
doi:10.1086/312537.

ANNINOS, P., FRAGILE, P.C. AND SALMONSON, J.D.
Cosmos++: Relativistic Magnetohydrodynamics on Unstructured Grids with Local Adaptive Refinement.
ApJ , **635**, pp. 723–740 (2005).
doi:10.1086/497294.

ARBOLINO, M.V. AND RUFFINI, R.
The ratio between the mass of the halo and visible matter in spiral galaxies and limits on the neutrino mass.
A&A , **192**, pp. 107–116 (1988).

ARCHIDIACONO, M., COORAY, A., MELCHIORRI, A. AND PANDOLFI, S.
CMB Neutrino Mass Bounds and Reionization.
Phys. Rev., **D82**, p. 087302 (2010).
doi:10.1103/PhysRevD.82.087302.

ARKANI-HAMED, N., FINKBEINER, D.P., SLATYER, T.R. AND WEINER, N.
A Theory of Dark Matter.
Phys. Rev., **D79**, p. 015014 (2009).
doi:10.1103/PhysRevD.79.015014.

ARMANDROFF, T.E., OLSZEWSKI, E.W. AND PRYOR, C.
The Mass-To-Light Ratios of the Draco and Ursa Minor Dwarf Spheroidal Galaxies.I. Radial Velocities from Multifiber Spectroscopy.
AJ, **110**, pp. 2131–+ (1995).
doi:10.1086/117675.

ASAKA, T., BLANCHET, S. AND SHAPOSHNIKOV, M.
The nuMSM, dark matter and neutrino masses.
Phys. Lett., **B631**, pp. 151–156 (2005).
doi:10.1016/j.physletb.2005.09.070.

ASAKA, T. AND SHAPOSHNIKOV, M.
The nuMSM, dark matter and baryon asymmetry of the universe.
Phys. Lett., **B620**, pp. 17–26 (2005).
doi:10.1016/j.physletb.2005.06.020.

ASHTEKAR, A.
New Variables for Classical and Quantum Gravity.
Phys. Rev. Lett., **57**, pp. 2244–2247 (1986).
doi:10.1103/PhysRevLett.57.2244.

ASHTEKAR, A.
New Hamiltonian Formulation of General Relativity.
Phys. Rev., **D36**, pp. 1587–1602 (1987).
doi:10.1103/PhysRevD.36.1587.

ASHTEKAR, A. AND LEWANDOWSKI, J.
Background independent quantum gravity: A status report.
Class. Quant. Grav., **21**, p. R53 (2004).
doi:10.1088/0264-9381/21/15/R01.

ASTIER, P. ET AL.
The Supernova Legacy Survey: Measurement of Ω_M, Ω_Λ and w from the First Year Data Set.
Astron. Astrophys., **447**, pp. 31–48 (2006).
doi:10.1051/0004-6361:20054185.

AVIGNONE, III, F.T., ELLIOTT, S.R. AND ENGEL, J.
Double Beta Decay, Majorana Neutrinos, and Neutrino Mass.
Rev. Mod. Phys., **80**, pp. 481–516 (2008).
doi:10.1103/RevModPhys.80.481.

AVILA-REESE, V., COLIN, P., VALENZUELA, O., D'ONGHIA, E. AND FIRMANI, C.
Formation and structure of halos in a warm dark matter cosmology.
Astrophys. J., **559**, pp. 516–530 (2001).
doi:10.1086/322411.

BAHCALL, N.A. AND FAN, X.H.
The Most massive distant clusters: Determining omega and sigma8.
Astrophys.J., **504**, p. 1 (1998).
doi:10.1086/306088.

BALTZ, E.A. ET AL.
Pre-launch estimates for GLAST sensitivity to Dark Matter annihilation signals.
JCAP, **0807**, p. 013 (2008).
doi:10.1088/1475-7516/2008/07/013.

BARBERO G., J.F.
Real Ashtekar variables for Lorentzian signature space times.
Phys. Rev., **D51**, pp. 5507–5510 (1995a).
doi:10.1103/PhysRevD.51.5507.

BARBERO G., J.F.
Reality conditions and Ashtekar variables: A Different perspective.
Phys. Rev., **D51**, pp. 5498–5506 (1995b).
doi:10.1103/PhysRevD.51.5498.

BARDEEN, J.M., BOND, J.R., KAISER, N. AND SZALAY, A.S.
The Statistics of Peaks of Gaussian Random Fields.
Astrophys. J., **304**, pp. 15–61 (1986).
doi:10.1086/164143.

BARKANA, R. AND LOEB, A.
Line-of-Sight Anisotropy of the 21cm Fluctuations Prior to Reionization.
Astrophys. J., **624**, pp. L65–L68 (2005).
doi:10.1086/430599.

BARKANA, R. AND LOEB, A.
The Physics and Early History of the Intergalactic Medium.
Rept. Prog. Phys., **70**, p. 627 (2007).
doi:10.1088/0034-4885/70/4/R02.

BARKOV, M.V. AND KOMISSAROV, S.S.
Central engines of Gamma Ray Bursts. Magnetic mechanism in the collapsar model.
In F. A. Aharonian, W. Hofmann, & F. Rieger (ed.), *American Institute of Physics Conference Series*, volume 1085 of *American Institute of Physics Conference Series*, pp. 608–611 (2008).

doi:10.1063/1.3076747.

BAZZOCCHI, F., LATTANZI, M., RIEMER-SORENSEN, S. AND VALLE, J.W.
X-ray photons from late-decaying majoron dark matter.
JCAP, **0808**, p. 013 (2008).
doi:10.1088/1475-7516/2008/08/013.
* Brief entry *.

BEACOM, J.F., BELL, N.F. AND BERTONE, G.
Gamma-ray constraint on Galactic positron production by MeV dark matter.
Phys. Rev. Lett., **94**, p. 171301 (2005).
doi:10.1103/PhysRevLett.94.171301.

BEACOM, J.F. AND YUKSEL, H.
Stringent Constraint on Galactic Positron Production.
Phys. Rev. Lett., **97**, p. 071102 (2006).
doi:10.1103/PhysRevLett.97.071102.

BEGEMAN, K.G., BROEILS, A.H. AND SANDERS, R.H.
Extended rotation curves of spiral galaxies - Dark haloes and modified dynamics.
MNRAS , **249**, pp. 523–537 (1991).

BELYAEV, S. AND BUDKER, G.
Relativistic Kinetic Equation.
DAN SSSR, **107**, pp. 807–810 (1956).

BEREZINSKY, V. AND VALLE, J.W.F.
The KeV majoron as a dark matter particle.
Phys. Lett., **B318**, pp. 360–366 (1993).
doi:10.1016/0370-2693(93)90140-D.

BERGSTROM, L., BERTONE, G., BRINGMANN, T., EDSJO, J. AND TAOSO, M.
Gamma-ray and Radio Constraints of High Positron Rate Dark Matter Models Annihilating into New Light Particles.
Phys. Rev., **D79**, p. 081303 (2009).

BERGSTROM, L., BRINGMANN, T. AND EDSJO, J.
New Positron Spectral Features from Supersymmetric Dark Matter - a Way to Explain the PAMELA Data?
Phys. Rev., **D78**, p. 103520 (2008).
doi:10.1103/PhysRevD.78.103520.

BERNABEI, R. ET AL.
Investigating pseudoscalar and scalar dark matter.
Int. J. Mod. Phys., **A21**, pp. 1445–1470 (2006).
doi:10.1142/S0217751X06030874.

BERNARDINI, M.G., BIANCO, C.L., CAITO, L., DAINOTTI, M.G., GUIDA, R. AND RUFFINI, R.
GRB 970228 and a class of GRBs with an initial spikelike emission.
A&A , **474**, pp. L13–L16 (2007).
doi:10.1051/0004-6361:20078300.

BERTONE, G., CIRELLI, M., STRUMIA, A. AND TAOSO, M.
Gamma-ray and radio tests of the e+e- excess from DM annihilations.
JCAP, **0903**, p. 009 (2009).
doi:10.1088/1475-7516/2009/03/009.

BERTONE, G., HOOPER, D. AND SILK, J.
Particle dark matter: Evidence, candidates and constraints.
Phys. Rept., **405**, pp. 279–390 (2005).
doi:10.1016/j.physrep.2004.08.031.

BEST, P.N. AND CONSORTIUM, T.L.U.
LOFAR-UK White Paper: A Science case for UK involvement in LOFAR (2008).

BETHE, H.A.
Supernova mechanisms.
Reviews of Modern Physics, **62**, pp. 801–866 (1990).
doi:10.1103/RevModPhys.62.801.

BIANCO, C.L., RUFFINI, R., VERESHCHAGIN, G. AND XUE, S.S.
Equations of motion, initial and boundary conditions for GRB.
J.Korean Phys.Soc., **49**, pp. 722–731 (2006).

BISNOVATYI-KOGAN, G.S. AND MURZINA, M.V.A.
Early stages of relativistic fireball expansion.
Phys. Rev. D, **52**, pp. 4380–4392 (1995).

BLANCHARD, A., DOUSPIS, M., ROWAN-ROBINSON, M. AND SARKAR, S.
An alternative to the cosmological 'concordance model'.
Astron. Astrophys., **412**, pp. 35–44 (2003).
doi:10.1051/0004-6361:20031425.

BODE, P., OSTRIKER, J.P. AND TUROK, N.
Halo formation in warm dark matter models.
Astrophys.J., **556**, pp. 93–107 (2001).
doi:10.1086/321541.

BOEHM, C. AND FAYET, P.
Scalar dark matter candidates.
Nucl. Phys., **B683**, pp. 219–263 (2004).
doi:10.1016/j.nuclphysb.2004.01.015.

BOEHM, C., FAYET, P. AND SILK, J.
Light and heavy dark matter particles.
Phys. Rev., **D69**, p. 101302 (2004).
doi:10.1103/PhysRevD.69.101302.

BOEHM, C. AND UWER, P.
Revisiting bremsstrahlung emission associated with light dark matter annihilations (2006).

BOEHM, C. AND SCHAEFFER, R.
Constraints on dark matter interactions from structure formation: Damping lengths (2004).

BOND, J.R., EFSTATHIOU, G. AND SILK, J.
Massive neutrinos and the large-scale structure of the universe.
Phys. Rev. Lett., **45**, pp. 1980–1984 (1980).
doi:10.1103/PhysRevLett.45.1980.

BOWERS, R.L. AND WILSON, J.R.
Numerical modeling in applied physics and astrophysics (1991).

BOWMAN, J.D., ROGERS, A.E.E. AND HEWITT, J.N.
Toward Empirical Constraints on the Global Redshifted 21 cm Brightness Temperature During the Epoch of Reionization.
ApJ , **676**, pp. 1–9 (2008).
doi:10.1086/528675.

BRIDGES, M., FEROZ, F., HOBSON, M.P. AND LASENBY, A.N.
Bayesian optimal reconstruction of the primordial power spectrum.
MNRAS , **400**, pp. 1075–1084 (2009).
doi:10.1111/j.1365-2966.2009.15525.x.

BRIDGES, M., LASENBY, A.N. AND HOBSON, M.P.
WMAP 3-yr primordial power spectrum.
MNRAS , **381**, pp. 68–74 (2007).
doi:10.1111/j.1365-2966.2007.11778.x.

BRIDGES, M., LASENBY, A.N. AND HOBSON, M.P.
A Bayesian analysis of the primordial power spectrum.
Mon. Not. Roy. Astron. Soc., **369**, pp. 1123–1130 (2006).
doi:10.1111/j.1365-2966.2006.10351.x.

BRINGMANN, T.
Particle Models and the Small-Scale Structure of Dark Matter.
New J. Phys., **11**, p. 105027 (2009).
doi:10.1088/1367-2630/11/10/105027.

BULLOCK, J.S. ET AL.
Profiles of dark haloes: evolution, scatter, and environment.
Mon. Not. Roy. Astron. Soc., **321**, pp. 559–575 (2001).
doi:10.1046/j.1365-8711.2001.04068.x.

BURKERT, A.
The Structure of dark matter halos in dwarf galaxies.
IAU Symp., **171**, p. 175 (1996).

CAITO, L., BERNARDINI, M.G., BIANCO, C.L., DAINOTTI, M.G., GUIDA, R. AND RUFFINI, R.
GRB060614: a "fake" short GRB from a merging binary system.
A&A , **498**, pp. 501–507 (2009).
doi:10.1051/0004-6361/200810676.

CALCAGNI, G. AND MERCURI, S.
The Barbero-Immirzi field in canonical formalism of pure gravity.
Phys. Rev., **D79**, p. 084004 (2009).
doi:10.1103/PhysRevD.79.084004.

CALDWELL, R.R. AND KAMIONKOWSKI, M.
The Physics of Cosmic Acceleration.
Ann. Rev. Nucl. Part. Sci., **59**, pp. 397–429 (2009).
doi:10.1146/annurev-nucl-010709-151330.

CALZETTI, D., GIAVALISCO, M. AND RUFFINI, R.
The normalization of the correlation functions for extragalactic structures.
A&A , **198**, pp. 1–2 (1988).

CALZETTI, D., GIAVALISCO, M., RUFFINI, R., EINASTO, J. AND SAAR, E.
The correlation function of galaxies in the direction of the Coma cluster.
Ap&SS, **137**, pp. 101–106 (1987).

CHANDIA, O. AND ZANELLI, J.
Topological invariants, instantons and chiral anomaly on spaces with torsion.
Phys. Rev., **D55**, pp. 7580–7585 (1997).
doi:10.1103/PhysRevD.55.7580.

CHANDIA, O. AND ZANELLI, J.
Reply to the comment by D. Kreimer and E. Mielke.
Phys. Rev., **D63**, p. 048502 (2001).
doi:10.1103/PhysRevD.63.048502.

CHANG, J. ET AL.
An excess of cosmic ray electrons at energies of 300.800 GeV.
Nature, **456**, pp. 362–365 (2008).
doi:10.1038/nature07477.

CHANG, L.N. AND SOO, C.
Massive torsion modes from Adler-Bell-Jackiw and scaling anomalies (1999).

CHEN, F., CLINE, J.M. AND FREY, A.R.
A new twist on excited dark matter: implications for INTEGRAL, PAMELA/ATIC/PPB-BETS, DAMA.
Phys. Rev., **D79**, p. 063530 (2009).
doi:10.1103/PhysRevD.79.063530.

CHEN, H., WILKS, S.C., BONLIE, J.D., LIANG, E.P., MYATT, J., PRICE, D.F., MEYERHOFER, D.D. AND BEIERSDORFER, P.
Relativistic Positron Creation Using Ultraintense Short Pulse Lasers.
Phys. Rev. Lett. , **102(10)**, pp. 105001–+ (2009).
doi:10.1103/PhysRevLett.102.105001.

CHEN, X.L. AND KAMIONKOWSKI, M.
Particle decays during the cosmic dark ages.
Phys. Rev., **D70**, p. 043502 (2004).
doi:10.1103/PhysRevD.70.043502.

CHIKASHIGE, Y., MOHAPATRA, R.N. AND PECCEI, R.D.
Are There Real Goldstone Bosons Associated with Broken Lepton Number?
Phys. Lett., **B98**, p. 265 (1981).
doi:10.1016/0370-2693(81)90011-3.

CHOLIS, I., DOBLER, G., FINKBEINER, D.P., GOODENOUGH, L. AND WEINER, N.
The Case for a 700+ GeV WIMP: Cosmic Ray Spectra from ATIC and PAMELA (2008).

CHOLIS, I., GOODENOUGH, L. AND WEINER, N.
High Energy Positrons and the WMAP Haze from Exciting Dark Matter.
Phys. Rev., **D79**, p. 123505 (2009).
doi:10.1103/PhysRevD.79.123505.

CHURAZOV, E., SUNYAEV, R., REVNIVTSEV, M., SAZONOV, S., MOLKOV, S., GREBENEV, S., WINKLER, C., PARMAR, A., BAZZANO, A., FALANGA, M. ET AL.
INTEGRAL observations of the cosmic X-ray background in the 5-100 keV range via occultation by the Earth.
A&A , **467**, pp. 529–540 (2007).
doi:10.1051/0004-6361:20066230.

CHURAZOV, E., SUNYAEV, R., SAZONOV, S., REVNIVTSEV, M. AND VARSHALOVICH, D.
Positron annihilation spectrum from the Galactic Centre region observed by SPI/INTEGRAL.

MNRAS , **357**, pp. 1377–1386 (2005).
doi:10.1111/j.1365-2966.2005.08757.x.

CHUZHOY, L.
Impact of Dark Matter Annihilation on the High-Redshift Intergalactic Medium (2007).

CIANFRANI, F. AND MONTANI, G.
The Immirzi parameter from an external scalar field.
Phys. Rev., **D80**, p. 084040 (2009).
doi:10.1103/PhysRevD.80.084040.

CIARDI, B. AND MADAU, P.
Probing Beyond the Epoch of Hydrogen Reionization with 21 Centimeter Radiation.
Astrophys. J., **596**, pp. 1–8 (2003).
doi:10.1086/377634.

CIRELLI, M., FRANCESCHINI, R. AND STRUMIA, A.
Minimal Dark Matter predictions for galactic positrons, anti-protons, photons.
Nucl. Phys., **B800**, pp. 204–220 (2008).
doi:10.1016/j.nuclphysb.2008.03.013.

CIRELLI, M., IOCCO, F. AND PANCI, P.
Constraints on Dark Matter annihilations from reionization and heating of the intergalactic gas.
JCAP, **0910**, p. 009 (2009a).
doi:10.1088/1475-7516/2009/10/009.

CIRELLI, M., KADASTIK, M., RAIDAL, M. AND STRUMIA, A.
Model-independent implications of the e+, e-, anti-proton cosmic ray spectra on properties of Dark Matter.
Nucl. Phys., **B813**, pp. 1–21 (2009b).
doi:10.1016/j.nuclphysb.2008.11.031.

CIRELLI, M. AND PANCI, P.
Inverse Compton constraints on the Dark Matter e+e- excesses.
Nucl. Phys., **B821**, pp. 399–416 (2009).
doi:10.1016/j.nuclphysb.2009.06.034.

CIRELLI, M. AND STRUMIA, A.
Minimal Dark Matter predictions and the PAMELA positron excess (2008).

CIRELLI, M., STRUMIA, A. AND TAMBURINI, M.
Cosmology and Astrophysics of Minimal Dark Matter.
Nucl. Phys., **B787**, pp. 152–175 (2007).
doi:10.1016/j.nuclphysb.2007.07.023.

COLE, S. ET AL.
The 2dF Galaxy Redshift Survey: Power-spectrum analysis of the final dataset and cosmological implications.
Mon. Not. Roy. Astron. Soc., **362**, pp. 505–534 (2005).
doi:10.1111/j.1365-2966.2005.09318.x.

COLEMAN, S.R.
Why There Is Nothing Rather Than Something: A Theory of the Cosmological Constant.
Nucl. Phys., **B310**, p. 643 (1988).
doi:10.1016/0550-3213(88)90097-1.

COLIN, P., VALENZUELA, O. AND AVILA-REESE, V.
On the Structure of Dark Matter Halos at the Damping Scale of the Power Spectrum with and without Relict Velocities.
Astrophys. J., **673**, pp. 203–214 (2008).
doi:10.1086/524030.

COORAY, A.R. AND FURLANETTO, S.R.
Free-Free Emission at Low Radio Frequencies.
Astrophys. J., **606**, pp. L5–L8 (2004).
doi:10.1086/421241.

CUMBERBATCH, D.T., LATTANZI, M., SILK, J., LATTANZI, M. AND SILK, J.
Signatures of clumpy dark matter in the global 21 cm background signal.
Phys. Rev., **D82**, p. 103508 (2010).
doi:10.1103/PhysRevD.82.103508.

CUMBERBATCH, D.T., ZUNTZ, J., ERIKSEN, H.K.K. AND SILK, J.
Can the WMAP Haze really be a signature of annihilating neutralino dark matter?
(2009).

DALCANTON, J.J. AND HOGAN, C.J.
Halo Cores and Phase Space Densities: Observational Constraints on Dark Matter Physics and Structure Formation.
Astrophys. J., **561**, pp. 35–45 (2001).
doi:10.1086/323207.

DAMOUR, T. AND RUFFINI, R.
Quantum electrodynamical effects in Kerr-Newman geometries.
Phys. Rev. Lett. , **35**, pp. 463–466 (1975).

DE BARROS, G., RUFFINI, R. AND VERESHCHAGIN, G.V.
On hydrodynamic phase of grb sources.
Astronomy and Astrophysics, **submitted** (2009).

DE BOER, W.
Indirect Dark Matter Signals from EGRET and PAMELA compared.
AIP Conf. Proc., **1166**, pp. 169–178 (2009).
doi:10.1063/1.3232175.

DEHNEN, W. AND MCLAUGHLIN, D.
Dynamical insight into dark-matter haloes.
Mon. Not. Roy. Astron. Soc., **363**, pp. 1057–1068 (2005).
doi:10.1111/j.1365-2966.2005.09510.x.

DI MATTEO, T., PERNA, R., ABEL, T. AND REES, M.J.
Radio Foregrounds for the 21cm Tomography of the Neutral Intergalactic Medium at High Redshifts.
Astrophys. J., **564**, pp. 576–580 (2002).
doi:10.1086/324293.

DICKINSON, C., BATTYE, R.A., CARREIRA, P., CLEARY, K., DAVIES, R.D. ET AL.
High sensitivity measurements of the CMB power spectrum with the extended Very Small Array.
Mon.Not.Roy.Astron.Soc., **353**, p. 732 (2004).
doi:10.1111/j.1365-2966.2004.08206.x.

DIEMAND, J. ET AL.
Clumps and streams in the local dark matter distribution.
Nature, **454**, pp. 735–738 (2008).
doi:10.1038/nature07153.

DIEMAND, J., KUHLEN, M. AND MADAU, P.
Formation and evolution of galaxy dark matter halos and their substructure.
Astrophys. J., **667**, p. 859 (2007).
doi:10.1086/520573.

DOBLER, G., FINKBEINER, D.P., CHOLIS, I., SLATYER, T.R. AND WEINER, N.
The Fermi Haze: A Gamma-Ray Counterpart to the Microwave Haze.
Astrophys. J., **717**, pp. 825–842 (2010).
doi:10.1088/0004-637X/717/2/825.

DODELSON, S. AND WIDROW, L.M.
Sterile-neutrinos as dark matter.
Phys.Rev.Lett., **72**, pp. 17–20 (1994).
doi:10.1103/PhysRevLett.72.17.

DOLGOV, A.D.
Neutrinos in cosmology.
Phys. Rep. , **370**, pp. 333–535 (2002).

DONATO, F., MAURIN, D., BRUN, P., DELAHAYE, T. AND SALATI, P.
Constraints on WIMP Dark Matter from the High Energy PAMELA $\bar{p}/p$ data.
Phys. Rev. Lett., **102**, p. 071301 (2009).
doi:10.1103/PhysRevLett.102.071301.

DONATO, F. AND SALUCCI, P.
Cores of Dark Matter Halos Correlate with Disk Scale Lengths.
Mon. Not. Roy. Astron. Soc., **353**, pp. L17–L22 (2004).

DÖNMEZ, O.
Solving 1-D special relativistic hydrodynamics (SRH) equations using different numerical methods and results from different test problems.
Applied Mathematics and Computation, **181**, p. 256270 (2006).
doi:10.1016/j.amc.2006.01.031.

DREXLIN, G.
KATRIN: Direct measurement of a sub-eV neutrino mass.
Nucl. Phys. Proc. Suppl., **145**, pp. 263–267 (2005).
doi:10.1016/j.nuclphysbps.2005.04.019.

DUNKLEY, J. ET AL.
Five-Year Wilkinson Microwave Anisotropy Probe (WMAP) Observations: Likelihoods and Parameters from the WMAP data.
Astrophys. J. Suppl., **180**, pp. 306–329 (2009).
doi:10.1088/0067-0049/180/2/306.

EGUCHI, K. ET AL.
First results from KamLAND: Evidence for reactor anti- neutrino disappearance.
Phys. Rev. Lett., **90**, p. 021802 (2003).
doi:10.1103/PhysRevLett.90.021802.

EVANS, N.W., FERRER, F. AND SARKAR, S.
A 'Baedecker' for the dark matter annihilation signal.
Phys. Rev., **D69**, p. 123501 (2004).
doi:10.1103/PhysRevD.69.123501.

FELDMAN, D., LIU, Z., NATH, P. AND PEIM, G.
Multicomponent Dark Matter in Supersymmetric Hidden Sector Extensions.
Phys. Rev., **D81**, p. 095017 (2010).
doi:10.1103/PhysRevD.81.095017.

FIELD, G.B.
An Attempt to Observe Neutral Hydrogen Between the Galaxies.
ApJ , **129**, pp. 525–+ (1959).
doi:10.1086/146652.

FINKBEINER, D.P., PADMANABHAN, N. AND WEINER, N.
CMB and 21-cm Signals for Dark Matter with a Long-Lived Excited State.
Phys. Rev., **D78**, p. 063530 (2008).
doi:10.1103/PhysRevD.78.063530.

FINKBEINER, D.P. AND WEINER, N.
Exciting Dark Matter and the INTEGRAL/SPI 511 keV signal.
Phys. Rev., **D76**, p. 083519 (2007).
doi:10.1103/PhysRevD.76.083519.

FLORES, R.A. AND PRIMACK, J.R.
Observational and theoretical constraints on singular dark matter halos.
Astrophys. J., **427**, pp. L1–4 (1994).

FREEDMAN, W.L. ET AL.
Final Results from the Hubble Space Telescope Key Project to Measure the Hubble Constant.
Astrophys. J., **553**, pp. 47–72 (2001).
doi:10.1086/320638.

FRIEMAN, J., TURNER, M. AND HUTERER, D.
Dark Energy and the Accelerating Universe.
Ann. Rev. Astron. Astrophys., **46**, pp. 385–432 (2008).
doi:10.1146/annurev.astro.46.060407.145243.

FUKUDA, Y. ET AL.
Evidence for oscillation of atmospheric neutrinos.
Phys. Rev. Lett., **81**, pp. 1562–1567 (1998).
doi:10.1103/PhysRevLett.81.1562.

FURLANETTO, S. AND FURLANETTO, M.
Spin Exchange Rates in Electron-Hydrogen Collisions.
Mon. Not. Roy. Astron. Soc., **374**, pp. 547–555 (2007a).
doi:10.1111/j.1365-2966.2006.11169.x.

FURLANETTO, S. AND FURLANETTO, M.
Spin Exchange Rates in Proton-Hydrogen Collisions.
Mon. Not. Roy. Astron. Soc., **379**, pp. 130–134 (2007b).
doi:10.1111/j.1365-2966.2007.11921.x.

FURLANETTO, S., OH, S.P. AND BRIGGS, F.
Cosmology at Low Frequencies: The 21 cm Transition and the High-Redshift Universe.
Phys. Rept., **433**, pp. 181–301 (2006a).
doi:10.1016/j.physrep.2006.08.002.

FURLANETTO, S.R., OH, S.P. AND PIERPAOLI, E.
The Effects of Dark Matter Decay and Annihilation on the High-Redshift 21 cm Background.
Phys. Rev., **D74**, p. 103502 (2006b).
doi:10.1103/PhysRevD.74.103502.

GALLI, S., IOCCO, F., BERTONE, G. AND MELCHIORRI, A.
CMB constraints on Dark Matter models with large annihilation cross-section.
Phys. Rev., **D80**, p. 023505 (2009).
doi:10.1103/PhysRevD.80.023505.

GAO, J.G. AND RUFFINI, R.
Relativistic limits on the masses of self-gravitating systems of degenerate neutrinos.
Physics Letters B, **97**, pp. 388–390 (1980).

GAO, L.
Mon. Not. Roy. Astron. Soc., **387**, p. 536 (2008).

GATES, JR., S.J., KETOV, S.V. AND YUNES, N.
Seeking the Loop Quantum Gravity Barbero-Immirzi Parameter and Field in 4D, $\mathcal{N}$ = 1 Supergravity.
Phys. Rev., **D80**, p. 065003 (2009).
doi:10.1103/PhysRevD.80.065003.

GEHRELS, N., SARAZIN, C.L., O'BRIEN, P.T., ZHANG, B., BARBIER, L., BARTHELMY, S.D., BLUSTIN, A., BURROWS, D.N., CANNIZZO, J., CUMMINGS, J.R. ET AL.
A short γ-ray burst apparently associated with an elliptical galaxy at redshift z = 0.225.
Nature , **437**, pp. 851–854 (2005).
doi:10.1038/nature04142.

GELMINI, G., SCHRAMM, D.N. AND VALLE, J.W.F.
MAJORONS: A SIMULTANEOUS SOLUTION TO THE LARGE AND SMALL SCALE DARK MATTER PROBLEMS.
Phys. Lett., **B146**, p. 311 (1984).
doi:10.1016/0370-2693(84)91703-9.

GENTILE, G., SALUCCI, P., KLEIN, U., VERGANI, D. AND KALBERLA, P.
The cored distribution of dark matter in spiral galaxies.
Mon. Not. Roy. Astron. Soc., **351**, p. 903 (2004).
doi:10.1111/j.1365-2966.2004.07836.x.

GENTILE, G., SALUCCI, P., KLEIN, U. AND GRANATO, G.L.
NGC 3741: dark halo profile from the most extended rotation curve.

Mon. Not. Roy. Astron. Soc., **375**, pp. 199–212 (2007).
doi:10.1111/j.1365-2966.2006.11283.x.

GERSTNER, E.
Laser physics: Lasing at the limit.
Nature Physics, **6**, pp. 638–+ (2010).
doi:10.1038/nphys1785.

GIAVALISCO, M.
Ph.D. thesis, University of Rome "La Sapienza" (1992).

GIDDINGS, S.B. AND STROMINGER, A.
Loss of Incoherence and Determination of Coupling Constants in Quantum Gravity.
Nucl. Phys., **B307**, p. 854 (1988).
doi:10.1016/0550-3213(88)90109-5.

GIOCOLI, C., PIERI, L. AND TORMEN, G.
Analytical approach to subhalo population in dark matter haloes.
MNRAS , **387**, pp. 689–697 (2008).
doi:10.1111/j.1365-2966.2008.13283.x.

GIOCOLI, C., PIERI, L., TORMEN, G. AND MORENO, J.
A merger tree with microsolar mass resolution: application to γ-ray emission from subhalo population.
MNRAS , **395**, pp. 1620–1630 (2009).
doi:10.1111/j.1365-2966.2009.14649.x.

GIUDICE, G.F., KOLB, E.W. AND RIOTTO, A.
Largest temperature of the radiation era and its cosmological implications.
Phys. Rev., **D64**, p. 023508 (2001).
doi:10.1103/PhysRevD.64.023508.

GOULD, R.J.
Kinetic theory of relativistic plasmas.
Physics of Fluids, **24**, pp. 102–107 (1981).

GRAJEK, P., KANE, G., PHALEN, D., PIERCE, A. AND WATSON, S.
Is the PAMELA Positron Excess Winos?
Phys. Rev., **D79**, p. 043506 (2009).
doi:10.1103/PhysRevD.79.043506.

GREEN, A.M., HOFMANN, S. AND SCHWARZ, D.J.
The power spectrum of SUSY-CDM on sub-galactic scales.
Mon. Not. Roy. Astron. Soc., **353**, p. L23 (2004).

GREEN, A.M., HOFMANN, S. AND SCHWARZ, D.J.
The first WIMPy halos.
JCAP, **0508**, p. 003 (2005).
doi:10.1088/1475-7516/2005/08/003.

GROSS, D.J., PISARSKI, R.D. AND YAFFE, L.G.
QCD and Instantons at Finite Temperature.
Rev. Mod. Phys., **53**, p. 43 (1981).
doi:10.1103/RevModPhys.53.43.

HALL, L.J. AND SUZUKI, M.
Explicit R-Parity Breaking in Supersymmetric Models.
Nucl. Phys., **B231**, p. 419 (1984).
doi:10.1016/0550-3213(84)90513-3.

HAMANN, J., HANNESTAD, S., RAFFELT, G.G. AND WONG, Y.Y.Y.
Isocurvature forecast in the anthropic axion window.
JCAP, **0906**, p. 022 (2009).
doi:10.1088/1475-7516/2009/06/022.

HARKER, G. ET AL.
Non-parametric foreground subtraction for 21cm epoch of reionization experiments (2009).

HAYASHI, E., NAVARRO, J.F., TAYLOR, J.E., STADEL, J. AND QUINN, T.R.
The Structural Evolution of Substructure.
Astrophys. J., **584**, pp. 541–558 (2003).
doi:10.1086/345788.

HINSHAW, G. ET AL.
Three-year Wilkinson Microwave Anisotropy Probe (WMAP) observations: temperature analysis.
Astrophys.J.Suppl., **170**, p. 288 (2007).
doi:10.1086/513698.

HIRATA, C.M.
Wouthuysen-Field coupling strength and application to high-redshift 21 cm radiation.
Mon. Not. Roy. Astron. Soc., **367**, pp. 259–274 (2006).
doi:10.1111/j.1365-2966.2005.09949.x.

HIRSCH, M., DIAZ, M.A., POROD, W., ROMAO, J.C. AND VALLE, J.W.F.
Neutrino masses and mixings from supersymmetry with bilinear R-parity violation: A theory for solar and atmospheric neutrino oscillations.
Phys. Rev., **D62**, p. 113008 (2000).
doi:10.1103/PhysRevD.62.113008.

HIRSCH, M. AND VALLE, J.W.F.
Supersymmetric origin of neutrino mass.
New J. Phys., **6**, p. 76 (2004).
doi:10.1088/1367-2630/6/1/076.

HISANO, J., MATSUMOTO, S. AND NOJIRI, M.M.
Explosive dark matter annihilation.
Phys. Rev. Lett., **92**, p. 031303 (2004).
doi:10.1103/PhysRevLett.92.031303.

HISANO, J., MATSUMOTO, S., NOJIRI, M.M. AND SAITO, O.
Non-perturbative effect on dark matter annihilation and gamma ray signature from galactic center.
Phys. Rev., **D71**, p. 063528 (2005).
doi:10.1103/PhysRevD.71.063528.

HOFMANN, S., SCHWARZ, D.J. AND STOECKER, H.
Damping scales of neutralino cold dark matter.
Phys. Rev., **D64**, p. 083507 (2001).
doi:10.1103/PhysRevD.64.083507.

HOGAN, C.J. AND DALCANTON, J.J.
New dark matter physics: Clues from halo structure.
Phys. Rev., **D62**, p. 063511 (2000).
doi:10.1103/PhysRevD.62.063511.

HOOPER, D., BLASI, P. AND SERPICO, P.D.
Pulsars as the Sources of High Energy Cosmic Ray Positrons.
JCAP, **0901**, p. 025 (2009a).
doi:10.1088/1475-7516/2009/01/025.

HOOPER, D., FINKBEINER, D.P. AND DOBLER, G.
Evidence Of Dark Matter Annihilations In The WMAP Haze.
Phys. Rev., **D76**, p. 083012 (2007).
doi:10.1103/PhysRevD.76.083012.

HOOPER, D., STEBBINS, A. AND ZUREK, K.M.
Excesses in cosmic ray positron and electron spectra from a nearby clump of neutralino dark matter.
Phys. Rev., **D79**, p. 103513 (2009b).
doi:10.1103/PhysRevD.79.103513.

HOOPER, D., TAYLOR, J.E. AND SILK, J.
Can supersymmetry naturally explain the positron excess?
Phys. Rev., **D69**, p. 103509 (2004).
doi:10.1103/PhysRevD.69.103509.

Hooper, D. and Zurek, K.M.
The PAMELA and ATIC Signals From Kaluza-Klein Dark Matter.
Phys. Rev., **D79**, p. 103529 (2009).
doi:10.1103/PhysRevD.79.103529.

Ibata, R.A., Wyse, R.F.G., Gilmore, G., Irwin, M.U. and Suntzeff, N.B.
The Kinematics, Orbit, and Survival of the Sagittarius Dwarf Spheroidal Galaxy.
Astron. J., **113**, pp. 634–655 (1997).
doi:10.1086/118283.

Ichiki, K., Oguri, M. and Takahashi, K.
WMAP Constraints on Decaying Cold Dark Matter.
Phys. Rev. Lett., **93**, p. 071302 (2004).
doi:10.1103/PhysRevLett.93.071302.

Immirzi, G.
Quantum gravity and Regge calculus.
Nucl. Phys. Proc. Suppl., **57**, pp. 65–72 (1997a).
doi:10.1016/S0920-5632(97)00354-X.

Immirzi, G.
Real and complex connections for canonical gravity.
Class. Quant. Grav., **14**, pp. L177–L181 (1997b).
doi:10.1088/0264-9381/14/10/002.

Izzo, L. and et al.
In *Proceedings of the First Galileo - Xu Guangqi meeting held in October 26-30, 2009 Shanghai (China)* (In press, 2010).

Janka, H., Langanke, K., Marek, A., Martínez-Pinedo, G. and Müller, B.
Theory of core-collapse supernovae.
Phys. Rep. , **442**, pp. 38–74 (2007).
doi:10.1016/j.physrep.2007.02.002.

Jenkins, A. et al.
Evolution of structure in cold dark matter universes.
Astrophys. J., **499**, p. 20 (1998).
doi:10.1086/305615.

Jones, W.C., Ade, P., Bock, J., Bond, J., Borrill, J. et al.
A Measurement of the angular power spectrum of the CMB temperature anisotropy from the 2003 flight of BOOMERANG.
Astrophys.J., **647**, pp. 823–832 (2006).
doi:10.1086/505559.

Kamionkowski, M. and Profumo, S.
Early Annihilation and Diffuse Backgrounds in Models of Weakly Interacting Massive Particles in Which the Cross Section for Pair Annihilation Is Enhanced by 1/v.
Phys. Rev. Lett., **101**, p. 261301 (2008).
doi:10.1103/PhysRevLett.101.261301.

Kaplinghat, M., Lopez, R.E., Dodelson, S. and Scherrer, R.J.
Improved Treatment of Cosmic Microwave Background Fluctuations Induced by a Late-decaying Massive Neutrino.
Phys. Rev., **D60**, p. 123508 (1999).
doi:10.1103/PhysRevD.60.123508.

Katz, J.I.
A Cubic Micron of Equilibrium Pair Plasma?
ApJS , **127**, pp. 371–373 (2000).
doi:10.1086/313350.

Klapdor-Kleingrothaus, H.V., Krivosheina, I.V., Dietz, A. and Chkvorets, O.
Search for neutrinoless double beta decay with enriched 76Ge in Gran Sasso 1990-2003.
Phys. Lett., **B586**, pp. 198–212 (2004).
doi:10.1016/j.physletb.2004.02.025.

Knebe, A., Arnold, B., Power, C. and Gibson, B.K.
The Dynamics of Subhalos in Warm Dark Matter Models (2008).

Knodlseder, J. et al.
The all-sky distribution of 511-keV electron positron annihilation emission.
Astron. Astrophys., **441**, pp. 513–532 (2005).
doi:10.1051/0004-6361:20042063.

Kolb, E.W. and Turner, M.S.
The Early Universe (Frontiers in Physics, Reading, MA: Addison-Wesley, 1990).

Komatsu, E. et al.
Five-Year Wilkinson Microwave Anisotropy Probe (WMAP) Observations:Cosmological Interpretation.
Astrophys. J. Suppl., **180**, pp. 330–376 (2009).
doi:10.1088/0067-0049/180/2/330.

Komatsu, E. et al.
Seven-Year Wilkinson Microwave Anisotropy Probe (WMAP) Observations: Cosmological Interpretation (2010).

KREIMER, D. AND MIELKE, E.W.
Comment on: Topological invariants, instantons, and the chiral anomaly on spaces with torsion.
Phys. Rev., **D63**, p. 048501 (2001).
doi:10.1103/PhysRevD.63.048501.

KUHLEN, M., DIEMAND, J. AND MADAU, P.
The Dark Matter Annihilation Signal from Galactic Substructure: Predictions for GLAST (2008).

KUHLEN, M., MADAU, P. AND MONTGOMERY, R.
The spin temperature and 21cm brightness of the intergalactic medium in the pre-reionization era.
Astrophys. J., **637**, pp. L1–L4 (2006).
doi:10.1086/500548.

KUO, C.L., ADE, P., BOCK, J., BOND, J., CONTALDI, C. ET AL.
Improved Measurements of the CMB Power Spectrum with ACBAR.
Astrophys.J., **664**, pp. 687–701 (2007).
doi:10.1086/518401.

KUZNETSOVA, I., HABS, D. AND RAFELSKI, J.
Thermal reaction processes in a relativistic QED plasma drop.
Phys. Rev. D, **81(5)**, pp. 053007–+ (2010).
doi:10.1103/PhysRevD.81.053007.

LARSON, D., DUNKLEY, J., HINSHAW, G., KOMATSU, E., NOLTA, M. ET AL.
Seven-Year Wilkinson Microwave Anisotropy Probe (WMAP) Observations: Power Spectra and WMAP-Derived Parameters (2010).

LATTANZI, M., RUFFINI, R. AND VERESHCHAGIN, G.
On the possible role of massive neutrinos in cosmological structure formation.
In M. Novello and S.E. Perez Bergliaffa (eds.), *Cosmology and Gravitation*, volume 668 of *American Institute of Physics Conference Series*, pp. 263–287 (2003).

LATTANZI, M., RUFFINI, R. AND VERESHCHAGIN, G.V.
Joint constraints on the lepton asymmetry of the Universe and neutrino mass from the Wilkinson Microwave Anisotropy Probe.
Phys. Rev. D, **72(6)**, pp. 063003–+ (2005).
doi:10.1103/PhysRevD.72.063003.

LATTANZI, M., RUFFINI, R. AND VERESHCHAGIN, G.V.
Do WMAP data constraint the lepton asymmetry of the Universe to be zero?
In *Albert Einstein Century International Conference*, volume 861 of *American Institute of Physics Conference Series*, pp. 912–919 (2006).
doi:10.1063/1.2399677.

LATTANZI, M. AND VALLE, J.W.F.
Decaying warm dark matter and neutrino masses.
Phys. Rev. Lett., **99**, p. 121301 (2007).
doi:10.1103/PhysRevLett.99.121301.

LATTANZI, M.
The majoron: a new dark matter candidate.
J. Kor. Phys. Soc., **56**, p. 1677 (2010).

LATTANZI, M. AND MERCURI, S.
A solution of the strong CP problem via the Peccei-Quinn mechanism through the Nieh-Yan modified gravity and cosmological implications.
Phys.Rev., **D81**, p. 125015 (2010).
doi:10.1103/PhysRevD.81.125015.

LATTANZI, M. AND SILK, J.I.
Can the WIMP annihilation boost factor be boosted by the Sommerfeld enhancement?
Phys. Rev., **D79**, p. 083523 (2009).
doi:10.1103/PhysRevD.79.083523.

LAVALLE, J., YUAN, Q., MAURIN, D. AND BI, X.
Full calculation of clumpiness boost factors for antimatter cosmic rays in the light of ΛCDM N-body simulation results. Abandoning hope in clumpiness enhancement?
A&A , **479**, pp. 427–452 (2008).
doi:10.1051/0004-6361:20078723.

LEE, B.W. AND WEINBERG, S.
Cosmological lower bound on heavy-neutrino masses.
Phys. Rev. Lett. , **39**, pp. 165–168 (1977).

LEIGH, R.G., HOANG, N.N. AND PETKOU, A.C.
Torsion and the Gravity Dual of Parity Symmetry Breaking in AdS4/CFT3 Holography.
JHEP, **03**, p. 033 (2009).
doi:10.1088/1126-6708/2009/03/033.

LESGOURGUES, J. AND PASTOR, S.
Massive neutrinos and cosmology.
Phys. Rept., **429**, pp. 307–379 (2006).
doi:10.1016/j.physrep.2006.04.001.

LEWIS, A., CHALLINOR, A. AND LASENBY, A.
Efficient Computation of CMB anisotropies in closed FRW models.
Astrophys. J., **538**, pp. 473–476 (2000).
doi:10.1086/309179.

LISZT, H.
The spin temperature of warm interstellar H I.
A&A , **371**, pp. 698–707 (2001).
doi:10.1051/0004-6361:20010395.

LIU, A., TEGMARK, M., BOWMAN, J., HEWITT, J. AND ZALDARRIAGA, M.
An Improved Method for 21cm Foreground Removal (2009a).

LIU, J., YIN, P.F. AND ZHU, S.H.
Prospects for Detecting Neutrino Signals from Annihilating/Decaying Dark Matter to Account for the PAMELA and ATIC results.
Phys. Rev., **D79**, p. 063522 (2009b).
doi:10.1103/PhysRevD.79.063522.

LOEB, A. AND ZALDARRIAGA, M.
The small-scale power spectrum of cold dark matter.
Phys. Rev., **D71**, p. 103520 (2005).
doi:10.1103/PhysRevD.71.103520.

LYTH, D.H. AND STEWART, E.D.
Axions and inflation: String formation during inflation.
Phys. Rev., **D46**, pp. 532–538 (1992).
doi:10.1103/PhysRevD.46.532.

MA, C.P. AND BERTSCHINGER, E.
Cosmological perturbation theory in the synchronous and conformal Newtonian gauges.
Astrophys. J., **455**, pp. 7–25 (1995).
doi:10.1086/176550.

MACK, G.D., JACQUES, T.D., BEACOM, J.F., BELL, N.F. AND YUKSEL, H.
Conservative Constraints on Dark Matter Annihilation into Gamma Rays.
Phys. Rev., **D78**, p. 063542 (2008).
doi:10.1103/PhysRevD.78.063542.

MADAU, P., MEIKSIN, A. AND REES, M.J.
21-cm Tomography of the Intergalactic Medium at High Redshift.
Astrophys. J., **475**, p. 429 (1997).
doi:10.1086/303549.

MALTONI, M., SCHWETZ, T., TORTOLA, M.A. AND VALLE, J.W.F.
Status of global fits to neutrino oscillations.
New J. Phys., **6**, p. 122 (2004).
doi:10.1088/1367-2630/6/1/122.

MARCH-RUSSELL, J., WEST, S.M., CUMBERBATCH, D. AND HOOPER, D.
Heavy Dark Matter Through the Higgs Portal.

JHEP, **07**, p. 058 (2008).
doi:10.1088/1126-6708/2008/07/058.

MARCH-RUSSELL, J.D. AND WEST, S.M.
WIMPonium and Boost Factors for Indirect Dark Matter Detection.
Phys. Lett., **B676**, pp. 133–139 (2009).
doi:10.1016/j.physletb.2009.04.010.

MARTINS, C.J.A.P., MENEGONI, E., GALLI, S., MANGANO, G. AND MELCHIORRI, A.
Varying couplings in the early universe: correlated variations of α and G.
Phys. Rev., **D82**, p. 023532 (2010).
doi:10.1103/PhysRevD.82.023532.

MATHEWS, G., LAN, N. AND KOLDA, C.
Late Decaying Dark Matter, Bulk Viscosity and the Cosmic Acceleration.
Phys.Rev., **D78**, p. 043525 (2008).
doi:10.1103/PhysRevD.78.043525.

MCKINNEY, J.C.
General relativistic magnetohydrodynamic simulations of the jet formation and large-scale propagation from black hole accretion systems.
MNRAS , **368**, pp. 1561–1582 (2006).
doi:10.1111/j.1365-2966.2006.10256.x.

MCQUINN, M., ZAHN, O., ZALDARRIAGA, M., HERNQUIST, L. AND FURLANETTO, S.R.
Cosmological Parameter Estimation Using 21 cm Radiation from the Epoch of Reionization.
Astrophys. J., **653**, pp. 815–830 (2006).
doi:10.1086/505167.

MELCHIORRI, A., DE BERNARDIS, F. AND MENEGONI, E.
Limits on the neutrino mass from cosmology.
AIP Conf. Proc., **1256**, pp. 96–106 (2010).
doi:10.1063/1.3473882.

MENEGONI, E., PANDOLFI, S., GALLI, S., LATTANZI, M. AND MELCHIORRI, A.
Constraints on the Dark Energy Equation of State in Presence of a Varying Fine Structure Constant.
International Journal of Modern Physics D, **19**, pp. 507–512 (2010).
doi:10.1142/S0218271810016506.

MENEGONI, E.
New constraints on variations of fine structure constant from cosmic microwave background anisotropies.

AIP Conf. Proc., **1256**, pp. 288–292 (2010).
doi:10.1063/1.3473868.

MENEGONI, E., GALLI, S., BARTLETT, J.G., MARTINS, C.J.A.P. AND MELCHIORRI, A.
New Constraints on variations of the fine structure constant from CMB anisotropies.
Phys. Rev., **D80**, p. 087302 (2009).
doi:10.1103/PhysRevD.80.087302.

MERCURI, S.
Peccei–Quinn mechanism in gravity and the nature of the Barbero–Immirzi parameter.
Phys. Rev. Lett., **103**, p. 081302 (2009).
doi:10.1103/PhysRevLett.103.081302.

MERCURI, S. AND TAVERAS, V.
Interaction of the Barbero–Immirzi Field with Matter and Pseudo-Scalar Perturbations.
Phys. Rev., **D80**, p. 104007 (2009).
doi:10.1103/PhysRevD.80.104007.

MEREGHETTI, S.
The strongest cosmic magnets: soft gamma-ray repeaters and anomalous X-ray pulsars.
A&A Rev., **15**, pp. 225–287 (2008).
doi:10.1007/s00159-008-0011-z.

MESZAROS, P.
Gamma-ray bursts.
Reports of Progress in Physics, **69**, pp. 2259–2322 (2006).

MÉSZÁROS, P., LAGUNA, P. AND REES, M.J.
Gasdynamics of relativistically expanding gamma-ray burst sources - Kinematics, energetics, magnetic fields, and efficiency.
ApJ , **415**, pp. 181–190 (1993).

MIHALAS, D. AND MIHALAS, B.W.
Foundations of Radiation Hydrodynamics (New York, Oxford University Press, 1984).

MIRALDA-ESCUDÉ, J.
A Test of the Collisional Dark Matter Hypothesis from Cluster Lensing.
ApJ , **564**, pp. 60–64 (2002).
doi:10.1086/324138.

MOORE, B.
Evidence against dissipationless dark matter from observations of galaxy haloes.
Nature, **370**, p. 629 (1994).
doi:10.1038/370629a0.

MOORE, B., QUINN, T.R., GOVERNATO, F., STADEL, J. AND LAKE, G.
Cold collapse and the core catastrophe.
Mon. Not. Roy. Astron. Soc., **310**, pp. 1147–1152 (1999).
doi:10.1046/j.1365-8711.1999.03039.x.

MUSTAFA, M.G. AND KÄMPFER, B.
Gamma flashes from relativistic electron-positron plasma droplets.
Phys. Rev. A, **79(2)**, pp. 020103–+ (2009).
doi:10.1103/PhysRevA.79.020103.

MYATT, J., DELETTREZ, J.A., MAXIMOV, A.V., MEYERHOFER, D.D., SHORT, R.W., STOECKL, C. AND STORM, M.
Optimizing electron-positron pair production on kilojoule-class high-intensity lasers for the purpose of pair-plasma creation.
Phys. Rev. E, **79(6)**, pp. 066409–+ (2009).
doi:10.1103/PhysRevE.79.066409.

NARAYAN, R., PACZYNSKI, B. AND PIRAN, T.
Gamma-ray bursts as the death throes of massive binary stars.
ApJ , **395**, pp. L83–L86 (1992).

NATARAJAN, A. AND SCHWARZ, D.J.
Dark matter annihilation and its effect on CMB and Hydrogen 21 cm observations.
Phys. Rev., **D80**, p. 043529 (2009).
doi:10.1103/PhysRevD.80.043529.

NAVARRO, J.F., FRENK, C.S. AND WHITE, S.D.M.
The Structure of Cold Dark Matter Halos.
Astrophys. J., **462**, pp. 563–575 (1996).
doi:10.1086/177173.

NAVARRO, J.F., FRENK, C.S. AND WHITE, S.D.M.
A Universal Density Profile from Hierarchical Clustering.
Astrophys. J., **490**, pp. 493–508 (1997).

NAVARRO, J.F. ET AL.
The Diversity and Similarity of Cold Dark Matter Halos (2008).

NIEH, H.T. AND YAN, M.L.
AN IDENTITY IN RIEMANN-CARTAN GEOMETRY.
J. Math. Phys., **23**, p. 373 (1982).
doi:10.1063/1.525379.

OBUKHOV, Y.N., MIELKE, E.W., BUDCZIES, J. AND HEHL, F.W.
On the chiral anomaly in non-Riemannian spacetimes.
Found. Phys., **27**, pp. 1221–1236 (1997).
doi:10.1007/BF02551525.

OH, S.P. AND MACK, K.J.
Foregrounds for 21cm Observations of Neutral Gas at High Redshift.
Mon. Not. Roy. Astron. Soc., **346**, p. 871 (2003).

OSTRIKER, J.P. AND STEINHARDT, P.J.
New light on dark matter.
Science, **300**, pp. 1909–1913 (2003).
doi:10.1126/science.1085976.

PADMANABHAN, N. AND FINKBEINER, D.P.
Detecting Dark Matter Annihilation with CMB Polarization : Signatures and Experimental Prospects.
Phys. Rev., **D72**, p. 023508 (2005).
doi:10.1103/PhysRevD.72.023508.

PAGE, L. ET AL.
Three year Wilkinson Microwave Anisotropy Probe (WMAP) observations: polarization analysis.
Astrophys.J.Suppl., **170**, p. 335 (2007).
doi:10.1086/513699.

PAGELS, H. AND PRIMACK, J.R.
Supersymmetry, Cosmology and New TeV Physics.
Phys. Rev. Lett., **48**, p. 223 (1982).
doi:10.1103/PhysRevLett.48.223.

PANDOLFI, S., GIUSARMA, E., LATTANZI, M. AND MELCHIORRI, A.
Inflation with primordial broken power law spectrum as an alternative to the concordance cosmological model.
Phys. Rev., **D81**, p. 103007 (2010a).
doi:10.1103/PhysRevD.81.103007.

PANDOLFI, S. ET AL.
Harrison-Z'eldovich primordial spectrum is consistent with observations.
Phys. Rev., **D81**, p. 123509 (2010b).
doi:10.1103/PhysRevD.81.123509.

PANDOLFI, S. ET AL.
Impact of general reionization scenarios on extraction of inflationary parameters (2010c).

PATO, M., PIERI, L. AND BERTONE, G.
Multi-messenger constraints on the annihilating dark matter interpretation of the positron excess (2009).

PECCEI, R.D.
Discrete and global symmetries in particle physics (1998).

PECCEI, R.D. AND QUINN, H.R.
Constraints Imposed by CP Conservation in the Presence of Instantons.
Phys. Rev., **D16**, pp. 1791–1797 (1977a).
doi:10.1103/PhysRevD.16.1791.

PECCEI, R.D. AND QUINN, H.R.
CP Conservation in the Presence of Instantons.
Phys. Rev. Lett., **38**, pp. 1440–1443 (1977b).
doi:10.1103/PhysRevLett.38.1440.

PEEBLES, P.J.E.
Principles of physical cosmology (Princeton Series in Physics, Princeton, NJ: Princeton University Press, —c1993, 1993).

PEEBLES, P.J.E. AND RATRA, B.
The cosmological constant and dark energy.
Rev. Mod. Phys., **75**, pp. 559–606 (2003).
doi:10.1103/RevModPhys.75.559.

PENGELLY, R.M.
Recombination spectra, I.
MNRAS , **127**, pp. 145–+ (1964).

PERLMUTTER, S. ET AL.
Measurements of Omega and Lambda from 42 High-Redshift Supernovae.
Astrophys. J., **517**, pp. 565–586 (1999).
doi:10.1086/307221.

PIACENTINI, F., ADE, P., BOCK, J., BOND, J., BORRILL, J. ET AL.
A Measurement of the polarization-temperature angular cross power spectrum of the cosmic microwave background from the 2003 flight of BOOMERANG.
Astrophys.J., **647**, pp. 833–839 (2006).
doi:10.1086/505557.

PIERI, L., BERTONE, G. AND BRANCHINI, E.
Dark Matter Annihilation in Substructures Revised.
Mon. Not. Roy. Astron. Soc., **384**, p. 1627 (2008).
doi:10.1111/j.1365-2966.2007.12828.x.

PIERI, L., PIZZELLA, A., CORSINI, E.M., BONTA', E.D. AND BERTOLA, F.
Could the Fermi-LAT detect gamma-rays from dark matter annihilation in the dwarf galaxies of the Local Group?
Astron. Astrophys., **496**, p. 351 (2009a).

PIERI, L., LATTANZI, M. AND SILK, J.
Constraining the Sommerfeld enhancement with Cherenkov telescope observations of dwarf galaxies (2009b).

PILLA, R.P. AND SHAHAM, J.
Kinetics of Electron-Positron Pair Plasmas Using an Adaptive Monte Carlo Method.
ApJ , **486**, pp. 903–+ (1997).
doi:10.1086/304534.

PIRAN, T.
Gamma-ray bursts and the fireball model.
Phys. Rep. , **314**, pp. 575–667 (1999).

PIRAN, T., SHEMI, A. AND NARAYAN, R.
Hydrodynamics of Relativistic Fireballs.
MNRAS , **263**, pp. 861–867 (1993).

POSPELOV, M. AND RITZ, A.
Astrophysical Signatures of Secluded Dark Matter.
Phys. Lett., **B671**, pp. 391–397 (2009).
doi:10.1016/j.physletb.2008.12.012.

PRANTZOS, N., BOEHM, C., BYKOV, A.M., DIEHL, R., FERRIERE, K., GUESSOUM, N., JEAN, P., KNOEDLSEDER, J., MARCOWITH, A., MOSKALENKO, I.V. ET AL.
The 511 keV emission from positron annihilation in the Galaxy.
ArXiv e-prints (2010).
Submitted to Rev. Mod. Phys.

PREPARATA, G., RUFFINI, R. AND XUE, S.
The dyadosphere of black holes and gamma-ray bursts.
A&A , **338**, pp. L87–L90 (1998).

PRESS, W.H. AND SCHECHTER, P.
Formation of galaxies and clusters of galaxies by selfsimilar gravitational condensation.
Astrophys. J., **187**, pp. 425–438 (1974).
doi:10.1086/152650.

PRITCHARD, J.R. AND FURLANETTO, S.R.
21 cm fluctuations from inhomogeneous X-ray heating before reionization.

Mon. Not. Roy. Astron. Soc., **376**, pp. 1680–1694 (2007).
doi:10.1111/j.1365-2966.2007.11519.x.

PRITCHARD, J.R. AND LOEB, A.
Evolution of the 21 cm signal throughout cosmic history.
Phys. Rev., **D78**, p. 103511 (2008).
doi:10.1103/PhysRevD.78.103511.

PROFUMO, S.
TeV gamma-rays and the largest masses and annihilation cross sections of neutralino dark matter.
Phys. Rev., **D72**, p. 103521 (2005).
doi:10.1103/PhysRevD.72.103521.

PROFUMO, S., SIGURDSON, K. AND KAMIONKOWSKI, M.
What mass are the smallest protohalos?
Phys. Rev. Lett., **97**, p. 031301 (2006).
doi:10.1103/PhysRevLett.97.031301.

PURCELL, E.M. AND FIELD, G.B.
Influence of Collisions upon Population of Hyperfine States in Hydrogen.
ApJ , **124**, pp. 542–+ (1956).
doi:10.1086/146259.

READHEAD, A., MASON, B., CONTALDI, C., PEARSON, T.J., BOND, J. ET AL.
Extended mosaic observations with the Cosmic Background Imager.
Astrophys.J., **609**, pp. 498–512 (2004).
doi:10.1086/421105.

REES, M.J. AND MESZAROS, P.
Relativistic fireballs - Energy conversion and time-scales.
MNRAS , **258**, pp. 41P–43P (1992).

REES, M.J. AND MESZAROS, P.
Unsteady outflow models for cosmological gamma-ray bursts.
ApJ , **430**, pp. L93–L96 (1994).
doi:10.1086/187446.

RIESS, A.G. ET AL.
Observational Evidence from Supernovae for an Accelerating Universe and a Cosmological Constant.
Astron. J., **116**, pp. 1009–1038 (1998).
doi:10.1086/300499.

RIPAMONTI, E., MAPELLI, M. AND FERRARA, A.
Intergalactic medium heating by dark matter.
Mon. Not. Roy. Astron. Soc., **374**, pp. 1067–1077 (2007).

doi:10.1111/j.1365-2966.2006.11222.x.

ROBERTSON, B. AND ZENTNER, A.
Dark Matter Annihilation Rates with Velocity-Dependent Annihilation Cross Sections.
Phys. Rev., **D79**, p. 083525 (2009).

ROGERS, A.E.E. AND BOWMAN, J.D.
Spectral Index of the Diffuse Radio Background Measured from 100 TO 200 MHz.
AJ, **136**, pp. 641–648 (2008).
doi:10.1088/0004-6256/136/2/641.

RUFFINI, R.
On the de Vaucouleurs density-radius relation and the cellular intermediate large-scale structure of the universe.
In H.G. Corwin Jr. and L. Bottinelli (eds.), *World of Galaxies (Le Monde des Galaxies)*, pp. 461–472 (1989).

RUFFINI, R., AKSENOV, A.G., BERNARDINI, M.G., BIANCO, C.L., CAITO, L., CHARDONNET, P., DAINOTTI, M.G., DE BARROS, G., GUIDA, R., IZZO, L. ET AL.
The Blackholic energy and the canonical Gamma-Ray Burst IV: the "long," "genuine short" and "fake-disguised short" GRBs.
In M. Novello and S. Perez (eds.), *American Institute of Physics Conference Series*, volume 1132 of *American Institute of Physics Conference Series*, pp. 199–266 (2009).
doi:10.1063/1.3151839.

RUFFINI, R., BERNARDINI, M.G., BIANCO, C.L., CAITO, L., CHARDONNET, P., DAINOTTI, M.G., FRASCHETTI, F., GUIDA, R., ROTONDO, M., VERESHCHAGIN, G. ET AL.
The Blackholic energy and the canonical Gamma-Ray Burst.
In *American Institute of Physics Conference Series*, volume 910 of *American Institute of Physics Conference Series*, pp. 55–217 (2007).
doi:10.1063/1.2752480.

RUFFINI, R., BIANCO, C.L., FRASCHETTI, F., XUE, S. AND CHARDONNET, P.
On the Interpretation of the Burst Structure of Gamma-Ray Bursts.
ApJ , **555**, pp. L113–L116 (2001).
doi:10.1086/323176.

RUFFINI, R., SALMONSON, J.D., WILSON, J.R. AND XUE, S.S.
On the pair electromagnetic pulse of a black hole with electromagnetic structure.
A&A , **350**, pp. 334–343 (1999).

RUFFINI, R., SALMONSON, J.D., WILSON, J.R. AND XUE, S.S.

On the pair-electromagnetic pulse from an electromagnetic black hole surrounded by a baryonic remnant.
A&A , **359**, pp. 855–864 (2000).

RUFFINI, R., SONG, D.J. AND TARAGLIO, S.
The 'ino' mass and the cellular large-scale structure of the universe.
A&A , **190**, pp. 1–2 (1988).

RUFFINI, R., VERESHCHAGIN, G. AND XUE, S.S.
Electron-positron pairs in physics and astrophysics.
Physics Reports, **487**, pp. 1–140 (2010).

SALUCCI, P. AND BURKERT, A.
Dark Matter Scaling Relations.
Astrophys. J., **537**, pp. L9–L12 (2000).
doi:10.1086/312747.

SALUCCI, P. ET AL.
The universal rotation curve of spiral galaxies. II: The dark matter distribution out to the virial radius.
Mon. Not. Roy. Astron. Soc., **378**, pp. 41–47 (2007).
doi:10.1111/j.1365-2966.2007.11696.x.

SCHECHTER, J. AND VALLE, J.W.F.
Neutrino Masses in SU(2) x U(1) Theories.
Phys. Rev., **D22**, p. 2227 (1980).
doi:10.1103/PhysRevD.22.2227.

SCHECHTER, J. AND VALLE, J.W.F.
Neutrino Decay and Spontaneous Violation of Lepton Number.
Phys. Rev., **D25**, p. 774 (1982).
doi:10.1103/PhysRevD.25.774.

SEAGER, S., SASSELOV, D.D. AND SCOTT, D.
A New Calculation of the Recombination Epoch.
Astrophys. J., **523**, pp. L1–L5 (1999).
doi:10.1086/312250.

SEAGER, S., SASSELOV, D.D. AND SCOTT, D.
How exactly did the Universe become neutral?
Astrophys. J. Suppl., **128**, pp. 407–430 (2000).
doi:10.1086/313388.

SELJAK, U., MAKAROV, A., MCDONALD, P. AND TRAC, H.
Can sterile neutrinos be the dark matter?
Phys. Rev. Lett., **97**, p. 191303 (2006).
doi:10.1103/PhysRevLett.97.191303.

SERRA, P. ET AL.
No Evidence for Dark Energy Dynamics from a Global Analysis of Cosmological Data.
Phys. Rev., **D80**, p. 121302 (2009).
doi:10.1103/PhysRevD.80.121302.

SHAVER, P.A., WINDHORST, R.A., MADAU, P. AND DE BRUYN, A.G.
Can the reionization epoch be detected as a global signature in the cosmic background?
A&A , **345**, pp. 380–390 (1999).

SHCHEKINOV, Y.A. AND VASILIEV, E.O.
Particle decay in the early universe: predictions for 21 cm.
Mon. Not. Roy. Astron. Soc., **379**, pp. 1003–1010 (2007).
doi:10.1111/j.1365-2966.2007.11715.x.

SHEMI, A. AND PIRAN, T.
The appearance of cosmic fireballs.
ApJ , **365**, pp. L55–L58 (1990).

SHEN, B. AND MEYER-TER-VEHN, J.
Pair and γ-photon production from a thin foil confined by two laser pulses.
Phys. Rev. E, **65(1)**, pp. 016405–+ (2002).
doi:10.1103/PhysRevE.65.016405.

SHETH, R.K. AND TORMEN, G.
An Excursion set model of hierarchical clustering : Ellipsoidal collapse and the moving barrier.
Mon. Not. Roy. Astron. Soc., **329**, p. 61 (2002).
doi:10.1046/j.1365-8711.2002.04950.x.

SHULL, J.M. AND VAN STEENBERG, M.E.
X-ray secondary heating and ionization in quasar emission-line clouds.
ApJ , **298**, pp. 268–274 (1985).
doi:10.1086/163605.

SILK, J. AND SREDNICKI, M.
Cosmic-ray antiprotons as a probe of a photino-dominated universe.
Phys. Rev. Lett., **53**, p. 624 (1984).
doi:10.1103/PhysRevLett.53.624.

SJOSTRAND, T. ET AL.
High-energy physics event generation with PYTHIA 6.1.
Comput. Phys. Commun., **135**, pp. 238–259 (2001).
doi:10.1016/S0010-4655(00)00236-8.

SMITH, F.J.
Hydrogen atom spin-change collisions.
Planet. Space Sci., **14**, pp. 929–+ (1966).
doi:10.1016/0032-0633(66)90130-9.

SOMMERFELD, A.
.
Annalen der Physik, **403**, p. 257 (1931).

SOO, C.
Adler-Bell-Jackiw anomaly, the Nieh-Yan form and vacuum polarization.
Phys. Rev., **D59**, p. 045006 (1999).
doi:10.1103/PhysRevD.59.045006.

SPERGEL, D.N. ET AL.
First Year Wilkinson Microwave Anisotropy Probe (WMAP) Observations: Determination of Cosmological Parameters.
Astrophys. J. Suppl., **148**, pp. 175–194 (2003).
doi:10.1086/377226.

SPERGEL, D. ET AL.
Wilkinson Microwave Anisotropy Probe (WMAP) three year results: implications for cosmology.
Astrophys.J.Suppl., **170**, p. 377 (2007).
doi:10.1086/513700.

SPRINGEL, V. ET AL.
Prospects for detecting supersymmetric dark matter in the Galactic halo.
Nature, **456N7218**, pp. 73–80 (2008a).
doi:10.1038/nature07411.

SPRINGEL, V. ET AL.
The Aquarius Project: the subhalos of galactic halos.
Mon. Not. Roy. Astron. Soc., **391**, pp. 1685–1711 (2008b).
doi:10.1111/j.1365-2966.2008.14066.x.

SREEKUMAR, P. ET AL.
EGRET observations of the extragalactic gamma ray emission.
Astrophys. J., **494**, pp. 523–534 (1998).
doi:10.1086/305222.

STEPNEY, S.
Two-body relaxation in relativistic thermal plasmas.
MNRAS , **202**, pp. 467–481 (1983).

STRONG, A.W., MOSKALENKO, I.V. AND REIMER, O.

A new determination of the extragalactic diffuse gamma-ray background from EGRET data.
Astrophys. J., **613**, pp. 956–961 (2004).
doi:10.1086/423196.

TAVERAS, V. AND YUNES, N.
The Barbero-Immirzi Parameter as a Scalar Field: K- Inflation from Loop Quantum Gravity?
Phys. Rev., **D78**, p. 064070 (2008).
doi:10.1103/PhysRevD.78.064070.

TAYLOR, J.E. AND SILK, J.
The clumpiness of cold dark matter: Implications for the annihilation signal.
Mon. Not. Roy. Astron. Soc., **339**, p. 505 (2003).
doi:10.1046/j.1365-8711.2003.06201.x.

TEGMARK, M., AGUIRRE, A., REES, M. AND WILCZEK, F.
Dimensionless constants, cosmology and other dark matters.
Phys. Rev., **D73**, p. 023505 (2006a).
doi:10.1103/PhysRevD.73.023505.

TEGMARK, M., VILENKIN, A. AND POGOSIAN, L.
Anthropic predictions for neutrino masses.
Phys. Rev., **D71**, p. 103523 (2005).
doi:10.1103/PhysRevD.71.103523.

TEGMARK, M. ET AL.
The 3D power spectrum of galaxies from the SDSS.
Astrophys. J., **606**, pp. 702–740 (2004).
doi:10.1086/382125.

TEGMARK, M. ET AL.
Cosmological Constraints from the SDSS Luminous Red Galaxies.
Phys. Rev., **D74**, p. 123507 (2006b).
doi:10.1103/PhysRevD.74.123507.

THOMA, M.H.
Colloquium: Field theoretic description of ultrarelativistic electron-positron plasmas.
Reviews of Modern Physics, **81**, pp. 959–968 (2009).
doi:10.1103/RevModPhys.81.959.

THOMPSON, K.W.
The special relativistic shock tube.
Journal of Fluid Mechanics, **171**, pp. 365–375 (1986).
doi:10.1017/S0022112086001489.

TORMEN, G., MOSCARDINI, L. AND YOSHIDA, N.
Properties of cluster satellites in hydrodynamical simulations.
MNRAS , **350**, pp. 1397–1408 (2004).
doi:10.1111/j.1365-2966.2004.07736.x.

TREMAINE, S. AND GUNN, J.E.
Dynamical role of light neutral leptons in cosmology.
Phys. Rev. Lett. , **42**, pp. 407–410 (1979).

TROTTA, R.
Bayes in the sky: Bayesian inference and model selection in cosmology.
Contemp. Phys., **49**, pp. 71–104 (2008).

TURNER, M.S.
Cosmic and Local Mass Density of Invisible Axions.
Phys. Rev., **D33**, pp. 889–896 (1986).
doi:10.1103/PhysRevD.33.889.

UEHLING, E.A.
Transport Phenomena in Einstein-Bose and Fermi-Dirac Gases. II.
Physical Review, **46**, pp. 917–929 (1934).
doi:10.1103/PhysRev.46.917.

UEHLING, E.A. AND UHLENBECK, G.E.
Transport Phenomena in Einstein-Bose and Fermi-Dirac Gases. I.
Physical Review, **43**, pp. 552–561 (1933).
doi:10.1103/PhysRev.43.552.

ULLIO, P., BERGSTROM, L., EDSJO, J. AND LACEY, C.G.
Cosmological dark matter annihilations into gamma-rays: A closer look.
Phys. Rev., **D66**, p. 123502 (2002).
doi:10.1103/PhysRevD.66.123502.

VALDES, M., FERRARA, A., MAPELLI, M. AND RIPAMONTI, E.
Constraining DM through 21 cm observations.
Mon. Not. Roy. Astron. Soc., **377**, pp. 245–252 (2007).
doi:10.1111/j.1365-2966.2007.11594.x.

VALLE, J.W.F.
Neutrino physics overview.
J. Phys. Conf. Ser., **53**, pp. 473–505 (2006).
doi:10.1088/1742-6596/53/1/031.

VASS, I., VALLURI, M., KRAVTSOV, A. AND KAZANTZIDIS, S.
Evolution of the Dark Matter Phase-Space Density Distributions of LCDM Halos.
Mon. Not. Roy. Astron. Soc., **395**, pp. 1225–1236 (2009).

VISINELLI, L. AND GONDOLO, P.
Dark Matter Axions Revisited.
Phys. Rev., **D80**, p. 035024 (2009).
doi:10.1103/PhysRevD.80.035024.

WALKER, M.G., MATEO, M., OLSZEWSKI, E.W., GNEDIN, O.Y., WANG, X., SEN, B. AND WOODROOFE, M.
Velocity Dispersion Profiles of Seven Dwarf Spheroidal Galaxies.
ApJ , **667**, pp. L53–L56 (2007).
doi:10.1086/521998.

WALKER, M.G. ET AL.
A Universal Mass Profile for Dwarf Spheroidal Galaxies.
Astrophys. J., **704**, pp. 1274–1287 (2009).
doi:10.1088/0004-637X/704/2/1274.

WECHSLER, R.H., BULLOCK, J.S., PRIMACK, J.R., KRAVTSOV, A.V. AND DEKEL, A.
Concentrations of Dark Halos from their Assembly Histories.
Astrophys. J., **568**, pp. 52–70 (2002).
doi:10.1086/338765.

WEIDENSPOINTNER, G., VARENDORFF, M., KAPPADATH, S.C., BENNETT, K., BLOEMEN, H., DIEHL, R., HERMSEN, W., LICHTI, G.G., RYAN, J. AND SCHÖNFELDER, V.
The cosmic diffuse gamma-ray background measured with COMPTEL.
In M. L. McConnell & J. M. Ryan (ed.), *American Institute of Physics Conference Series*, volume 510 of *American Institute of Physics Conference Series*, pp. 467–470 (2000).
doi:10.1063/1.1307028.

WEINBERG, S.
Cosmology (Oxford University Press, April 2008., 2008).

WEINBERG, S.
A New Light Boson?
Phys. Rev. Lett., **40**, pp. 223–226 (1978).
doi:10.1103/PhysRevLett.40.223.

WEINBERG, S.
Supersymmetry at Ordinary Energies. 1. Masses and Conservation Laws.
Phys. Rev., **D26**, p. 287 (1982).
doi:10.1103/PhysRevD.26.287.

WELDRAKE, D., DE BLOK, E. AND WALTER, F.
A High-Resolution Rotation Curve of NGC 6822: A Test-case for Cold Dark Matter.

Mon. Not. Roy. Astron. Soc., **340**, pp. 12–28 (2003).
doi:10.1046/j.1365-8711.2003.06170.x.

WILCZEK, F.
Problem of Strong p and t Invariance in the Presence of Instantons.
Phys. Rev. Lett., **40**, pp. 279–282 (1978).
doi:10.1103/PhysRevLett.40.279.

WILKS, S.C., KRUER, W.L., TABAK, M. AND LANGDON, A.B.
Absorption of ultra-intense laser pulses.
Physical Review Letters, **69**, pp. 1383–1386 (1992).
doi:10.1103/PhysRevLett.69.1383.

WILSON, J.R. AND MATHEWS, G.J.
Relativistic Numerical Hydrodynamics (2003).

WOOD-VASEY, W. ET AL.
Observational Constraints on the Nature of the Dark Energy: First Cosmological Results from the ESSENCE Supernova Survey.
Astrophys.J., **666**, pp. 694–715 (2007).
doi:10.1086/518642.

WOUTHUYSEN, S.A.
On the excitation mechanism of the 21-cm (radio-frequency) interstellar hydrogen emission line.
AJ, **57**, pp. 31–32 (1952).
doi:10.1086/106661.

YUAN, Q., YUE, B., BI, X., CHEN, X. AND ZHANG, X.
Leptonic dark matter annihilation in the evolving universe: constraints and implications.
JCAP, **1010**, p. 023 (2010).
doi:10.1088/1475-7516/2010/10/023.

YUKSEL, H., KISTLER, M.D. AND STANEV, T.
TeV Gamma Rays from Geminga and the Origin of the GeV Positron Excess.
Phys. Rev. Lett., **103**, p. 051101 (2009).
doi:10.1103/PhysRevLett.103.051101.

YUNES, N. AND PRETORIUS, F.
Dynamical Chern-Simons Modified Gravity I: Spinning Black Holes in the Slow-Rotation Approximation.
Phys. Rev., **D79**, p. 084043 (2009).
doi:10.1103/PhysRevD.79.084043.

ZANK, G.P. AND GREAVES, R.G.
Linear and nonlinear modes in nonrelativistic electron-positron plasmas.

Phys. Rev. E, **51**, pp. 6079–6090 (1995).
doi:10.1103/PhysRevE.51.6079.

ZDZIARSKI, A.A.
Spectra from pair-equilibrium plasmas.
ApJ , **283**, pp. 842–847 (1984).
doi:10.1086/162370.

ZHANG, B., DAI, X., LLOYD-RONNING, N.M. AND MÉSZÁROS, P.
Quasi-universal Gaussian Jets: A Unified Picture for Gamma-Ray Bursts and X-Ray Flashes.
ApJ , **601**, pp. L119–L122 (2004).
doi:10.1086/382132.

ZHANG, L., CHEN, X.L., LEI, Y.A. AND SI, Z.G.
The impacts of dark matter particle annihilation on recombination and the anisotropies of the cosmic microwave background.
Phys. Rev., **D74**, p. 103519 (2006).
doi:10.1103/PhysRevD.74.103519.